VERTICAL CAVITY SURFACE EMITTING LASERS

by: **TERENCE EDWARD SALE**

September 1993.

A thesis submitted for the degree of Doctor of Philosophy in the Department of Electronic and Electrical Engineering of the University of Sheffield.

VERTICAL CAVITY SURFACE EMITTING LASERS

by: T. E. SALE.

Abstract

Vertical cavity surface emitting laser (VCSEL) structures have been grown by both metal-organic chemical vapour deposition (MOCVD) and molecular beam epitaxy (MBE). These incorporate 3 strained InGaAs / GaAs quantum wells placed resonantly in a two wavelength long optical cavity, formed between AlAs / GaAs quarter wave dielectric reflector stacks through which current is injected.

The reflection spectra of these stacks is studied in detail; the effects on the laser threshold gain of absorption due to impurities and of errors in growth are investigated. Methods of disruption of the AlAs / GaAs heterointerfaces have been used to reduce the operating voltage. The completed designs use 200Å intermediate layers containing 30 or 50% aluminium or a superlattice graded region simpler than that used in previous designs. The effectiveness acceptor dopants; Be in MBE, C and Zn in MOCVD; is studied also. Modulation doping was employed to reduce the effects of optical absorption.

Devices were fabricated into mesas by $SiCl_4$ reactive ion etching or defined by proton implant isolation. MBE grown devices were resonant at wavelengths in the range 950 to 1059nm with essentially constant (at ~1020nm) e_1hh_1 transition energies in the wells. A detailed study of the wavelength variation of threshold current density ($J_{th}(\lambda)$) was made. A minimum of 366A.cm^{-2} was measured at 1018nm in mesa devices. A similar relation is found for ion-implanted devices but the minimum is increased to 535A.cm^{-2} by incomplete isolation. Gain calculations, including strain effects, are used to explain the $J_{th}(\lambda)$ variation.

Implanted devices offer superior c.w. performance due to reduced thermal and ohmic resistances. The relative offset between the gain spectrum and cavity resonance was examined for c.w. operation. It was found that carrier thermal effects limit the output power rather than shifts in the offset.

The bias voltage of MOCVD grown devices is as low as 1.7V and the threshold current is as low as 764A.cm^{-2}. This is higher than for MBE grown devices because of growth thickness errors and non-optimal alignment of the gain spectrum and cavity mode. The uniformity in emission wavelength is ±1% over 80% of a 2inch diameter wafer, offering suitability for very large uniform arrays.

Vertical Cavity Surface Emitting Lasers

By: T. E. Sale. 1993

Contents:

This thesis is dedicated....

To my parents

.......for their continued support and encouragement.

.....And all this science I don't understand
It's just my job five days a week......

R.Dwight & B.Taupin.

Acknowledgements

I would like to say a few words of thanks to those people who have offered assistance, encouragement or just been there during the course of my work for this thesis.

Many thanks go to Dr. Jon Woodhead and to Professor Peter Robson for their help and guidance in their role as supervisors of this work, and for proof reading this thesis.

Thanks also to all the staff of the SERC III-V central facility at the University of Sheffield and in particular; to Dr. Bob Grey for MBE growth of the complex VCSEL structures reported in this work despite the enormous workload of his reactor, to Dr. John Roberts for his patience in carrying out my suggestions for MOCVD growth, to Malcolm Pate for performing reactive ion etching and to Dr. John David for performing low temperature photoluminescence measurements.

Thankyou to Dr. Chris Jeynes and Dr. Zaeem Jafri at the ion beam facility at the University of Surrey for performing proton isolation implants, and to the SERC for providing a pump priming grant to fund this.

During the course of my studies I was supported by a Science and Engineering Research Council (SERC) postgraduate studentship. Extra funding was supplied under the European Community FOCUS basic research program. Thankyou also to Professor Peter Robson for making available departmental funds to feed me during the period between the end of my grant and the start of my research appointment, for which I am grateful to Dr. Graham Rees for allowing me to start before the submission of this thesis.

I would also like to thank those who have not been directly involved in this work but whose presence has nonetheless been invaluable: I would like to acknowledge all my fellow postgraduate students and postdoctoral researchers during my time at Sheffield, in particular Dr. Mike Reddy, Mark Morley, Arbinder (Pebbles) Pabla, Dr. Tae-Woo Lee, Andy Wolstenholme, Mike Woodward and S.R.D. Kalingamudali. Thanks are also due to all the technical staff who maintain the departmental cleanrooms and other facilities. Thankyou to my parents, to whom I dedicate this thesis, for always supporting me in what I chose to do. Last but by no means least, special thanks to Laurie Miller for her continued help and encouragement not to mention the semi-permanent loan of her printer which has been used in the production of this thesis.

Thanks very much to you all!

Abbreviations

The following abbreviations have been used in this thesis:

c.w.	Continuous wave
CMOS	Complimentary metal oxide silicon
d.c.	Direct current
fig.	Figure
FP	Fabry-Perot
FWHM	Full width at half maximum
I-V	Current versus voltage
L-I	Current versus light
MBE	Molecular beam epitaxy
MOCVD	Metal organic chemical vapour deposition
PC	Personal computer
PL	Photoluminescence
s.d.	Standard deviation
SEL	Surface emitting laser
TMA	Trimethylaluminium
TMG	Trimethylgallium
TMI	Trimethylindium
DEZ	Diethylzinc
VLSI	Very large scale integration
VCSEL	Vertical cavity surface emitting laser
2-D	Two dimensional

Standard chemical abbreviations such as GaAs - gallium asenide have been used. Quantities have been quoted in S.I. or cgs units in keeping with those generally used in the literature.

1. Introduction

The vertical cavity surface emitting laser (VCSEL) offers the possibility of large 2-dimensional (2-D) arrays of coherent light sources[1]. Laser arrays have applications in optical computing and offer the promise of new types of displays. The low divergence circular beam profile of a device with circular geometry is more efficiently coupled into an optical fibre than the elliptical output profile from a conventional semiconductor laser with a stripe geometry. Integration with other devices, for example optical thyristors[2] and transistors[3], allows for large arrays of optical processing elements, suitable for massive parallel processing.

VCSELs were first made in 1979 [4] but operated at very large currents. Improvement was slow for the next decade, until the use of epitaxially grown dielectric Bragg reflectors as cavity mirrors[5] allowed for lasers incorporating as little as one quantum well in the active region. The small active volume in these devices give rise to a low threshold current. This milestone in the history of the VCSEL established the VCSEL as a viable device. In the few years since 1989 the growing interest in the scientific community has produced approximately 1000 publications on the subject of these devices; this is compared with approximately half a dozen in the preceding ten years. So great has been the interest that there have been two feature articles on the subject in the popular science magazine *Scientific American*[6].

The work for this thesis started a few months after the publications by Jewell *et al.*[7] and Lee *et al.*[5], which presented results on the first low threshold ($<5000 \mathrm{A.cm}^{-2}$) microresonator devices. This work investigates many of the possible variations on the AlGaAs / GaAs based device incorporating strained InGaAs active quantum wells and epitaxially grown multilayer Bragg reflectors. The design of the Bragg reflector stacks is examined in detail with particular attention paid to the effect of absorption caused by dopant species (chapter 2) and disruption schemes of the heterointerfaces to reduce the resistance (chapter 5). Gain spectra are estimated (chapter 3) and used to explain wavelength variation of device operating characteristics (chapter 8). Devices were grown by both MBE and MOCVD (chapters 4, 6 & 7) and a number of features are included to provide low power operation. These include use of resonant periodic gain, various schemes of interface disruption in the reflectors and modulation doping. Chapter 8 examines in detail the relation between the gain spectra and device operation and thermal effects due to resistive heating.

1.1. Background topics

1.1.1. Semiconductor lasers

The possibility of stimulated emission of radiation was first suggested by Einstein. However, it was not until 1960 that laser action was first demonstrated[8], this was in the ruby laser which exploits transitions between states of Cr^{3+} ions in an Al_2O_3 crystal. Shortly after this in 1961 stimulated emission in semiconductors was demonstrated[9,10]. These early devices used no cavity so could not really be termed lasers. With the advent of the dielectric waveguide laser[11] light could be confined to the plane of the semiconductor junction. Partial mirrors could then be formed from parallel cleaved semiconductor facets to form an optical cavity typically 500μm in length. The reflectivity of each facet mirror is ~0.3. This is the basis of the stripe geometry laser (fig. 1.1) which has been the generic form of semiconductor lasers over the last 30 years. Current is injected through a stripe contact to produce population inversion in the semiconductor junction underneath. The optical mode is confined to the junction plane by the dielectric variation in the semiconductor heterostructure. Lateral optical confinement is provided by the absorbing material outside of the stripe region (where there is no current injection), extra confinement may be produced by etching a ridge loaded waveguide structure.

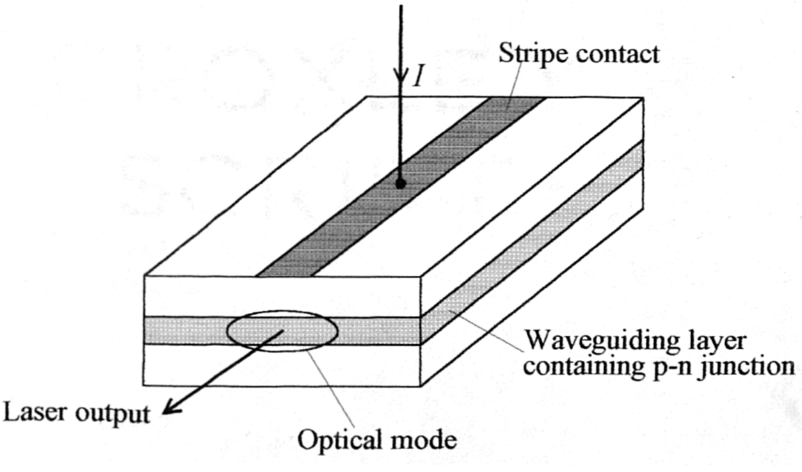

Fig. 1.1. Basic form of edge emitting semiconductor stripe laser.

The early demonstrations of stimulated emission required currents of the order 10^5A.cm^{-2} to reach threshold and were performed at liquid nitrogen temperatures (77K). With further advances in materials technology, continuous wave (c.w.) operation at room temperature (300K) was possible and by 1975 the room temperature threshold current density of an AlGaAs laser operating c.w. was reduced to 500A.cm^{-2} [12]. The semiconductor laser had now become a reliable compact coherent light source.

1.1.2. Common applications of optoelectronics

With the improvements in optical fibre technology the semiconductor laser has become the basis of modern telecommunications systems. Using high modulation speeds, very high data rates, typically 1Gbit.s^{-1} which is sufficient for 16000 uncompressed telephone channels, may be sent down a single monomode fibre which takes up very little space in cable trunking and costs around 5 pence per metre (traditionally coaxial cables were used which employ large amounts of the semi-precious metal copper). The cost of telecommunications has reduced, as much of the major trunk system in Europe and the U.S.A. has turned to optoelectronics. Our requirement for any resource often tends to grow as it becomes more available; computer communications, fax machines, video telephony and cable T.V. have continued to fill the increased capacity of the global network. We are far from the bandwidth limits of the fibres (possibly several THz); higher modulation speeds may be envisaged, by at least a factor of 10, and together with the use of wavelength division multiplexing our lust for information may continue to be satisfied.

The semiconductor laser is the only form of laser to have found a secure place in our homes. Philips developed the compact disc audio system in the early 1980's and in its first decade it has become the primary audio storage medium for home entertainment and for radio broadcasters. This is a result of the faithful reproduction afforded by 16 bit digital sampling. The data rate required for sound of this quality is 1.4Mbit.s^{-1}; a 70 minute disc contains almost 6Gbits of information. To cram this amount of information on a disc less than 5" in diameter, requires data to be stored in areas of size comparable to the wavelength of light. An AlGaAs double heterostructure laser operating at a wavelength of 780nm is used to read information off a reflective pits pressed into the disc with tracks spaced by 1.6μm. This was the first widespread home use for epitaxially grown semiconductor heterostructures. The compact disc system has proved very reliable and discs may still be played when they are quite severely scratched.

There are a number of other uses for lasers. In many of these semiconductor lasers are preferred due to their small size, low cost, and ease of operation. These include applications in interferometry, pump sources for solid state lasers and applications in computing.

A wide range of III-V material systems are used for the production of semiconductor lasers. Each allows operation in different areas of the optical spectrum. Table 1.1 lists a number of these together with their applications.

Material system	Wavelength	Application
AlGaAs / GaAs	750→890nm	Solid state laser pumps. Optical data storage (CDs). General purpose infra red source.
InGaAs / GaAs	950→1100nm	Low power sources. Erbium fibre laser pump.
InGaAsP / InP	1.0→1.7μm	Optical fibre applications in transmission windows at 1.3μm and 1.55μm.
AlGaInAsP / GaAs	600→700nm	Visible applications. Polymer short haul fibres. High temperature operation.

Table 1.1. Material systems used for semiconductor lasers, output wavelengths possible and typical applications.

1.1.3. Optics in computing

The possibility of an optical computer has long been awaited. Speed of light transmission between processing elements and the fast nature of many optical processes would allow computing at far higher speeds than using electronics.

We see some of the advantages of optics in fibre optic networking between machines. Recently, studies were carried out under the EEC directive OLIVES[13], to develop strategies for optical communication along bus planes in a computing system to speed the transfer of information between processors and to memory. It is hoped that this will increase the effectiveness of distributed processing architectures.

1.1.4. Neural and related architectures

The continued rapid progress of CMOS VLSI technology has made it difficult for other technologies to compete. There is still much improvement to come with further reduced gate lengths and integration moving towards the wafer scale. Any competitor, not aimed just at niche markets, must offer some distinct advantage which an increase in processing speed alone cannot overcome.

A planar optical processor based on active waveguide elements is unlikely to offer any advantage in functionality over an electronic implementation since the architecture is still confined to two dimensions. Implementations of array processors and systems displaying artificial intelligence require very large amounts of data to be transferred between processing elements and memory. In these non-serial or nonnumber crunching applications the limiting factor is the Von Neuman bottleneck[14]. This is the limit of data which can be transferred between chips through a small number of pins (no more than ~300) and can prevent the internal processors from operating at full capacity. In large chips, several millimetres across, even internal communications can be limiting (The RC time constant of a metallic trace of length l varies as l^2 whilst for free space transmission the delay varies as l). There is also a topological connection problem when working in a finite number of stacked 2D interconnect planes.

By using light it is possible to propagate many signals in parallel through free space without interference. For chip to chip communications this could consist of a 2D array of sources operating at GHz frequencies driven by a processor chip to which they are bonded using solder bump flip-chip technology[15]. A simple lens arrangement or hologram can be used to image the array onto an array of detectors on a number of other processors. Fig.1.2 indicates a possible architecture.

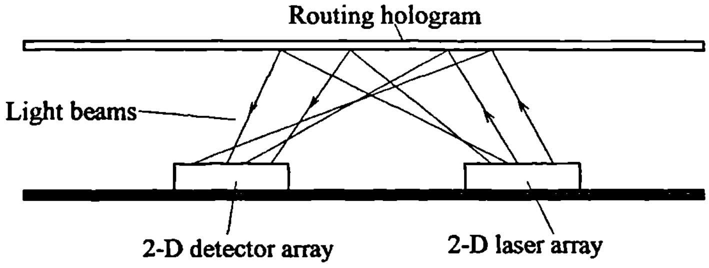

Fig. 1.2. High capacity optical interconnect between 2-D laser array and 2-D detector array. A hologram may me used to refocus the sources onto the detector array or may have a more complex routing function. Communication may be inter- or infra-chip.

More interesting are architectures of the form shown in fig. 1.3. An input pattern is imaged onto plane *1* which consists of an array of many pixels. A mathematical function is applied to the optical signal falling on each pixel and the output emerges from the other side of the plane, which then passes through free space to a second plane *2*. Between the two planes some form of beam steering is employed. This could be a hologram or a collection of holograms and lenses[16,17].

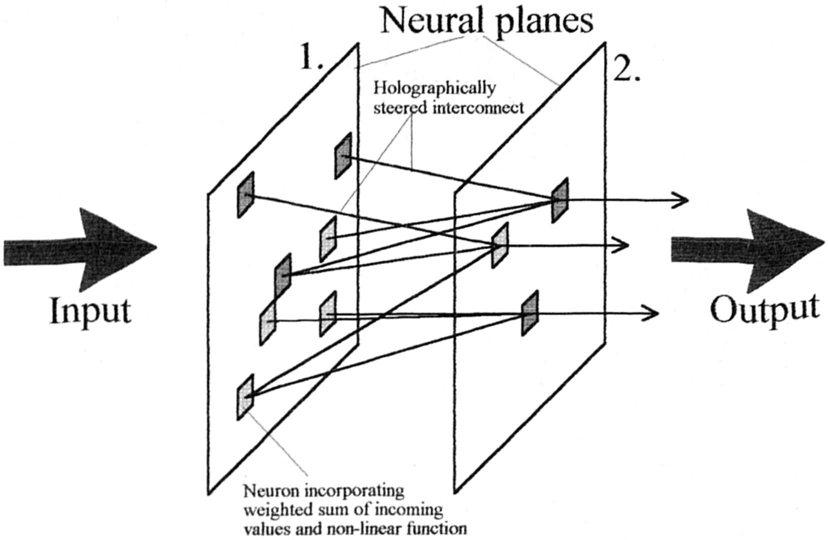

Fig. 1.3. Proposed structure for optical computer.

Any number of planes could be included to provide the desired function. The simplest system uses pixels with linear transfer characteristics but this system may only perform matrix multiplications and has no greater function than a single plane of interconnect, except the signals may be amplified. If the pixels are non-linear the system becomes much more powerful. A function as simple as a sigmoid function (1.1) is sufficient, this is a weak threshold function which has an output value 0.5 for an input $x=x_o$.

$$y=\frac{1}{1-e^{(x_o-x)/\sigma}} \qquad (1.1)$$

The non-linear array processor is the basis of neural networks[18,19]. Hidden planes and feedback may be used to provide temporal dependence (memory). Such a system operates in a similar way to the human brain at the neuron level. It can exhibit some traits of artificial intelligence and is particularly well adapted to certain tasks such as image processing and interpretation.

In a processing architecture containing active optical elements, it is usually desirable to supply power so that the signal amplitude is not diminished between elemental processes. This is more readily done electrically by using optoelectronic devices than by using all optical processes. Semiconductor lasers activated by phototransistors may be used to provide the non-linear function.

1.2. Lasers for optical computing

The applications of optics in computing described in section 1.1.4 (array processors and highly parallel chip to chip or on chip communications) require 2-dimensional arrays of light sources. Lasers are preferred over LEDs because they are more power efficient, when operated suitably above threshold, and provide coherent emission which is desired for holography.

1.2.1. Conventional lasers

The semiconductor laser is conventionally based on the stripe geometry device shown in fig. 1.1. Light emission occurs from the edge of devices cleaved from the wafer. 1-D arrays may be made using a number of parallel stripes but the production of 2-D arrays is more difficult. There are two ways of doing this in the stripe geometry: (i) A conventional stripe laser with 45° reflectors etched to turn the emitted light into the vertical direction[20]; (ii) Distributed feedback (DFB) or distributed Bragg reflector (DBR) lasers with adapted gratings to couple light into the vertical direction[21]. There is a variant on (ii); the surface emitting circular grating DBR laser[22]. The cavity length required in the plane of the semiconductor wafer for these structures is of the order 500μm. This limits the packing density of sources in an array.

1.2.2. Vertical cavities

For a high density 2-D array of semiconductor lasers it is desirable to arrange the laser cavity to be normal to the plane of the semiconductor wafer. The underlying principle of operation of a vertical cavity surface emitting laser (VCSEL) is the same as for a conventional edge emitting laser. Fig. 1.4. illustrates a laser with a vertical cavity. Current is injected vertically into a p-i-n active layer of length L, cavity mirrors with reflectivities R_1 and R_2. Device area on a chip is dependant on the area into which current is injected. This can easily be smaller than 5μm diameter, thus allowing very large packing densities[5].

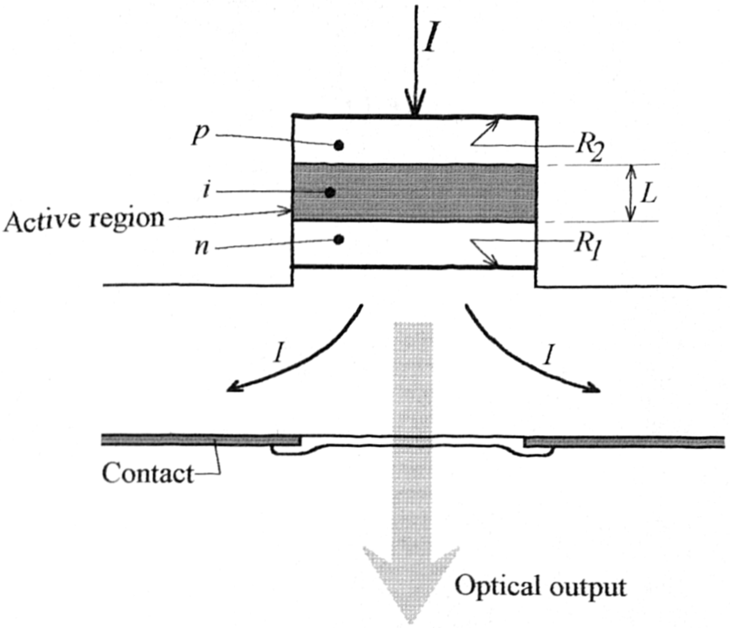

Fig. 1.4. Basic geometry of vertical cavity surface emitting laser.

For an electromagnetic wave travelling in through a region with gain g the photon density p grows with distance x as (1.2).

$$\rho(x) = \rho_o e^{(g-\alpha)x} \tag{1.2}$$

Where α is included to account for any optical loss mechanisms. The threshold gain g_{th} is therefore given by the familiar expression (1.3).

$$g_{th} = \alpha + \frac{1}{2L\Gamma} \cdot \ln\frac{1}{R_1 R_2} \tag{1.3}$$

This is the gain at which losses due to the absorption α and the mirrors R_1 and R_2 is overcome. Γ is the transverse confinement factor of the optical field in the active layer.

The thickness of an epitaxially grown vertical active region is limited by practical considerations to around 5μm. Assuming a maximum optical gain of 10^3.cm^{-1} [23], a confinement factor Γ=1.0 and assuming R_1=R_2=R we calculate the necessary reflectivity R=0.61. This is easily provided by thin metallic reflectors above and below the active region.

1.3. Development of the surface emitting laser

1.3.1. The story so far

The first surface emitting laser with a vertical cavity was produced in 1979 by Soda *et al.*[4] This incorporates a 1.8μm GaInAsP active region, requiring mirror reflectivities of ~85%. Metallic reflectors complete the cavity. The device operates at

77K with a pulsed threshold current density of 44kA.cm^{-2}. The threshold current is high because of the large active volume. Minor improvements produced a steady reduction of the threshold. A shift to a wider bandgap material system, AlGaAs / GaAs, was necessary to reduce the Auger recombination current at the high threshold carrier concentration sufficiently to enable room temperature operation[24,25].

To reduce the threshold current further required the reduction of the active volume. In the limit we have a laser with single quantum well active region. Considering such a laser with a single 100Å active quantum well and again assuming a maximum gain of 10^{3}.cm^{-1} [23]. Using the threshold relation of (1.3) and assuming identical top and bottom cavity reflectors, we find the necessary reflectivity for each mirror is 0.999.

Specular metal reflectors, such as thick Au films, are limited in reflectivity to ~0.980 by the high absorption of the material. Dielectric optical materials, such as semiconductors at photon energies below their bandgap, have a very low absorption coefficient (~0.3.cm^{-1} for pure GaAs[26]). At a dielectric discontinuity between two compounds with different refractive index there is a reflection due to the change of wave impedance. In the AlGaAs system the greatest reflectivity occurs for an AlAs / GaAs interface which provides a reflectivity of ~0.07 at wavelengths close to 1000nm. This is not very useful on its own but in a resonant (Bragg) multilayer structure reflections from a number of interfaces may add in phase to produce a large reflection. The low absorption coefficient means that the limit of reflectivity is higher than for a metallic reflector. In chapter 2 we predict that, notwithstanding scattering effects, the limiting reflectivity in an AlAs / GaAs Bragg reflector is 0.999 for an absorption coefficient of 10.cm^{-1} or 0.9999 at 1.0.cm^{-1}.

The first structure to use such reflectors was a novel distributed feedback laser by Ogura *et al.*[27] in 1987. This employed lateral current injection into a reflector stack to stimulate emission from within the reflector itself. The active volume in this device is still rather large and the carrier injection scheme not very efficient. A number of other structures from the group of Iga at the Tokyo Institute of technology used epitaxially grown AlAs / AlGaAs Bragg reflectors[28] or plasma deposited SiO_2 / TiO_2 reflector stacks[29], but no significant improvements were made until the work of Jewell *et al.*[7] and Lee *et al.*[5] in 1989. Theirs was the first use of very high reflectivity mirrors (R~0.999) which allowed very small active volumes. Lasing was obtained from a single active quantum well[5] allowing the threshold current density to be reduced to 1800A.cm^{-2}, more than a factor of five reduction from the previous lowest value. 5μm diameter devices operated at currents just over 1mA. These new structures made use of compressively strained $In_{0.2}Ga_{0.8}As$ / GaAs quantum wells which have several points in their favour. (i) Compressively strained quantum wells exhibit enhanced optical gain in the TE polarization due to the splitting of the light and heavy hole confined states[30], see chapter 3. (ii) The emission from InGaAs wells is at ~980nm, which is below the band edge of GaAs at 890nm; this means that the substrate may be used to couple light out of the device, simplifying the contacting of devices and the design of the upper reflector. (iii) The short wavelength emission means that AlAs / GaAs multilayer reflectors may be used with little absorptive loss, these employ the largest dielectric step possible in the lattice matched AlGaAs material system. The VCSEL was now a useful device able to operate at low powers at room temperature; operation at 77K was now of little interest.

One problem with epitaxially grown Bragg reflectors is that of high resistance. This is a result of the band edge offset between semiconductors of different composition which provides barriers to current flow (see chapter 5). The large number of reverse biased heterointerfaces in a VCSEL structure meant that the bias voltage for these early devices was often in excess of 15V. By disrupting these interfaces the resistance may be reduced significantly. Geels *et al.*[31] (1990) employ a superlattice grade of the mirror interfaces to reduce the threshold voltage to 4V. Other refinements made in their design reduced the threshold current density to 600A.cm^{-2}.

Over the next two years there were no further reductions in the threshold current but many publications appeared concerning such things as theoretical and fabrication issues. In 1992 Sugimoto *et al.*[32] used continuous grading of the interfaces and by selective doping of the reflectors produced a low resistance structure with minimal dopant induced absorption. This allowed a single well device to operate at a threshold current density of 450A.cm^{-2}.

1.3.2. In this thesis

In this work, using a simpler superlattice grading structure at the reflector interfaces than Geels *et al.*[31] (section 5.3.2) and by modulation doping, VCSELs were produced with threshold current densities of 366A.cm^{-2}. The structure incorporates more highly strained quantum wells (23.5% In) than in previous VCSELs and devices were available with cavity resonances covering a wide range of wavelengths[33]. The variation in cavity wavelength allowed a detailed investigation of the relative offset between the resonance and quantum well ground state transition wavelength (see chapters 6 and 8). Since this work there has been no report of further reduction of the threshold current density to date (September 1993) by any authors.

All the high finesse structures mentioned above were grown by MBE. In this work structures were also grown by MOCVD. There has been very little published results on such devices grown using this process[34]; this is perhaps due to the generally less predictable growth rates (see chapter 4). The different dopant species commonly available when growing by this process (see chapter 4) enable more effective doping in the reflectors. Together with low oxygen incorporation when using purified growth precursors[35] it was possible to reduce the threshold voltage of devices to 1.7V which is comparable to the lowest yet reported for structures with injection through the reflectors[36]. The only such structure with a lower voltage operates at 1.5V [37], this incorporates continuously graded reflectors which are much more difficult to grow in a controlled manner than staircase graded ones (see section 5.3.2). The threshold current of the MOCVD grown devices reported here was as low as 764A.cm^{-2}. This is not as low as for the MBE grown devices because the absorption in the structures is higher and there are errors in the layer dimensions of the structure, both of these tend to reduce the finesse of the laser cavity (see chapter 3).

1.3.3. Trends in VCSEL development

VCSELs have advanced rapidly, particularly in the last four years. Table 1.2 lists the major advances in device technology. The threshold current density serves as a useful indicator of this advancement. Fig. 1.5. shows graphically how the threshold current has reduced over these years. Our expectations for future development are discussed in the next section.

First named author	Date Published	J_{th}(77K) A.cm^{-2}	J_{th}(300K) A.cm^{-2}	Comments
H.Soda[4]	Dec. 1979	44000	—	First demonstration of VCSEL
H.Okuda[38]	Feb. 1981	40000	—	—
K.Iga[39]	June 1983	15900	—	
A.Ibaraki[24]	Feb. 1984	—	380000	First room temperature VCSEL
K.Iga[25]	Aug. 1984	—	162000	Un-alloyed reflector metal
K.Iga[40]	June 1985	—	98700	—
M.Ogura[27]	May 1987	—	10000	Novel distributed structure
T.Sakaguchi[28]	July 1988	—	28300†	First use of epitaxial reflectors
J.L.Jewell[7]	Aug. 1989	—	10200†	3 quantum well active region
Y.H.Lee[5]	Sep.1989	—	1800	Quantum well active region
R.S.Geels[31]	Feb. 1990	—	600	3 wells, polyimide passivated
M.Sugimoto[32]	Feb. 1992	—	450	Uses modulation doped mirrors
T.Uchida[41]	Mar. 1992	455	—	High reflectivity oxide mirrors
T.E.Sale[33]	Nov. 1992	—	366	This work

Table 1.2. Progress in VCSEL technology indicated by state of the art low threshold current devices. †Not included in fig. 1.5.

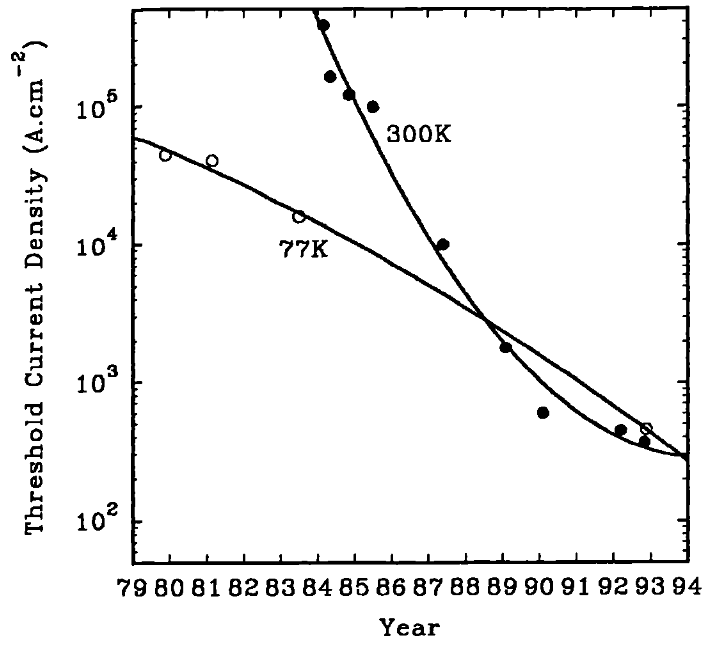

Fig. 1.5. Trends in the reduction of threshold current density. State of the art devices are indicated by the minimum threshold value reported to date.

1.3.4. The future

It appears that the early progress in the reduction of threshold current has slowed now that the VCSEL device is better understood. However by using increased compressive strain in the active region and using a low loss cavity it should be possible to reduce the threshold current density for a single well device below 100A.cm^{-2} within the next few years. A 10μm diameter device with smooth sidewalls would have a threshold current of ~40μA. Smaller devices are possible but only with the penalty of higher threshold current densities because of reduced optical confinement and increased surface effects. Very small devices may not be able to supply useful amounts of optical power unless as parts of much larger arrays. The use of quantum wire and quantum box structures may allow further reductions in operating current.

There are several developed commercial applications in which VCSELs could be used. As arrays, they could serve as print heads in laser printers or as multi-track readout heads from optical data storage media.

There is also the possibility of operating at other emission wavelengths than available in the InGaAs / GaAs material system. Devices in the InGaAsP / InP system were the first to be demonstrated[3] but due to the inability to grow high reflectivity (R~0.998) mirrors lattice matched to the substrate, low threshold current densities have not been possible. This material system is compatible with low loss fibre communications in the 1.3μm and 1.55μm bands, and the low angular divergence output from a circular aperture is more efficiently coupled into a fibre than the highly elliptical far field pattern from an edge emitting laser. Use of hybrid or strain relieved mirrors may allow devices for this purpose.

Deep-red emitters naturally have many practical uses. Apart from uses in high density optical data storage and short haul polymer optic fibres, visible VCSELs may be used for display applications. Examples of these include image projection systems and lightweight helmet mounted head up displays. The latter will be useful for controllers of complex systems, in particular pilots: the display mounted on the helmet will always remain within the field of view. If sufficiently cheap such systems will be of use to rally drivers and to sports aviators.

Visible VCSELs at 770nm wavelength were first produced in the AlGaAs material system[42]. The human eye is not particularly sensitive at this wavelength but unfortunately the AlGaAs system has an indirect bandgap[26], i.e. is not suitable for lasers, for compounds with a gap much narrower than this. The InAlGaP / AlGaAs system may be used to produce lasers with emission at ~620nm (and possibly to shorter wavelengths) and it is still possible to make use of AlGaAs compounds for reflectors. Schneider *et al.* (1993) have produced electrically injected VCSELs in this system emitting at wavelengths as short as 639nm [43]. The threshold current density for these devices is 9500A.cm^{-2}, this is rather high compared to InGaAs based devices. Visible VCSELs are still in their infancy and significant improvements are sure to come.

References:

[1] M.Orenstein, A.C.Von Lehmen, C.Chang-Hasnain, N.G.Stoffel, J.P.Harbison & L.T.Florez, *Matrix addressable vertical cavity surface emitting laser array*, Electron. Lett., **27**, 5, pp437-438, 1991.

[2] I.Ogura, H.Kosaka, T.Numai, M.Sugimoto & K.Kasahara, *Cascadable optical switching characteristics in vertical-to-surface transmission electrophotonic devices operated as vertical cavity lasers*, Appl. Pys. Lett., **60**, 7, pp799-801, 1992.

[3] R.P.Bryan, W.S.Fu & G.R.Olbright, *Hybrid integration of bipolar transistors and microlasers: Current-controlled microlaser smart pixels*, Appl. Phys. Lett., **62**, 11, pp1230-1232, 1993.

[4] H.Soda, K.Iga, C.Kitahara & Y.Suematsu, *GaInAsP / InP Surface emitting injection lasers*, Jpn. J. Appl. Phys., **18**, 12, pp2329-2330, 1979.

---

[5] Y.H.Lee, J.L.Jewell, A.Scherer, S.L.Mc.Call, J.P.Harbison and L.T.Florez., *Room-temperature continuous-wave vertical cavity single-quantum-well microlaser diodes*, Electron. Lett., **25**, 20, pp1377-1378, 1989.

[6] J.L.Jewell, J.P.Harbison and A.Scherer, *Microlasers*, Sci. American, **265**, 5, pp56-62, 1992. *and* E.Corocoran, *Diminishing dimensions*, Sci. American, **263**, 3, pp74-83, 1990.

[7] J.L.Jewell, A.Scherer, S.L.McCall, Y.H.Lee, S.Walker, J.P.Harbison & L.T.FLorez, *Low-threshold electrically pumped vertical-cavity surface-emitting microlasers*, Electron. Lett., **25**, 17, pp123-1124, 1989.

[8] T. H. Maiman, *Stimulated emission of optical radiation in ruby masers*, Nature, **137**, p.493, 1960.

[9] N.G.Baasov, O.N.Krokhin & Y.M.Popov, *Production of negative temperature states in P-N states of degenerate semiconductors*, J.E.T.P., **40**, p.1320, 1961.

[10] M.I.Nathan, W.P.Dumke, G.Burns, F.H.Dill Jr. & G.Lasher, *Stimulated emission of radiation from GaAs p-n junctions*, Appl. Phys. Lett., **1**, pp62-64, 1962.

[11] A.Yariv & R.C.C.Leite, *Dielectric waveguide mode of light propagation in p-n junctions*, Appl. Phys. Lett., **2**, p.55, 1963.

[12] M.Ettenberg, *Very low threshold double heterojunction* $Al_xGa_{1-x}As$ *injection lasers*, Appl. Phys. Lett., **27**, 12, p652-654, 1975.

[13] D.Selviah, *Review of OLIVES program*, progress meeting of EEC FOCUS program, Madrid, 1990.

[14] N.Streibl, K-H.Brenner, A.Huang, J.Jahns, J.Jewell, A.W.Lohmann, D.A.B.Miller, M.Murdocca, M.E.Prise & T.Sizer, *Digital Optics*, Proc. IEEE, 7, 12, pp1954-1969, 1989.

[15] C.Edge, R.M.Ash, C.G.Jones & M.J.Goodwin, *Flip-chip solder bond mounting of laser diodes*, Electron. Lett., **27**, 6, pp499-501, 1991.

[16] M.Murdoca, *Connection routing for microoptic systems*, Appl. Optics, **29**, 8, pp1106-1110, 1990,

[17] T.Sakano, K.Noguchi & T.Matsumoto, *Optical limits for spatial interconnection networks using 2-D optical array devices*, Appl. Optics, **29**, 8, pp1094-1100, 1990.

[18] J.J.Hopfield, *Artificial neural networks*, IEEE circuits and devices magazine, pp3-10, September 1988.

---

[19] N.H.Farhat, *Optoelectronic neural networks and learning machines*, IEEE circuits and devices magazine, pp32-41, September 1989.

[20] W.D.Goodhue, J.P.Donnelly, C.A.Wang, G.A.Lincoln, K.Rauschenbach, R.J.Bailey & G.D.Johnson, *Monolithic two-dimensional surface-emitting strained-layer InGaAs / AlGaAs and AlInGaAs / AlGaAs diode laser arrays with over 50% differential quantum efficiencies*, Appl. Phys. Lett., **59**, 6, pp632-634, 1991.

[21] K.Kojima, S.Noda, K.Mitsunaga, K.Kyuma, K.Hamanaka & T.Nakayama, *Edge and surface emitting distributed Bragg reflector laser with multi quantum well active / passive waveguides*, Appl. Phys. Lett., **50**, pp227-229, 1987.

[22] C.Wu, M.Svilans, M.Fallahi, I.Templeton, T. Makino, J.Glinski, R.Maciejko, S.I.Najafi, C.Maritan, C.Blaauw & G.Knight, *Room temperature operation of electrically pumped surface-emitting circular grating DBR laser*, Electron. Lett., **28**, 11, pp1037-1039, 1992.

[23] B.Saint-Cricq, F.Lozes-Dupuy & G.Vassilieff, *Well width dependence of gain and threshold current in GaAlAs single quantum well lasers*, IEEE J. Quantum Electron., **22**, 5, pp625-630, 1986.

[24] I.Ibaraki, S.Ishikawa, S.Ohkouchi & K.Iga, *Pulsed oscillation of GaAlAs / GaAs surface-emitting injection laser*, Electron. Lett., **20**, 10, pp420-422, 1984.

[25] K.Iga, S.Ishikawa, S.Ohkouchi & T.Nishimara, *Room-temperature pulsed oscillation of GaAlAs / GaAs surface emitting laser*, Appl. Phys. Lett., **45**, 4, p348-350, 1984.

[26] J.S.Blakemore, *Semiconducting and other major properties of gallium arsenide*, J. Appl. Phys., **53**, 10, ppR123-R181, 1982.

[27] M.Ogura, W.Hsin, M-C.Wu, S.Wang, J.R.Whinnery, S.C.Wang & J.J.Yang, *Surface-emitting laser diode with vertical GaAs / GaAlAs quarter-wavelength multilayer and lateral buried heterostructure*, Appl. Phys. Lett., **51**, 21, pp1655-1657, 1987.

[28] T.Sakaguchi, F.Koyama & K.Iga, *Vertical cavity surface-emitting laser with AlGaAs / GaAs Bragg reflector*, Electron. Lett., **24**, 15, pp928-929, 1988.

[29] H.Uenohara, F.Koyama & K.Iga, *AlGaAs / GaAs mulltiquantum-well (MQW) surface-emitting laser*, Electron. Lett., **25**, 12, pp770-771, 1989.

[30] A.R.Adams, *Band-structure engineering for low-threshold high-efficiency semiconductor lasers*, Electron. Lett., **22**, 5, pp249-251, 1986.

---

[31] R.S.Geels, S.W.Corzine, J.W.Scott, D.B.Young & L.A.Coldren, *Low threshold planarized vertical-cavity surface-emitting lasers*, IEEE Photon. Technol. Lett., **2**, 4, pp234-236, 1990.

[32] M.Sugimoto, H.Kosaka, K.Kurihara, I.Ogura, T.Numai & K,Kasahara, *Very low threshold current density in vertical-cavity surface-emitting laser diodes with periodically doped distributed Bragg reflectors*, Electron. Lett., **28**, 4, ppp385-387, 1992.

[33] T.E.Sale, J.Woodhead, R.Grey & P.N.Robson, *Wide operating wavelength range and low threshold current* $In_{0.24}Ga_{0.76}As$ */ GaAs vertical-cavity surface-emitting lasers*, IEEE Photon. Technol. Lett., **4**, 11, pp1192-1194, 1992.

[34] P.Zhou, J.Cheng, C.F.Schaus, S.Z.Sun, K.Zheng, E.Armour, C.Hains, W.Hsin, D.R.Myers & G.A.Vawter, *Low series resistance high-efficiency GaAs / AlGaAs vertical-cavity surface-emitting lasers with continuously graded mirrors grown by MOCVD*, IEEE Photon. Technol. Lett., **3**, 7, pp591-593, 1991.

[35] J.S.Roberts, T.E.Sale, C.C.Button, J.P.R.David & A.Jennings, *High performance microcavity resonator devices grown by atmospheric pressure MOVPE*, J. Crystal Growth, **124**, pp792-800, 1992.

[36] D.Vakshoori, J.D.Wynn, G.D.Zydzik, R.E.Leibenguth, M.T.Asom, K.Kojima & R.A.Morgan, *Top-surface emitting lasers with 1.9V threshold voltage and the effect of spatial hole burning on their transverse mode operation and efficiencies*, Appl. Phys. Lett., **62**, 13, pp1448-1450, 1993.

[37] K.L.Lear, S.A.Chalmers & K.P.Killeen, *Low threshold voltage vertical cavity surface-emitting laser*, Electron. Lett., **29**, 7, pp584-586, 1993.

[38] H.Okuda, H.Soda, K.Moriki, Y.Motegi & K.Iga, *GaInAsP / InP surface emitting laser with buried heterostructures*, Jpn. J. Appl. Phys., **20**, 8, ppL563-L566, 1981.

[39] K.Iga, H.Soda, T.Terakado & S.Shimizu, *Lasing performance of improved GaInAsP / InP surface emitting injection lasers*, Electron. Lett., **19**, 13, pp457-458, 1983.

[40] K.Iga, S.Ishikawa, S.Ohkouchi & T.Nishimura, *Room temperature pulsed operation of GaAlAs / GaAs surface emitting junction laser*, IEEE J. Quantum Electron., **21**, 6, pp663-668, 1985.

[41] T.Uchida, N.Yokouchi, T.Miyamoto, Y.Inaba, F.Koyama & K.Iga, *GaInAsP / InP surface emitting laser grown by chemical beam epitaxy*, Electron. Lett., **28**, 6, pp550-551, 1992.

---

[42] Y.H.Lee, B.Tell, K.F.Brown-Goebeler, R.E.Leibenguth & V.D.Mattera, *Deep-red continuous wave top-surface-emitting vertical-cavity AlGaAs superlattice diodes*, IEEE Photon. Technol. Lett., **3**, 2, pp108-109, 1991.

[43] R.P.Schneider Jr. & J.A.Lott, *Cavity design for improved electrical injection in InAlGaP / AlGaAs visible (639-661nm) vertical-cavity surface-emitting laser diodes*, Appl. Phys. Lett., **63**, 7, pp917-919, 1993.

2. Theory of Dielectric Reflectors and VCSEL Cavities.

This chapter concerns the distributed Bragg reflectors required to provide high reflectivities needed for the high finesse cavity of a low threshold current vertical cavity surface emitting laser (VCSEL) (refer to chapter1). The variation of the reflectivity with the number of layer pairs and the material absorption is discussed in relation to the optical design of the device.

2.1. Bragg reflectors

2.1.1. Methods for calculation of reflection coefficient

The reflection coefficient of a multilayer dielectric stack may be found in several ways. One is Yariv's method[1], based on coupled mode theory, which introduces a coupling coefficient κ(λ) for the coupling per unit length of the perturbed guide between the forward and reverse travelling waves. For a periodic guide with alternate layers of index n_1 and n_2, the coupling constant is found to be given by (2.1) and the reflectivity is found to be given by (2.2).

$$\kappa(\lambda)=\frac{2\pi}{3\lambda}\frac{\left(n_1^2-n_2^2\right)}{n_2}\left[1+\frac{3}{2\pi}\frac{\lambda}{\left(n_2^2-n_1^2\right)^{\frac{1}{2}}}+\frac{3}{4\pi}\frac{\lambda^2}{n_2^2-n_1^2}\right] \tag{2.1}$$

$$R=\tanh^2(\kappa.L) \tag{2.2}$$

The method used by McLeod[2] is perhaps more appropriate being a discrete method. It is thus applicable to numerical solution for finite structures. The following is in essence that given in his book[2] but extended to include imaginary refractive indeces necessary to describe absorption losses. Consider a layer of dielectric material *b* (see fig. 2.1). The layer is clad on either side by layers *a* and *c*. A transverse electromagnetic wave at normal incidence propagates through the layer in the *z* direction. By considering the electric and magnetic fields (*E* & *H*) at either side of the layer using Maxwell's equations, a transmission matrix relating these fields is found (2.3). k_b is the phase propagation constant in the layer, n_b the refractive index and η_o the impedance of free space, *b* refers to the dielectric layer and *j* is the unit imaginary number. α_b is the linear absorption coefficient in the layer (Note: the figure usually referred to is the power absorption coefficient which is twice this value).

2.1.2. Transmission matrix formulation

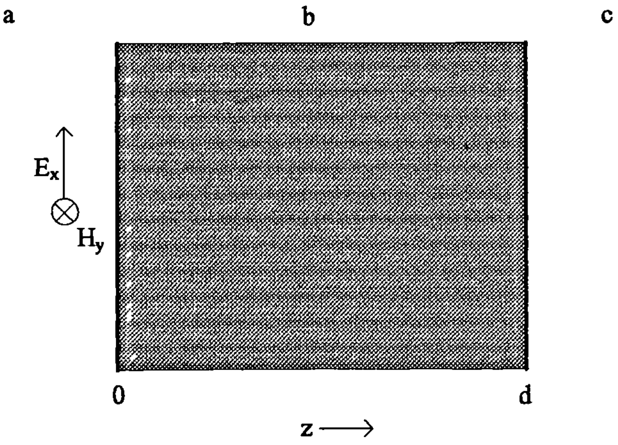

Fig. 2.1. Transmission matrix is formed by solution of Maxwell's equation at either side of layer b.

$$\begin{pmatrix} E(0) \\ H(0) \end{pmatrix} = \begin{pmatrix} \cos(k_b d + j\alpha_b d) & \frac{j\eta_o}{n_b}\sin(k_b d + j\alpha_b d) \\ \frac{jn_b}{\eta_o}\sin(k_b d + j\alpha_b d) & \cos(k_b d + j\alpha_b d) \end{pmatrix} \cdot \begin{pmatrix} E(d) \\ H(d) \end{pmatrix} \quad (2.3)$$

$$k_b = \frac{2\pi}{n_b \lambda_o} \quad (2.4)$$

For a multilayer stack a matrix $\mathbf{M}_i$ is formed for each layer i and of thickness d_i in the stack. So by considering the effect of all layers in stack of length L we have a matrix $\mathbf{M}$ which relates the input and output fields (2.5-7).

$$L = \sum_i d_i \quad (2.5)$$

$$\begin{pmatrix} E(0) \\ H(0) \end{pmatrix} = \mathbf{M} \cdot \begin{pmatrix} E(L) \\ H(L) \end{pmatrix} \quad (2.6)$$

$$\mathbf{M} = \prod_i \mathbf{M}_i = \begin{pmatrix} m_{11} & m_{12} \\ m_{21} & m_{22} \end{pmatrix} \quad (2.7)$$

The amplitude reflection coefficient of the stack r is found to be given by (2.8) where the terms m_{ij} are the elements of $\mathbf{M}$, the Y's are addmittances and o and s refer to the incident medium and substrate respectively. Note that the m_{ij} are all strong functions of wavelength.

$$r = \frac{Y_o m_{11} + Y_o m_{12} - m_{21} - Y_s m_{22}}{Y_o m_{11} + Y_o m_{12} + m_{21} + Y_s m_{22}} \quad (2.8)$$

If we have a layer of index n_1 between layers of lower index o and s Then the reflection from the front interface has a phase of π radians relative to the incident wave due to the positive index step. At the rear interface the forward travelling wave is reflected with a relative phase of 0 as here there is a negative index step. If the thickness of the layer is a quarter wavelength the two reflections add in phase at the front interface due to the π round trip phase delay for the second reflection. For a stack with many alternate ¼ wave (or more generally (*n*/2+¼) wave: *n* integral) thicknesses of low and high index, all interfacial reflections will add in phase and the reflection coefficient will approach unity provided the absorption loss is negligible. This stack constitutes a quarter wave Bragg reflector and forms the basis of the VCSEL cavity mirrors.

For a Bragg reflector made from alternate quarter wavelength layers of indeces n_1 and n_2, the reflectivity R at the resonant wavelength of a stack with $m+½$ non-absorbing dielectric pairs is given by (2.9). This is found to be a discrete form of equation (2.1). This problem can also be thought of as an array of quarter-wave transformers.

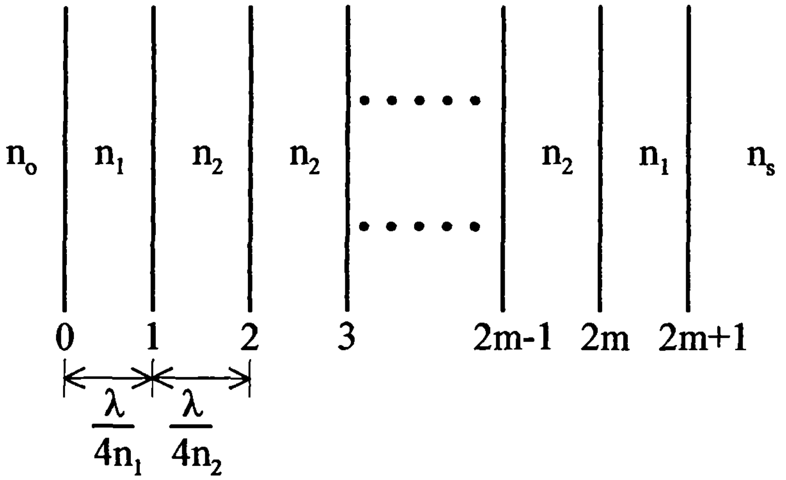

Fig. 2.2. Schematic of quarter wave Bragg reflector incorporating m+½ pairs of indices n_1 *and* n_2.

$$\sqrt{R}=\frac{1-\frac{n_1^2}{n_o n_s}\cdot\left(\frac{n_1}{n_2}\right)^{2m}}{1+\frac{n_1^2}{n_o n_s}\cdot\left(\frac{n_1}{n_2}\right)^{2m}} \tag{2.9}$$

Equation (2.9) is only valid at the resonant wavelength. At other wavelengths the reflectivity will be less as the layers will not now be of quarter wave thickness and reflections will not add in phase.

2.1.3. AlAs / GaAs reflector stacks

Let us consider quarter wave stacks made in the $Al_xGa_{1-x}As$ material thickness. For photon energies below the band gap the refractive indices of materials in this system may be accurately found using a single oscillator Sellmeier equation (2.10)[3].

$$n^2 = A + \frac{B}{\lambda_o^2 - C} - D\lambda_o^2 \qquad (2.10)$$

λ_o is the free space wavelength in μm and the coefficients A, B, C and D are given in table 2.1[3]. Values from these equations agree well with the famous results of Casey, Sell and Panish[4,5]. For wavelengths around 1.0μm the agreement is better than 0.01 in most cases.

	GaAs	**$Al_xGa_{1-x}As$**
A	10.9060	10.9060-2.92x
B	0.97501	0.97501
C	0.27969	$(0.52868-0.735x)^2 : x \leq 0.36$ $(0.30386-0.105x)^2 : x > 0.36$
D	0.002467	$0.002467 \cdot (1.41x+1)$

Table 2.1. Sellmeier coefficients[3] for refractive index calculation in $Al_xGa_{1-x}As$.

For the binary compounds AlAs and GaAs the index difference is large for a semiconductor system. At a wavelength of 1.0μm the indeces are 3.508 and 2.999 respectively. Using these values Bragg reflectors have been modelled using the stack dimensions given in table 2.2.

d_{AlAs}	834Å
d_{GaAs}	713Å

Table 2.2. Bragg stack dimensions for 1.0μm operation

These are quarter wave thicknesses at a wavelength of 1.0μm. Using the Sellmeier equations the transmission matrix for the complete stack **M** is calculated numerically. These calculations are easily implemented on an IBM-PC compatible computer, however for modelling some of the more complex structures reported later in this thesis a fast machine incorporating a numeric floating point co-processor is essential. Considering r in the form:

$$r = \sqrt{R}.e^{j\phi} \tag{2.11}$$

Where R is the power reflection coefficient and ϕ is the phase of the reflection with respect to the top of the stack. Reflection spectra were computed, fig. 2.3 shows examples for 5½, 15½ and 25½ pairs. Both the substrate and superstrate layers are GaAs. ϕ is taken in the range $-\pi>\phi\geq\pi$. In these calculations an absorption coefficient of $1.0.\text{cm}^{-1}$ (power) is considered in all layers.

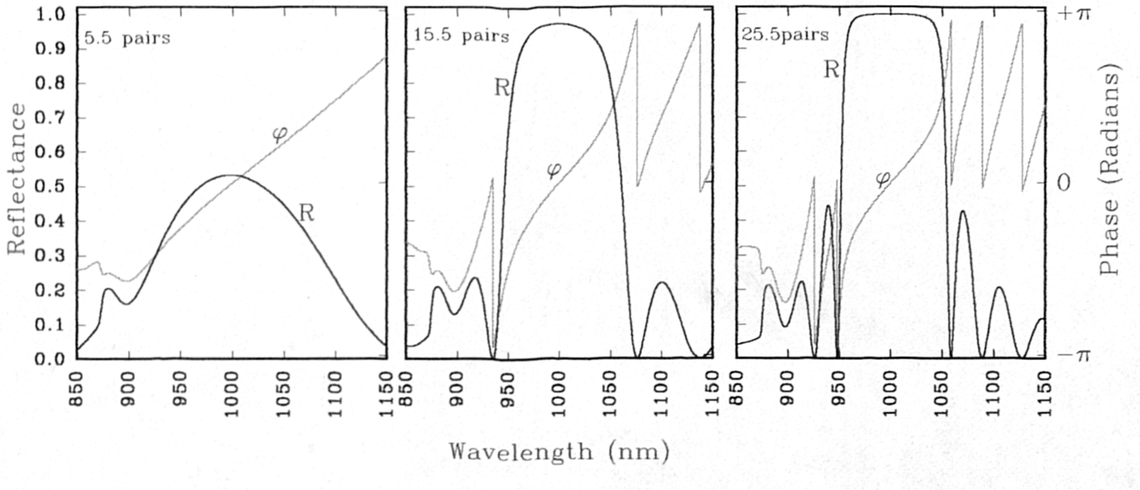

Fig. 2.3. Reflection spectra from quarter wave AlAs/GaAs Bragg stacks with 5½, 15½ and 25½ reflector pairs in GaAs.

It can be seen that as the number of reflector pairs is increased that the peak reflectivity approaches unity asymptotically and the shape of the spectrum approaches a square bandpass (in reflection) of 100nm bandwidth, centred on 1000nm. It is perhaps more useful to compare these spectra on a probability scale which allows the high reflectivities to be better compared (see fig. 2.4).

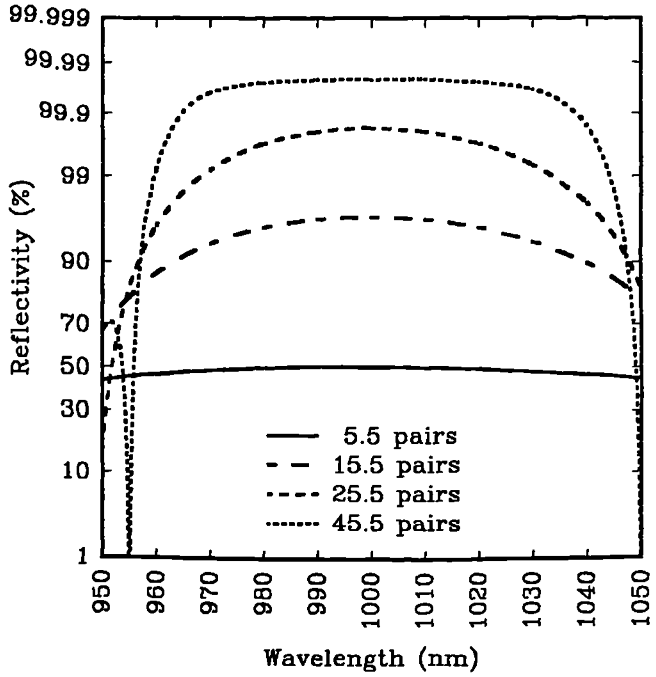

Fig. 2.4. Reflectivity of AlAs/GaAs Bragg reflectors shown on probability scale.

Thus we see that to achieve a reflectivity in excess of 0.998 required for a VCSEL (refer to chapter 1), approximately 25 AlAs / GaAs reflector pairs are necessary. The bandwidth for high reflectivity is not as wide as it appears on a linear scale e.g. for the 25½ pair reflector R falls from a maximum of 0.9985 to 0.9970, an increase in the reflection loss by a factor of two, over a bandwidth of 43.0nm.

The phase plots show that at the resonant wavelength there is a change of phase with wavelength of approximately $\phi'=73.\mu m^{-1}$ when measured in units of radians. This figure has important implications for the resonance of short cavities and will be referred to as the ***phase compensation***, the meaning of which shall be seen later.

2.1.4. Effects of absorption

The curves of figures 2.3 and 2.4 were calculated for a power absorption of coefficient of $1.cm^{-1}$. The effect of this is to limit the maximum reflectivity which can be obtained as is seen in the flattening of the spectrum for the 45½ pair structure. In a practical VCSEL structure absorption losses may be much larger due to high dopant concentrations used and this will reduce the reflectivity which may be provided by their reflectors[6]. It is useful to compare the maximum reflectivity obtainable from these stacks as a function of absorption coefficient. Fig. 2.5 shows this relation. The loss L is the sum of absorption and reflection losses at the peak reflectivity and is defined as (2.12).

$$L = 1 - R_{max} \qquad (2.12)$$

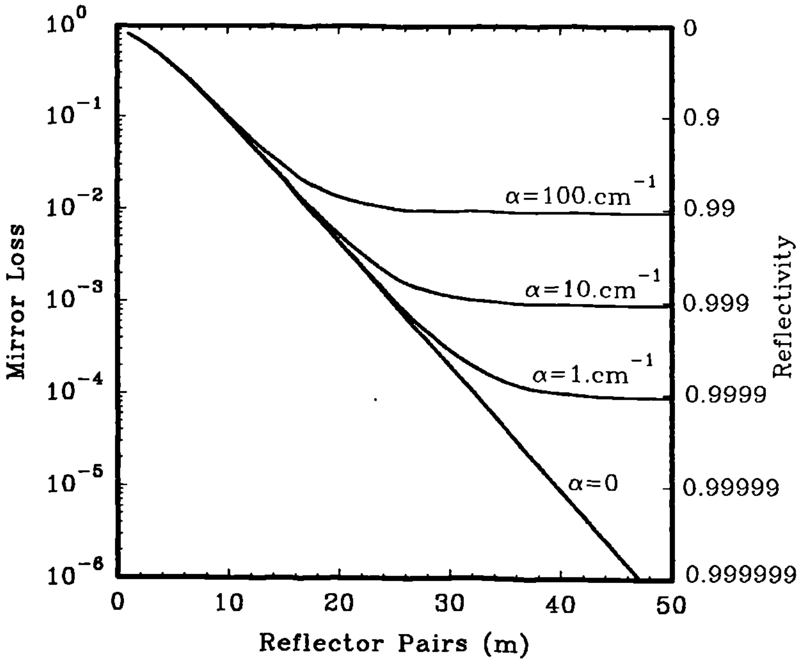

Fig. 2.5. Graph of minimum loss of AlAs / GaAs Bragg reflectors with m+½ pairs, plotted for power absorption coefficients of 0, 1.0, 10 and 100.cm^{-1}.

The inclusion of absorption limits the maximum reflection obtainable. From fig. 2.5 we see that the limiting reflectivity for a quarter wave AlAs /GaAs Bragg reflector is given approximately by (2.13): where we find $\alpha_0=10^4.\text{cm}^{-1}$.

$$R_{m\to\infty}=1-\frac{\alpha}{\alpha_o} \qquad (2.13)$$

Thus for moderately doped material, reflectivities of 0.999 should be reasonably obtainable.

Some designs for VCSELs have included as many as 45 pairs in the reflector stacks[7,8]. Such large stacks are not beneficial and only complicate the material growth, increase the ohmic resistance and reduce the laser efficiency.

For any particular value of absorption the limiting values of reflection of equation (2.13) are not achievable in a practical laser structure since we must be able to take light output through one of the mirrors. If the size of the Bragg stack is large so that the limiting value of reflectivity is approached, most of the radiation lost from the cavity will be lost in absorption in the reflector. Fig. 2.6 illustrates the variation of output coupling efficiency with stack size and absorption coefficient. The output coupling efficiency is the percentage transmission loss of the total mirror loss. The graph illustrates how for low absorptions and short stacks most of the non-reflected light is efficiently coupled to the output. As the size of the stack is increased absorption loses begin to reduce the proportion of the total loss which is transmitted eventually reducing it to zero in very large stacks. Thus if the Bragg stacks are too large the laser external quantum efficiency will reduce since this is dependant on the output coupling efficiency. There is also a growth penalty on thick reflector stacks. Table 2.3 summarises the results of fig. 2.6. by listing stack sizes for which the coupling efficiency is reduced to 50% for the different absorption coefficients.

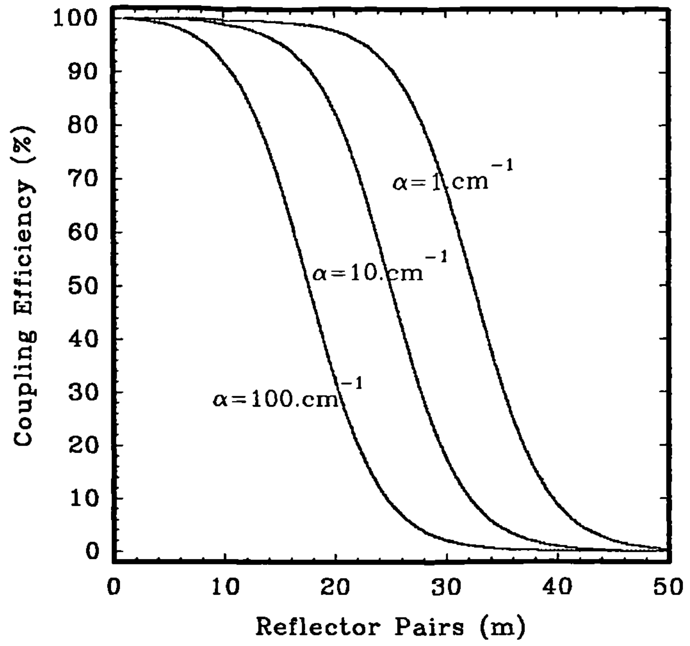

Fig. 2.6. Effect of size of Bragg reflector on the optical output coupling efficiency of the reflector.

α	m	R
1.cm^{-1}	32	99.989%
10.cm^{-1}	25	99.897%
100.cm^{-1}	18	99.090%

Table 2.3. Limiting stack sizes in pairs (m) and corresponding peak reflectivities for output coupling efficiency of 50%.

In these models we have not considered the effect of roughness in the reflector layer interfaces. This will have the effect of scattering light randomly and reducing the reflectivity. In the structures considered in this thesis roughness has not been a problem.

2. Design of laser structure

2.2.1. Reflector requirements

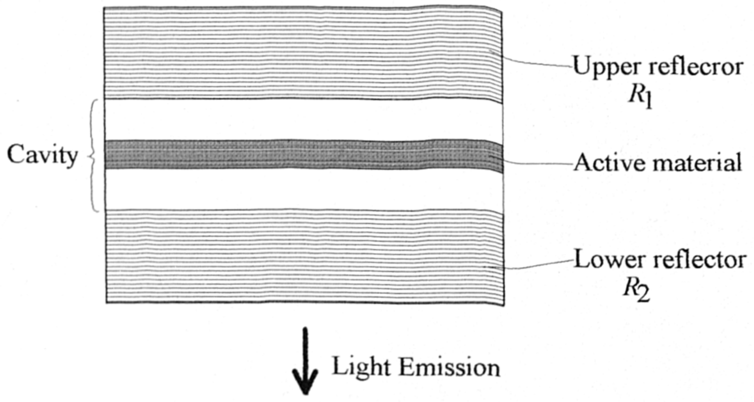

Fig. 2.7. Basic structure of VCSEL.

The basic laser structure is shown in fig.2.7. If we assume that a fairly modest optical gain of 500.cm^{-1} is obtainable from 100Å quantum wells the gain per pass is 5×10^{-4}. Using the threshold relation (1.3) with $\Gamma=1$ and assuming identical top and bottom cavity mirrors we calculate the number of pairs of AlAs / GaAs (i.e. using the highest index difference possible in the system) in the Bragg stacks required to provide suitable cavity finesse for lasing (for the moment neglecting any resonant placement of the gain material). The total growth thickness required to produce the complete structure, i.e. thickness of Bragg reflectors plus cavity region containing quantum wells spaced by half wavelengths (see next section), is calculated for different numbers of wells. Identical AlAs / GaAs top and bottom reflectors were assumed for the calculation. This function is plotted in fig. 2.8.

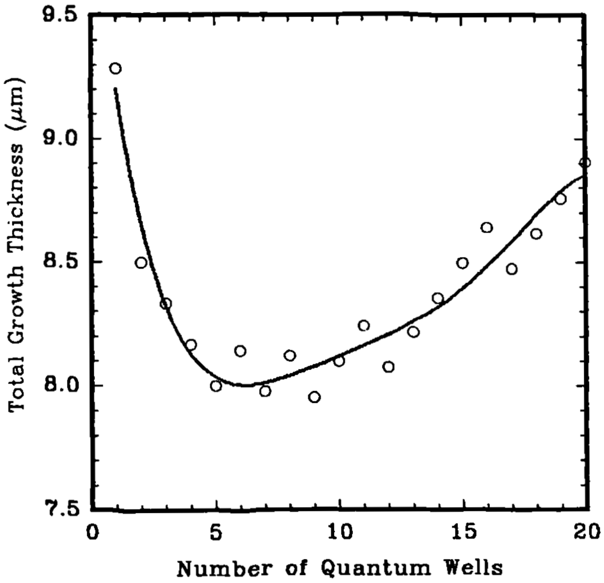

Fig. 2.8. Variation of total VCSEL device thickness with number of quantum wells.

For a device containing a single quantum well the reflector stacks must be thick to provide sufficient reflectivity to account for the small gain length (100Å). For 3 to 14 wells there is little difference in the total device thickness which is in the range 7.9 to 8.4μm. Outside of this range the structure is thicker since the increase in cavity length cannot be offset by the removal of reflector pairs. A value of three wells was chosen noting that more wells imply a larger active volume and hence a higher threshold current since the same gain condition was assumed in each case. 1 or 2 wells do not allow sufficient margin for unaccounted losses and may require a much higher gain at threshold if the mirror absorption is particularly high.

2.2.2 Resonant periodic gain

Consider an optical resonator comprising two highly reflecting parallel mirrors and that a standing wave exists in the cavity so formed. For a high finesse cavity with only a small amount of gain (as in a VCSEL). We consider forward and reverse travelling waves E^+ and E^- of equal amplitude E_0 and with propagation constants β (2.14).

$$E^+ = E_0 e^{j(\beta z-\omega t)} \tag{2.14a}$$

$$E^- = E_0 e^{j(-\beta z-\omega t)} \tag{2.14b}$$

The net field is therefore:

$$E = E^+ + E^- = 2E_0 e^{-j\omega t}\cos(\beta z) \tag{2.15}$$

The power density P in the standing wave is given by (2.16)

$$P = \tfrac{1}{2} n\sqrt{\varepsilon_0} EE^* = 2n\sqrt{\varepsilon_0} E_0^2 \cos^2(\beta z) \tag{2.16}$$

This is spatially variant with a mean value of $n\sqrt{\varepsilon_0}E_0^2 = P_{av}$ and a maximum value of $2P_{av}$ at antinodes situated at $\beta z = m\pi$: m=0,1,2.... The power falls to zero at nodes between midway between these points. Fig. 2.9 illustrates this.

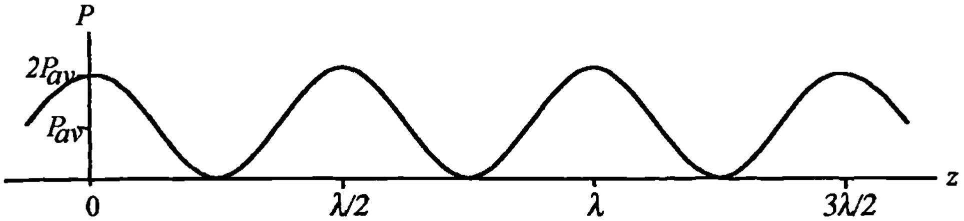

Fig. 2.9 Standing wave resulting from counter-propagating waves in high finesse optical resonator.

In a material with optical gain g, the intensity variation with distance due to this gain is (2.17):

$$\frac{dP}{dz} = gP = 2gP_{av}\cos^2(\beta z) \tag{2.17}$$

If g is spatially variant also we may define an effective gain length G(2.18).

$$G = \int_{-\infty}^{\infty} g(z)\frac{P}{P_{av}}dz \tag{2.18}$$

For a uniform gain g' extending over a length L, which is many or a whole number of half wavelengths, the gain length is (2.19).

$$G = g'L \tag{2.19}$$

If now we put the gain medium only in thin layers situated at the antinodes of the standing wave by splitting it into m short segments of length l [9,10], see fig. 2.10.

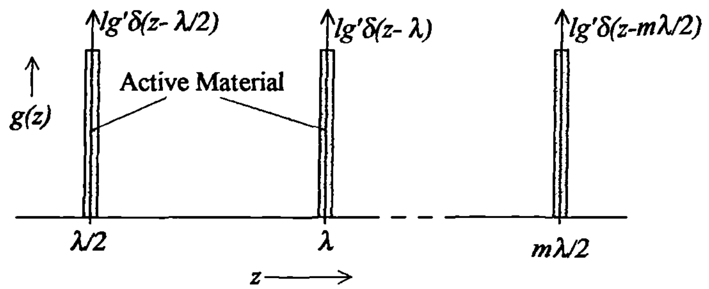

Fig. 2.10. Resonant periodic gain. Gain medium is spit into m short segments and situated at positions of antinodes of the optical standing wave.

The spatial variation of gain is given approximately by (2.20)

$$g(z) = \sum_{i=1}^{m} g'l.\delta(z - \lambda/2) \tag{2.20}$$

The total gain length is the same (2.21)

$$L = ml \tag{2.21}$$

Performing the integral (2.18) we see that the gain length is now doubled (2.22) over the case for a uniform gain medium.

$$G = 2g'L \tag{2.22}$$

Alternatively placing the active layers at the nodes of the standing wave produces a zero effective gain.

In conclusion: by placing the active material only at antinodes of the optical standing wave in a high finesse laser cavity it is possible to double the effective optical gain as compared with random placement (i.e. uniform gain medium over complete cycles of the standing wave). Misplacement of the active material at nodes of the standing wave results in zero net gain as there is no electromagnetic field to perturb the gain medium. Preferential placement of the gain medium in this way is known as ***resonant periodic gain***[9,10].

We are fortunate in the case of the VCSEL in two respects. Firstly, due to the short cavity in the vertical geometry it is possible to know exactly where the nodes and antinodes of the longitudinal mode with the highest finesse will be situated; the position of these will not change appreciably due to any changes in refractive index. Secondly, since the epitaxial growth direction is along the axis of the vertical cavity, it a relatively simple matter to form quantum wells which are thin compared to the optical wavelength at the antinode positions. The quantization effects in quantum wells[11] result in reduced threshold carrier densities and combined with the small active volume give rise to low threshold current densities (see chapter 1). By placing the active material only where it is most needed we eliminate the effects of spatial hole burning for the longitudinal mode (lateral hole burning effects[12] may still exist however).

2.2.3. Details of full laser structure

For a three well device as described above the threshold condition is given by $R_1.R_2=0.997$ assuming a quantum well gain of $500.\text{cm}^{-1}$. Each mirror requires 23 or more pairs. In order that a significant fraction of the output light is not lost through the second mirror, it is desirable that one reflector be much more highly reflecting than the other. To this end we chose the output reflector to have 23 pairs (R=0.9976) and the other to have 14.5 pairs plus a gold layer to augment the reflection (R=0.9996). The reflectivity of a Au layer in air is approximately 0.98 at a wavelength of 1000nm (Melles Griot data[13]). We model this as a refractive index of 262. For a GaAs based device it is only possible to utilise a Au layer in this way when using InGaAs wells; the bandgap being lower than that of GaAs allows light output to be taken through the transparent substrate. The Au layer also forms an electrical contact for current injection. The top and bottom Bragg reflectors are doped p and n type respectively to form a p-i-n diode structure with the quantum wells in the undoped cavity region. This is the basic structure behind the experimental part of this thesis and is similar to that used by a number of other authors[14,15].

Fig. 2.11 shows the standing wave detail of the electromagnetic field in the laser structure where we have employed the advantages of resonant periodic gain. Note that due to the phase of the reflection at the GaAs / AlAs interface, the quantum wells are spaced by $\lambda/2$ from the first AlAs mirror layers. The complete cavity is 2λ long, at 1000nm in GaAs this is 5701Å. Also note the $\lambda/2$ phase matching layer required below the Au mirror.

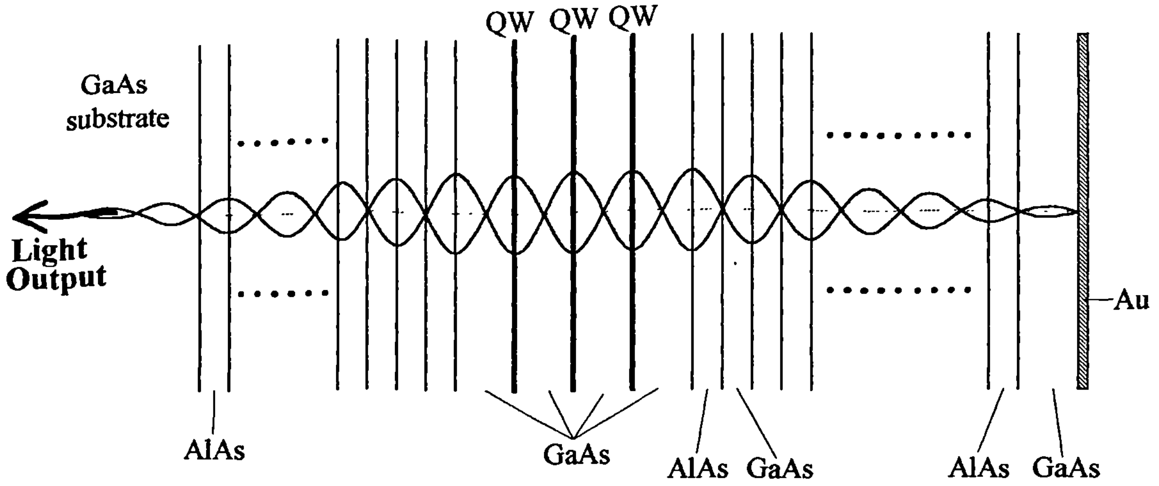

Fig. 2.11. Complete VCSEL structure showing detail of electromagnetic standing wave and the quantum wells positioned at antinodes.

A two wavelength long cavity has only one longitudinal mode within the high reflectance band of the Bragg reflectors. Consequently there can be only one longitudinal lasing mode supported in this device. The lasing wavelength will therefore be determined by the cavity and mirror dimensions rather than the wavelength for maximum gain in the gain medium (the latter is generally true for Fabry-Perot edge emitting lasers). There will be many transverse modes supported in a cylindrical mesa etched device. These will be closely spaced, sub nanometer for devices of 5μm diameter[16,17]. Only those close in wavelength to the fundamental TE mode will have sufficient gain to lase. Note that modes with significant TM component will have reduced gain due to the strain effects in the active quantum wells.

2.2.4. The effect of errors in growth thickness

Since the operating wavelength is determined by the cavity and mirror dimensions, it is necessary to consider the effects of growth error on the cavity mode. An error of ±10% in the thickness of a 100Å quantum well will have a very small effect (±2.7nm, refer to fig. 3.12) on the transition energies but a general error in growth rate will give a ±10% linear shift of the resonant wavelength i.e. ±10nm about a 1000nm operating wavelength; this is significant when compared to the shape of the quantum well gain spectrum.

It is also important to consider resonance shifts introduced by layer to layer growth fluctuations caused by poor control of GaAs / AlAs deposition rates or by monolayer fluctuations. Weber *et al.* consider the effect of error in a single layer of a reflector[18], here we consider the effect of error in all layers in the VCSEL. In the following model we create VCSEL structures numerically with random errors in the thickness of the epitaxially grown layers. Fig. 2.12 illustrates these results. Each data point on the graph is the result of 1000 randomly generated structures. Each layer in the structure is subjected to a percentage error about the nominal value with a normal distribution. There are three lines plotted, for error in all layers, error only in mirror layers and error in cavity layer only; the cavity region is modelled as a single GaAs layer. The results show the effect on the position of the cavity resonance caused by the errors as the standard deviation of the shift of the resonant wavelength about the nominal value, in all cases there is no significant shift of the mean value of the resonance. The nominal structure is that described above (section 2.2.3) i.e. 2λ cavity and 14 pair top and 23 pair bottom AlAs / GaAs quarter wave reflectors.

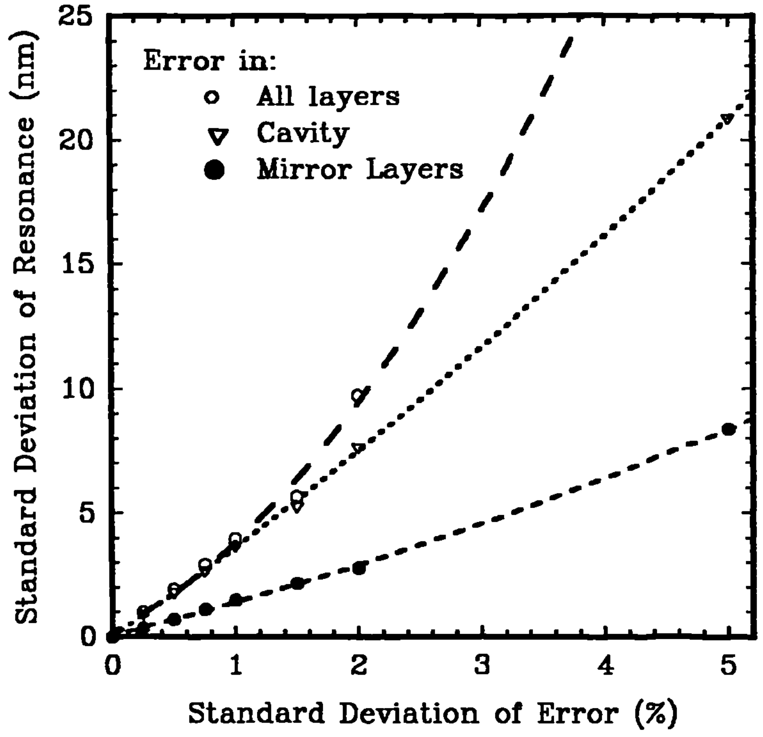

Fig. 2.12. Variation of cavity resonant wavelength due to random layer fluctuations

From this figure it can be seen that for small percentage errors there is a linear relation between the resonance shift and the growth error and that most important is the error in the mirror layers. This is a result of there being many layers in the mirrors and small errors in just one layer near to the cavity may produce large changes in the phase of the reflection from the stack. For larger errors the shift increases super linearly as phase compensation effects of the reflectors are limited (see section 2.2.5). For errors in excess of 5% it becomes impossible to find a solution for some of the structures generated as the resonance moves out of the high reflectance band of the mirrors.

2.2.5. Short cavity effects

It is noted that for errors in the cavity length the shift of the resonance is not as large as would be expected in a resonator with fixed metallic reflectors. This is due to the phase compensation effect of the dielectric mirrors (sec. 2.1.2). To understand this we consider the condition for resonance of the cavity. Let the cavity have length l and have mirrors with amplitude reflection coefficients $r_1 e^{j\phi_1}$ and $r_2 e^{j\phi_2}$. A quality factor Q is assigned to the cavity, this is given by (2.23) and is very large over a very narrow band if r_1 and r_2 approach unity. The quality factor is a measure of the amplitude of the standing wave in the cavity compared to the input power (from gain) required to sustain it.

$$Q = \frac{1}{\left|1 - r_1 r_2 e^{-j(\phi_1+\phi_2-2\beta l)}\right|^2} = \frac{1}{1+R_1R_2\left[1-2\cos(\phi_1+\phi_2-2\beta l\right]} \tag{2.23}$$

$$\left(\phi_1+\phi_2-2\beta l\right)=0 \tag{2.24}$$

Where β is the propagation constant of the wave in the medium of the cavity. Fig. 2.13 shows the variation of Q with wavelength for the structure described above for a number of absorption coefficients. The figure illustrates a small error in the dimensions used giving a shift in the resonance of ~0.12nm, or 0.012%, from the nominal 1000nm. For low absorptions the linewidth of $Q(\lambda)$ is very narrow. The laser will tend to operate where Q reaches a maximum and this occurs when the cavity round trip phase reaches zero (modulus 2π) (2.24). Table 2.4 lists the values of Q_{max} and the linewidths of $Q(\lambda)$ for the different absorptions. For absorptions of the order 10.cm^{-1} the maximum is not seriously reduced but at 100.cm^{-1} it is.

α	**Q_{max}**	**FWHM linewidth of $Q(\lambda)$**
0.cm^{-1}	701	0.09nm
1.cm^{-1}	652	0.11nm
10.cm^{-1}	401	0.17nm
100.cm^{-1}	82.7	0.81nm

Table 2.4. Maximum values and FWHM linewidths of $Q(\lambda)$.

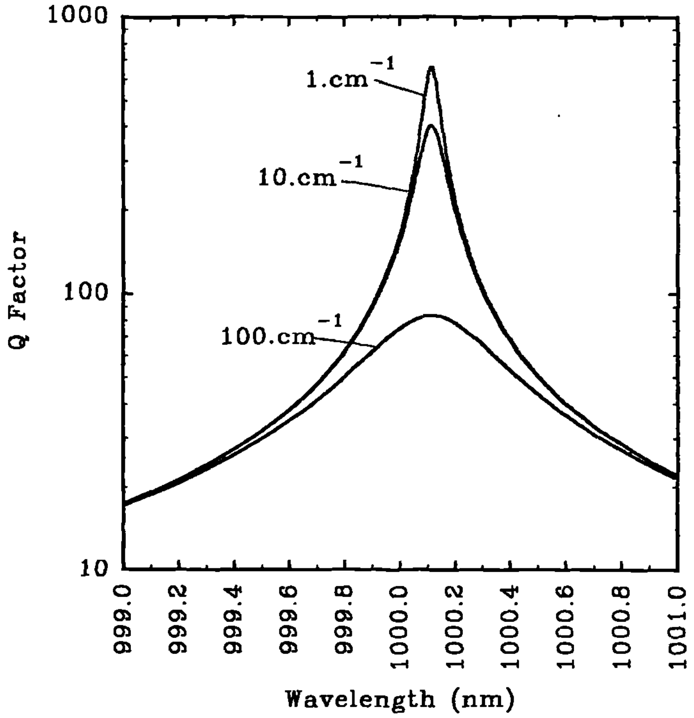

Fig. 2.13. Q factor plotted against wavelength for VCSEL structure with 23 pair bottom reflector 14.5 pair plus Au layer top reflector and 2λ cavity for uniform absorption coefficients of 1, 10 and 100.cm^{-1}.

The threshold condition may now be rewritten as (2.25):

$$Q_{\max} = \frac{1}{e^{2g_{th}L_a} - 1} \qquad (2.25)$$

Where g_{th} is the optical power gain coefficient and L_a is the active length. Since the active length $g_{th}L_a$ is short we have:

$$g_{th} \approx \frac{1}{2Q_{\max}L_a} \qquad (2.26)$$

For a nominal resonance at λ_o, variation $\Delta\lambda$ is caused by error in ϕ_1, ϕ_2, and l. Considering an error in the cavity length: $l=l_o+\Delta l$ a phase change due to a shift in wavelength is needed to maintain resonance so that:

$$\left(\phi_1 + \phi_2 - 2\beta.(l+\Delta l)\right)\Big|_{\lambda_o} + \Delta\lambda\left(\frac{\partial\phi_1}{\partial\lambda} + \frac{\partial\phi_2}{\partial\lambda} - 2\frac{\partial\beta}{\partial\lambda}l\right) = 0 \qquad (2.27)$$

$$2\beta.\Delta l = \left(\frac{\partial\phi_1}{\partial\lambda} + \frac{\partial\phi_2}{\partial\lambda} + 2\frac{2\pi n_c}{\lambda^2}l\right)\cdot\Delta\lambda \qquad (2.28)$$

But it is found that, irrespective of any $\Delta\phi$, sufficiently close to λ_0 the phase compensation is (2.29):

$$\frac{\partial\phi_1}{\partial\lambda} = \frac{\partial\phi_2}{\partial\lambda} = \phi' = 73.\mu\text{m}^{-1} \tag{2.29}$$

Thus:

$$\frac{\partial l}{\partial\lambda}\cdot\frac{1}{l} = \frac{\lambda\phi'}{2\pi n_c l} + \frac{1}{\lambda} \tag{2.30}$$

So for a short cavity, the proportional change in wavelength with cavity length $(\partial\lambda/\lambda)/(\partial l/l)$ is reduced below the value of 1.0 expected in a cavity with metallic reflectors. This is very useful as the cavity region must be grown at a lower temperature than the rest of the structure to ensure high quality quantum wells. Growth rates are temperature dependant and accuracy may be difficult to maintain especially by MOCVD where there is no in situ feedback. Fig. 2.14. illustrates the reduced shift for small cavity lengths by plotting the shift against error in cavity length for 1λ, 2λ, 4λ and a long cavity. These results were obtained by simulating structures with random errors as in fig. 2.12. The structure with a short cavity and a small number of quantum wells is more attractive as the shift in resonance due to errors in the cavity may be reduced by up to 80% in the case of the 1λ cavity. For large errors (>2% s.d.) the improvement is not so great as the extent of phase compensation is limited.

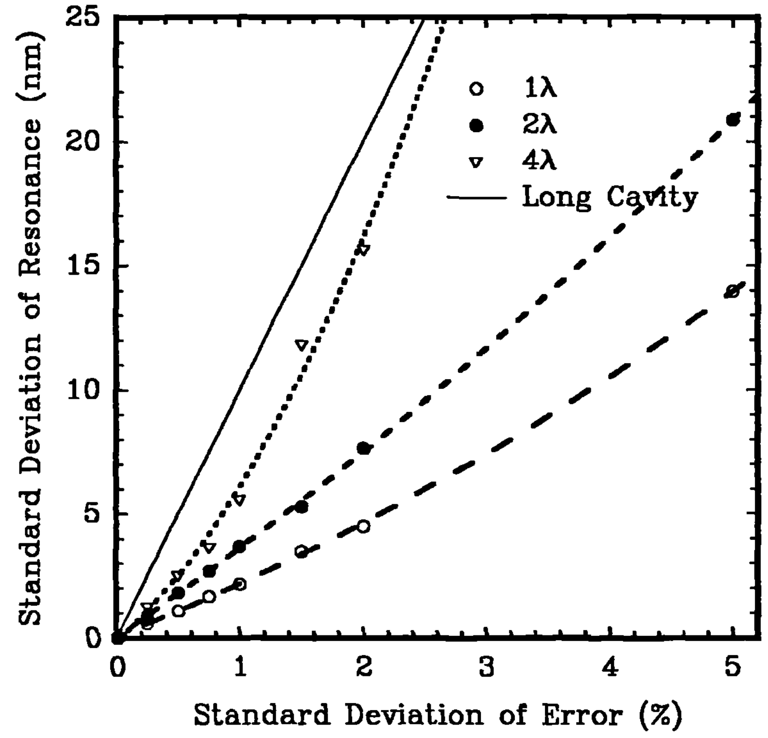

Fig. 2.14. Variation of resonance wavelength with cavity error for different cavity lengths. Each point represents 1000 randomly generated structures.

If, due to errors in layer thicknesses, there is some shift in the resonant wavelength from the nominal value we must consider the effect on Q_{max} due to the variation of the mirror reflectivities with wavelength. Fig. 2.15 shows the variation with wavelength of the maximum value of Q which can be obtained for a device resonant at that wavelength. In this we assume that the reflectors are not in error but we may find the effect of reflector error by displacing the curves along the wavelength axis.

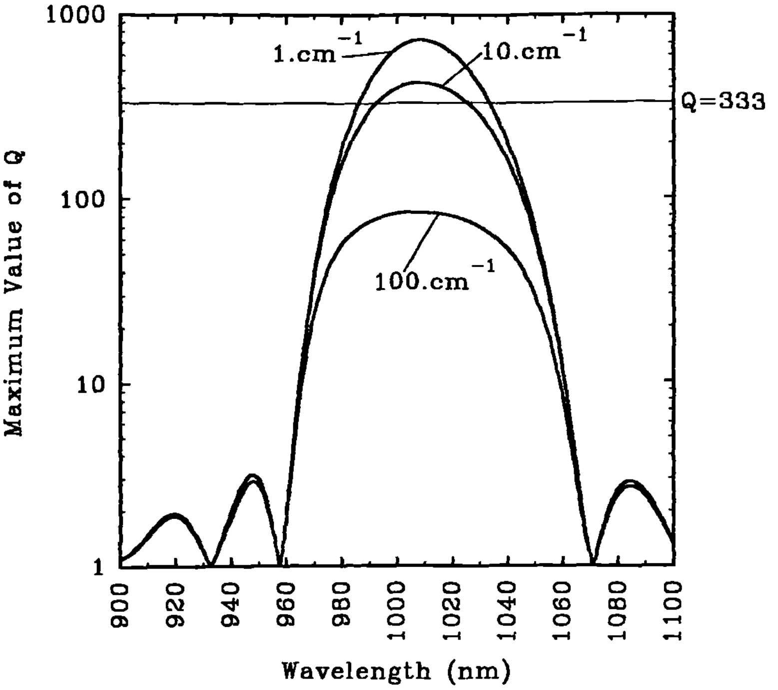

Fig. 2.15. Wavelength variation of maximum obtainable Q considering displacements of the resonant wavelength. The line at Q=333 corresponds to the threshold condition for a quantum well gain of 500.cm^{-1}.

For a quantum well gain of 500.cm^{-1} the threshold condition is satisfied for Q=333. For an absorption of 1.cm^{-1} this may be satisfied over a bandwidth of 47.2nm (±23.6nm). At 10.cm^{-1} this is reduced by 30 % to 33.2nm (±16.6nm) and at 100.cm^{-1} the threshold condition cannot be met. In a laser using purely dielectric reflectors these bandwidths would be much reduced but here the use of a Au contact layer considerably broadens the high reflectivity band of the upper reflector. For the 2λ cavity resonance shifts of 23.6 and 16.6nm result from errors in cavity length of 5.5 and 4.2% respectively (see fig. 2.14).

2.2.6. Effect of absorption

Since the value of Q_{max} mentioned above determines the threshold gain it is interesting to look at the effect of absorption on this value in more detail. Carriers are injected into the active region through the Bragg reflectors. These must therefore have as low an ohmic resistance as possible to give low operating voltage and lasing efficiency. As there are a large number of heterointerfaces in the reflectors, half of which are reverse biased it is necessary to dope them to a high level so as to allow efficient tunnelling across the junctions (see chapter 4), these impurities increase the free carrier absorption. Figure 2.16. shows the proportional reduction in Q_{max} caused by adding absorption to the structure. The value g_{min} is the minimum value of threshold gain required in a structure with zero absorption and g_{th} is the increased value of gain required for an absorbing structure. Curves on the figure illustrate the effect of placement of absorbing material.

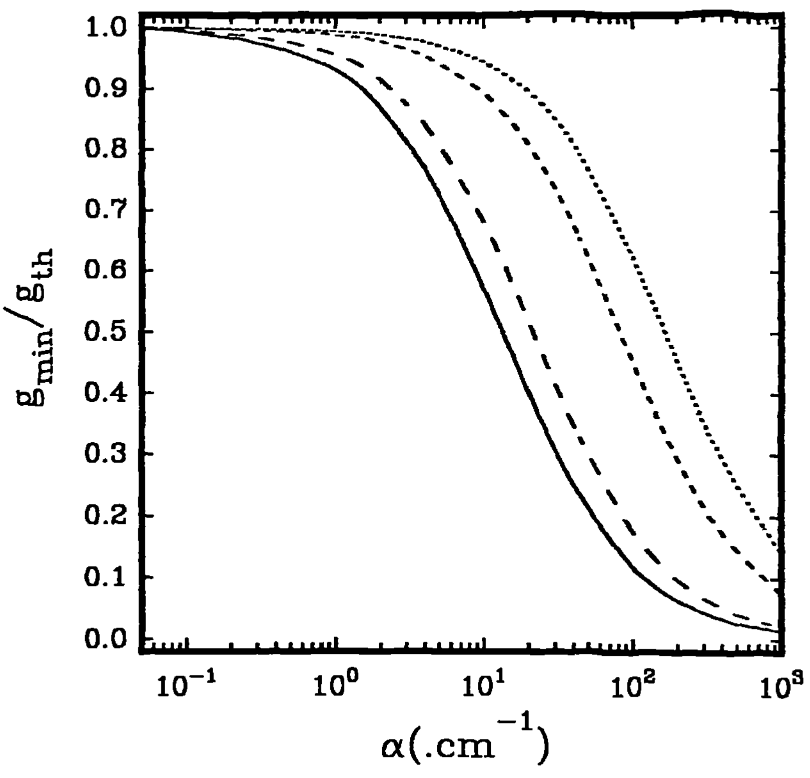

Fig. 2.16. Graph reduction in cavity quality with increasing absorption. Absorption in all layers (——), mirror layers only (— —), interface layers only (– – –), reverse biased interface layers only (- - - -).

The solid line shows the effect of absorption in all layers; in this case an absorption of 10.cm^{-1} is sufficient to double the gain required for threshold. The cavity region should be intrinsic and thus have a low absorption; the second line shows this case of absorption only in mirror layers and here the absorption to double the threshold gain is 20.cm^{-1}. Since the high mirror doping is only useful in the vicinity of the heterointerfaces where it increases the band bending for reduction the tunnelling resistance (see chapter 5), it is sensible to only dope regions close to these interfaces to a high level, the rest of the mirror can be doped to a much more lightly.

The other lines in fig.2.11 therefore show the effect of only doping a 200Å wide region about the AlAs / GaAs interfaces, the first is for doping in all interfaces and the second for doping only at the reverse biased interfaces. In these cases the absorption can be increased to 80.cm^{-1} and 160.cm^{-1} respectively for a doubling in the threshold gain over the lossless case. Since the absorption of GaAs at 1000nm for an acceptor concentration of 10^{18}.cm^{-1} is estimated at 20.cm^{-1} [19]the reduction in threshold gain by modulation doping can be significant[20,21], i.e. a factor of two. Table 2.5 summarises these results.

Absorbing material located in	**α for double threshold gain**
All layers	10.cm^{-1}
Mirror layers only	20.cm^{-1}
200Å layers at interfaces	80.cm^{-1}
200Å layers at reverse biased interfaces	160.cm^{-1}

Table 2.5. Absorption coefficients required to double threshold gain of otherwise lossless laser for different placements of the absorbing material.

2.3. Conclusions

The basic optical design of a VCSEL has been produced with discussion on the effects of absorption and growth thickness errors. The optical cavity is formed between two multilayer Bragg reflectors of AlAs / GaAs: 23 pairs in the bottom reflector and 14.5 pairs plus a Au contact layer in the top reflector. The optical cavity is two wavelengths long at the resonant wavelength of 1000nm and incorporates 3 resonantly placed InGaAs quantum wells as the active layer. Light output may be taken through the transparent GaAs substrate. This is similar to structures used by a number of other authors[14,15].

Provided background absorption is below $\sim$20.cm^{-1} the laser should perform well with a threshold gain below 500.cm^{-1}. Layer to layer thickness variations in the reflectors will have to be below ~5% to prevent excessive shift of the resonant wavelength. Greater shifts result from errors in the cavity length and such errors are more likely due to the reduced growth temperature for the cavity region (chapter4): for a background absorption of 10.cm^{-1} errors of ±16.6nm which results from thickness a cavity thickness error of 4.2%. Short cavity effects are useful in reducing such errors.

Absorption in high purity GaAs material is less than 0.3.cm^{-1} at 1000nm but with the addition of impurities such as dopant atoms it will increase. Absorption has the effect of reducing the reflectivity and perhaps more seriously the output coupling efficiency of reflector stacks. By judicious placement of the dopant only where it is absolutely necessary (at reverse biased hetero-interfaces) detrimental effects are kept to a minimum[20,21].

References:

[1] A.Yariv, *Optical electronics*, 3rd. Edition; Holt, Rinehart & Winston, New York, 1985.

[2] McLeod, *Thin film optical filters*, Adam Hilger Ltd., Bristol.

[3] Boyd, *Theory of parametric oscillation phase matched in GaAs thin film waveguides*, IEEE J. Quantum Electron., **8**, 10, p788, 1972.

[4] H.C.Casey Jr., D.D.Sell & M.B.Panish, *Refractive index of* $Al_xGa_{1-x}As$ *between 1.2 and 1.8eV*, Appl. Phys. Lett., **24**, 2, pp63-65, 1974.

[5] D.D.Sell, H.C.Casey & K.W.Wecht, *Concentration dependence of the refractive index of n- and p-type GaAs between 1.2 and 1.8eV*, J. Appl. Phys., **45**, 6, pp2650-2657, 1974.

[6] D.I.Babic & S.W.Corzine, *Analytic expressions for the reflection delay, penetration depth and absorbtance of quarter-wave dielectric mirrors*, IEEE J. Quantum Electron., **28**, 2, pp514-524, 1992.

[7] M.Ogura, W.Hsien, M-C.Wu, S.Wang, J.R.Winnery, S.C.Wang & J.J.Yang, *Surface-emitting laser diode with vertical GaAs / GaAlAs Quarter-wavelength multilayers and lateral buried heterostructure*, Appl. Phys. Lett., **51**, 21, pp1655-1657, 1987.

[8] A.Scherer, J.L.Jewell, M.Walther, J.P.Harbison & L.T.Florez, *Fabrication of low threshold voltage microlasers*, Electron. Lett., **28**, 13, pp1224-1226, 1992.

[9] S.W.Corzine, R.S.Geels, J.W.Scott, R-H.Yan & L.A.Coldren, *Design of Fabry-Perot surface-emitting lasers with a periodic gain structure*, IEEE J. Quantum. Electron., **25**, 6, pp1513-1524, 1989.

[10] M.Y.A.Raja, S.R.J.Brueck, M.Osinski, C.F.Schaus, J.G.McInnery, T.M.Brennan & E.M.Hammons, *Resonant periodic gain surface-emitting semiconductor lasers*, IEEE J. Quantum. Electron., **25**, 6, pp1500-1512, 1989.

---

[11] C.Weisbuch, *Basic optical properties of low dimensional structures for applications to lasers, electro-optic and non-linear optical devices,* chapter in *Low dimensional structures in semiconductors,* A.R.Peaker & H.G.Grimmeiss Eds., NATO ASI Series B: Physics Vol. 281, Plenum, 1991.

[12] D.Vakshoori, J.D.Wynn, G.J.Zydzik, R.E.Leibenguth, M.T.Asom, K.Kojima & R.A.Morgan, *Top-surface emitting lasers with 1.9V threshold voltage and the effect of spatial hole burning on their transverse mode operation and efficiencies,* Appl. Phys. Lett., **63**, 13, pp1448-1450, 1993.

[13] *Optics guide 4,* Melles Griot.

[14] R.S.Geels, S.W.Corzine, J.W.Scott, D.B.Young & L.A.Coldren, *IEEE Photon. Technol. Lett.,* **2**, 4, pp234-236, 1990.

[15] M.Orenstein, A.C.Von Lehmen, C.Chang-Hasnain, N.G.Stoffel, J.P.Harbison, L.T.Florez, E.Clausen & J.E.Jewell, *Vertical cavity surface-emitting InGaAs / GaAs lasers with planar lateral definition,* Appl. Phys. Lett., **56**, 24, pp2384-2386, 1990.

[16] C.J.Chang-Hasnain, M.Orenstein, A.Von Lehmen, L.T.Florez, J.P.Harbison & N.G.Stoffel, *Transverse mode characteristics of vertical cavity surface-emitting lasers,* Appl. Phys. Lett., **57**, 3, pp218-220, 1993.

[17] J.L.Jewell, S.L.McCall, A.Scherer, H.H.Houh, N.A.Whittaker, A.C.Gossard & J.H.English, *Transverse modes, waveguide dispersion and 30ps recovery in submicron GaAs / AlAs microresonators,* Appl. Phys. Lett., **53**, 3 pp22-24, 1989.

[18] J-P.Weber, K.Malloy & S.Wong, *Effects of layer thickness variations on vertical-cavity surface-emitting lasers,* IEEE Photon. Technol. Lett., **2**, 3, pp162-164, 1990.

[19] J.S.Blakemore, *Semiconducting and other major properties of gallium arsenide,* J. Appl. Phys., **53**, 10, ppR123-R181, 1982.

[20] R.S.Geels & L.A.Coldren, *Low threshold, high power, vertical-cavity surface-emitting lasers,* Electron. Lett., **27**, 21, pp1984-1985, 1991.

[21] M.Sugimoto, H.Kosaka, K.Kurihara, I.Ogura, T.Numai & K.Kasahara, *Very low threshold current density in vertical-cavity surface-emitting laser diodes with periodically doped distributed Bragg reflectors,* Electron. Lett., **28**, 4, pp385-387, 1992.

3. Gain Calculations for Strained InGaAs / GaAs Quantum Wells

This chapter discusses how the density of electron states and the population of these states gives rise to optical gain. The optical gain spectra of strained InGaAs / GaAs quantum wells for different carrier concentrations are calculated using a simplified model of the valence band-structure using an infinite well approximation. The model is used in later chapter 8 to explain the experimental results of chapters 6 and 7.

The application of mechanical strain to semiconductor materials alters the band structure in a number of ways. Using strained layers such as InGaAs grown on GaAs the band structure may be engineered to reduce the density of valence states and produce lasing at lower carrier densities[1,2].

3.1. Basic theory of optically assisted transitions

Optical gain and thus stimulated emission in semiconductor materials results from the interaction of an electromagnetic field (e.m.) with particles in an excited state. These particles are electrons (or holes).

3.1.1. Two level systems

Let us consider the possible transitions in a two level system with ground state *k* and excited state *m*. There are three possible optically assisted transitions between the two states. These are illustrated in fig. 3.1.

(a) *Spontaneous emission,* an excited electron falls to the lower state and causes the emission of a photon.

(b) *Stimulated emission,* a photon triggers an excited electron to fall to the lower state and produce a second photon coherent with the initial photon - an optical amplification process.

(c) *Stimulated absorption,* this is the reverse process to (b), a photon promotes an electron from the lower level into the excited state and in the process is absorbed.

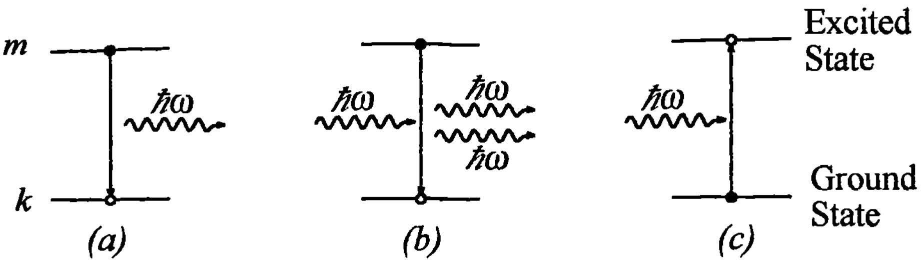

Fig. 3.1. Optically assisted processes in a two level electronic system with states m and k: (a) Spontaneous emission; (b) Stimulated emission and (c) Stimulated absorption.

The spontaneous emission rate depends on the probability of occupation of the excited state and the probability of the lower state being vacant, thus the transition rate R_{spon} is of the form of (3.1).

$$R_{spon} = Ap_m(1-p_k) \qquad (3.1)$$

Where p_m and p_k are the occupation probabilities of the m and k states respectively. A is the transition probability of an excited particle falling into a vacant lower state.

The stimulated emission rate R_{stim}, responsible for laser action, similarly depends on the same occupation probabilities but also on the density of photons $\rho(\omega)$ at the wavelength corresponding to the energy gap between the two states (3.2).

$$R_{stim} = Bp_m(1-p_k)\rho(\omega) \qquad (3.2)$$

Where B is the transition probability for stimulated emission.

The stimulated absorption rate R_{abs} is a similar process to stimulated emission but in reverse, so will depend on the probabilities of occupancy and vacancy in the lower and higher states respectively (3.3).

$$R_{abs} = Bp_k(1-p_m)\rho(\omega) \qquad (3.3)$$

From balance of particles in steady state it is found that the constant B is the same in equations (3.2) and (3.3). The net stimulated emission rate is therefore (3.4).

$$R_{net} = R_{stim} - R_{abs} = B\rho(\omega)(p_m - p_k) \qquad (3.4)$$

Thus the condition for net gain is given by equation (3.5) and is thus a non-equilibrium state. The limiting value $p_m=p_k$ is known as the transparency condition because it is when the material becomes lossless to light at the frequency ω.

$$p_m > p_k \qquad (3.5)$$

The transition rate w in a two level system, between two states m and k is given by Fermi's Golden Rule[3] (3.6).

$$w = \frac{\pi|H_{mk}|^2}{2\hbar^2} = B\rho(\omega) \qquad (3.6)$$

Where $\left|\overline{H}_{mk}\right|^2$ is the Hamiltonian matrix element for the transition between the two states *m* and *k* as given in (3.7a).

$$\overline{H}_{mk} = \int u_m^* . \overline{H}(\underline{r}) . u_k d\tau \qquad (3.7a)$$

$$H' = \overline{H}(\underline{r}) \cos \omega t \qquad (3.7b)$$

Where u_m and u_k are the Bloch functions of the two states and H' is the perturbation Hamiltonian due to the electromagnetic field which is of the form given in (3.7b). The matrix element is thus related to the overlap integral of the two Bloch states.

In an electromagnetic plane wave of amplitude E_o the time invariant perturbation $\overline{H}$ is of the form (3.8):

$$\overline{H} = e\boldsymbol{E}_o . \boldsymbol{r} \qquad (3.8)$$

Where *e* is the electronic charge. Hence the Hamiltonian matrix element is (3.9):

$$\left|\overline{H}_{mk}\right| = eE_o \left|\langle u_m | r | u_k \rangle\right| \qquad (3.9)$$

In a medium with refractive index *n* the field E_o is equivalent to an energy flux $I(\omega)$ at the angular frequency ω as given by (3.11):

$$I(\omega) = \tfrac{1}{2} \varepsilon_o n E_o^2 c \qquad (3.10)$$

Where *c* is the speed of light. And from (3.6) we find the transition rate *w* (assuming the radiation is polarized in the direction of any particle wavevector):

$$w = I(\omega) \cdot \pi e^2 \frac{\left|\langle u_m | r | u_k \rangle\right|^2}{\varepsilon_o n \hbar^2 c} \qquad (3.11)$$

3.1.2. Transitions between states in a semiconductor

In a conventional semiconductor laser, the excited state corresponds to a conduction band electron state and the lower state to a valence band electron state; alternatively thought of as a state filled by a hole. The *m*→*k* transition can be thought of as an electron-hole recombination.

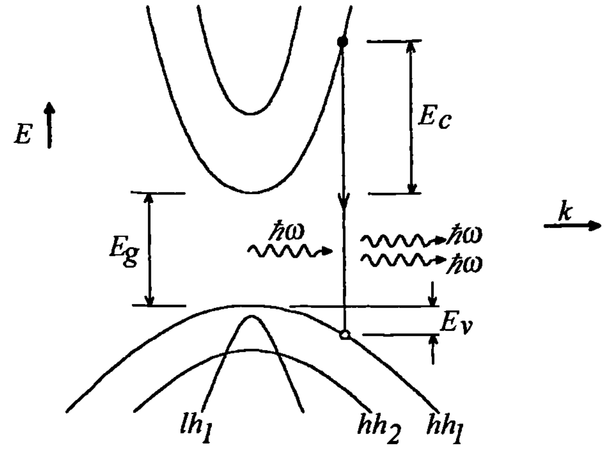

Fig. 3.2. Illustration of approximate band structure for quantum well showing energies relevant to k-selected transitions.

Let us consider the case of a quantum well. Fig. 3.2. shows the simplified band dispersion curves for states in a GaAs type quantum well. Let us consider the e_1 to hh_1 transition between the lowest electron and heavy hole states. We wish to consider only vertical transitions which do not require any phonon interaction. In pure material these ***'k-selected'*** transitions should dominate[4]. Also only transitions between states of the same quantum number (i.e. $e_1 \to hh_1$, $e_2 \to hh_2$, $e_1 \to lh_1$ etc.) where the matrix element is significant will be considered.

We can assume pseudo-equilibrium conditions for electrons and holes separately and assign conduction and valence Fermi functions f_c and f_v (3.12). Equation (3.4) now becomes (3.13) and the transition energy is given by (3.14)

$$f_c = \frac{1}{1+\exp\left(\frac{(E_c - E_{fn})}{kT}\right)};f_v = \frac{1}{1+\exp\left(\frac{(E_v - E_{fp})}{kT}\right)} \qquad (3.12\text{a,b})$$

$$R_{net} = B\rho(\omega)(f_c + f_v - 1) \qquad (3.13)$$

$$\hbar\omega = E_g + E_c + E_v = E_{tr} \qquad (3.14)$$

The gain at photon energy E_{tr} is dependant on the density of electron and hole states at energies E_c and E_v: $n_e(E_c)$ and $n_v(E_v)$. In a model quantum well the density of states in each confined level is a constant[5] but in a strained well the bands are strongly non-parabolic[6] and the densities vary with energy. Thus we find the net stimulated emission rate per unit volume (3.15).

$$\frac{R_{net}}{V}=n_c(E_c).n_v(E_v)\frac{\pi e^2\left|\langle u_m|r|u_k\rangle\right|^2 I(\omega)}{\varepsilon_o\hbar^2 nc}(f_c+f_v-1) \qquad (3.15)$$

If the electromagnetic wave propagates an elemental distance δx through an area A in a time δt, the net stimulated photons N_{net} in the volume is given by (3.16).

$$N_{net}=\frac{R_{net}}{V}\delta x.\delta t.A \qquad (3.16)$$

The stimulated photons are coherent with the original field and give rise to an increase in intensity δI (3.17) after travelling this distance.

$$\delta I=\frac{N_{net}\hbar\omega}{A\,\delta t} \qquad (3.17)$$

The optical gain per unit length at frequency ω is defined as the relative increase in intensity with distance and is therefore found to be (3.18):

$$g(\omega)=\frac{\delta I}{I.\delta x}=\frac{R_{net}}{VI(\omega)}\hbar\omega \qquad (3.18a)$$

$$g(\omega)=n_c(E_c).n_v(E_v)\frac{\pi e^2\omega\left|\langle u_m|r|u_k\rangle\right|^2}{\varepsilon_o nc\hbar}(f_c+f_v-1) \qquad (3.18b)$$

The transparency condition for transitions corresponding to frequency ω (3.5) can now be written as (3.19).

$$E_{fn}-E_{fp}>\hbar\omega \qquad (3.19)$$

The lowest energy transition occurs when $\hbar\omega=E_g$. To calculate the gain spectrum, we must know the density of states functions for electrons and holes and these are dependent on the band-structure.

3.1.3. Spontaneous recombination

We must also consider spontaneous recombinations which cause a loss of carriers in the absence of an optical field. It is found[3] that the spontaneous emission coefficient A is:

$$A=\frac{n^3q^2\omega^2}{\pi\varepsilon_o c^3\hbar}\left|\langle u_m|r|u_k\rangle\right|^2 \qquad (3.20)$$

From (3.1) we find the spontaneous emission rate for the semiconductor:

$$r_{spon}(\omega)=n_c n_v\frac{n^3q^2\omega^2}{\pi\varepsilon_o c^3\hbar}\left|\langle u_m|r|u_k\rangle\right|^2\cdot f_c f_v \qquad (3.21)$$

The current density due to spontaneous emission in a well of width L is found by integrating over all frequencies:

$$J_{spon} = L\int_0^{\infty} r_{spon}(\omega).d\omega \qquad (3.22)$$

Computed spontaneous emission spectra of the form (3.21) may be found in a number of references[7,8].

3.2. Band structure of strained InGaAs quantum wells

3.2.1. Introduction to strain effects

An unstrained bulk semiconductor such as GaAs has a valence band structure as shown in fig. 3.3[9]. Note that there are two bands, the so called light and heavy hole bands (*lh* and *hh*), degenerate at the zone centre. The *hh* effective mass is large (low curvature).

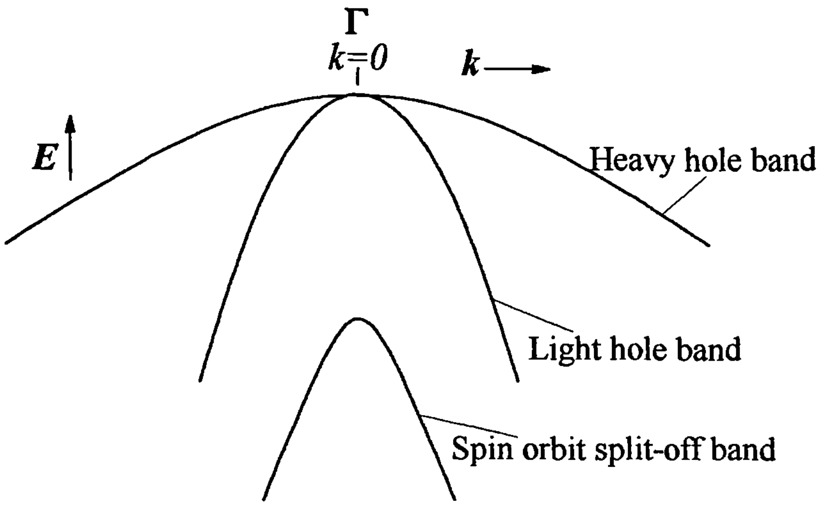

Fig. 3.3. Valence band structure of unstrained bulk semiconductor such as GaAs.

A large hole mass is not desirable for laser operation as a large carrier density (n_{tr}) is required to move the valence Fermi level into the band to achieve transparency. This relation (derived from equation (3.19)) is shown in (3.23) and fig. 3.4 shows the variation of n_{tr} with effective hole mass m_h assuming parabolic bands and a constant electron mass m_e=0.067m_o.

$$n_{tr}(E_g) = 2\left(\frac{kT}{2\pi\hbar^2}\right)^{3/2} \cdot (m_e m_h)^{3/4} \qquad (3.23)$$

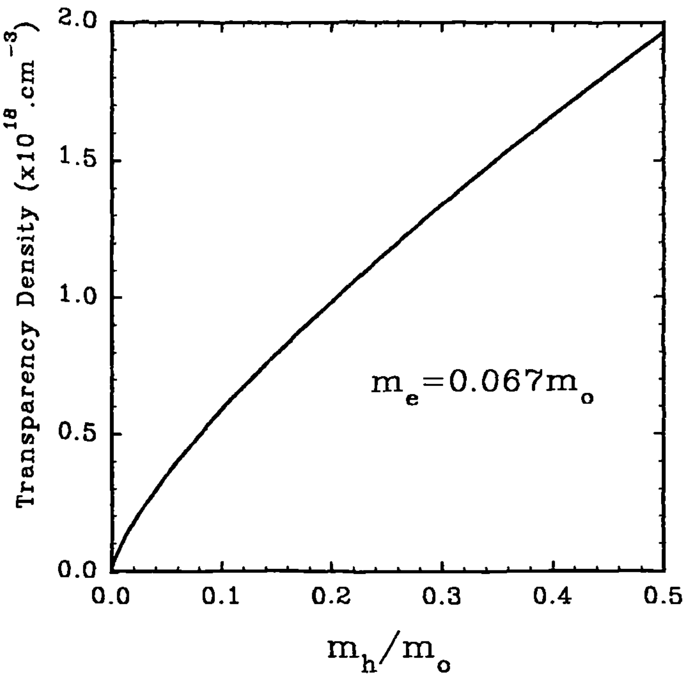

Fig. 3.4. Variation of transparency carrier density with m_h, assuming parabolic bands and a constant electron mass m_e=0.067m_o.

For bulk GaAs m_h=0.48m_o, giving a transparency density of 1.9×10^{18}.cm^{-3}. The light hole effective mass of $In_{0.2}Ga_{0.8}As$ is 0.071m_o. If we could make use of this light hole mass[10], the transparency density would be significantly reduced to 4.3× 10^{17}.cm^{-3}, a fourfold reduction.

A similar expression to (3.24) may be derived for the transparency carrier density in a quantum well with a single parabolic band. For a more realistic well with a number of occupied bands a general solution may not be derived analytically. In this case the bulk model may be used for a practical comparison.

A large carrier density results in large radiative and non-radiative carrier losses. Radiative carrier losses (spontaneous emission) tend to vary as n^2. Important non-radiative carrier loss mechanisms include the Auger processes; these vary as n^3. Increasing the carrier density therefore gives a superlinear increase in threshold current. Low effective masses are therefore very attractive.

Application of a biaxial stress breaks the cubic symmetry of the lattice[11] and splits the degeneracy at the zone centre by an energy S. With a biaxial compressive strain the energy of the heavy hole band is raised and the light hole band is lowered in the plane of the strain. In the perpendicular direction the reverse is true (fig. 3.5).

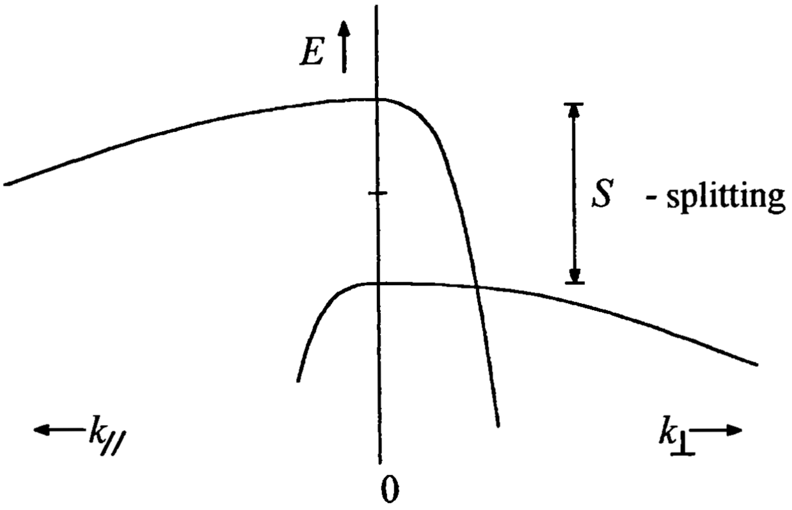

Fig. 3.5. Band structure of biaxially strained bulk semiconductor. Heavy and light hole bands are split by an energy S. Splitting for in-plane (//) and out of plane (⊥) directions are in opposite senses.

If we grow a thin epilayer of for example $In_xGa_{1-x}As$ (lattice constant a_c) on a substrate such as GaAs which has a smaller lattice constant (a_s) then if the epilayer is lattice matched it will be under a biaxial compressive strain in the plane of the layer (fig. 3.6). If it is sufficiently thin we can assume that all of the strain is confined to the layer. The in plane strain is therefore:

$$\varepsilon_{//} = \varepsilon_{xx} = \varepsilon_{yy} = \frac{a_s - s_c}{a_c} \tag{3.24}$$

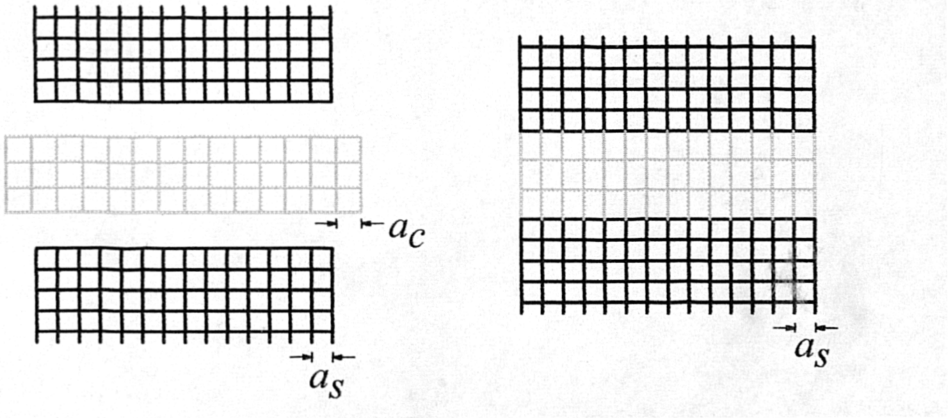

(a) *(b)*

Fig. 3.6. Illustration of thin epilayer of lattice constant a_c grown under biaxial compression on substrate with lower lattice constant a_s. (a) Layer and substrate in free state; (b) Strained layer epitaxially grown on substrate with capping layer applied.

The perpendicular strain is given by:

$$\varepsilon_{\perp} = -\frac{C_{12}}{C_{11}}\left(\varepsilon_{xx} + \varepsilon_{yy}\right) = -2\frac{C_{12}}{C_{11}}\varepsilon_{//} \qquad (3.25)$$

Where C_{11} is the in plane elastic constant of the material and C_{12} is the elastic constant for strain in the direction normal to the applied stress. For most materials, the ratio C_{12}/C_{11} is approximately ½. It is useful to think of these strains in terms of hydrostatic and axial components:

$$\varepsilon_{ax} = \varepsilon_{\perp} - \varepsilon_{//} = \frac{C_{11}+2C_{12}}{C_{11}}\varepsilon_{//} \qquad (3.26)$$

$$\varepsilon_{vol} = \varepsilon_{xx} + \varepsilon_{yy} + \varepsilon_{zz} = \frac{2\left(C_{11}-C_{12}\right)}{C_{11}}\varepsilon_{//} \qquad (3.27)$$

The hydrostatic strain ε_{vol} causes the band gap to change by ΔE_g (3.28) and the axial strain ε_a causes the *lh hh* splitting, *S* (3.29). Thus for an InGaAs well in GaAs we find that the light and heavy holes are confined as shown in fig. 3.6.

$$\Delta E_g = a.\varepsilon_{vol} \qquad (3.28)$$

$$S = b.\varepsilon_{ax} \qquad (3.29)$$

Where the material parameters *a* and *b* are known as the deformation potentials. For the $In_xGa_{1-x}As$ system the deformation potentials in eV are given in table 3.1, after Anderson *et al.*[12]

a	8.67-5.66*x* (eV)
b	1.7+0.1*x* (eV)

Table 3.1. $In_xGa_{1-x}As$ hydrostatic and shear deformation potentials[12].

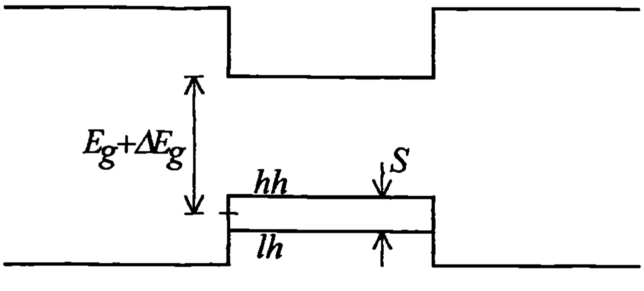

GaAs InGaAs GaAs

Fig. 3.7. Heavy hole, light hole and electron confinement in InGaAs quantum well under biaxial compression lattice matched to GaAs.

Fig. 3.7 illustrates the separate wells confining heavy and light holes due to the strain induced deformation potentials. If we take the preferred value of bulk valence band offset of 0.33, there is no confinement and well is type II for light holes.

There is a limit to the thickness of a strained layer which may be grown epitaxially on a substrate before dislocations are formed. The model of *Matthews and Blakeslee*[13] considers this critical layer thickness L_C as the thickness of strained material which may be grown before there is sufficient strain energy to propagate strain relieving misfit dislocations through the strained layer. The critical layer thickness is given by equation (3.30).

$$\varepsilon_{//} = \frac{b\left(1 - v\cos^2\alpha\right)}{2\pi L_C\left(1 + v\right)\cos\lambda} \cdot \left[\ln\left(\frac{L_C}{b}\right) + 1\right] \tag{3.30}$$

Where b is the dislocation length, α is the angle between the slip plane normal vector and the Burgers vector of the dislocation, λ is the angle between the slip plane normal direction and its projection in the growth direction onto the interface plane of the epilayer and v is the Poisson ratio. For InGaAs layers grown on the (001) plane of GaAs misfit dislocations are found to occur in the (101) and $(\bar{1}01)$ directions and the slip plane is in the (111) direction[14]. The dislocation is one atomic spacing in magnitude hence the dislocation Burgers vector is $\frac{1}{2}a_S(101)$ and its magnitude $b = a_S/\sqrt{2}$. Note that the lattice constant is the thickness of two monolayers since there are two sub-lattices; As and Ga. Fig. 3.8 illustrates the situation.

From this it can be seen that $\alpha = \lambda = 30°$. Using this model the critical layer thickness for $In_xGa_{1-x}As$ grown on GaAs was calculated as a function of the indium fraction x. This function is shown graphically in fig. 3.9 from which it is seen that the critical layer thickness for $In_{0.20}Ga_{0.80}As$ on GaAs is 144Å and for $In_{0.30}Ga_{0.70}As$ it is 85Å. Layers grown thicker than L_C are found to be strain relieved by the presence of many dislocations[15]. The crystal quality of such a layer is not adequate for laser operation. It is possible to grow quality strained layers thicker than L_C under certain conditions but dislocations form rapidly at the carrier densities required for lasing and prevent useful operation[16].

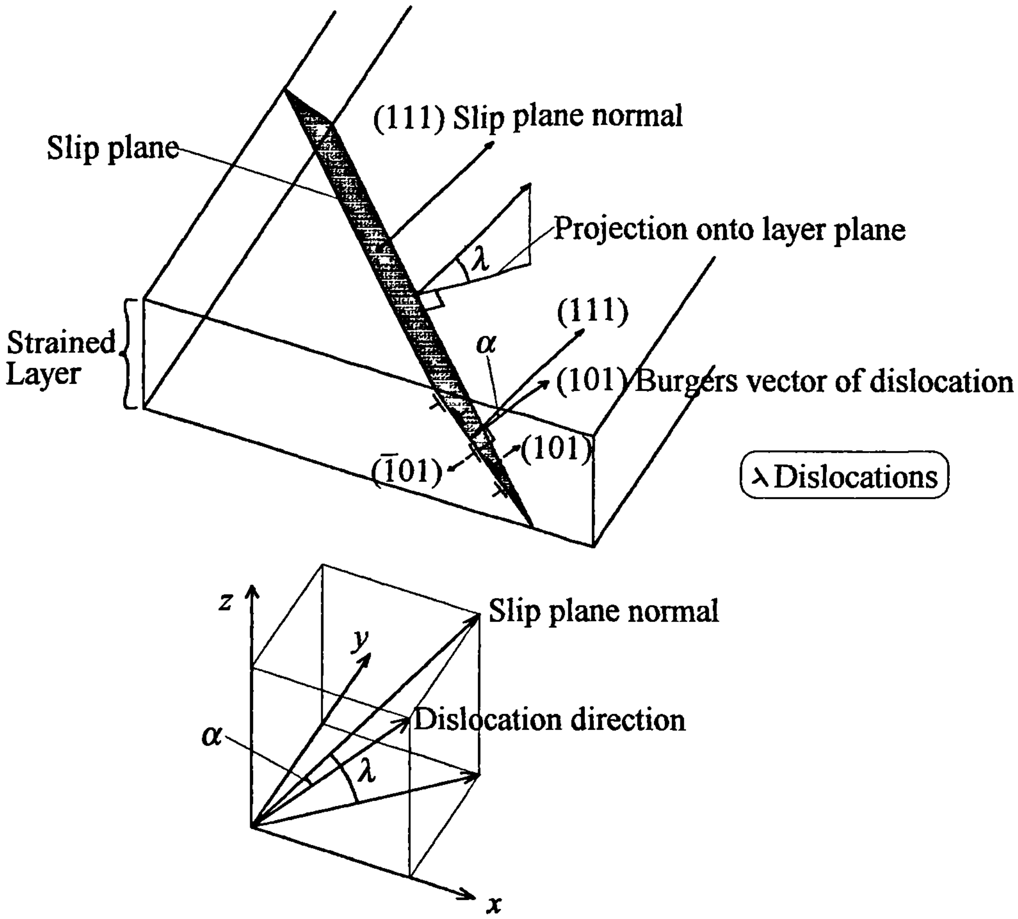

Fig. 3.8. Illustration of dislocation formation in InGaAs on GaAs grown on the {100} axis showing the angles α and λ.

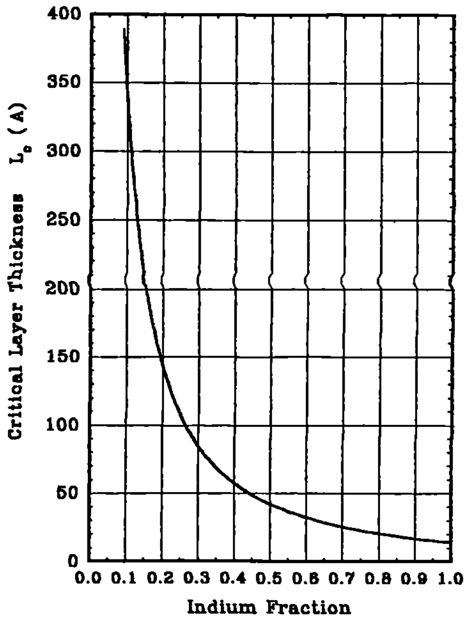

Fig. 3.9. Critical layer thickness L_C for epitaxial growth of $In_xGa_{1-x}As$ on GaAs as a function of the indium fraction x.

3.2.2. Calculation of energy levels in InGaAs / GaAs quantum wells

The energy levels in a square potential well are readily estimated using the Kronig-Penney model[17]. In a periodic square potential such as in a multiple quantum well (MQW) with potential steps of size V, the energy levels are found to be given by solutions of the equation (3.25). See fig. 3.10.

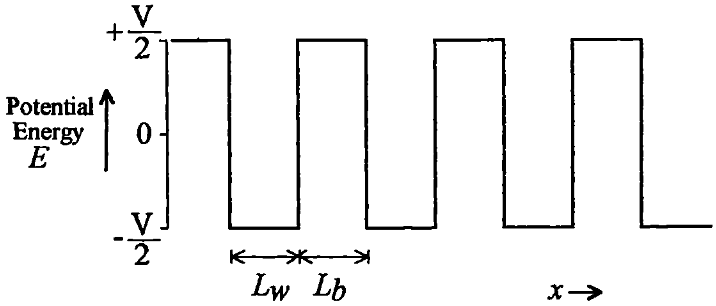

Fig. 3.10. Square spatial potential function for multiple quantum well with offset V.

$$\cos\left(k\left[L_w + L_b\right]\right) = \frac{m\left[L_w + L_b\right]}{\hbar^2} V L_b \frac{\sin(\eta)}{\eta} + \cos(\eta) \qquad (3.31)$$

Where:

$$\eta = \left[L_w + L_b\right] \cdot \frac{\sqrt{2m^* E}}{\hbar} \qquad (3.32)$$

L_w and L_b are the well and barrier widths, m^* is the effective mass and E is the energy. Since the wavenumber k is real for non-evanescent wavefunctions in the MQW, the range of equation (3.32) is from -1 to +1. Fig. 3.11 illustrates a graphical solution for this, the shaded regions indicate allowable bands for the value η and hence for E.

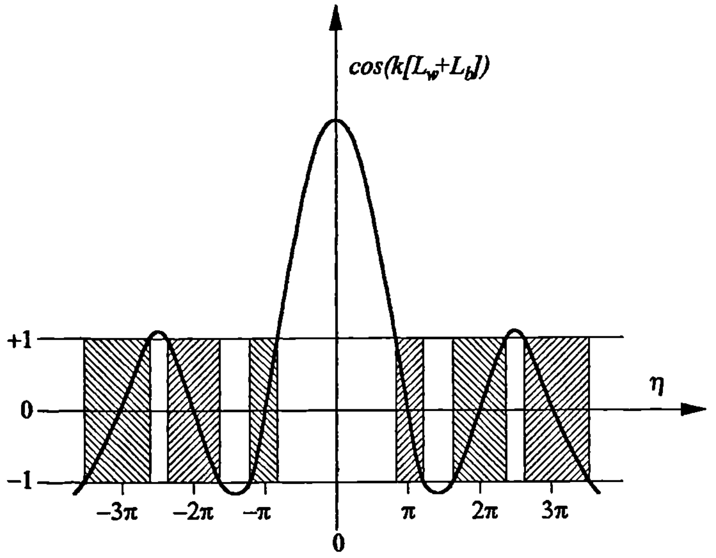

Fig. 3.11. Solution of equation (3.25) to find minibands in MQW.

For a single quantum well L_b is allowed to tend to infinity. In this case the crossings become infinitely steep and the minibands collapse to give single quantized energies. For numerical calculations, a barrier width of 300Å is used: this is large enough to reduce the coupling between wells and allow the position of levels in a single well to be calculated to an accuracy better than 10μeV.

Programs using this method have been used to calculate the conduction and valence band states for strained $In_xGa_{1-x}As$ / GaAs wells. These were based on programs M.Lakrimi, J.Woodhead[18] and M.Reddy adapted to run faster and give more accurate solutions.

V_{bo}	0.33	Valence band offset[17]
m_{hb}	$0.48m_0$	GaAs effective hole mass[9]
m_{eb}	$0.067m_0$	GaAs effective electron mass[9]
a_c	$5.65325-0.40515x$ (Å)	$In_xGa_{1-x}As$ lattice constant[19]
a_s	5.65325 Å	GaAs lattice constant[9]
a	$8.67-5.66x$ (eV)	Hydrostatic deformation potential[12]
b	$1.7+0.1x$ (eV)	Shear deformation potential[12]
C_{11}	$12.25-3.61x$	In plane elastic constant[19]
C_{12}	$5.7-0.85x$	Out of plane elastic constant[19]
E_{gb}	$1.519-\dfrac{5.405\times10^{-4}T^2}{204+T}$ (eV)	GaAs bandgap[9]
E_{gw}	$E_{gb}-1.53x+0.45x^2+\Delta$	$In_xGa_{1-x}As$ bandgap in well at: 300 K[20]
	$E_{gb}-1.47x+0.375x^2+\Delta$	77 K[20]
	$E_{gb}-1.24x+0.18x^2+\Delta$	20 K[19]
	$E_{gb}-1.5837x+0.475x^2+\Delta$	4 K[20]
Δ	$\Delta E_g \pm S/2$	Strain induced shift for heavy (+) and light (–) hole bands
m_{ew}	$(0.067-0.044x)m_0$	$In_xGa_{1-x}As$ effective electron mass[19]
m_{hhw}	$(0.48-0.08x)m_0$	$In_xGa_{1-x}As$ heavy hole effective mass[19]
m_{lhw}	$(0.082-0.056x)m_0$	$In_xGa_{1-x}As$ light hole effective mass[19]

Table 3.2. Material parameters used in Kronig-Penney model to find energy levels in InGaAs / GaAs quantum wells. x is the indium mole fraction in the well and T is the temperature in K.

A sequential seek routine using coarse energy steps is used to identify the approximate position of minibands. A linear interpolation method is then used to home in on the band edge energies to an accuracy of 10μeV. The program searches for electron, heavy hole and light hole states. The constants used in the calculations are shown in table 3.2.

Fig. 3.12 shows the results from this model for single wells. The e_1hh_1 transition energy is plotted against well width for various indium fractions. Also shown on the figure is the Matthews and Blakeslee critical layer thickness[13]. Photoluminescence measurements at low temperature agree well with this model [18,21]. Fig. 3.13. Shows the confined levels in an 85Å well for x=0.20. Note that a valence band offset of 33% [18] implies that there is no confinement in the light hole well and in further calculations we take the lh_1 state to be bound at the GaAs band edge.

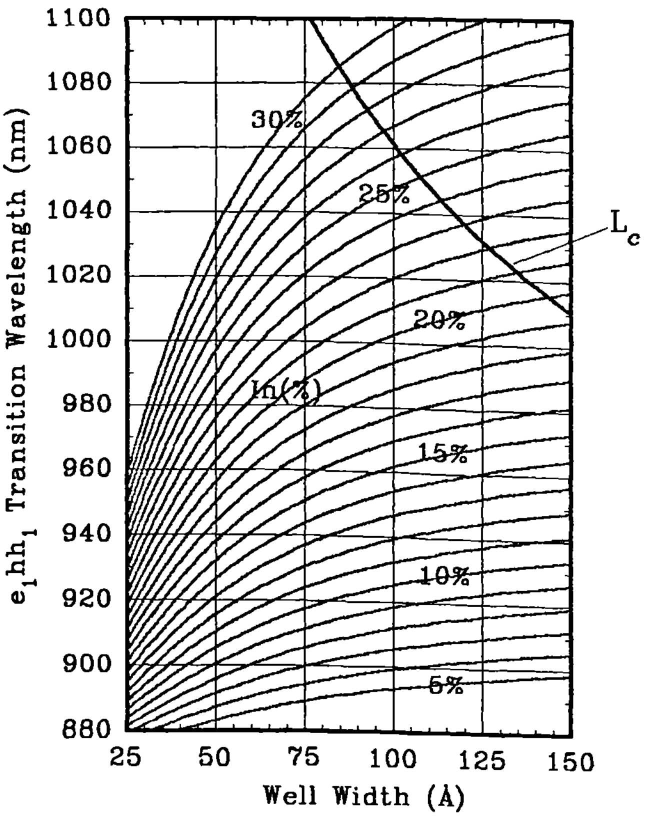

Fig. 3.12. Room temperature (300K) e_1hh_1 transition energies in InGaAs / GaAs single quantum wells as a function of well width and composition, calculated using above model. L_c indicates the Matthews and Blakeslee critical layer thickness[13].

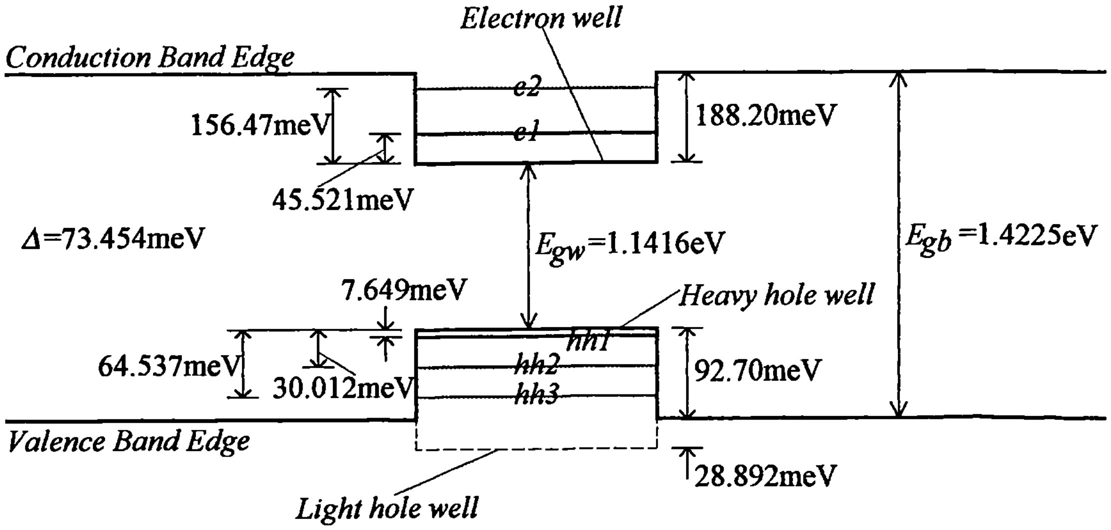

Fig. 3.13. Confined energies in an 85Å x=0.25 well at 300K. Note there is no light hole confinement.

3.2.3. Sub-band dispersion curves

The solutions of the Kronig-Penney model above give the ground states of the sub-bands in the InGaAs / GaAs well, i.e. for $k_x=k_y=0$. For finite in plane momentum the sub-band dispersion in the presence of zero band interaction is proportional to k^2. Using the Luttinger-Kohn Hamiltonian[22] after *O'Reilly and Witchlow*[6,11], by analogy with a bulk strained semiconductor, the in plane dispersion is found to be

$$E_{hh1}(k) = E_{hh1}(0) + (\gamma_1 + \bar{\gamma}).k^2 \tag{3.33a}$$

$$E_{hh2}(k) = E_{hh2}(0) + (\gamma_1 + \bar{\gamma}).k^2 \tag{3.33b}$$

$$E_{lh1}(k) = E_{lh1}(0) + (\gamma_1 - \bar{\gamma}).k^2 \tag{3.33c}$$

etc. for further valence bands. Where $E_{hh1}(0)$ is the ground state of the first heavy hole band as found above and similarly for the second heavy hole and first light hole bands. For GaAs the γ values are[23]:

$$\gamma_1 = 6.85\cdot\frac{\hbar^2}{2m_o}; \qquad \bar{\gamma} = 2.58\cdot\frac{\hbar^2}{2m_o} \tag{3.34}$$

The effective mass in the bands is:

$$m_{h/l} = \frac{m_o}{(\gamma_1 \pm \bar{\gamma})} \tag{3.35}$$

Notice that the heavy hole band (spin 3/2 state) is effectively light hole like in the plane of the well and the light hole band (spin 1/2 state) is effectively heavy hole like in the plane of the well. Light effective masses such as this are measured for transport in the plane by Reddy[24].

From the Hamiltonian in the plane of the well $\boldsymbol{H}$, we find the following interactions between states with wave functions $f_m^{\pm}$ and $f_n^{\pm}$, where ± refers to heavy / light hole states[6].

$$\left\langle f_m^{\pm} \middle| \boldsymbol{H} \middle| f_n^{\pm} \right\rangle = 0; \quad \text{m} \neq \text{n} \tag{3.36}$$

$$\left\langle f_m^{\pm} \middle| \boldsymbol{H} \middle| f_n^{\mp} \right\rangle = \pm 2\sqrt{3}k \left\langle f_m^{\pm} \middle| \frac{\partial}{\partial z} \middle| f_n^{\mp} \right\rangle + \sqrt{3}k^2 \bar{\gamma} \left\langle f_m^{\pm} \middle| f_n^{\mp} \right\rangle \tag{3.37}$$

In an infinite well approximation the cross-correlations of the state wavefunctions and the correlations with the derivatives in (3.37) are either zero or 1. For the 85Å x=0.20 InGaAs well we consider the hh_1, hh_2, hh_3, and unbound lh_1 states (see fig. 3.13). The following matrix gives the mixing of these states using the infinite well approximation[6,11]:

$$E\begin{pmatrix} f_1^{+} \\ f_2^{+} \\ f_3^{+} \\ f_1^{-} \end{pmatrix} = \begin{pmatrix} E_{hh1}(0)+\left(\gamma_1+\bar{\gamma}\right)k^2 & 0 & 0 & \sqrt{3}k^2\bar{\gamma} \\ 0 & E_{hh2}(0)+\left(\gamma_1+\bar{\gamma}\right)k^2 & 0 & 16\sqrt{3}\frac{k}{L} \\ 0 & 0 & E_{hh3}(0)+\left(\gamma_1+\bar{\gamma}\right)k^2 & 0 \\ \sqrt{3}k^2\bar{\gamma} & 16\sqrt{3}\frac{k}{L} & 0 & E_{lh1}(0)+\left(\gamma_1-\bar{\gamma}\right)k^2 \end{pmatrix} \cdot \begin{pmatrix} f_1^{+} \\ f_2^{+} \\ f_3^{+} \\ f_1^{-} \end{pmatrix}$$

(3.38)

Where L is the well width. We find the eigenvalues E of the above equation for finite values of k. Note that the hh3 band does not interact with the other bands and the calculation is only a 3×3 problem. Fig. 3.14 shows the band dispersion numerically calculated from this model for 85Å InGaAs / GaAs for x=0.20 and x=0.25.

Note that the infinite well approximation overestimates the interaction away from the band centre and the curves in fig. 3.14 diverge more than in the real case. The general shape of the curves is correct and the agreement for $k \leq 500.\mu\text{m}^{-1}$ is very close. A full solution[25,26] of the problem is too involved for this work.

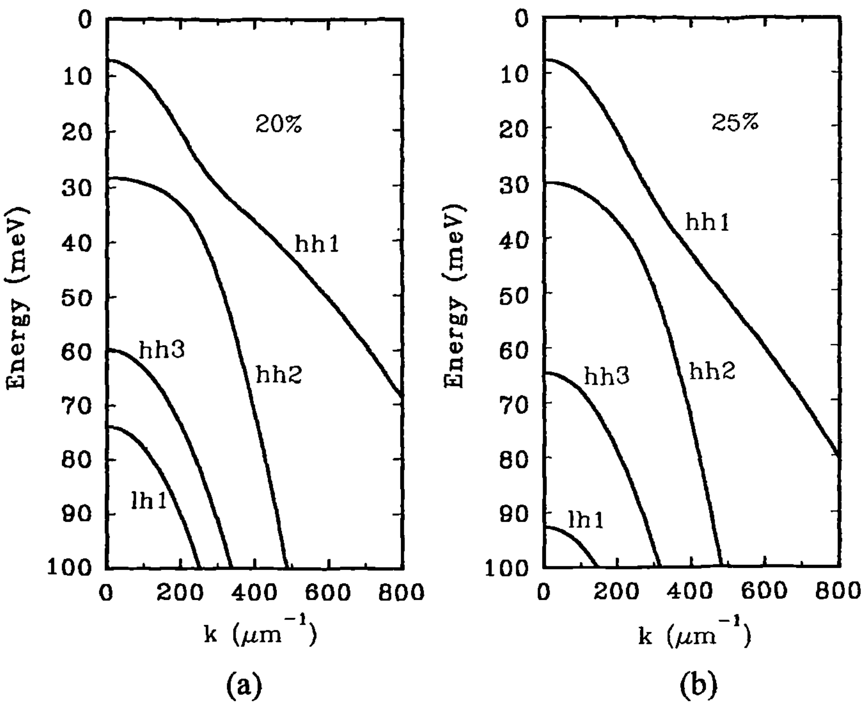

(a) (b)

Fig. 3.14. Valence band dispersion curves calculated for 85Å $In_xGa_{1-x}As$ / GaAs quantum wells using infinite well approximation described in the text: (a) x=0.20; (b) x=0.25.

3.2.4. Compressive or tensile strain?

An epilayer with a lattice constant larger than the substrate will be under biaxial compressive strain. As described above, this layer will exhibit a reduced hole mass in the plane of the layer and a heavy mass in the perpendicular direction. If the epilayer has a lattice constant smaller than that of the substrate it will be under biaxial tensile strain. In this case the band splitting is in the reverse sense: i.e. the in-plane hole mass will be heavy and the out of plane mass light. InGaAs on GaAs is compressively strained so has a light in-plane mass. This will reduce the transparency carrier density for an electromagnetic field polarized in the plane of the well[1,2,10]. Thus in conventional edge emitting lasers the TE mode gain is preferentially enhanced by the application of the strain and the TM mode gain is suppressed[27,28]. InGaAs grown on InP may be either under tensile or compressive strain depending on the indium fraction. For tensile material the out of plane mass is light and in an edge emitting laser the TM mode gain is enhanced. Thus in the same way as compressive strain may be used to lower the threshold current of an edge emitting laser, tensile strain may be used also[29,30].

For a surface emitting laser with a vertical cavity more than a few wavelengths across, the electromagnetic field may be thought of as a plane wave propagating in the vertical direction. Thus there are no out of plane field components and the situation is equivalent to the TE mode in the edge emitting geometry. Compressive strain may be used to enhance the gain of the optical mode and reduce the threshold current. Tensile strain will only decrease the gain so is of no use.

3.2.5. Density of states in a two dimensional system

Consider a system where particles are confined to two dimensions (2D) x and y. If the band structure is parabolic we can define an effective mass m^* and the particle energy above the ground state is given by (3.39). More generally (3.40) applies for some function $f(k^2)$.

$$E = \frac{\hbar^2}{2m^*}\left(k_x^2 + k_y^2\right) \tag{3.39}$$

$$E = f\left(k_x^2 + k_y^2\right) \tag{3.40}$$

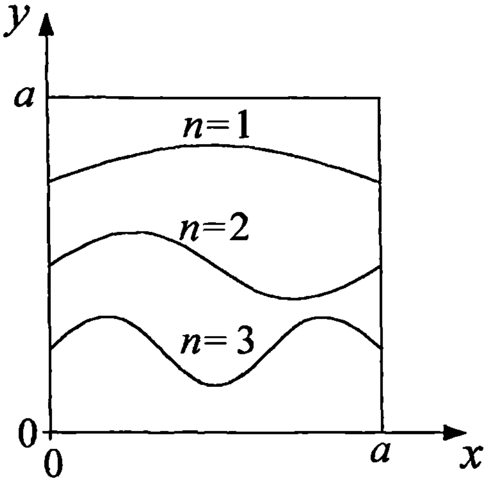

Fig. 3.15 Particle confined to 2D box of side a in x and y directions. Lowest confined states for m=0 are shown.

Consider states in a two dimensional box (or square) of side a (fig. 3.15); these are quantized (3.41) in the orthogonal directions x and y.

$$k_x = \frac{n\pi}{a}; \quad n = 1,2,3,4.....etc. \tag{3.41a}$$

$$k_y = \frac{m\pi}{a}; \quad m = 1,2,3,4.....etc. \tag{3.41b}$$

Thus we may write (3.40) in the form:

$$E = f\left(\frac{\pi^2}{a^2}\left(n^2 + m^2\right)\right) = f\left(\frac{\pi^2 r^2}{a^2}\right) \tag{3.42}$$

Where r is defined as:

$$r = \sqrt{n^2 + m^2} \tag{3.43}$$

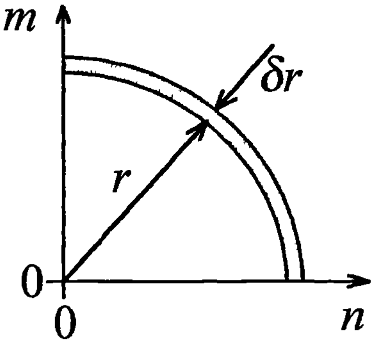

Fig. 3.16. State space for x and y mode numbers n and m, areas refer to number of states. The shaded region gives the extra states from an increase in r of δr.

Fig. 3.16 shows the state space of r; in an energy region E to $E+\delta E$ the shaded region corresponds to the extra states. This has area A:

$$A = \frac{\pi r}{2}\delta r \tag{3.44}$$

Thus the density of states per unit energy range, per unit volume, $N(E)$, in a well of width L is given by (3.45). Note the extra factor of 2 for consideration of both up and down spin states.

$$N(E) = \frac{\pi r}{a^2 L}\cdot\frac{dr}{dE} = \frac{k}{\pi L(dE/dk)} \tag{3.45}$$

For parabolic bands:

$$k\frac{\partial k}{\partial E} = \frac{m^*}{\hbar^2} \tag{3.46}$$

Thus the density of states in 2D for a constant effective mass is a constant[5]:

$$N(E) = \frac{m^*}{\pi L \hbar^2} \tag{3.47}$$

Using (3.45) the density of states functions for holes in the two InGaAs wells previously studied (85Å, x=0.20 and x=0.25) are calculated from the valence sub-band dispersion relations of fig. 3.14. These results are shown in fig. 3.17. notice that at the band centre the hh_1 band has a low density of states corresponding to low effective mass, but at higher energies the band mixing causes greater dispersion and hence a higher density of states (compare with results of Corzine *et al.*[24]). There is no degeneracy in the band structure for electrons in bulk InGaAs so a constant effective electron mass may be assumed for the quantum well.

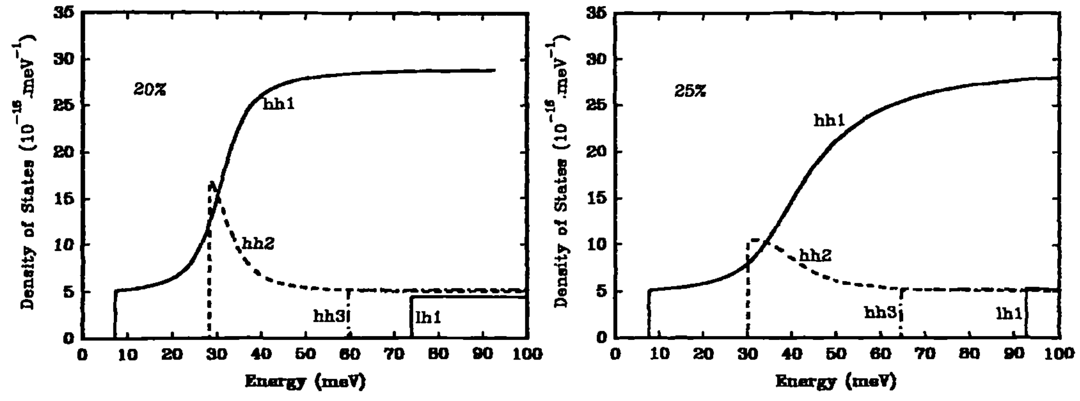

(a) (b)

Fig. 3.17. Density of states functions for valence sub-bands in 85Å $In_xGa_{1-x}As$ / GaAs quantum wells: (a) x=0.20; (b) x=0.25.

3.3. Details of gain calculations

3.3.1. Matrix elements

For a strained semiconductor quantum well the matrix element of equation (3.6) is given by (3.48).

$$\left|\langle u_m|r|u_k\rangle\right|^2 = M_{ij}^2 \cdot \frac{1}{m_o^2\omega^2} \tag{3.48}$$

Where M_{ij} is the momentum matrix element for a transition between states in the i'th confined electron and the j'th hole sub-bands. This is related to the momentum matrix element of the bulk material M_O by (3.49)[7].

$$M_{ij} = \tfrac{1}{2}O_{ij}M_o \quad \text{- for heavy holes} \tag{3.49a}$$

$$M_{ij} = \tfrac{3}{2}O_{ij}M_o \quad \text{- for light holes} \tag{3.49b}$$

Where the O_{ij} are the spatial overlap integrals of the wavefunctions of the i'th and j'th states. M_O is given by (3.50) after Kane[31]:

$$M_O = \frac{m_O E_g^u\left(E_g^u + \Delta\right)}{6m_e^u\left(E_g^u + \frac{2}{3}\Delta\right)} \tag{3.50}$$

Where E_g^u is the unstrained band gap, m_e^u is the effective mass in the bulk material, Δ is the spin orbit split-off energy and m_O is the free electron mass.

In these calculations it is reasonable to assume orthogonal wavefunctions i.e.

$$O_{ij}=1 \ : \ i=j \tag{3.51a}$$

$$O_{ij}=0 \ : \ i\neq j \tag{3.51b}$$

In reality the O_{ij} vary slightly with k since the bands are non-parabolic. Also as noted by Yan[32] *et al.* there is a correction factor to be applied to equation (3.50) due to effects of the non-parabolicity. In this work simplifications have been made to calculate the band structure, here we shall make a further simplification by putting:

$$\omega\left|\langle u_m|r|u_k\rangle\right|^2 = C \ : \ i=j \tag{3.52a}$$

$$\omega\left|\langle u_m|r|u_k\rangle\right|^2 = 0 \ : \ i\neq j \tag{3.52b}$$

For some constant C. This is reasonable since ω changes by less than 10% over the range of interest. This is sufficient to find the shape of the gain spectra suitable to explain the results obtained from VCSEL devices.

3.3.2. Calculations

With the density of states functions calculated in section 3.2.4 above we can now use equation (3.18) to find the gain spectra $g(\omega)$. This is done at a number of different carrier concentrations N. The carrier concentration for an intrinsic well is related to the Fermi levels E_{fp} and E_{fn} as follows:

$$N = \sum_i \int_{E_i}^{\infty} n_{ci}(E) f_c(E).dE \tag{3.53}$$

Where the sum is over the sub-bands i at energies E_i, and similarly for the valence band.

For the conduction band where we have assumed parabolic band structure the relation is:

$$N = \frac{m_e}{L\hbar^2}\sum_i \int_{E_i}^{\infty} 1\Big/\left(1+\exp\left[\frac{E-E_{fn}}{kT}\right]\right).dE = \frac{m_e}{L\hbar^2}kT\sum_i \ln\left(\frac{1}{f_c(E_i)}\right) \tag{3.54}$$

and for the valence band using a change of basis:

$$N = \sum_{hhi,lhi} \int_0^{\infty} \frac{k}{\pi L} f_v\left(E_{hhi,lhi}(k)\right).dk \tag{3.55}$$

We are now in a position to compute the gain curves numerically. The procedure is:

(i) Compute energy levels for quantum well of interest.

(ii) Calculate dispersion of valence bands using reduced Hamiltonian in (3.38).

(iii) For any particular value of E_{fp}, calculate the carrier concentration N using (3.49) and the valence band dispersion curves.

(iv) Solve (3.48) for N to find E_{fn}.

(v) Take each allowed transition in turn (i.e. $e_1 \rightarrow hh_1$, $e_2 \rightarrow hh_2$, $e_1 \rightarrow lh_1$) and for incremental values of k from zero, use the Fermi levels to evaluate the Fermi functions f_c and f_v for the transition between states at wavenumber k for the carrier concentration N.

(vi) Use equation (3.18) directly to find $g(E_{tr})$ where $E_{tr}=E_g+E_c(k)+E_v(k)$.

(vii) Continue to increment k and Repeat (v) and (vi) until the full gain spectrum is found for energies of interest.

(viii) Repeat calculations for other transitions.

(ix) Calculate spontaneous current density by summing contributions over all bands as in (3.22).

(x) Repeat for different E_{fp} to give a family of curves $g(E_{tr})$ for various N.

3.3.3. Results of calculations

Gain calculations were made for a number of InGaAs / GaAs quantum wells . Fig. 3.17 shows the results of these calculations for 85Å wide wells of 20 and 25% In plotted on a wavelength scale. Note that the gain is in arbitrary units because of the simplification made in equation (3.52). In these graphs it was important to consider the effect of band gap narrowing at high carrier concentrations. The bandgap shift in eV ΔE_g for electron and hole carrier concentrations N and P (in .cm^{-3}) is given by[33]:

$$\Delta E_g = 1.6 \times 10^{-8}\left(N^{\frac{1}{3}} + P^{\frac{1}{3}}\right) \qquad (3.56)$$

For intrinsic wells $N=P$.

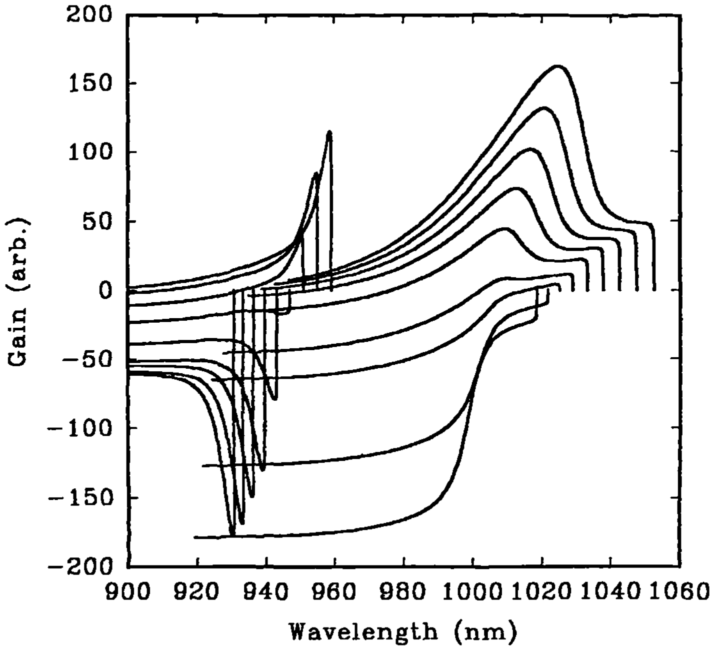

(a) 20% In. Curves show gain at carrier densities of: 0.76, 1.1, 1.6, 2.2, 3.1, 4.3, 5.8, 7.6 and 9.8×10^{18}.cm^{-3}.

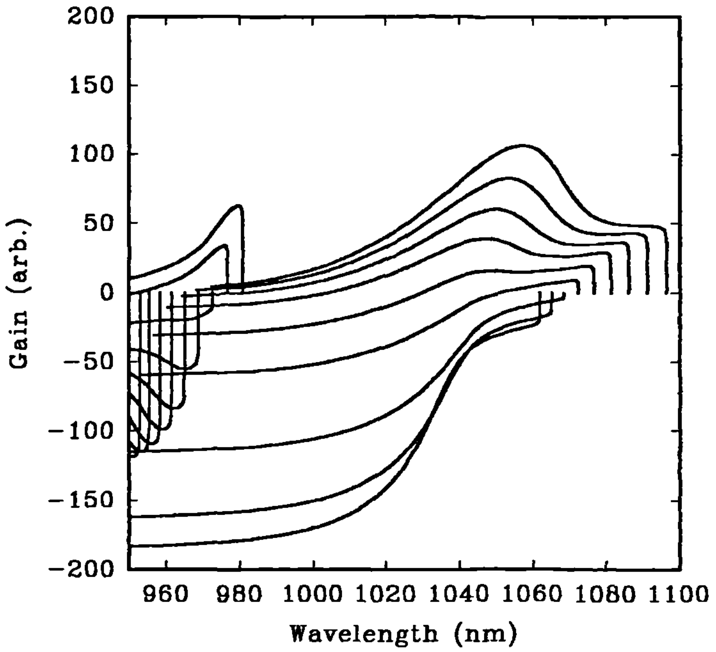

(b) 25% In. Curves show gain at carrier concentrations of: 0.60, 0.86, 1.2, 1.8, 2.5, 3.4, 4.6, 6.1 and 8.0×10^{18}.cm^{-3}.

Fig. 3.18 Optical gain spectra for strained InGaAs / GaAs quantum wells. (a) 85Å well 20% and (b) 85Å well 25% In. Main curves indicate e_1hh_1 transitions. Curves to shorter wavelengths indicate e_2hh_2 transitions.

The curves of fig. 3.18 indicate that for the e_1hh_1 transition, band edge transparency occurs at carrier densities of ~1.5×10^{18}.cm^{-3} for the 20% In well and at the slightly lower density of ~1.4×10^{18}.cm^{-3} for the 25% well[10]. At low carrier densities the peak of the gain spectra occurs at the band edge as would be expected in an idealised well with a purely parabolic band structure. With increasing carrier density carriers fill higher states in the well and holes begin to significantly populate states around the hh_2 sub-band edge. Holes in the hh_1 band at these energies experience a much increased density of states due to mixing with the lh_1 and hh_2 bands (see figs. 3.14 and 3.17). This increased density of states causes a second peak to develop to short wavelengths in the gain spectra. Elsewhere (chapter 8) this has been referred to as the ***'state expansion peak'*** due to its origin. Note that at carrier concentrations above 2.5×10^{18}.cm^{-3} this forms the dominant peak in the gain spectrum. A similar behaviour is observed in the spectra produced by Li *et al.*[7]

Comparing the curves for the two indium fractions we note that the larger separation of the hh_1 and hh_2 for the higher (25%) indium fraction results in the light hole like behaviour of the hh_1 band being maintained to higher energies. Whilst this has little effect on the transparency density where higher energy states are not filled, it does give rise to an enhanced differential gain for shorter wavelengths (as seen by careful inspection of fig. 3.18). This also produces wider spectra for the 25% well allowing a wider range of lasing wavelengths or shorter pulses from a mode-locked laser to be obtained.

For deeper wells the e_2hh_2 and e_1hh_1 transitions are separated more. Thus in the case of the 25% In well spontaneous emission would be reduced as the second order transition would be suppressed. The only advantage of a well with low indium fraction would be for a device requiring a very high threshold gain since the state expansion peak rises higher for the 20% In well due to the increased sub-band interaction.

The calculations performed here are rather crude in many respects but a totally complete solution would be almost impossible. More exact models could be used but are beyond the scope of this thesis. The simple models used here give a qualitative feel for the gain spectra in strained InGaAs / GaAs quantum wells (see for example Li *et al.*[7]). The spectra are used later (chapter 8) to provide a good explanation for the variation between VCSEL devices with different cavity resonant wavelengths. The spectra are also used to suggest improvements to the laser structures studied in this thesis.

References:

[1] A.R.Adams, *Band structure engineering for low-threshold high-efficiency semiconductor lasers*, Electron. Lett. **22**, pp249-250, 1986.

[2] E.Yablonovitch & E.O.Kane, *Band structure engineering of semiconductor lasers for optical communications*, J. Lightwave Technol., **6**, 8, p1292-1299, 1988.

[3] P.C.W.Davies, *Quantum mechanics*, Routlege & Kegan Paul, London, 1984.

[4] G.Lasher & F.Stern, *Spontaneous and stimulated recombination radiation in semiconductors*, Phys. Rev., **133**, 2A, ppA553-A563, 1964.

[5] M.Jaros, *Physics and applications of semiconductor microstructures*, Oxford University Press, Oxford, 1989.

[6] E.P.O'Reilly & G.P.Witchlow, *Theory of the hole subband dispersion in strained and unstrained quantum wells*, Phys. Rev. B, **34**, 8, pp6030-6033, 1986.

[7] Z-M.Li, M.Dion, S.P.McAlister, R.L.Williams & G.C.Aers, *Incorporation of strain into a two-dimensional model of quantum-well semiconductor lasers*, IEEE J. Quantum Electron., **29**, 2, pp346-354, 1993,

[8] P.Blood, A.I.Kucharska, J.P.Jacobs & K.Griffiths, *Measurement and calculation of spontaneous recombination current and optical gain in GaAs-AlGaAs structures*, J. Appl. Phys., **70**, 3, pp1144-1156, 1991.

[9] J.S.Blakemore, *Semiconducting and other major properties of gallium arsenide*, J. Appl. Phys., **53**, 10, ppR123-R181, 1982.

[10] J.J.Coleman, K.J.Beernick & M.E.Givens, *Threshold current density in strained layer* $In_xGa_{1-x}As$ *- GaAs quantum well heterostructure lasers*, IEEE J. Quantum Electron., **28**, 10, pp1983-1989, 1992.

[11] E.P.O'Reilly, *Valence band engineering in strained layer structures*, Semicond. Sci. Technol., **4**, pp121-137, 1989.

[12] N.G.Anderson, W.D.Laidig, R.M.Kolbas & Y.C.Lo, *Optical characterisation of pseudomorphic* $In_xGa_{1-x}As$ *- GaAs single-quantum-well heterostructures*, J. Appl. Phys., **60**, 7, pp2361-2367, 1986

[13] J.W.Matthews & A.E.Blakeslee, *Defects in epitaxial multilayers*, J. Crystal Growth, **27**, pp118-125, 1974.

[14] J.W.Matthews, *Defects associated with the accommodation of misfit between crystals*, Semicond. Sci. Technol., **12**, 1, pp126-133, 1975.

---

[15] T.G.Andersson, Z.G.Chen, V.D.Kulakooskii, A.Uddin & J.T.Vallin, *Variation of the critical layer thickness with In content in strained* $In_xGa_{1-x}As$ *- GaAs quantum wells grown by molecular beam epitaxy*, Appl. Phys. Lett., **51**, 10, pp752-754, 1987.

[16] P.J.A.Thijs, *Strained MQW lasers for optical communications*, Rank Prize Funds Mini Symposium on *Strained layer optoelectronic & electronic devices*, Grasmere, 1992.

[17] L.Solymar & D.Walsh, *Lectures on the electrical properties of materials*, revised 3rd Ed., Oxford University Press, Oxford, 1985.

[18] J.Woodhead, F.Gonzalez Sanz, P.A.Claxton & J.P.R.David, *On the bandgap of InGaAs / GaAs strained quantum wells*, Semicond. Sci. Technol., **3**, pp601-604, 1988.

[19] N.G.Anderson, W.Laidig, G.Lee, Y.Lo & M.Oztürk, *Luminescence properties of* $In_xGa_{1-x}As$ *- GaAs strined-layer superlattices*, in *Layered structures and epitaxy*, J.M.Gibson & L.R.Dawson Eds., Mat. Res. Soc. Proc., **37**, pp223-238, 1985.

[20] F.Gonzalez Sanz, *Estruturas de pozo cuántico u su aplicatión a transistores pseudomórficos FET de* $In_xGa_{1-x}As$ */ GaAs*, PhD Thesis, Universidad Politecnica de Madrid, 1990.

[21] J.Woodhead, *Photoluminescence measurements on various InGaAs / GaAs quantum well samples at 10K and 300K provides a calibration relation for the shift of the transition energy between the two temperatures*, Private communication.

[22] J.M.Luttinger & W.Kohn, Phys. Rev., **97**, p896, 1955.

[23] Landölt-Bornstein, *Numerical data and functionships in science and technology*, O.Madelung Ed., New Series III, Vol 17 & 22, Springer, Berlin, 1982.

[24] M.Reddy, *P-channel MODFETs incorporating strained AlGaAs / InGaAs heterostructures*, PhD Thesis, University of Sheffield, 1992.

[25] S.W.Corzine, R.H.Yan & L.A.Coldren, *Theoretical gain in strained InGaAs / GaAs quantum wells including valence band mixing effects*, Appl. Phys. Lett., **57**, 26, pp2835-2837, 1990.

[26] G.Crow, R.W.Kelsall & R.A.Abram, *Monte Carlo simulations of low field hole transport in strained InGaAs quantum wells*, submitted to Semicond. Sci. Technol., 1992.

[27] M.Sugimoto, N.Hamao, H.Yokogama & K.Nishi, *Indium composition dependant threshold current density in strained InGaAs / AlGaAs quantum well lasers*, Jap. J. Appl. Phys., **30**, 12B, ppL2098-L2100, 1991.

---

[28] T.C.Chong & C.G.Fonstad, *Theoretical gain of strained-layer semiconductors in the large strain regime*, IEEE J. Quantum Electron., **25**, 2, pp171-178, 1989.

[29] M.P.C.M.Krijn, G.W.t'Hooft, M.J.B.Boermans, P.J.A.Tijhs, T.van Dongen, J.J.M.Binsma, L.F.Tiemeijer & C.J.van der Poel, *Improved performance of compressively as well as tensile strained quantum-well lasers*, Appl. Phys. Lett., **61**, 15, pp1772-1774, 1992.

[30] T.Y.Wang & G.B.Stringfellow, *Strain effects on* $Ga_xIn_{1-x}As$ */ InP single quantum wells grown by organometallic vapour-phase epitaxy with* $0 \leq x \leq 1$, J. Appl. Phys., **67**, 1, pp344-352, 1992.

[31] E.O.Kane, *Thomas-Fermi approach to impure semiconductor band structure*, Phys. Rev., **131**, pp79-88, 1963.

[32] R.H.Yan, S.W.Corzine, L.A.Coldren & I.Suemene, *Corrections to the expression for gain in GaAs*, IEEE J. Quantum Electron., **26**, 2, pp213-216, 1990.

[33] F.Stern, *Calculated spectral dependence of gain in excited GaAs*, J. Appl. Phys., **47**, 12, pp5382-5386, 1976.

4. Materials Growth and Device Fabrication

4.1. Growth

The production of complicated semiconductor heterostructures, low in lattice defects, as is necessary for optoelectronic devices, requires the use of epitaxial growth techniques. There are two important growth processes available metal-organic vapour phase epitaxy (MOCVD) and molecular beam epitaxy (MBE). These are described below.

4.1.1. Metal-Organic Chemical Vapour Deposition (MOCVD)

MOCVD is also known as metal-organic vapour phase epitaxy (MOVPE). A typical MOCVD growth reactor is shown in fig. 4.1.

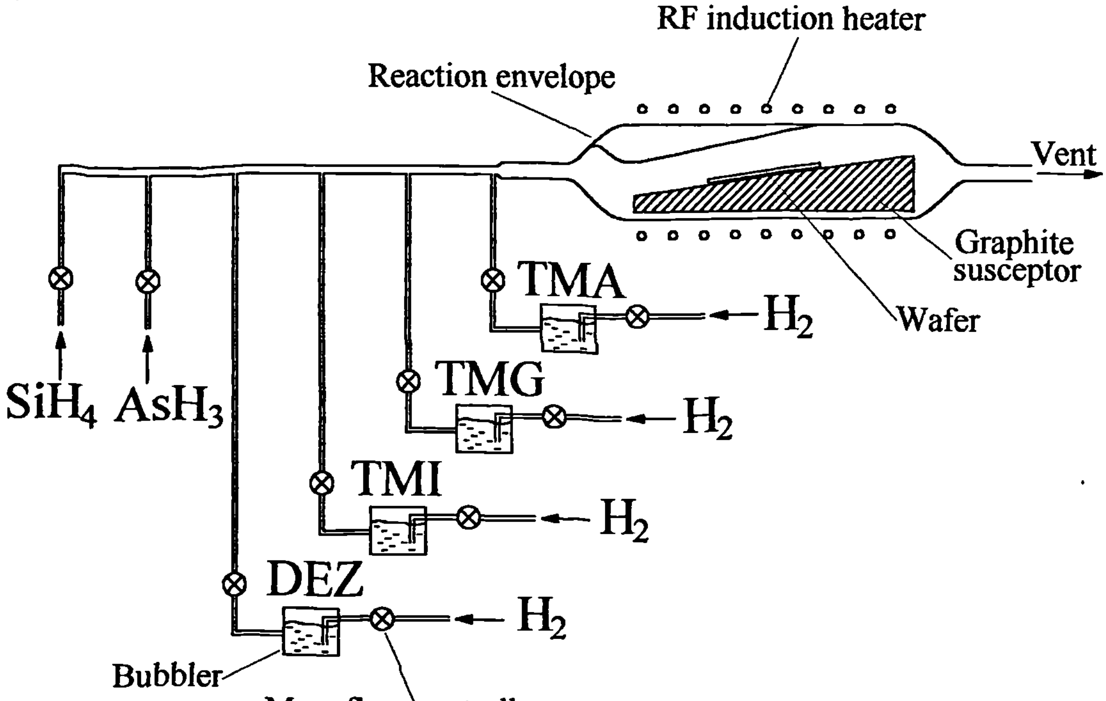

Fig. 4.1. Simplified diagram of MOCVD growth reactor.

The substrate wafer to be grown upon acts as a seed for the deposition of the epitaxial layers. It lies on a graphite susceptor which is heated by an RF induction coil to a temperature of 500 to 700°C, depending on the compound to be grown. The growth is performed in a hydrogen atmosphere at a pressure between 100 and 700torr. Growth results from the reaction of the products created when the growth precursors decompose on contact with the hot substrate. The group V precursors are hydrides (e.g. arsine, AsH_3) and those for group III are metal-organics (e.g. trimethylgallium $Ga(CH_3)_3$ abbreviated to TMG). Silicon and zinc dopants are provided by silane and diethylzinc. Table 4.1 lists all those used in the production of the VCSEL structures studied here[1].

Element	Precursor	
Ga	Trimethylgallium	$Ga(CH_3)_3$
Al	Trimethylaluminium	$Al(CH_3)_3$
As	Arsine	AsH_3
In	Trimethylindium	$In(CH_3)_3$
Si	Silane	SiH_4
Zn	Diethylzinc	$Zn(C_2H_5)_2$

Table 4.1. Metal-organic and hydride precursors used in the growth of doped InGaAs and AlGaAs compounds.

The metal-organic vapours are produced by bubbling hydrogen gas through the precursor compounds which are liquids. For quality growth and uniformity it is important to have smooth laminar flow of vapour across the growth substrate. Transport of precursors to the growth surface is by diffusion across the boundary layer of the vapour flow. The basic reaction for the formation of GaAs is shown in (4.1). This is an overall reaction, in reality it is much more complicated and involves several reaction steps and there are several possible paths[2]. Other reaction products are carried away with the vent gases.

$$Ga(CH_3)_3 + AsH_3 \xrightarrow{heat} GaAs + 3CH_4 \qquad (4.1)$$

There is some unintentional incorporation of carbon from decomposition of the methyl group. For GaAs growth this can be low ($\sim 1\times10^{15}.cm^{-3}$) but for AlGaAs compounds is much higher (typically $2\times10^{18}.cm^{-3}$ for AlAs). The incorporated carbon can be useful as a p-type dopant but for n-type material strong Si counter doping must be used.

AlGaAs compounds are grown at 700°C whilst InGaAs quantum wells are grown at a lower temperatures of 500 to 600°C for optimum crystal quality. The growth rate is typically $2.5\mu m.hr^{-1}$.

4.1.2. Molecular Beam Epitaxy (MBE)

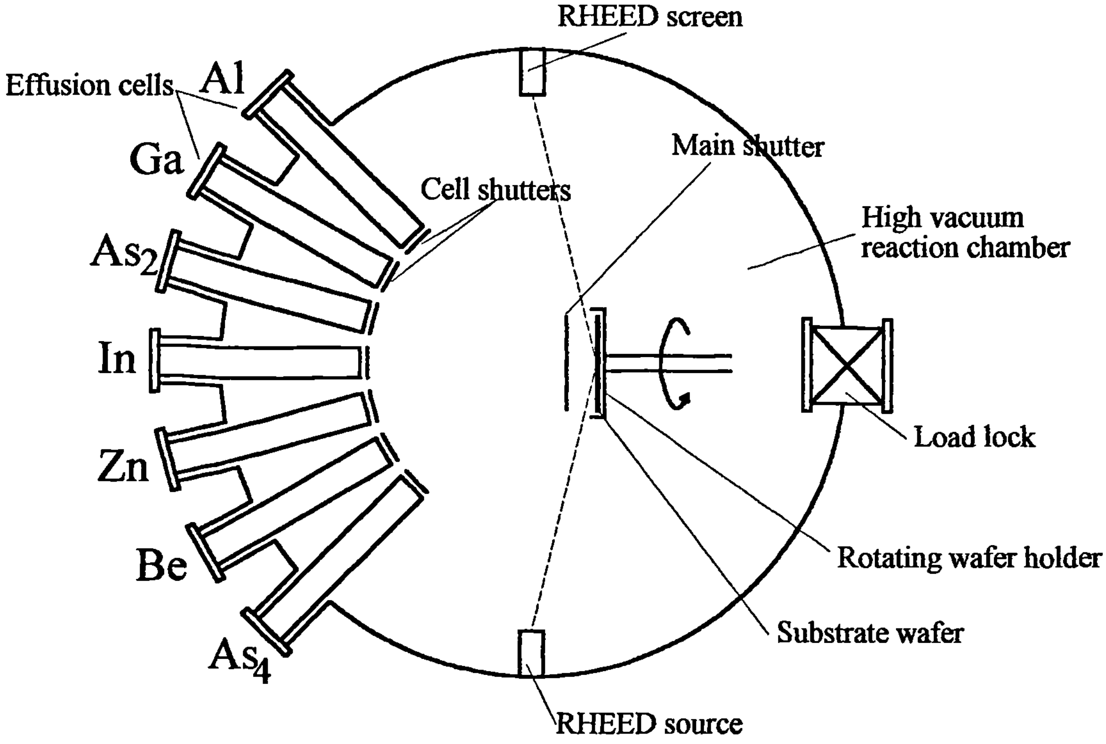

Fig. 4.2. Schematic diagram of MBE growth reactor for growth of doped AlGaAs and InGaAs compounds.

A typical MBE reactor is shown in fig 4.2[3]. Growth materials are contained separately in effusion cells in elemental form. Each cell contains a crucible with an electrical heater which melts the charge of material (Al, Ga, As_2 etc.). Molecules evaporate off from the crucibles under the high vacuum condition maintained in the reactor. The flux of molecules is controlled by varying the cell temperatures and operating the shutters control which species are allowed to pass to the substrate. The growth chamber is kept at very high vacuum typically 10^{-10}torr. After the chamber has been opened up to atmosphere, it takes two weeks to pump the chamber to this vacuum, out-gas to remove all contaminants and to bake and prepare the cells before the reactor is ready to grow high quality material[4]. At this pressure the mean free path of a free molecule in the chamber is very long, thus molecules emitted from the effusion cells typically undergo no scattering and travel directly towards the substrate as a molecular beam. Group III and group V molecules arriving on the heated substrate are adsorbed onto the crystal lattice and epitaxial growth results. Al, Ga, In and As_2 or As_4 cells are used for the growth of AlGaAs and InGaAs compounds. Be and Si cells provide p and n-type dopants. The substrate is rotated during growth to reduce the effects of beam non-uniformity.

Also shown in fig. 4.2 are: load-lock, this is used to transfer substrates in and out of the reactor without having to open the chamber up to the atmosphere; resonant high energy electron diffraction (RHEED) system, a phosphor screen displays the diffraction pattern of a high energy electron beam diffracted by the growing layers on the substrate, the diffraction pattern allows the quality of the crystal growth to be monitored monolayer by monolayer.

AlGaAs compounds are grown at 600°C whilst InGaAs quantum wells are grown at the reduced temperature of 540°C. The growth rate is typically 1.0μm.hr^{-1}.

4.1.3. Other growth processes

Other growth processes include metal-organic molecular beam epitaxy (MOMBE), chemical beam epitaxy (CBE) and liquid phase epitaxy (LPE). MOMBE and CBE are closely related; they use a combination of metal-organic and hydride precursors as used in MOCVD and solid sources, but in an ultra high vacuum MBE system[5]. The process compromises both the advantages and disadvantages of MBE and MOCVD growth. LPE relies on crystal growth from liquid melt[3]. This is the earliest epitaxial process and whilst able to produce high crystalline quality is not suited to growth of VCSEL structures as abrupt interfaces cannot be grown and growth is restricted to small (a few cm^2) substrate areas.

LPE, CBE or MOMBE growth was not available for this work.

4.2. Comparisons of MBE and MOCVD

A full VCSEL structure requires some 7μm of epitaxial growth (see chapter 2). The faster growth rate used in MOCVD means the structure can be easily grown in a working day including the time needed to set up the reactor and perform routine maintenance. By MBE the growth requires an extended working day to complete.

MOCVD reactors are much more easily serviced: the growth chamber may be opened for servicing and then used for growth immediately after being purged with hydrogen. Reagents are stored away from the reactor in bottles and can be changed between growth runs. As mentioned above an MBE reactor may not be used for growth for two weeks after it has been opened up to atmosphere. This must be done occasionally for maintenance and to replace spent or damaged effusion cells. MOCVD is thus more suited to industrial use and reactors are available which can grow on 12 or more 2" wafers simultaneously. There are some MBE machines capable of growing on several wafers simultaneously.

4.2.1. Layer thickness control and growth uniformity

In the absence of in-situ monitoring, MOCVD growth thickness is calibrated by growing a test layer and measuring its thickness by X-ray diffractometry. However the growth rate is affected by substrate temperature. As much as 15% reduction in growth rate is seen by reducing the growth temperature from 700°C to 650°C. Small fluctuations between growth runs and the lack of in situ monitoring give rise to a variation of up to 5%. The VCSEL cavity region is grown at a lower temperature than the reflector stacks since it contains InGaAs wells. A change in the deposition rate in mid growth can make it difficult to achieve a longitudinal cavity resonance coherent with minimum loss in the Bragg reflector stacks as required for low threshold devices. The introduction of in-situ optical monitoring[6,7] could alleviate this problem and is discussed briefly in 2.2.5.

Careful control of the susceptor angle is used to alter the condition of the boundary layer of the laminar gas flow over the substrate wafer and hence the deposition uniformity. Optimisation of this has produced a VCSEL layer with 80% of the 2" diameter wafer having a cavity resonance wavelength ±10nm of 1010nm. This corresponds to a ±1.0% layer thickness variation over this area (see fig. 4.3).

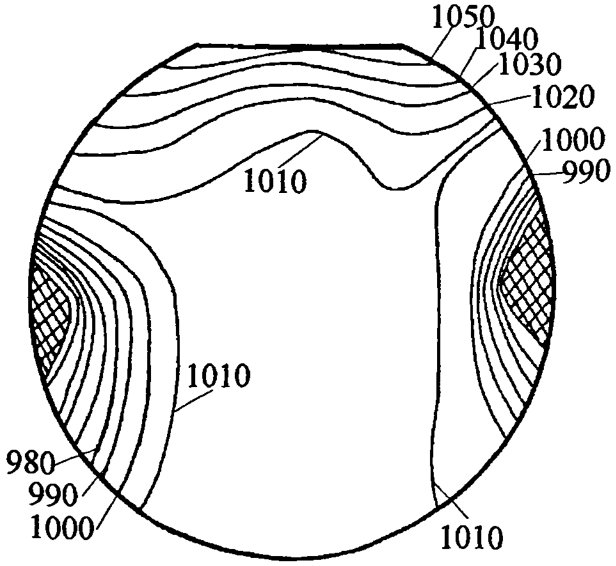

Fig. 4.3. Wafer map of MOCVD grown VCSEL structure QT421 showing uniformity of resonance wavelength across the wafer.

This wafer is suitable for the production of large arrays of lasers with uniform operating characteristics.

MBE crystal growth is monitored by RHEED oscillations[8] and beam flux monitors. This allows very accurate control of the growth thickness and hence the resonant wavelength of VCSEL structures. At the wafer centre this can be controlled to better than ±1%. The layer to layer control is even better than this: the relative error in the thicknesses of the reflector stacks and the cavity region is imperceptible at all positions across the wafer. Therefore a high finesse longitudinal cavity mode will always be found.

The uniformity across the wafer has a paraboloid profile which is circularly symmetric as a result of substrate rotation during growth. Fig. 4.4 illustrates this by showing the uniformity across a typical 2" diameter wafer.

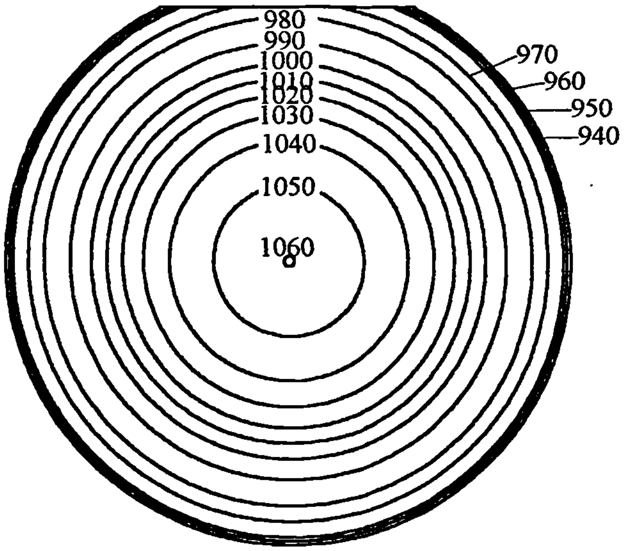

Fig. 4.4. Wafer map of MBE grown VCSEL structure RMB627 showing uniformity of resonance wavelength across the wafer.

As the figure shows there is a variation ±6% in deposition thickness across the wafer with increasing non-uniformity towards the wafer edge. This is very useful for research purposes as it provides a wide variety of slightly different devices. It is not desired for the production of large arrays of similar devices. Luckily by better design of the effusion cell geometry the uniformity may be greatly improved. Bandgap Technology Corp. claim to achieve ±0.2% variation across a wafer[9]; this means that all devices fabricated from it will be essentially identical. It also means that if there are errors, all of the devices will work poorly.

4.2.2. Quantum well quality

Efficient low threshold laser operation requires the growth of a high quality quantum well active region. This should be free from dislocations and impurities which will capture carriers and promote non-radiative recombinations. When grown epitaxially on GaAs, InGaAs is under a compressive biaxial strain (see section 3.2.1). A strained quantum well below the critical layer thickness is in a metastable state[10] and if grown or processed at too high a temperature, thermal activation may cause it to partially relax. At high growth temperatures indium will tend to desorb from the surface, but in MBE and MOCVD to prevent this, the growth temperature for the cavity section is minimised.

The most useful technique for assessing the quality of quantum wells is low temperature photoluminescence (PL). At low temperatures, typically 15K, the absorption coefficient of the thick AlAs / GaAs Bragg reflectors to the Ar$^+$-ion laser pump is reduced and the reflector resonance is shifted away from the quantum well emission wavelength. Thermal broadening of the emission is small so the linewidth is indicative of the well quality (*kT* ~ 1.3meV at 15K). Bright PL emission implies a high radiative emission efficiency and thus a long carrier lifetime.

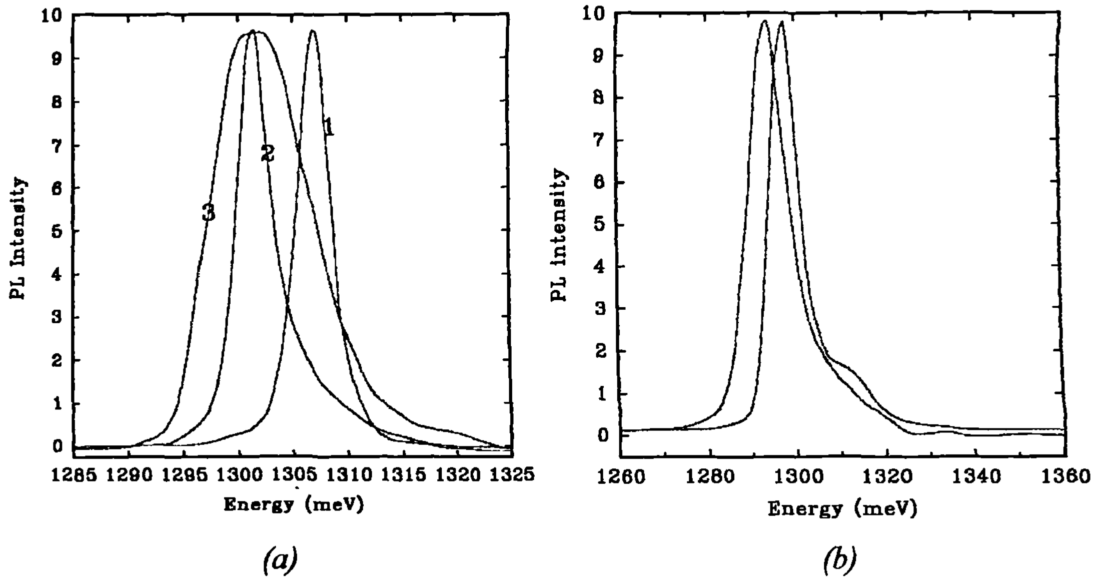

Fig. 4.5. 15K PL spectra from quantum wells in VCSEL structures showing the extent of variation across the wafers: (a) MOCVD grown QT421; (b) MBE grown RMB627.

Typical PL spectra from MBE and MOCVD grown VCSEL structures are shown in fig. 4.5. These were taken at 15K using an Ar$^+$-ion pump and a Fourier transform spectrometer. The FWHM linewidth of PL from the MBE grown structure RMB627 is 7 to 10meV and from the MOCVD grown structure QT421 is 3meV in the central part of the wafer increasing to 10meV towards the periphery. The emission from both samples is bright indicating high quality wells. The narrow linewidth indicates material with a low density of recombination centres, including crystal defects, the best quality material being in the centre of the wafer QT421. The material is therefore suitable for the production of lasers.

There is variation in the PL spectrum across both wafers as a result of variations in the growth thickness and material composition. For the MBE grown layer the ±6% growth thickness variation also affects the quantum wells. This should give rise to a ±5meV shift in the lowest transition energy. The variation is less than this, from these data we deduce a virtually constant indium fraction (±0.2% In) across the wafer. In the case of MOCVD layers grown at 640°C one observes a rapid deterioration of well quality in the downstream direction along the reactor. This is due to depletion of TMI from the gas phase which results in a reduction in the In mole fraction with distance, eventually to zero. By reducing the temperature to 510°C (the minimum temperature for quality growth of GaAs) the best uniformity of In composition is obtained. In this case, as for QT421, the variation in In fraction indicated from PL measurements is 21.3→23.2% (±1.0% In).

4.2.3. Resistance considerations

In MOCVD, Zn is used as the p-type dopant and Si as the n-type. C is incorporated during AlGaAs growth which also acts as an acceptor. In MBE Be and Si are used as dopants.

The interfaces of Bragg reflectors must be doped very highly to reduce the series resistance by enhancing tunnel currents. Be does not dissolve to high concentrations in Al rich compounds so the level of p-type doping by MBE is limited. C and Zn allow much more effective doping of these structures although incorporation of oxygen may reduce the effect of dopants by creating deep traps. This is a particular problem in MOCVD grown AlAs where concentrations of $2\times10^{18}.\text{cm}^{-3}$ are typical. Use of fractionally distilled TMA[1] allows particularly low incorporation of O ($5\times10^{17}.\text{cm}^{-3}$) into AlGaAs layers grown by MOCVD and further reduction in Bragg resistance. This is discussed more fully in chapters 5, 6 and 7. One improvement to the MBE system would be to add a carbon effusion cell, but this is not simple to do.

4.3. Fabrication of devices

Once the VCSEL structure has been grown it remains to define individual devices and make contact to them. There are two basic options for the fabrication: i) mesa isolation by etching and ii) implant definition. These are described in the following.

4.3.1. Etched mesa isolation

Fig. 4.6 shows two methods of etching a mesa device. Wet chemical etches (fig.4.6a) tend to undercut the etch mask by a distance similar to the etch depth. This is not ideal for producing deeply etched (~5μm) small diameter devices, 20μm or less.

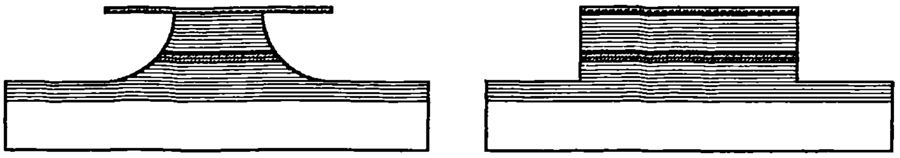

(a) *(b)*

Fig. 4.6. (a) Schematic of wet etched mesa showing undercut of the mask and tapering of the mesa; (b) RIE etched mesa with vertical sidewalls.

Reactive ion etching (RIE) using $SiCl_4$ (fig. 4.6b) can produce etch depths in excess of 10μm through AlAs / GaAs multilayers whilst maintaining smooth vertical sidewalls, as shown in fig. 4.7, provided the etch is not interrupted and performed at a controlled rate[11]. For small devices a vertical dielectric waveguide is effectively formed. A convenient etch mask is a metal film. For back surface emitting devices gold contact pads may serve as this mask and also act to enhance the reflectivity of the upper Bragg reflector stack (see section 2.2.3).

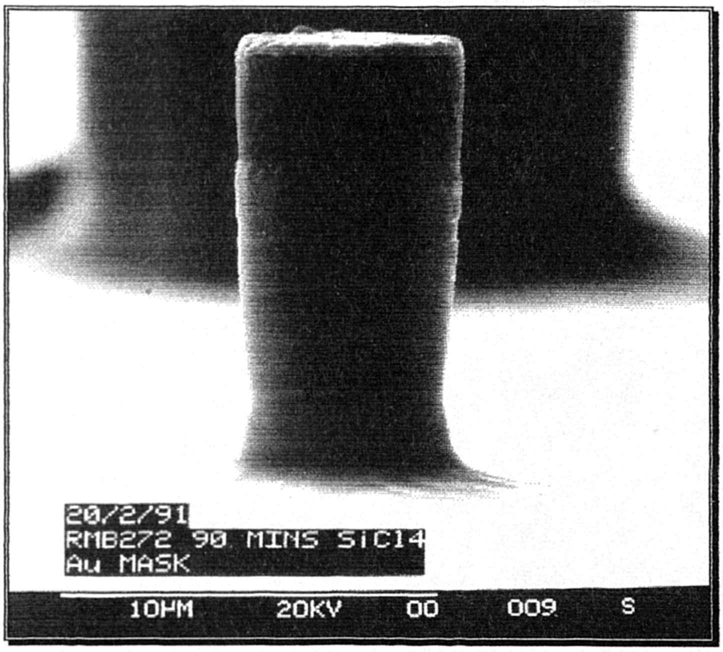

Fig. 4.7. Scanning electron micrograph showing smooth vertical sidewalls obtainable for VCSEL device of 5μm diameter etched to a depth in excess of 10μm using $SiCl_4$ RIE.

4.3.2. Implant defined devices

Ion implantation is a useful way of introducing foreign species into a semiconductor lattice with a controlled depth profile[3]. In this way dopants may be introduced or insulating regions created. Implanted oxygen ions or protons knock atoms off of their lattice sites and create highly resistive regions with a large number of carrier capture traps[12]. A 200keV proton implant may be used to produce a current blocking layer at a depth of ~1.4μm in AlGaAs materials[13]. In the VCSEL structures studied here this corresponds to just above the active region in lower part of the p-reflector. Thus current may be funnelled from large contact pads through small un-implanted regions to confine injected carriers to a small device area[14] (fig. 4.8). This allows small devices to be easily probed or wire bonded.

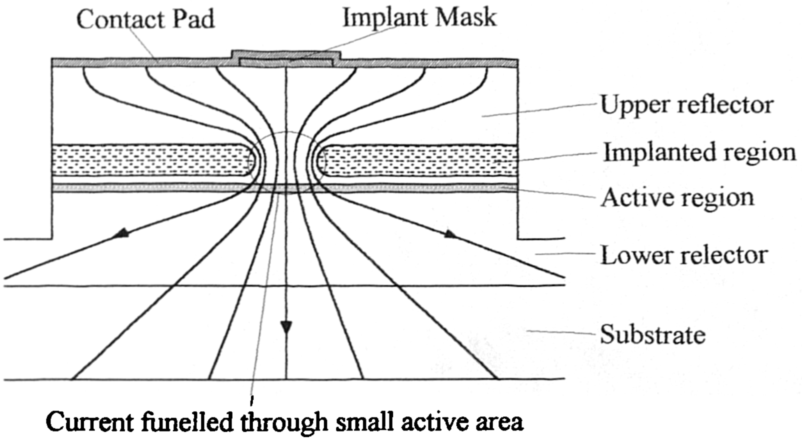

Fig. 4.8. Illustration of implant defined device showing funnelling of current from large contact pad through small active area.

The optical field is effectively gain guided, i.e. may build up in regions where there is gain but is attenuated in un-pumped regions[15]. There is some evidence that thermal lensing may produce waveguiding in this type of structure[16,17].

4.3.3. Fabrication detail of mesa etched devices

This section describes the process steps used to fabricate mesa etched devices. For further information on processing and cleanroom practice refer to Williams[18]. Fig. 4.9 shows a simplified view of the masks used to pattern the devices. Circular devices are arranged in 1×1mm arrays as shown, between which there is space for a 100μm wide square grid.

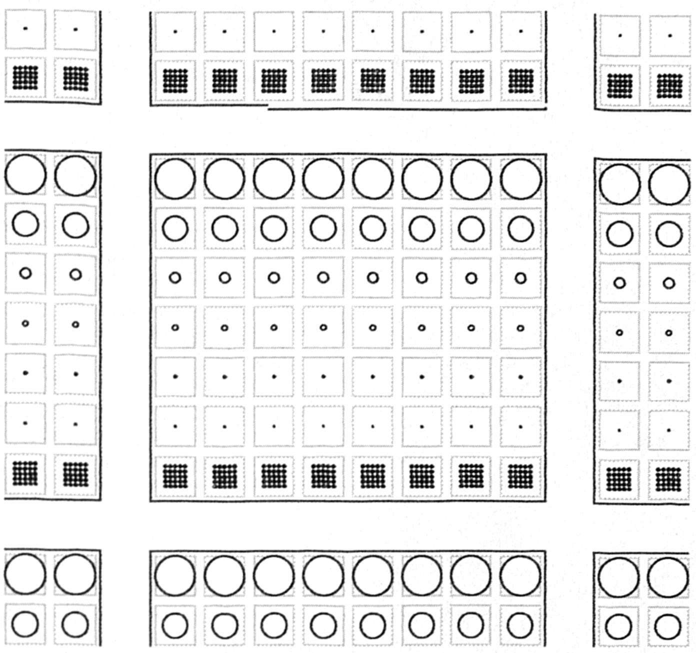

Fig. 4.9. Diagram of masks used to pattern devices. Device diameters of 80, 50, 20, 10, 5, 2 and 1μm and 5x5 arrays of 5μm devices are included on a 100μm pitch. Light grey squares indicate 80μm square pads included on a separate masking level. Between 1mm arrays of devices, a 100μm wide rear grid contact is aligned.

The n-type contact is made to the substrate side of the wafer. One can make use of a grid pattern to enable fabricated samples to be cleaved into pieces as small as 1mm^2 without having to re-apply contacts. Devices are aligned above the square windows in this contact to allow light emission through the substrate.

An ohmic contact is formed by degenerately doping the surface of the semiconductor so that there is no potential barrier preventing the flow of majority carriers between the semiconductor and metal[3,18]. This is usually achieved by evaporating the contact metal along with a dopant metal. The dopant is then diffused into the surface by annealing at an elevated temperature. For GaAs the n-type contact requires a higher annealing temperature so must be deposited first. Once a suitable piece of material has been cleaved from the wafer the substrate side is patterned with the grid contact. This is done by a lift-off process after evaporating metal. A Ni / AuGe / Ni / Au recipe is used. The contact is annealed to 450°C to diffuse in Ge and form the contact.

The devices are then defined on the grown side of the wafer. They must be accurately positioned above windows in the n-contact. Thus it is necessary to transfer the grid pattern to the opposite side of the sample. fig. 4.10 shows how this is done.

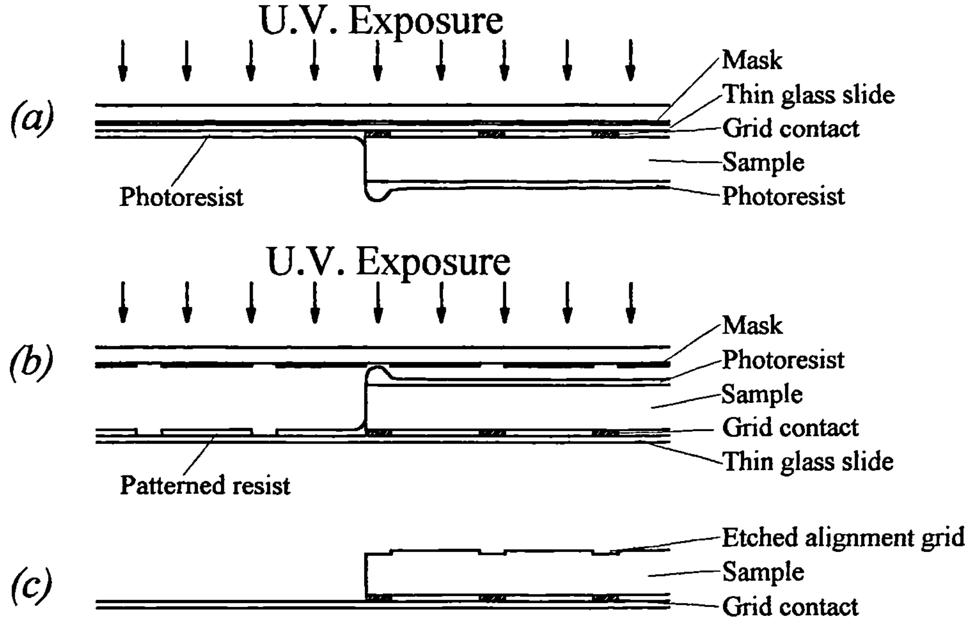

Fig. 4.10. Method by which rear contact grid pattern is transferred to front face of sample: (a) Expose resist pattern onto glass slide; (b) Use pattern on glass slide to align to patterned slide and expose resist on front surface; (c) Etch pattern onto front surface.

The sample is fixed substrate side down to a thin (100μm) glass slide using dental wax and is coated with photoresist. This arrangement is turned upside down and the grid pattern mask is aligned to the contacts on the substrate side of the sample. A ultra-violet (UV) exposure is made and, after developing, an aligned copy of the grid pattern is left in the photoresist on the glass slide. The sample may now be turned over and the mask re-aligned to the patterned resist. A second UV exposure is made and, after developing, the grid pattern has now been successfully transferred to the front surface. It is possible to pattern the remaining resist for the lift-off of device contacts but because of the handling received in the above processes it is usually contaminated and scratched by this stage of the processing. The sample is given an etch for 3 seconds in a 1:1:1 mixture of CH_3COOH : HBr : KCr_2O_7. This is a non-selective etch which will etch approximately 1000Å into the exposed semiconductor surface and leave a permanent grid pattern to allow accurate positioning of devices. We may now remove the old resist and spin on some clean.

Before patterning the resist for device definition it is necessary to remove the edge beading. This is a result of the spinning process used to apply the resist. Fig. 4.11 illustrates how the bead is given an intense UV overexposure and then developed away.

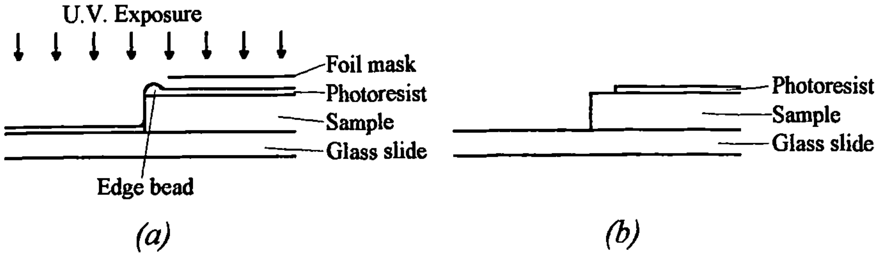

Fig. 4.11. Removal of edge beads. (a) Overexposure of bead using aluminium foil mask and (b) even resist coating left after development.

The sample is now ready for definition of devices. The pattern of device mesas is produced in the resist in alignment with the grid pattern etched into the surface. By removing the edge beads it is possible to get very intimate contact between the mask and resist which gives much improved resolution of lithography; 2 µm diameter contact pads may be routinely produced using this technique. The registration between front and back contact patterns should be better than 20µm: the design of the mask allows for errors of this magnitude. Contact metal is deposited over the resist and lift-off performed to leave circular pads. The contact recipes used were Au / Zn / Au and Cr / Au the latter being used for un-annealed contacts. Un-annealed contacts are preferred for minimal optical absorption in the upper reflector stack.

The sample is now ready for $SiCl_4$ RIE using the un-annealed contact pads as an etch mask. At least 0.5µm thickness of contact metallization is required since there is some erosion of the metal during RIE. The typical etch depth was 3.5→4.0µm; this is to a level slightly into the bottom Bragg reflector. Au / Zn / Au contacts were annealed to 400°C after etching. Un-annealed Cr / Au contacts perform well due to the doping in excess of $10^{19}.cm^{-3}$ of the capping layer of the VCSEL structures.

4.3.4. Passivation of mesa etched devices.

It was not possible to probe or bond directly to devices smaller than 20µm diameter using the equipment available. It is therefore desirable to put larger contact pads over the device mesas to allow for easier contacting. This requires an insulating layer to prevent the pad from shorting out to the substrate. It is desirable to have such a passivating insulator around the mesa to prevent the erosion of AlAs layers in a moist atmosphere. There are two basic options for passivation, regrowth and polymer layers.

Selective regrowth of current blocking layers of GaAs by LPE or MOCVD may be used to provide a high resistance coating around the devices and a planar coating on which contact pads may be placed[19].

Polyimide is a polymer coating specially developed to provide a smooth planar coating of surface relief features. It is a simple to process to apply the polyimide coating. Fig. 4.12 illustrates the process steps involved in passivating and applying contact pads in this way.

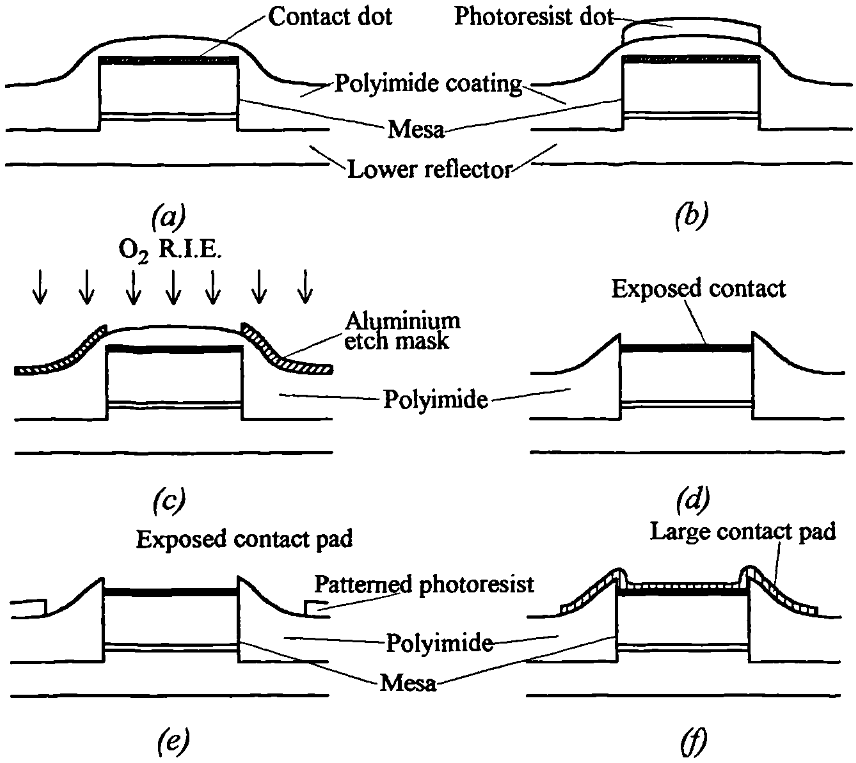

Fig. 4.12. Process steps to passivate VCSEL mesa devices and apply large contact pads: (a) Polyimide is spun onto the sample to planarize the surface. (b) Photoresist dots are produced over the mesas to pattern an evaporated aluminium etch mask. (c) The polyimide is etched using O_2 RIE to expose the mesas. (d) After curing the polyimide the aluminium is dissolved away. (e) Pattern of contact pads formed in resist. (f) Contact metal evaporated and lift-off performed to leave pads.

The polyimide is applied over the etched devices and spun to produce a thin layer (fig. 4.12a). It is then given a soft-bake at 150°C for one hour to solidify the coating. Usually two applications were necessary because of the deep mesa etch. To contact the devices, vias must be etched through the polyimide and aluminium is a suitable etch mask for the production of these. An aluminium layer is evaporated onto the sample. Lift-off is used to pattern the layer to create windows above the devices (fig. 4.12b). Alignment of this pattern may be difficult if the polyimide coating is thick and poor alignment can give rise to leakage paths down the side of the mesa and an increase in the device operating current. It proved difficult to perform lift-off of the aluminium since the surface was not completely planar which resulted in a very thin resist coating above the mesa centres. A 350°C bake is performed to complete the imidization process before O_2 RIE is used to remove the exposed polyimide above the mesas, the aluminium acting as an etch mask (fig. 4.12c). The aluminium is then removed by dissolving in a concentrated NaOH solution (fig. 4.12d). Now the vias are formed and contact pads may be applied. A resist pattern is produced (fig. 4.12e) which is used to lift-off Au metallization evaporated onto the sample and to leave the completed contact pads (fig. 4.12f). Fig. 4.13 shows a photograph of a completed array of devices passivated with polyimide and with contact pads applied. A variation on this process was first used by Geels *et al*[20].

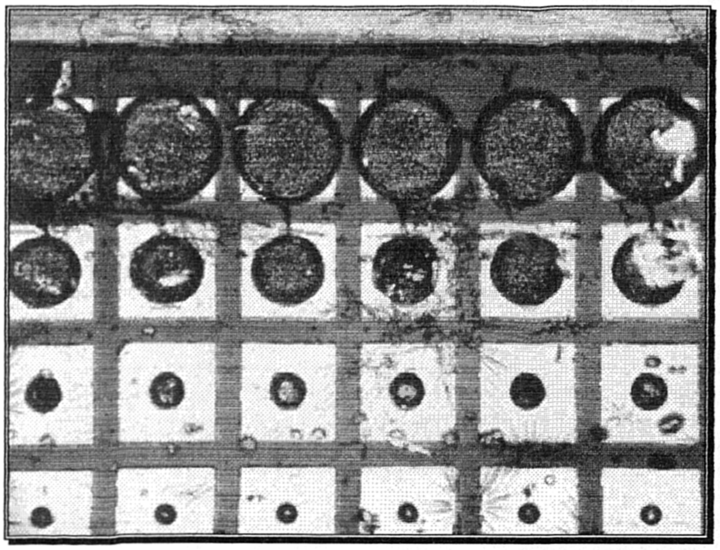

Fig. 4.13 Photograph showing square contact pads applied over polyimide passivated VCSEL devices. The pads contact circular device mesas underneath through etched via holes.

4.3.5. Implant defined devices

Using implant to define devices can improve the device performance. Current funnelling, as shown in fig. 4.8, gives a reduced series resistance. This means that the thermal power dissipated per unit current supplied will be less. Further, the extra surrounding semiconductor material will provide better heatsinking as compared to the etched device.

To provide current funnelling into the active region of the VCSEL structures studied, here a current blocking region should be at a depth just above the bottom of the p-reflector; which lies at a depth of around 2μm. This is quite deep for an implant so light ions with a high kinetic energy are required to penetrate this distance. Protons are the lightest ions (atomic weight = 1). Implanted into an AlGaAs crystal they knock atoms off their lattice sites and create semi-insulating material[12]. 200keV H^+

ions have a range of 1.4μm in GaAs[13]: the implant profile is approximately gaussian with a standard deviation σ, of 0.2μm. In gold the ions have a range d of 0.76μm with σ=0.2μm[13]. The ions have a lateral spread of order σ, which means that the current blocking layer will extend slightly under the mask.

A thickness of $d+3\sigma$ is required to stop 99.9% of the ions. The implanted region will effectively produce very little damage deeper than 2.0μm thus stopping just short of the active region. Using Au as an implant mask, a 1.36μm thickness is required to stop all but 0.1% of the ions. In the devices studied here a thickness of 1.0 μm was used. Although this will only stop 88% of the ions the remainder will be of much lower energy and have a reduced range in the semiconductor. The damage due to these ions will thus be limited to the uppermost layers of the p-type Bragg reflector. From published results on a similar structure[21] an ion dose of ~3.0×10^{13}.cm^{-2} was seen to be adequate to provide adequate current blocking without serious degradation in laser operation from ion damage. The effects of ion dose are examined more closely in section 7.7.

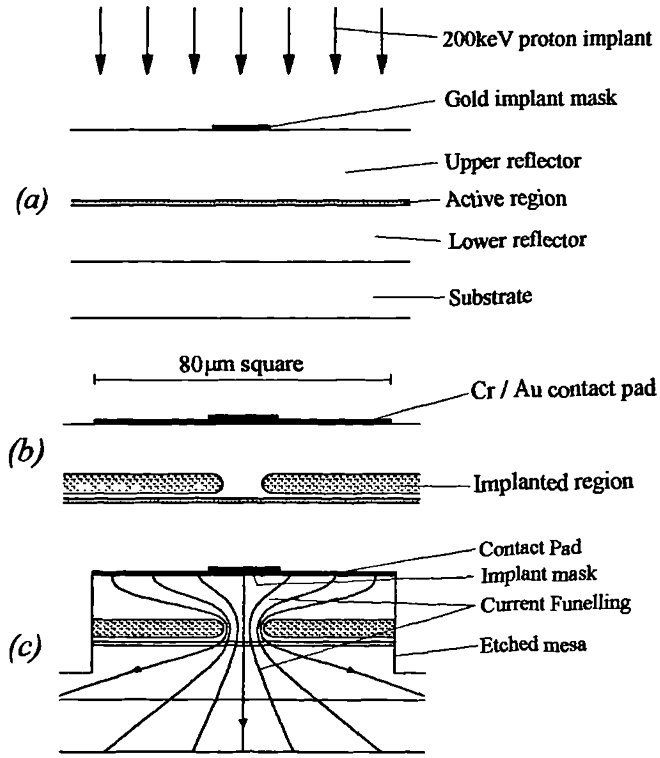

Fig. 4.14. Stages in fabrication of implant defined devices. Fabrication begins as for etched mesa devices: (a) Thick gold dots are used as a mask for a 200keV H^+ implant; (b) 80μm square contact pads are deposited, these are centred over the un-implanted regions; (c) Mesas are etched by RIE using the contact pads as a mask. The devices are now complete.

Device fabrication starts in the same way as for mesa etched devices. The process steps are shown in fig. 4.14. Contacts are lain down as before but for the top contact a thickness of 1.0μm is required. The top contact acts as the implant mask as described above. Implantation was performed at the ion beam facility at the University of Surrey. The implant leaves circular current funnels of 2 to 80μm diameter to define devices which must be isolated from each other. 80μm square Cr / Au contact pads were deposited over the devices using lift-off to pattern them. These pads are used as an etch mask for a 3.5μm deep $SiCl_4$ RIE to isolate the devices within 80μm square mesas. The large pads allow even the smallest active region to be easily probed.

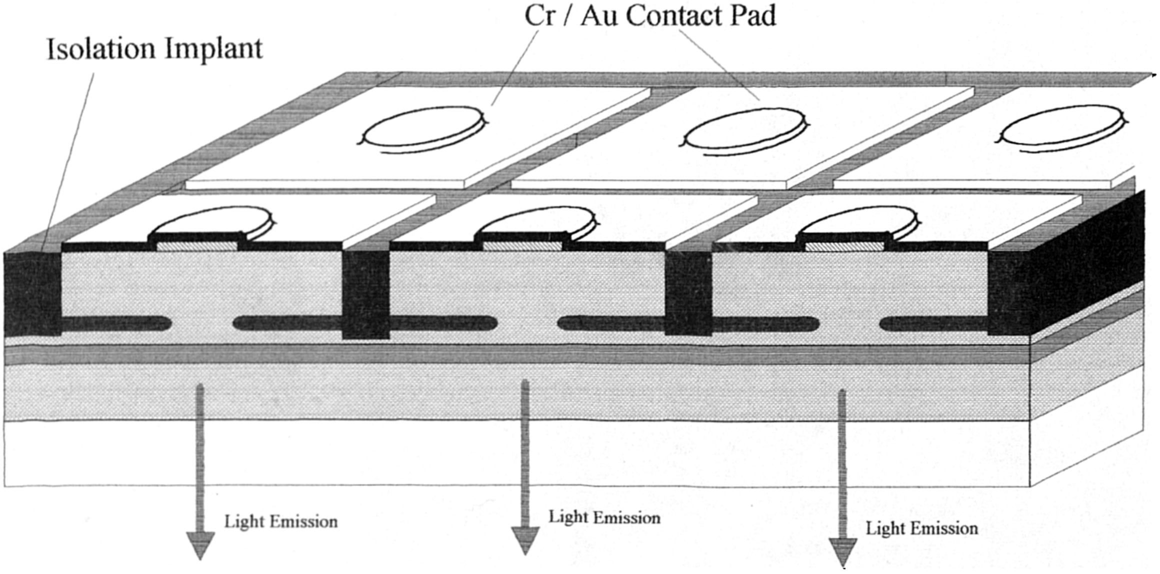

Fig. 4.15. Use of high dose implant to isolate neighbouring devices and form a fully planar array of VCSELs.

Rather than etch mesas, it would be possible to perform multiple implants[22] to produce a fully planar VCSEL array[21]. Fig. 4.15 shows how this may be done: After formation of the square contact pads the sample is returned to the ion implanter for a multiple energy proton implant of high dose. This produces highly insulating material between the devices and effectively isolates them. No etching is required and the planar surface makes it much easier to address the devices by depositing metal traces which may be supported on a thin insulating layer of silicon nitride or polyimide. Vias connect the traces to the underlying contact pads.

References:

[1] J.S.Roberts, T.E.Sale, C.C.Button, J.P.R.David & A.Jennings, *High performance microcavity resonator devices grown by atmospheric pressure MOVPE*, J. Crystal Growth, **124**, pp792-800, 1992

[2] M.R.Leys, *Metal organic chemical vapour phase epitaxy for the growth of semiconductor structures and strained layer lasers*, chapter in *Low dimensional structures in semiconductors*, A.R.Peaker & H.G.Grimmeiss Eds., NATO ASI Series B: Physics, **281**, Plenum, 1991.

[3] S.M.Sze, *Semiconductor devices, physics and technology*, Wiley, New York, 1985.

[4] R.Grey, Private Communication.

[5] K.Ploog, *Fabrication of artificially layered III-V semiconductors by beam epitaxy and aspects of additional lateral patterning*, chapter in *Low dimensional structures in semiconductors*, A.R.Peaker & H.G.Grimmeiss Eds., NATO ASI Series B: Physics, **281**, Plenum, 1991.

[6] K.Bacher, B.Pezeshki, S.M.Lord & J.S.Harris Jr., *Molecular beam epitaxial growth of vertical cavity optical devices with in situ corrections*, Appl. Phys. Lett., **61**, 12, pp1387-1389, 1992.

[7] S.A.Chalmers & K.P.Killeen, *Method for accurate growth of vertical-cavity surface-emitting lasers*, Appl. Phys. Lett., **62**, 11, pp1182-1184, 1993.

[8] J.D.Walker, D.M.Kuchta & J.S.Smith, *Vertical-cavity surface-emitting laser diodes fabricated by phase-locked epitaxy*, Appl. Phys. Lett., **59**, 17, pp2079-2081, 1991.

[9] J.L.Jewell & G.R.Olbright, *Surface-emitting lasers emerge from the laboratory*, Laser Focus World, pp212-223, May 1992.

[10] J.W.Matthews & A.E.Blakeslee, *Defects in epitaxial multilayers*, J. Crystal Growth, **27**, pp118-125, 1974.

[11] A.Scherer, J.L.Jewell, Y.H.Lee, J.P.Harbison & L.T.Florez, *Fabrication of microlasers & microresonator optical switches*, Appl. Phys. Lett., **55**, 26, pp2724-2726, 1989.

[12] D.C.D'Avanzo, *Proton isolation for GaAs integrated circuits*, IEEE Trans. Electron Devs., **29**, 7, pp1051-1059, 1982.

[13] C.Jeynes, *Results of calculations of ion scattering in materials performed at University of Surrey*, Private communication.

---

[14] Y.H.Lee, B.Tell, K.Brown-Goebeler, J.L.Jewell & J.V.Hove, *Top-surface-emitting GaAs four-quantum-well lasers emitting at 0.85μm*, Electron. Lett., **26**, 11, pp710-711, 1990.

[15] C.J.Chang-Hasnain, M.Orenstein, A.Von Lehmen, L.T.Florez, J.P.Harbison & L.T.Florez, *Transverse mode characteristics of vertical cavity surface-emitting lasers*, Appl. Phys. Lett., **57**, 3, pp218-220, 1990.

[16] N.K.Dutta, L.W.Tu, G.Hasnain, G.Zydzik, Y.H.Wang & A.Y.Cho, *Anomalous temperal response of gain guided surface emitting lasers*, Electron. Lett., **27**, 3, pp208-210, 1991.

[17] D.Vakshoori, J.D.Wynn, G.J.Zydzik, R.E.Leibenguth, M.T.Asom, K.Kojima & R.A.Morgan, *Top-surface emitting lasers with 1.9V threshold voltage & the effect of spatial hole burning on their transverse mode operation & efficiencies*, Appl. Phys. Lett., **62**, 13, pp1448-1450, 1993.

[18] R.E.Williams, *Gallium arsenide processing techniques*, Artech House, 1984.

[19] M.Ogura, S.Mukai, M.Shimada, T.Asaka, Y.Yamasaki, T.Seki & H.Iwano, *Surface-emitting laser diode with distributed Bragg reflector & buried heterostructure*, Electron. Lett., **26**, 1, pp18-19, 1990.

[20] R.S.Geels, S.W.Corzine, J.W.Scott, D.B.Young & L.A.Coldren, *Low threshold planarized vertical-cavity surface-emitting lasers*, IEEE Photon. Technol. Lett., **2**, 4, pp234-236, 1990.

[21] M.Orenstein, N.G.Stoffel, A.C.Von Lehmen, J.P.Harbison & L.T.Florez, *Efficient continuous wave operation of vertical-cavity semiconductor lasers using buried-compensation layers to optimize current flow*, Appl. Phys. Lett., **59**, 1, pp31-33, 1991.

[22] M.Orenstein, A.C.Von Lehmen, C.Chang-Hasnain, N.G.Stoffel, J P.Harbison, L.T.Florez, E.Clausen & J.E.Jewell, *Vertical-cavity surface-emitting InGaAs / GaAs lasers with planar lateral definition*, Appl. Phys. Lett., **56**, 24, pp2384-2386, 1990.

5. Resistance Considerations for Bragg Reflectors

This chapter discusses the transport of carriers across heterointerfaces in the AlAs / GaAs Bragg reflector stacks. The use of intermediate layers and superlattices to grade the interfaces and reduce the resistance to carrier flow is examined. The effect of grading on the optical reflectivity is also investigated.

5.1. Heterointerfaces

Consider a basic AlAs / GaAs dielectric reflector stack consisting of alternate quarter wave AlAs and GaAs layers. The AlGaAs system forms type I superlattices, that is wells are formed for both holes and electrons in the low bandgap material. The band structure of an AlAs / GaAs stack is shown in fig. 5.1, note that each heterointerface is associated with large (compared to kT) offset in both the valence and conduction bands, ΔE_C, ΔE_V (data from Adachi review[1]).

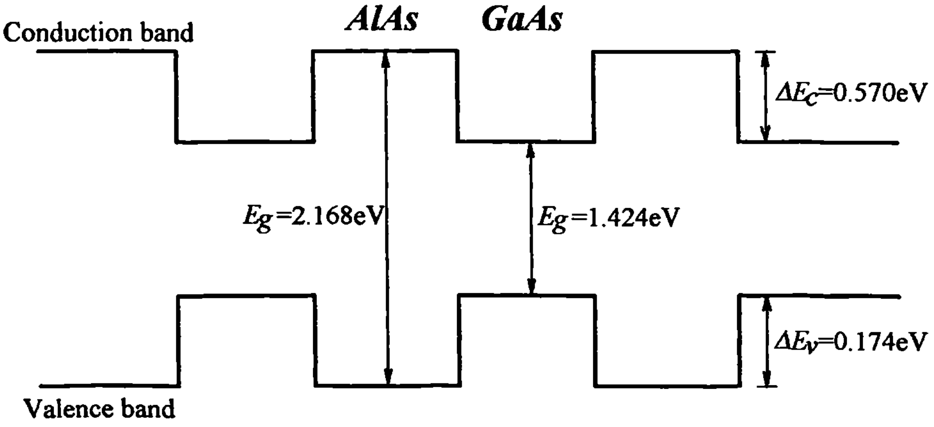

Fig. 5.1. Band structure of undoped AlAs / GaAs Bragg reflector[1].

In a typical VCSEL current is injected into the active region through the epitaxially grown reflector stacks. They are thus doped to form a p-i-n diode. The addition of dopant causes the Fermi level to lie close to the band edge in the doped regions and causes band bending to occur in the vicinity of the interfaces. Fig.5.2 shows the effect on the bands in a full VCSEL structure under zero bias. Notice how in the p-type reflector, the bands are bent in the vicinity of the heterointerfaces so that Fermi level lies close to the valence band over much of the stack. A similar situation for electrons exists in the n-type reflector.

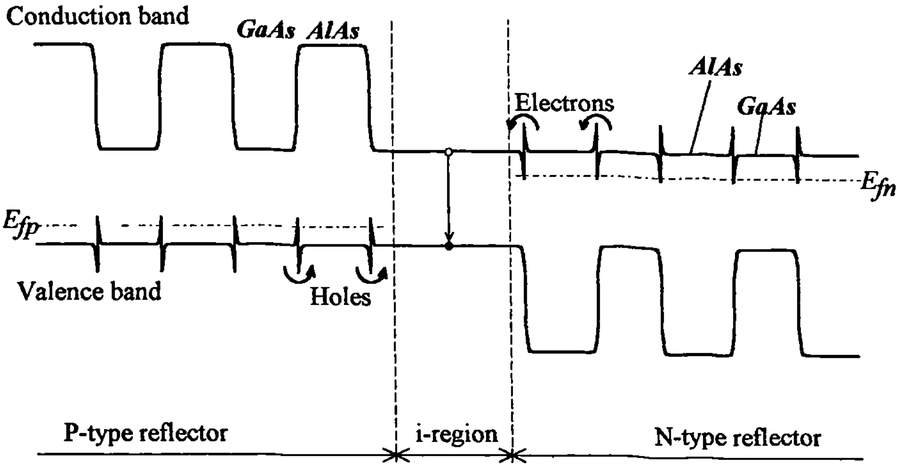

Fig. 5.2. Diagram of band edges in a full VCSEL structure for small forward current showing potential spikes created at heterointerfaces in the Bragg reflectors.

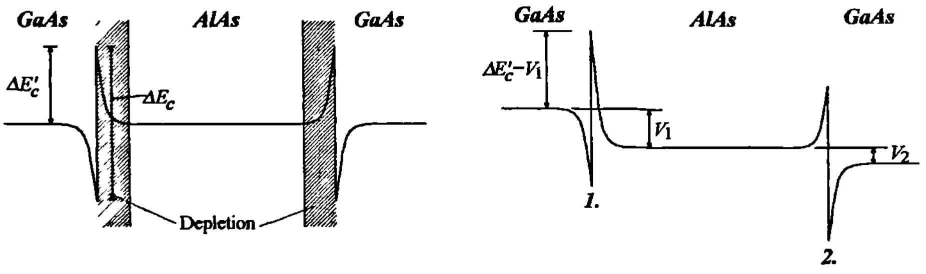

(a) *(b)*

Fig. 5.3. Conduction band edge for one pair of interfaces in n-type reflector stack: (a) Under zero bias showing depletion regions formed into higher bandgap material, (b) Under bias junction 1. is under a reverse bias V_1 and junction 2. is under a forward bias V_2.

Consider one of the n-type heterointerfaces (fig. 5.3): before the junction is made the Fermi level is close to the conduction band in both materials due to the high density of ionised donors. As the junction is made electrons flow from the AlAs into the GaAs where the electron affinity is larger and the Fermi level is at a lower energy. The AlAs thus becomes depleted near to the interface and on the GaAs side accumulation occurs. This movement of charge gives rise to the band bending needed to align the Fermi levels. The Fermi level cannot move far into the conduction band as the density of conduction states is very large, thus the depth of accumulation is limited. The separation of the Fermi level E_f from the conduction band edge E_c, away from the interface, is given by (5.1).

$$E_c - E_f = kT \ln\left(\frac{N_c}{N_d}\right) \qquad (5.1)$$

Where N_c and N_d are the effective density of conduction states and density of donors respectively. A similar relation applies for the valence band in p-type material. The relevant parameters for GaAs at 300K are given in table 5.1 [2]. From these values the separation is calculated for n and p-type GaAs at room temperature. Fig. 5.4. shows this relation.

N_c	$4.7\times10^{17}.\text{cm}^{-3}$
N_v	$7.0\times10^{18}.\text{cm}^{-3}$

Table 5.1. Effective density of conduction and valence states in GaAs at 300K after Sze[2].

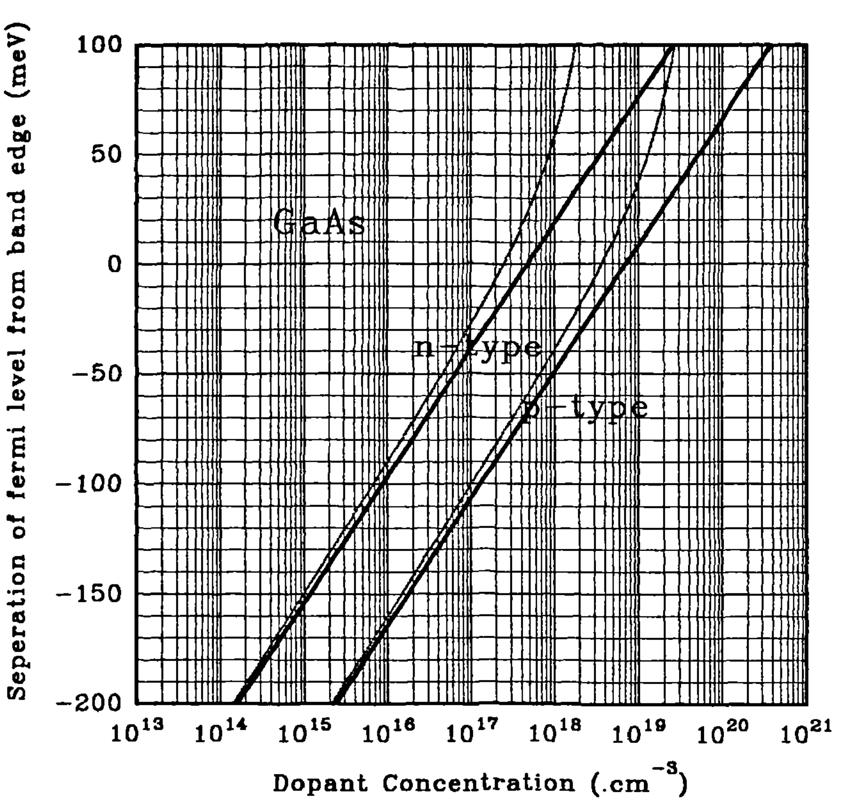

Note:
Grey lines indicate exact calculation using Fermi statistics

Fig. 5.4. Separation of Fermi Level From conduction band edge in n-type GaAs and separation from valence band edge in p-type GaAs. Values for 300K.

For a junction doped to a concentration of a few $10^{18}.\text{cm}^{-3}$ the Fermi energy is close to the band edge. This means that the potential barrier $\Delta E_c'$ for carriers approaching junction *1.* of fig. 5.3 is almost ΔE_c since the density of states above the band edge is very large effectively preventing the Fermi level from moving into the band. This is similar to an MOS diode in accumulation mode[2].

Considering for the moment the n-type junctions, the treatment is the same for the p-type interfaces but with the potentials and charges reversed. As fig. 5.5b shows, we consider a depletion region of width x_d, constituting a net positive charge $+Q$ in the AlAs (5.2). This is balanced by an accumulated negative charge of equal magnitude $-Q$ in the GaAs, which is considered to lie in a very thin layer where the conduction band bends close to the Fermi level.

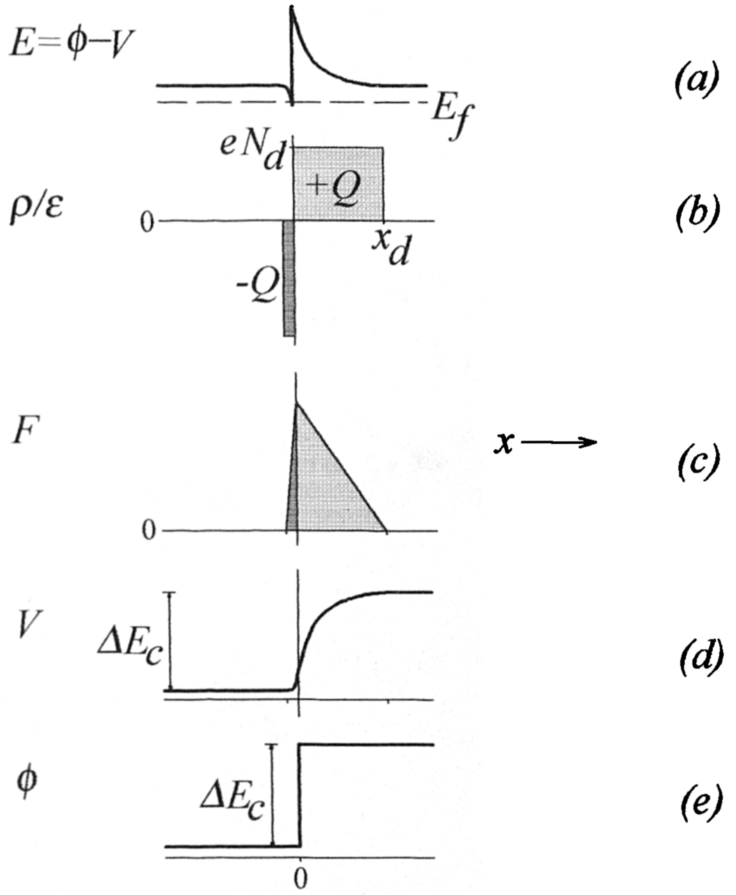

Fig. 5.5. Depletion region at n-type heterointerface. When the junction is made electrons from the higher bandgap material flow into towards the lower bandgap and it becomes depleted to a depth x_d. Diagrams show spatial distribution of: (a) Potential energy of electrons at the band edge, (b) Carrier density ρ, (c) Electric field F, (d) Built in voltage and (e) Intrinsic potential ϕ.

The Poisson equation (5.3) relates the built in potential V profile to the spatial charge density ρ.

$$Q = eN_d x_d \tag{5.2}$$

$$\frac{\partial^2 V}{\partial x^2} = -\frac{\rho}{\varepsilon_o \varepsilon_r} = -\frac{eN_d}{\varepsilon_o \varepsilon_r} : 0 \le x \le x_d \tag{5.3}$$

Integrating once and applying the boundary condition that no fields exist outside of the junction region, we find the electric field profile $F(x)$ (5.4), see fig. 5.5c.

$$F=-\frac{\partial V}{\partial x}=\frac{eN_d}{\varepsilon_o\varepsilon_r}\left(x-x_d\right):0\le x\le x_d \qquad (5.4)$$

Integrating once more and applying the boundary condition $V(x_d)=0$, we find the built in potential distribution $V(x)$ (5.5), see fig. 5.5d.

$$V=\frac{eN_d}{2\varepsilon_o\varepsilon_r}\left(-x^2+2xx_d-x_d^2\right):0\le x\le x_d \qquad (5.5)$$

The energy band profile for electrons can now be found by superimposing the potential V on the profile before the junction is made $\phi(x)$, which is due to the variation in electron affinity. This is shown in fig. 5.5d. From the condition $V(0)=\Delta E_c$ we find the depletion width x_d for the heterointerface is given by (5.6) and similarly for the valence depletion in the p-type reflector.

$$x_d=\sqrt{\frac{2\varepsilon_o\varepsilon_r}{eN_d}\Delta E_c} \qquad (5.6)$$

Here we assume that the entire band offset exists across the depleted region. Note that the refractive index ε_r refers to the depleted higher bandgap material. Using this equation the depletion width is calculated as a function of dopant density for both n and p-type heterointerfaces between AlAs and GaAs at a temperature of 300K (fig. 5.6). The AlAs relative dielectric constant was taken as 10.06 [1]. From fig. 5.6 one can see that at a dopant concentration of $2.0\times10^{18}.\mathrm{cm}^{-3}$ the depletion widths are approximately 180Å in the n-type junction and 100Å in the p-type junction.

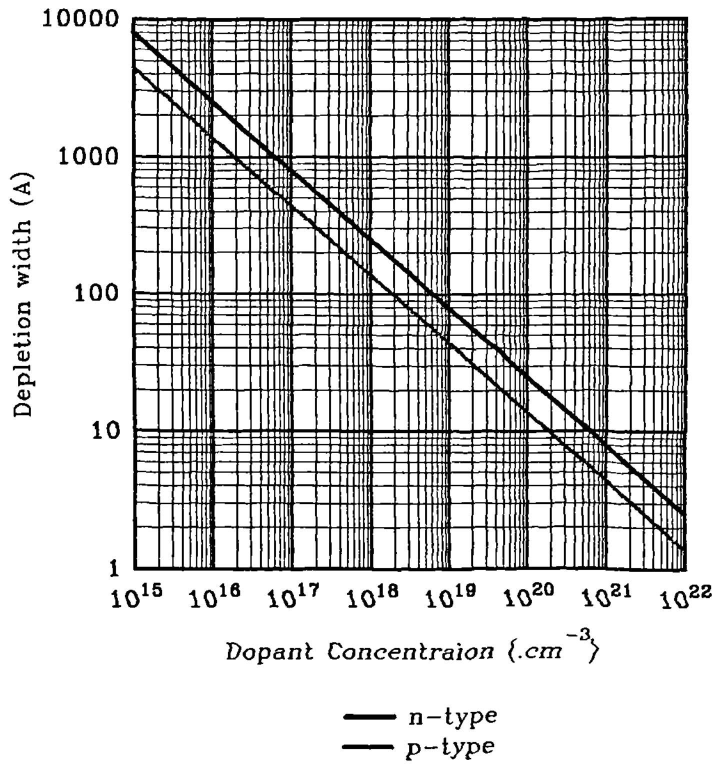

Fig. 5.6. Variation of depletion width at AlAs / GaAs heterointerface with donor (acceptor) concentration in n-type (p-type) junction.

5.2. Heterojunctions Under Bias

5.2.1. Tunnel currents through reverse biased interfaces

Consider one pair of layers in the AlAs / GaAs reflector stack. Fig. 5.3a shows such a pair under zero bias. When a bias *V* is applied, each junction is subject to a potential difference. For each such pair of layers in the stack there are two *p-p* or *n-n* heterojunctions, one of which is under a forward bias and one under reverse bias. Carrier flow across a junction is by one of two mechanisms: tunnelling through the potential spike or thermal emission over the barrier. The barrier to carrier flow in junction *1* of fig. 5.3b is large compared with *kT* and is not reduced under the reverse bias. The thermionic current will therefore be small and the electrical resistance will be very large unless the depletion width is sufficiently narrow to allow significant current to tunnel through the potential spike occurring at the depleted region. Junction *2* however presents no barrier to electrons travelling from the depleted AlAs region under the forward bias and thus offers a very low resistance to current flow.

In order to achieve a low series resistance in the VCSEL device it is necessary to ensure a significant tunnelling probability through the reverse biased junctions in the reflector stacks. This is done by doping to a sufficient level to give narrow depletion layers.

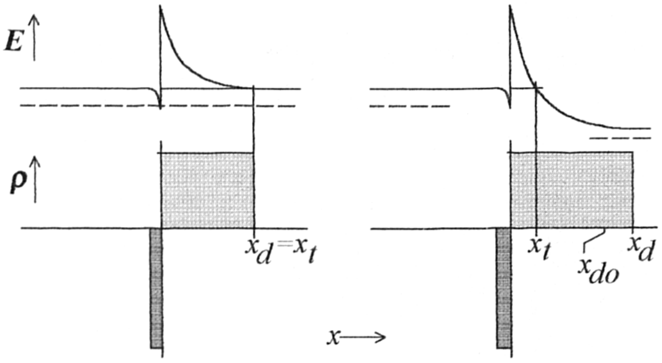

(a) Zero bias. *(b) Reverse bias.*

Fig. 5.7. Depletion width x_d at n-type heterointerface (a) under zero bias and (b) under finite reverse bias illustrating the effect on tunnel distance x_t

Under reverse bias V the depletion width of the heterojunction x_d widens as the junction potential increases (5.7) but the tunnelling distance x_t is reduced (5.8). Fig. 5.7 illustrates this.

$$x_d = \sqrt{\frac{2\varepsilon_0\varepsilon_r}{eN_d}\left(\Delta E_c + V\right)} \tag{5.7}$$

$$x_t = x_{do}\left(\sqrt{1+\frac{V}{\Delta E_c}} - \sqrt{\frac{V}{\Delta E_c}}\right) \tag{5.8}$$

Where x_{do} is the depletion width under zero bias. This relation is shown in fig. 5.8.

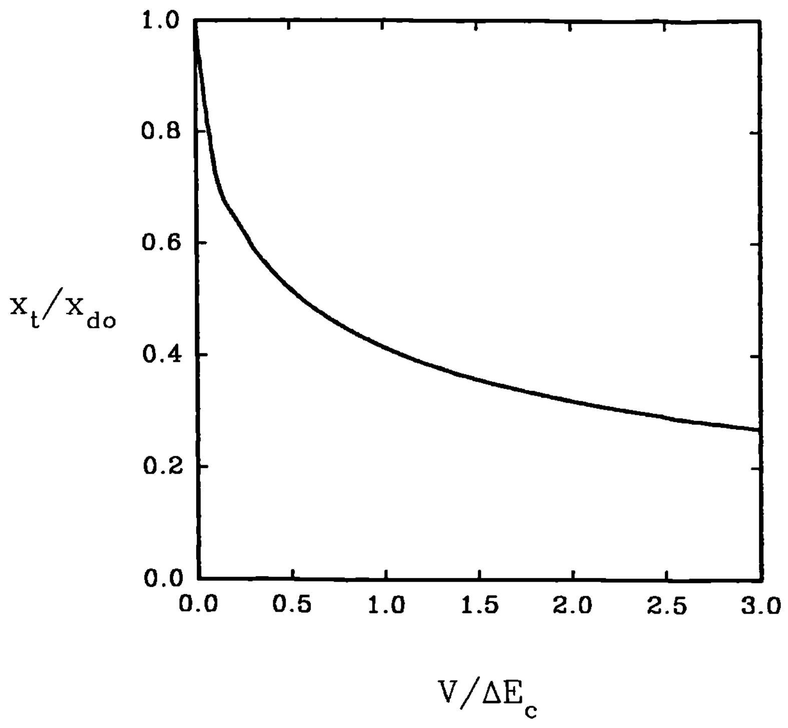

Fig. 5.8. Variation of tunnel distance x_t with applied bias V in a reverse biased heterointerface.

As will be seen in section 4.3, the bias across each reflector pair can vary from 0.1 to 2.0 times the band offset at the current densities of interest (1000A.cm^{-2}), so a significant narrowing by 20 to 70% of the depletion width may be expected. This will increase the tunnel probability equivalent to an increase in doping by a factor 1.5 to 10 see fig. 5.6.

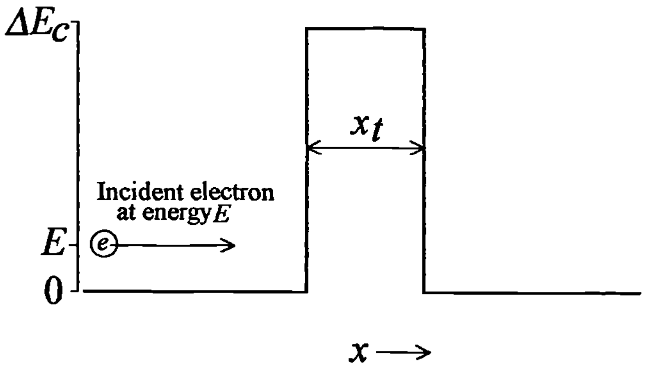

Fig. 5.9. Approximated barrier for estimate of heterointerface tunnelling.

We shall approximate the junction potential spike by a square barrier of height ΔE_c and of width x_t as shown in fig. 5.9. The transmission probability T of an electron incident on the barrier with energy E above the band edge is found using Schrödinger's equation[3], the solution of which is given in (5.9).

$$T = 1 \Bigg/ \left[1 + \left\{ \Delta E_c \sinh\left(x_t \sqrt{2m_n(\Delta E_c - E)/\hbar^2} \right) \right\}^2 \Bigg/ \left\{ 4E(\Delta E_c - E) \right\} \right] \qquad (5.9)$$

ΔE_c	$1.1x : x \leq 0.45$ $0.43+0.14x : x>0.45$
ΔE_v	$0.147x : x \leq 0.45$ $0.046-0.015x+0.143x^2 : x>0.45$
E_g	$1.424+1.247x : x \leq 0.45$ $1.900+0.125x+0.143x^2 : x>0.45$
m_n/m_o	$0.067+0.083x : x \leq 0.45$ $0.32-0.06x : x>0.45$
m_p/m_o	$0.62+0.14x$
ε_r	$13.18-3.12x$

Table 5.2. Material constants for compounds in the $Al_xGa_{1-x}As$ system after Adachi[1].

Using the relation of (5.9) and the $Al_xGa_{1-x}As$ material constants from table 5.2, the tunnel probabilities are calculated as a function of dopant concentration for both p and n-type heterojunctions. The results of these calculations are shown in fig. 5.10. The different curves show the effect of varying x for $Al_xGa_{1-x}As$ / GaAs interfaces. The incident carriers are considered to have an energy 1.0meV above the band edge.

Fig. 5.10 indicates that the transmission probability of majority carriers through p-type heterojunction spikes is generally higher than for n-type heterojunctions doped to the same concentration. This difference is due to the large offset in the conduction band in the AlGaAs / GaAs system. Reducing the aluminium fraction on the wide gap side of the interface increases the tunnel probability T by reducing the potential step due to the band offset. T is to a first approximation proportional to the conductance of the interface.

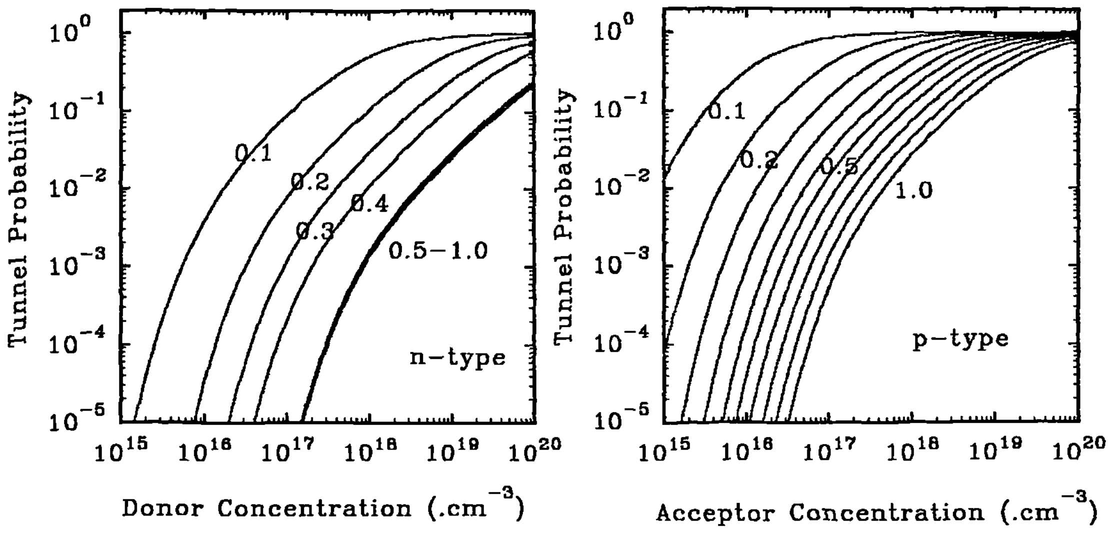

Fig. 5.10. Variation of tunnel probabilities with donor and acceptor concentrations for n and p type reverse biased GaAs / $Al_xGa_{1-x}As$ heterojunctions with $x=0.0 \rightarrow 1.0$.

From (5.9) we see that T also depends on the carrier mass. Thus for n-type GaAs / $Al_xGa_{1-x}As$ interfaces with $x>0.45$ we see little variation in T with x as the electron mass in the X-valley reduces with increasing x, compensating for the increase in band offset.

Note that by MBE it is a simple matter to dope AlAs and GaAs with silicon to produce n-type material with carrier concentrations in excess of $1\times10^{19}.cm^{-3}$. The usual acceptor dopant for MBE growth is Be which has limited solubility in materials with a high Al fraction[4]. It is therefore difficult to achieve active acceptor concentrations in excess of $2\times10^{17}.cm^{-3}$ in AlAs using Be. For p and n-type AlAs / GaAs Bragg stacks doped with acceptors to $2\times10^{17}.cm^{-3}$ and with donors to $2\times 10^{18}.cm^{-3}$ the transmission probabilities through the reverse biased interfaces are of similar magnitude being 2.5×10^{-3} and 5.8×10^{-3} respectively.

5.2.2. Split junctions

For a heterojunction with a wide depletion region and high resistance:

$$x_d\sqrt{\frac{2m_n\Delta E_c}{\hbar^2}} >> 1 \qquad (5.10)$$

The tunnel probability in this case approximates to:

$$T \approx \exp\left(-2x_d\sqrt{\frac{2m_n\Delta E_c}{\hbar^2}}\right) = \exp\left(-\sqrt{\frac{16m_n\Delta E_c^2\varepsilon_o\varepsilon_r}{\hbar^2 eN_D}}\right) \qquad (5.11)$$

Thus for a heterointerface we may expect the conductivity due to the tunnel current σ_{T1} to vary with the band offset as:

$$\sigma_{T1} \propto \exp\left(\frac{-\Delta E_C}{A}\right) \tag{5.12}$$

Where A is a *constant* and may be found from (5.11). If we split the junction into two smaller discontinuities each with a band offset of $\frac{1}{2}\Delta E_C$ by introducing an interfacial layer of an intermediate AlGaAs composition, as shown in fig 5.11, we expect the new tunnel conductance to be σ_{T2}.

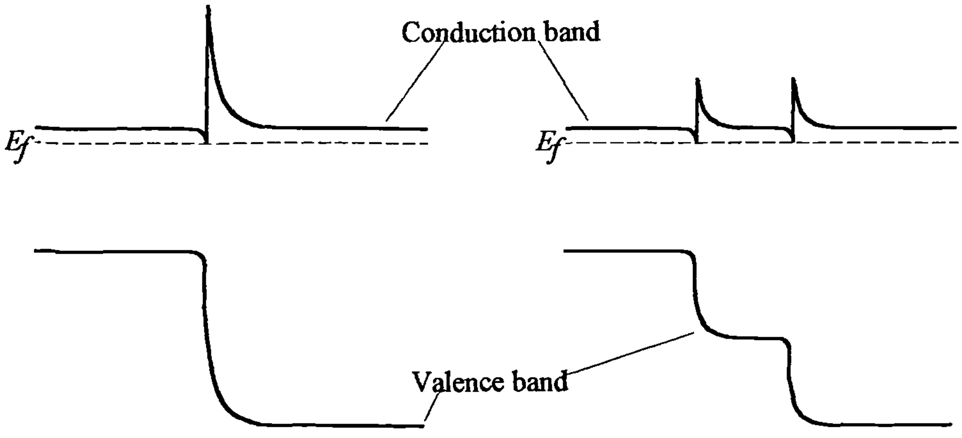

Fig. 5.11. Heterointerface between AlAs and GaAs layers may be split into two junctions of smaller band offset by the introduction of an intermediate AlGaAs layer.

$$\sigma_{T2} \propto \frac{1}{2}\exp\left(\frac{-\Delta E_C}{2A}\right) \tag{5.13}$$

Note the prefactor of ½ as there are now two junctions in series. The ratio of these two is:

$$\frac{\sigma_{T2}}{\sigma_{T1}} = \frac{1}{2}\exp\left(\frac{\Delta E_C}{2A}\right) \tag{5.14}$$

The assumption (5.10) above is equivalent to $\Delta E_C >> A$ thus:

$$\sigma_{T2} >> \sigma_{T1} \tag{5.15}$$

Thus for a high resistance heterointerface, splitting the junction into two smaller interfaces will significantly reduce the resistance. The two smaller junctions must be separated further than the extent of the depletion width for the above to be valid. More generally, splitting the junction into a number of smaller steps to produce a staircase grading of the interface will reduce the resistance still further. If the junction is split such that the band offsets of the individual smaller junctions are similar in magnitude to or smaller than kT then the thermionic current will start to become significant and a further reduction in resistance will be evident. In the limit of many junctions we approach a continual grade where there is no interface discontinuity.

5.3. Experimental

A number of mirror test structures were grown by both MBE and MOCVD. p- and n-type structures were doped with various impurities and with different concentrations. The effect of disrupting the discontinuity due to the band offsets was investigated by using interfacial layers of intermediate composition and by using superlattice grading. Electrochemical (Polaron) profiling was used to indicate the depth profile of the effective concentration of dopant incorporated into the structures. This measurement is made by eroding the semiconductor in an electrolyte and measuring the depletion capacitance at the exposed surface. It has a number of limitations; it does not reliably profile certain p-type structures and the measurement resolution deteriorates significantly with the depth profiled.

5.3.1. MOCVD Grown Reflectors

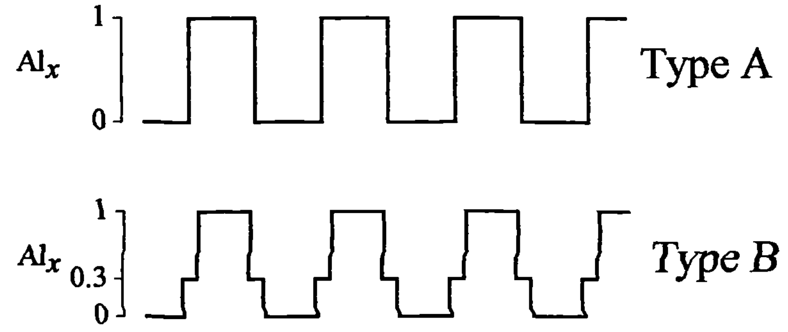

Fig.5.12. Bragg reflector designs used in MOCVD grown test structures. Type A is the basic reflector design and type B incorporates 200Å intermediate layers for the reduction of series resistance.

MOCVD grown reflectors were grown to two designs. Type A (see fig. 5.12) is the basic AlAs / GaAs reflector with abrupt interfaces. Type B is a staircase type reflector as described in section 5.2.2 with 200Å intermediate layers of $Al_xGa_{1-x}As$ at the AlAs / GaAs interfaces[5]. All of the structures were doped uniformly throughout the structure and were grown upon a conducting substrate at a temperature of 700°C. The n-reflectors were doped $\sim 2\times10^{18}.cm^{-3}$ (for details see table 5.3) with Si and the p-reflector $2\times10^{18}.cm^{-3}$ with Zn. Note that the AlAs layers also contain C at a concentration of approximately $2.0\times10^{18}.cm^{-3}$ from the decomposition of the metal organic precursor. These layers were grown using TMA direct from the manufacturer (see growth chapter) which generally contains water contamination. If subject to no further processing oxygen from this moisture is incorporated into the AlAs layers to a concentration of 2→3×10^{18}.cm^{-3}. Oxygen acts as a trap and reduces the effect of active dopants. The effects of reducing the oxygen contamination are investigated later in section 5.3.7.

Devices were made for resistance measurements in the following way: an ohmic back contact was formed on the substrate side of the sample. Ohmic contact pads were formed on the front (grown) side of the sample. Mesas were then wet etched through the reflector layers to complete the devices (see chapter 4) as shown in fig. 5.13.

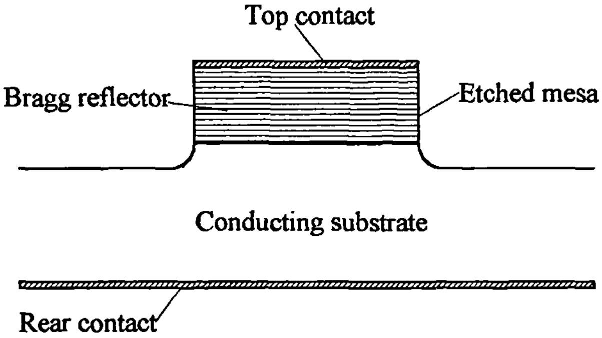

Fig. 5.13. Etched mesa device for measurement of current-voltage characteristic of reflector stacks.

Current voltage measurements were made under pulsed conditions using 0.5μs pulses at 18μs repetition rate. The use of short pulses eliminates the effects of ohmic heating and allows true comparison between reflectors with quite different resistances. A summary of the reflectors measured appears in table 5.3, also shown in the table are the voltages dropped at a pulsed current of 20mA for 50μm diameter mesas. Fig. 5.14. shows the *I-V* relationship for these reflectors normalised per reflector pair.

Layer No.	**Dopant**	**No. pairs**	**Voltage (V)**	**Type**	**Voltage / pair**
QT287	2.0×10^{18}.cm^{-3} **n**	14	1.4	B	0.10
QT255	2.0×10^{18}.cm^{-3} **p**	15	3.0	B	0.20
QT252	3.0×10^{18}.cm^{-3} **n**	10	2.9	A	0.29
QT303	1.5×10^{18}.cm^{-3} **n**	19	9.12	A	0.48

Table 5.3. Summary MOCVD grown Bragg reflectors together with voltage drops at 20 mA for pulsed measurements undertaken on 50μm diameter mesas.

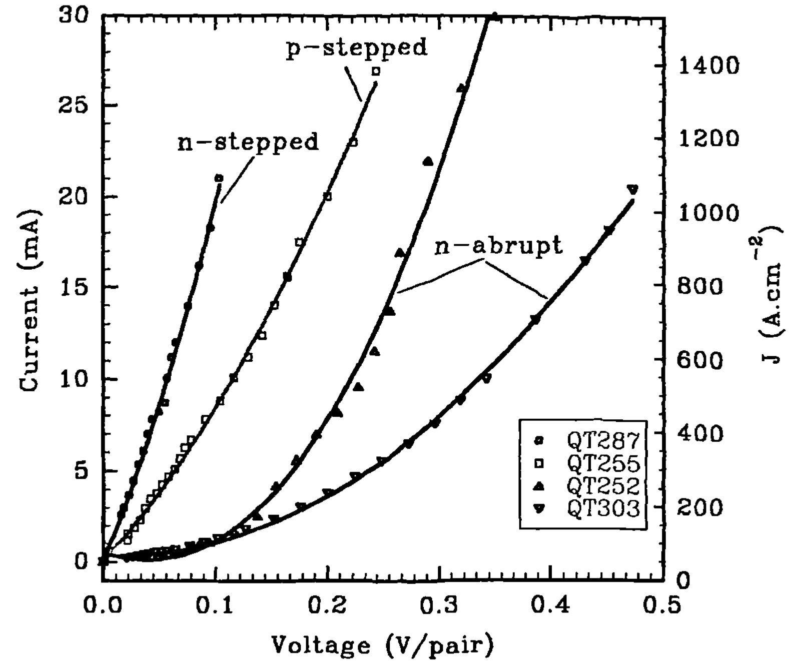

Fig. 5.12. Pulsed I-V measurements undertaken on Bragg reflectors in table 5.3.

For the n-type reflector it is seen that the splitting of the heterobarriers into two smaller barriers by the inclusion of the intermediate layer has reduced the bias voltage needed to pass a current of 20mA (a typical operating current) by a factor of nearly 3 compared to the best type A reflector. It is also noted that the stepped reflectors have a more linear I-V response. For a typical reflector for use in a VCSEL comprising 24 pairs, the voltage is reduced from 7.0 to 2.4V by the inclusion of the interfacial layers. Comparing the two n-type type A reflectors, the effect of increasing the donor concentration from 1.5 to 3.0×10^{18}.cm^{-3} is seen in a reduction in the voltage drop by a factor of 1.7 from 0.48 to 0.29V per pair for a current of 20mA.

The p-type reflector drops a voltage of 0.2V per pair at 20mA and exhibits an almost linear I-V response similar to the n-type structure with stepped interfaces. No separate p-type type A reflectors were grown for direct comparison with QT255 but for a full VCSEL structure consisting of 15 pair p-type top reflector active cavity region and 24.5 pair n-type lower reflector, both being type A reflectors, the bias voltage across a 50μm diameter mesa for a current of 20mA is 30V; this is the structure QT233 discussed in section 6.1. This indicates that the bias per pair for the p-type reflector pair is some 2V (allowing 9V drop across the n-type reflector and 1V diode potential). The type B structure therefore offers a significant improvement.

5.3.2. Ideal low resistance reflectors

For minimal resistance we would ideally produce continuous grading of the aluminium fraction across the interface region[5,6]. Fig. 5.15a illustrates this situation;

the interface region becomes depleted to align the Fermi levels and there is no abrupt junction to carrier flow. In a structure which can be grown in a more controlled way (see following text) (fig. 5.15b) the interface is composed of a number of compositional steps (e.g. 10). The band edge at the interface now consists of 10 small heterointerface spikes with a band offset of 57meV (n-type) or 17meV (p-type) which can pass a significant thermal current and have thin depletion regions for low tunnel resistance.

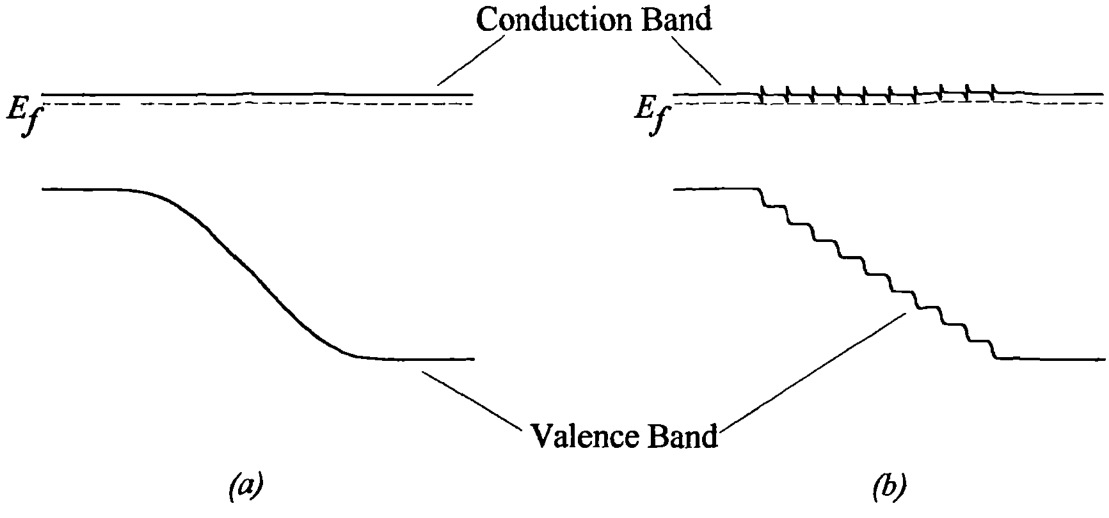

Fig. 5.15. (a) Continual grading of the AlAs / GaAs heterointerface and its effect on the band edge, (b) approximation to continual grading by stepped interface.

In an MOCVD growth reactor it is usual to set up channels in the gas flow equipment which are optimised for the growth of a particular alloy composition, GaAs or AlAs for example[7]. By opening both of these channels simultaneously an intermediate $Al_xGa_{1-x}As$ compound may be grown, x will depend on the relative growth rates of the binaries. In the absence of more channels the only way to produce a finer staircase or continual grading is to adjust the individual channel flow conditions during growth. Growth rates may be unpredictable for reset conditions giving rise to shifts in the reflector centre wavelengths. Shifts such as this can dramatically reduce the cavity finesse and prevent the possibility of lasing (see chapter 2). This problem may be overcome by in-situ optical monitoring of the stack dimensions during growth with feedback to adjust the metal-organic gas flows. The installation of the necessary equipment was prohibitive for use in this work but has been used successfully by others[8].

A similar situation precludes the inclusion of continual grades in MBE grown structures. The elemental sources Al, Ga, As, and In are contained within effusion cells. The temperature of each cell controls the flux of atoms from the cell. Motorised shutters provide on-off control of atoms from each cell. With Al, Ga and As shutters open an intermediate $Al_xGa_{1-x}As$ compound is grown, the composition depending on the relative group III fluxes and hence on the cell temperatures. Ramping of the cell temperatures can give a continuous grade but the thermal mass of the cell is quite large and does not allow accurate control of the growth. A multilevel staircase as in fig. 5.15b may be produced by interrupting the growth to allow resetting of the cell temperatures for each composition. Due to the complexity of the VCSEL structure this is not an ideal solution: a four level staircase structure has been used by Lee *et al.*[9]

One advantage of MBE as is a result of the slow growth rate (≈1µm.hour^{-1}) and accurate cell shutter control; these factors allow monolayer growth control. A short period superlattice incorporating just two alloy compositions may be used to give an effective grading of the interface from the close coupling of wells in the superlattice. Fig. 5.16a shows a superlattice used in several VCSEL designs[10,11]. Fig. 5.16b&c show the operation of the cell shutters during the growth of the superlattice.

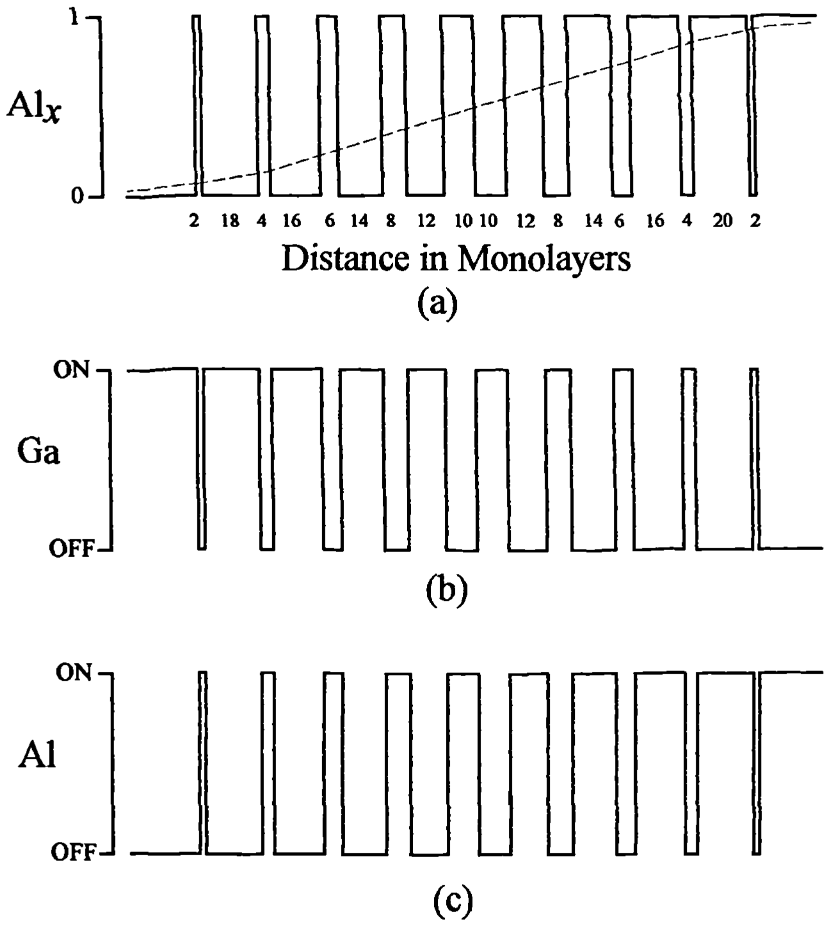

Fig. 5.16. (a) Short period superlattice to produce effective grading of AlAs / GaAs interface, the dotted line illustrates the position of the superlattice mini-band edge. (b) operation of Ga effusion cell shutter during growth of the superlattice. (c) corresponding Al cell shutter operation.

An alternative superlattice design developed during this work[12] is given in fig. 5.17. This superlattice utilises the $Al_{0.5}Ga_{0.5}As$ compound grown when both group III shutters are open. The wells of this superlattice are shallower so coupling between them will be stronger. This will reduce the tunnelling resistance of the interface. Note carefully the cell shutter operations. Compared with the design of fig. 5.15 many fewer shutter operations are required as only one element is switched at any one time. This will reduce the wear on the shutters and extend their limited life. Reflectors incorporating this superlattice were grown, these are discussed in section 5.3.4.

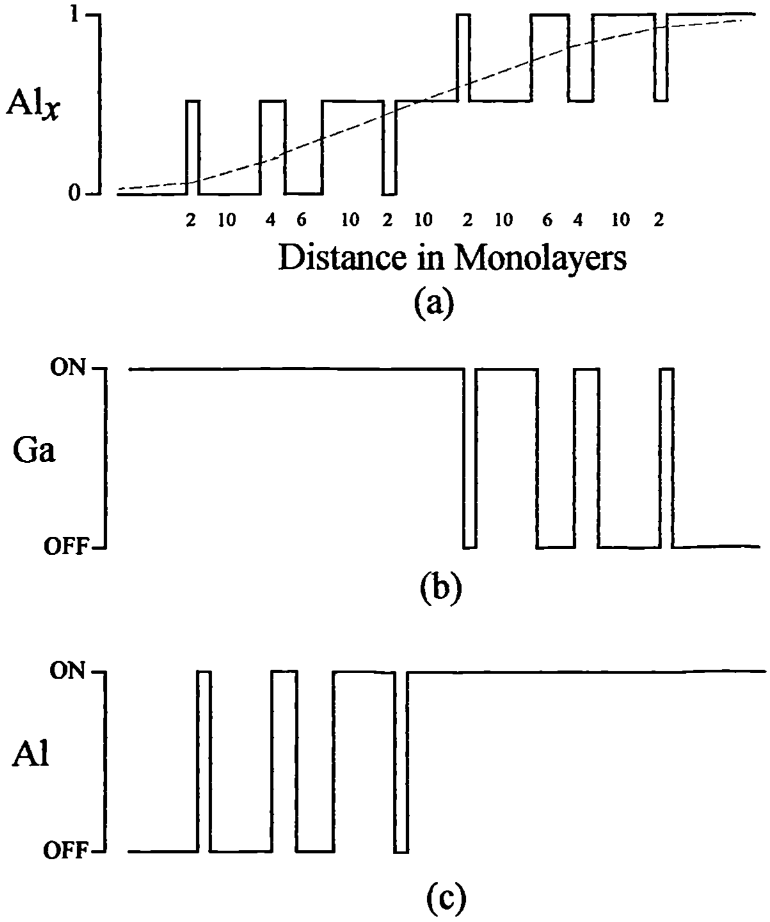

Fig. 5.17. (a) Improved short period superlattice to produce effective grading of AlAs / GaAs interface, the dotted line illustrates the position of the superlattice mini-band edge. (b) operation of Ga effusion cell shutter during growth of the superlattice. (c) corresponding Al cell shutter operation.

5.3.3. Modulation doping

The addition of large dopant concentrations to GaAs has a significant effect on the optical absorption coefficient at energies below the bandgap. In very pure GaAs at 1.0μm wavelength, the absorption coefficient is less than $0.3.cm^{-1}$. For impurity concentrations below $1\times10^{19}.cm^{-3}$, which covers the range of interest of this thesis, free carrier absorption is insignificant at this wavelength. Absorption arises from optically induced band to band transitions involving band tail states. The absorption is determined experimentally in references 198 and 225 in the Blakemore review[13]. This data is summarised in fig. 5.18.

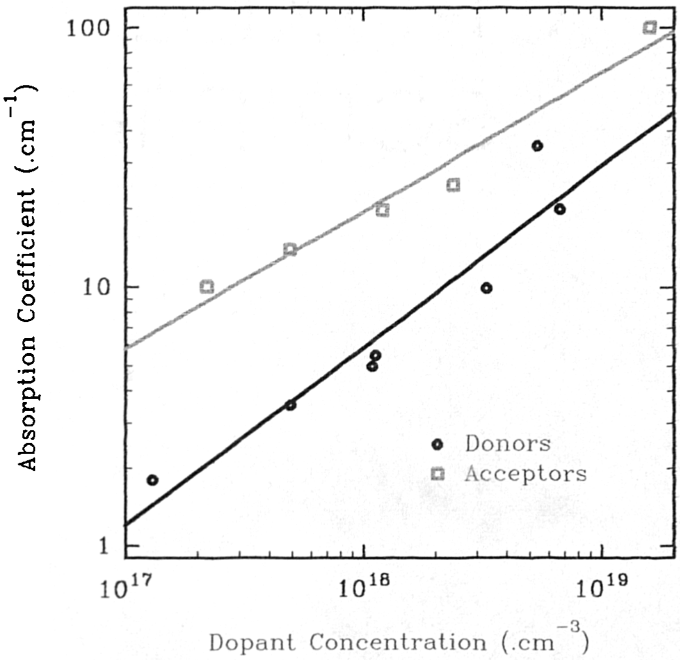

Fig. 5.18. Optical absorption at 1.0µm in doped GaAs at 300K as a function of donor and acceptor concentration, data from Blakemore[13].

As described in section 2.2.6 absorption coefficients in excess of 10.cm^{-1} begin to significantly reduce the optical finesse of the VCSEL cavity. A dopant impurity concentration of 10^{18}.cm^{-3} produces absorption of this order. To reduce the overall absorption in a Bragg reflector we can reduce the doping in parts of the stack away from the interfaces. The depletion region for an AlAs / GaAs interface doped to a concentration of 2.0×10^{18}.cm^{-3} extends 100Å at p-type and 180Å at n-type interfaces. High dopant concentrations outside these regions have little effect on the transport across the interfaces and can be reduced by an order of magnitude or more with little effect on the total stack resistance[11,14]. Calculations in section 2.2.6 show the improvement to the cavity finesse when the dopant is confined to a 200Å layer. Forward biased heterointerfaces in the stack have low resistance even if the depletion width is large, thus it is possible to reduce the dopant in these regions also. Fig. 5.19a illustrates the doping profile required in both stepped and superlattice graded reflectors. Note that the superlattice need only be included at the reverse biased interfaces. Fig. 5.19b shows the same doping schedule applied to a staircase type reflector.

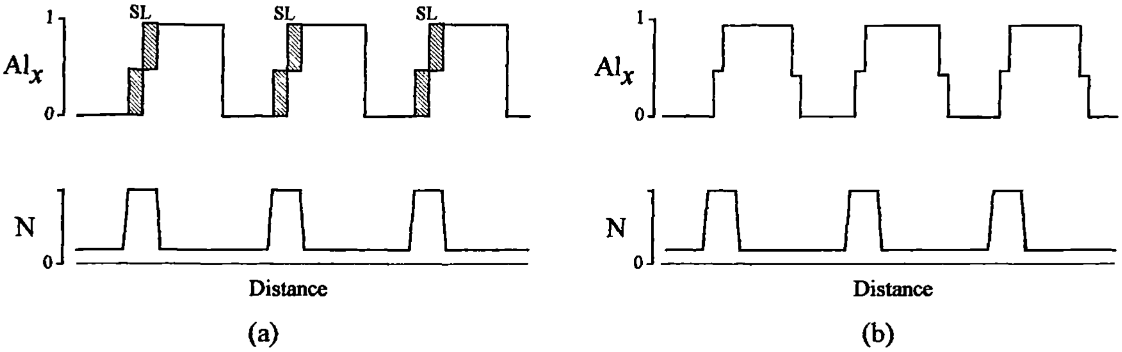

(a) (b)

Fig. 5.19. Modulation doping of Bragg reflectors. The doping concentration N is kept low to minimise optical absorption except in the vicinity of reverse biased heterointerfaces where it is large to aid tunnelling. In this figure carrier flow is from left to right, current flow depends on carrier polarity. SL denotes superlattice grading region.

5.3.4. P-type MBE grown reflectors

Two p-type test reflectors were grown by MBE using superlattice grading of the upper interfaces and modulation doping as shown in figs. 5.17 and 5.19. The structures were grown on a p-type buffer layer on an n-type substrate at a temperature of 600°C. Mesa devices were fabricated for resistance measurements as for the MOCVD mirrors in section 5.3.1 except in this case the lower contact is formed above the p buffer layer as shown in fig. 5.20. *I-V* measurements were made as before using 0.5μs pulses. Table 5.4. summarises the details of the two structures and the voltage drop required for a 50μm diameter device to pass 20mA.

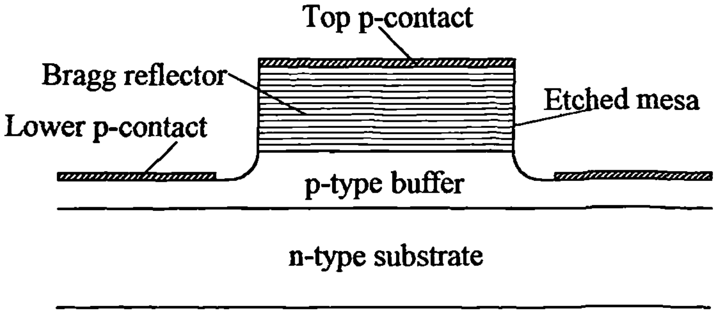

Fig. 5.20. Etched mesa device for resistance measurement of p-type Bragg reflector grown on n-type substrate.

	RMB607	**RMB637**
High N_a	$5\times10^{18}.cm^{-3}$	$1\times10^{19}.cm^{-3}$
Low N_a	$5\times10^{17}.cm^{-3}$	$1\times10^{18}.cm^{-3}$
No. Pairs	15	15
Voltage (V)	4.05	2.25
Voltage / pair	0.27	0.15

Table 5.4. Summary of data for p-type superlattice Bragg reflectors grown by MBE, voltages are for pulsed measurements at 20mA on 50μm diameter mesas. The high and low acceptor concentrations refer respectively to the values used in the region of the superlattice and the remainder of the structure.

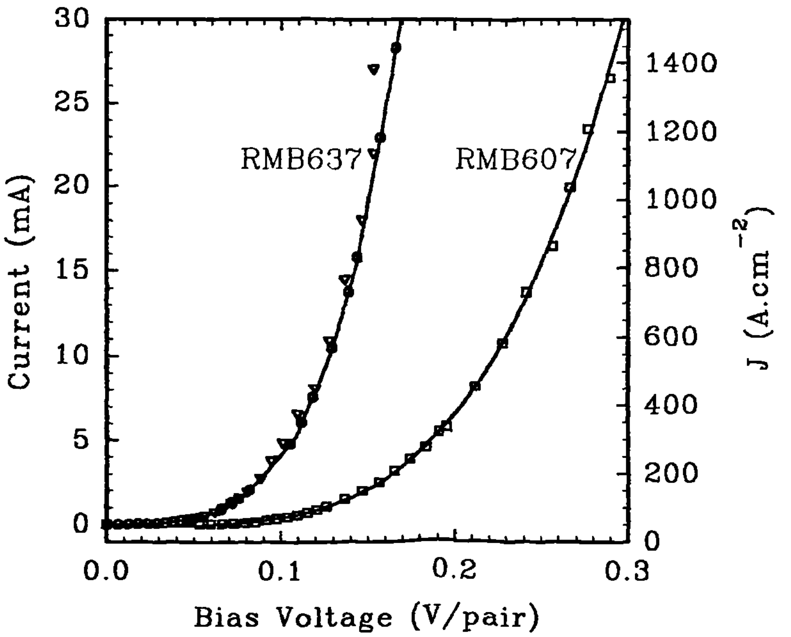

Fig. 5.21. I-V measurements on MBE grown p-type Bragg reflectors incorporating superlattice grading regions at the reverse biased heterointerfaces (O, □ pulsed, ▽ d.c.). RMB637 is doped to twice the concentration of RMB607, see text.

Full *I-V* data for these 50μm diameter mesa etched reflectors are presented in Fig. 5.21. At a current of 20 mA the voltage per pair is reduced by a factor of nearly 2 from 0.27 to 0.15V by a doubling of the acceptor concentration. The decrease is even more dramatic when lower currents are compared. This decrease indicates that tunnelling is the dominant transport mechanism in these reflectors.

Measurements presented in fig. 5.21 were for a reverse bias across the graded interfaces and a forward bias across the abrupt ones. It is interesting to note that with the bias polarity reversed these reflectors pass a current of just 0.25mA at a voltage of

10V. This is because the lightly doped and un-graded interfaces are now reverse biased and present a large barrier to carrier flow. This is evidence in support of the tunnelling model and the methodology of the design improvements made to the basic Bragg reflector.

Acceptor concentrations much in excess of $1\times10^{19}.\text{cm}^{-3}$ are not feasible in these reflectors. It should be noted that the voltage drop of RMB637 is not much lower than that of QT255 which is the p-type MOCVD grown reflector with intermediate interface layers. The acceptor concentration of QT255 is approximately $1\times10^{18}.\text{cm}^{-3}$ an order of magnitude lower than in RMB637. The reason for this is suggested in a paper by Kopf[4] *et al.* The very large resistance noted in reflector stacks grown by MBE results from the choice of acceptor dopant. Be is used almost universally as it evaporates cleanly producing a directional molecular beam, so is ideal for putting in an effusion cell. Unfortunately during growth at a temperature of 600°C it diffuses rapidly in AlAs towards the growing crystal surface. At an AlAs / GaAs interface the accumulated Be will incorporate into the GaAs increasing the doping level in the vicinity of the junction but in the side of the AlAs the acceptor concentration will be very low, it is in this side where the depletion region forms. By compositional profiling of MBE grown reflector stacks Kopf *et al.*[4] claim that the solubility limit of Be in AlAs is $5\times10^{17}.\text{cm}^{-3}$ even when the doping level is as high as $5\times10^{19}.\text{cm}^{-3}$. Data is also presented by Kopf[4] showing that no redistribution of Si (at $3\times10^{18}.\text{cm}^{-3}$) or C (at $2\times10^{19}.\text{cm}^{-3}$) dopants were detected in reflector stacks. Electrochemical profiling of the structures reported in this thesis support this view, whilst the resolution of the measurement cannot give very detailed depth information, it can be seen that the doping concentration in the stack falls to $2\times10^{17}.\text{cm}^{-3}$ in places.

An obvious solution to this problem would be to use C as a dopant, this requires a more sophisticated source than Be but is a planned improvement for the Sheffield III-V growth facility. MOCVD grown structures utilising C and Zn acceptor doping support the use of alternative dopants, active incorporation levels up to $3\times 10^{18}.\text{cm}^{-3}$ (value from Electrochemical profiling) can readily be achieved.

Künzel *et al.*[15] suggest that reducing the MBE growth temperature from the typical value of 600°C to 350→450°C prevents diffusion of Be and allows acceptor concentrations in excess of $10^{19}.\text{cm}^{-3}$ to be obtained. Our preliminary experiments on simple type A reflectors indicate that this is not the case or that the dopant does not become active. Minimum resistance is obtained for p-type reflectors grown at 600 °C, the highest growth temperature used.

5.3.5. N-type MBE grown reflectors

The n-type reflector for the MBE grown laser was of the simpler design incorporating single 200Å thick intermediate layers of $Al_{0.5}Ga_{0.5}As$ at the interfaces similar to the MOCVD grown reflectors described in section 5.3.1. The simpler design was chosen as the resistance of an n-reflector will be less than that of a similar p-reflector due to the full incorporation of Si dopant compared with Be as described above. RMB638 is a test reflector of this design. It consists of 23 pairs grown by MBE on an n-type substrate. The structure was doped uniformly with Si to a concentration of $1\times10^{18}.cm^{-3}$. Modulation doping was not deemed necessary as the absorption caused by donors is much less than that by acceptors (see fig. 5.18). Mesa devices were fabricated from this structure as described in section 5.3.1. Pulsed *I-V* measurements were performed on them. Fig. 5.22 gives the results of these measurements for a 50μm diameter mesa. For a current of 20mA the voltage drop per pair in the reflector is 0.4V which is 9.2V for the complete reflector. This is high compared with the similar MOCVD grown structure. This could be partly due to the different intermediate layer used. It should be possible to reduce the resistance to a similar level by increasing the dopant concentration by a factor of 2→5.

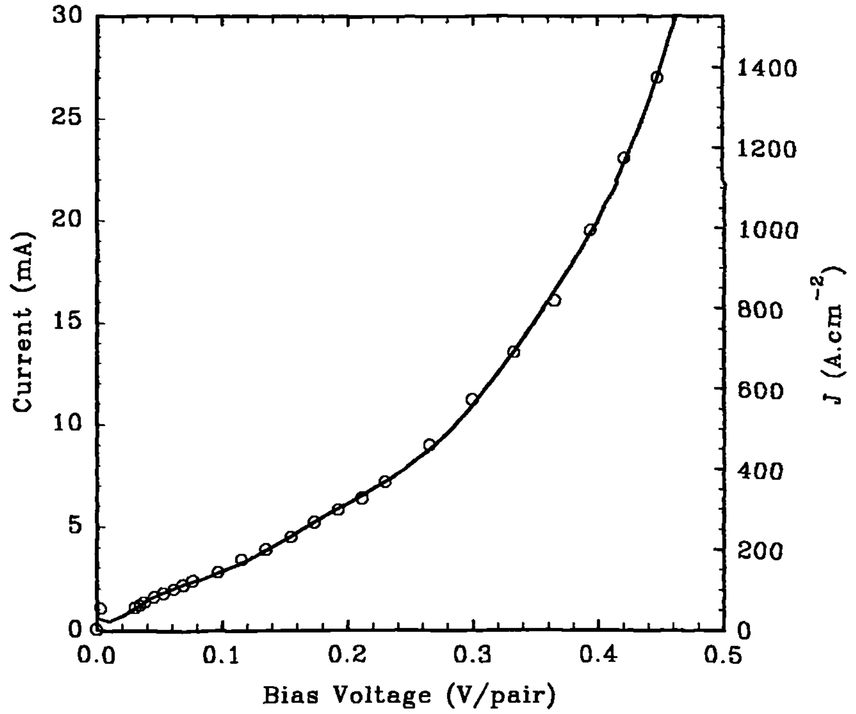

Fig. 5.22. Pulsed I-V measurements on RMB638 n-type Bragg reflector by MBE incorporating single $Al_{0.5}Ga_{0.5}As$ intermediate interface layers.

5.3.6. Full VCSEL structure grown by MBE

For the full VCSEL structure grown by MBE (RMB627) the reflector designs of RMB607 (15 pairs p-type superlattice graded) and RMB638 (23 pairs n-type with single intermediate interfacial layers) were grown on either side of an undoped cavity region containing $In_xGa_{1-x}As$ active quantum wells. An earlier design (RMB369) essentially the same but uses only abrupt AlAs / GaAs interfaces with no intermediate layers or grading region in the reflectors. Fig. 5.23 shows the results of *I-V* measurements conducted with 0.5μs pulses on 50μm diameter reactive ion etched mesas. Polaron profiling indicates that the minimum active doping concentrations in the n and p reflectors are below 2×10^{18}.cm^{-3} and 2×10^{17}.cm^{-3} respectively

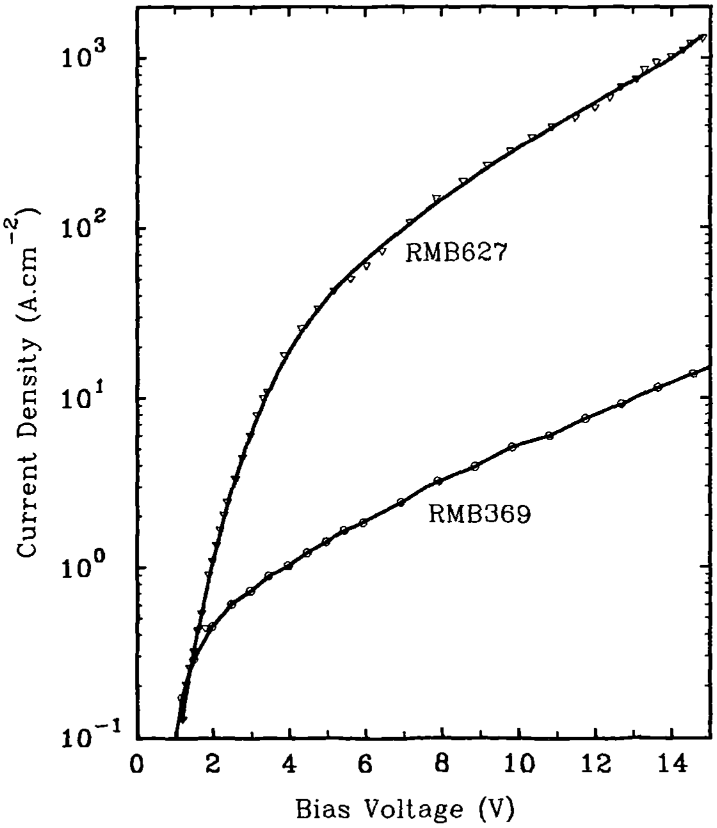

Fig. 5.23. Pulsed I-V measurements on MBE grown VCSEL structures. RMB369 incorporates simple abrupt AlAs / GaAs hetero interfaces, whilst RMB627 uses superlattice graded and stepped interfaces.

The *I-V* relation of RMB627 can be predicted from the test structures RMB607 and RMB638 if an allowance of 1V is made for the p-i-n diode drop. The difference between the resistance of the two lasers is dramatic. RMB627 lases with a threshold current as low as 366A.cm^{-2} at a bias of 7.8V. At the same current density the simpler structure RMB369 is under a bias greater than 27V and actually fails catastrophically within a few seconds, even under pulsed conditions and so will not lase. At a bias of 10V RMB627 passes 50 times the current of RMB369 illustrating the clear advantage of the improved design.

5.3.7. Improved MOCVD reflectors

The p and n-type Bragg reflectors described in section 5.3.1 were re-grown with the improvements of modulation doping and reduced oxygen contamination. The two structures are both of the type B design incorporating 200Å $Al_{0.3}Ga_{0.7}As$ intermediate layers and were grown at 700°C. To reduce the concentration of oxygen traps in the AlGaAs material the TMA source was fractionally distilled to remove alkoxyl contaminants and dried using a trimetal melt[16].

The n-type reflector, QT408, comprises 23 pairs uniformly doped to a level of $1.6\times10^{18}.cm^{-3}$ with Si, as determined by electrochemical profiling, and was grown on an n-type substrate. The p-type reflector, QT409, consists of 15 pairs grown on a p-type substrate. The Zn doping was modulated to reduce the resistance without introducing unnecessary dopant: the details of this are described more fully in section 7.2. The interfacial layers contain a Zn concentration of $2.0\times10^{18}.cm^{-3}$, the concentration being reduced away from the interface to $5.0\times10^{17}.cm^{-3}$ in the GaAs and to zero in the AlAs. Note that C is incorporated to a level of $2.0\times10^{18}.cm^{-3}$ in the AlAs from the decomposition of TMA so no Zn doping is required in this layer. Electrochemical profiling indicates a near uniform acceptor concentration of ~$2.0\times 10^{18}.cm^{-3}$ throughout the stack; although this cannot reveal very fine detail.

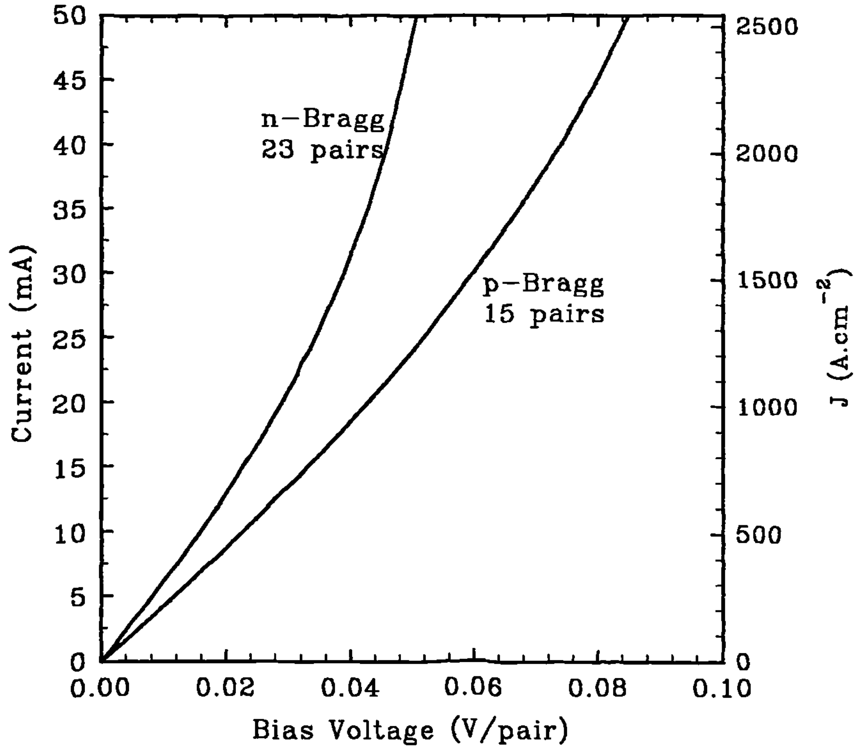

Fig. 5.24. D.C. I-V from QT408 and QT409 p and n-type reflectors grown using low oxygen containing TMA and incorporating modulation doped interfaces.

As in preceding sections wet etched mesas were fabricated and I-V measurements performed on 50μm diameter structures. Fig. 5.24 shows the results of d.c. I-V measurements. Note that due to the very low resistance of these reflectors there is no noticeable difference between the d.c. and pulsed measurements (not shown) as there is little heating. It is apparent that much less bias is required for these structures as compared to those of section 5.3.1. This difference is thought to be largely due to the difference in oxygen content which in the previous structures tends to reduce the effective dopant concentration.

Layer	Type	Pairs	Voltage (V)	Voltage / Pair
QT408	n	23	0.67	0.029
QT409	p	15	0.66	0.044

Table 5.5. Details of improved MOCVD Bragg stacks grown using low oxygen aluminium source. Voltage drops are measured on 50μm diameter mesas at 20mA d.c., pulsed measurements are very similar due to low ohmic heating effect.

Table 5.5 summarizes the results for currents of 20mA. At this current the improvements obtained are reductions in bias of: for the n-type reflector by a factor of 3.4 from 0.10 to 0.029V/pair and for the p-type reflector by a factor of 4.5 from 0.20 to 0.044V/pair. It is likely that, at these voltages, the contact resistance (not measured) is significant. These structures are clearly much improved by the reduction in oxygen contamination and in the case of the p-reflector also from the increased doping in the region of the intermediate $Al_{0.3}Ga_{0.7}As$ layer (although this cannot be seen in the electrochemical profile). These improved reflector structures were later used to produce the full VCSEL structure QT421, the major topic of chapter 7.

5.4. Optical Considerations

Before producing a laser, it is sensible to consider the effect of the inclusion of interfacial layers on the phase and amplitude of the reflectivity of a Bragg stack. The addition of regions with different refractive index will complicate the reflection of electromagnetic fields at the interfaces and it is important to asses this to ensure that the laser threshold condition may still be met (equation (1.3)). The reflectivity spectrum of a Bragg reflector is similar to a Fourier transform of the variation of the refractive index with optical distance (see chapter 2). Therefore if the thickness of an interfacial layer or grading region is small compared to the wavelength of light in the material (2850Å for 1.0μm radiation in GaAs) the effect on the reflectance will be small.

Using the RCAD simulation package[17] the reflectivity of the various modified AlAs / GaAs interfaces is calculated. Fig. 5.25 shows these interfaces and the reflectivities and the phase of the reflection compared to the x=0 plane at 1.0μm wavelength. As might be expected the reflection is reduced by up to 16% and the phase delayed by up to 5.77radians (33°) by the disruption of the interfaces. The reflection coefficient is effectively a coupling constant κ between forward and reverse waves in the stack, an reduction of 16% in this value implies that the stack should be increased in length by 16% to retain the same reflectivity.

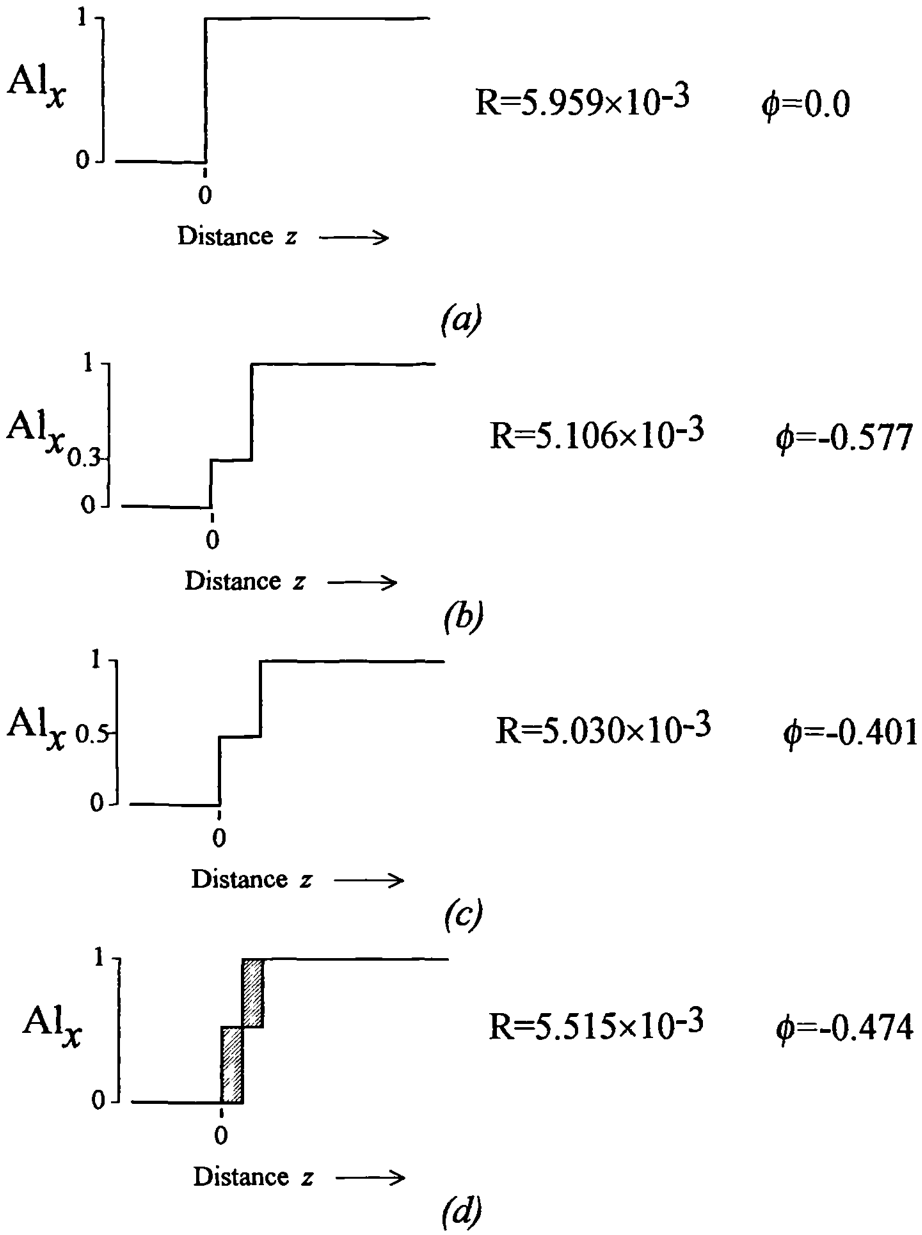

Fig. 5.25. Reflectivity and phase for modified AlAs / GaAs interface profiles.

For optimum stack reflectivity the stack dimensions must be adjusted so that the reflectivities of the modified interfaces add in phase. Again using RCAD[17] the phase angles are adjusted to zero at the x=0 plane by adjusting the dimensions. Fig. 5.26 shows the optimised dimensions for the four stack designs previously described.

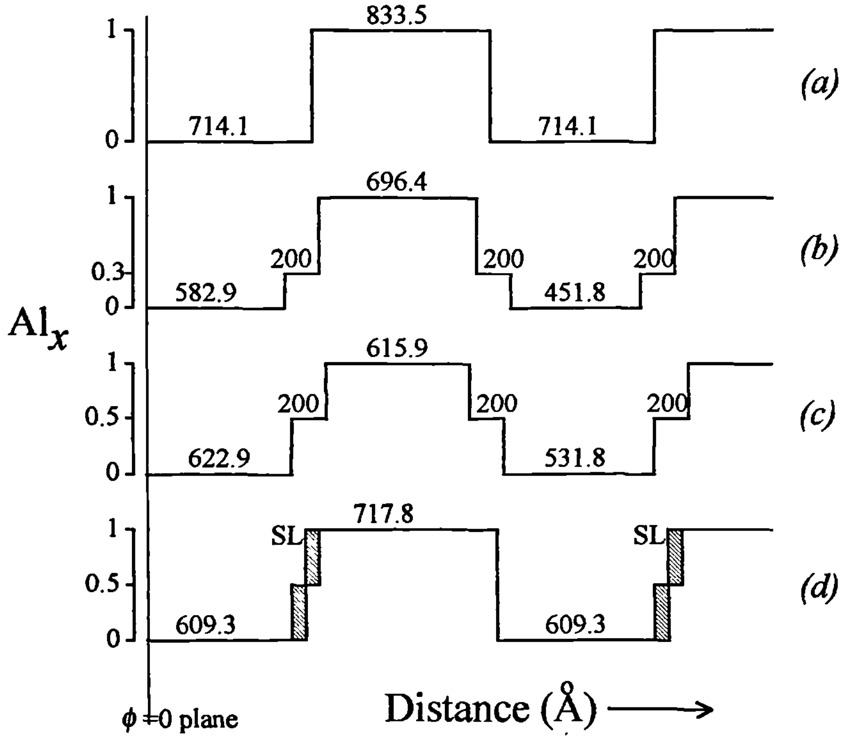

Fig. 5.26. Optimised stack dimensions for modified reflectors for 1.0μm operation; (a) basic quarter wave reflector (b) Stack with 30% Al intermediate layers (c) Stack with 50% Al intermediate layers (d) Stack with superlattice grading of fig. 5.17.

The reflectivity spectrum of a 24½ pair AlAs / GaAs reflector as in fig. 5.26a is shown in fig. 5.27. Also shown is the spectrum of the modified stack of fig. 5.26c including $Al_{0.5}As_{0.5}As$ intermediate layers. It is apparent that the spectrum of the reflector with stepped interfaces is slightly narrower as a result of the altered phase of internal stack reflections. On a linear scale the peak reflectivity seems not to change, table 5.6 lists the peak reflectivities and the reflection losses of 24½ and 15½ pair reflectors of the four designs in fig. 5.26.

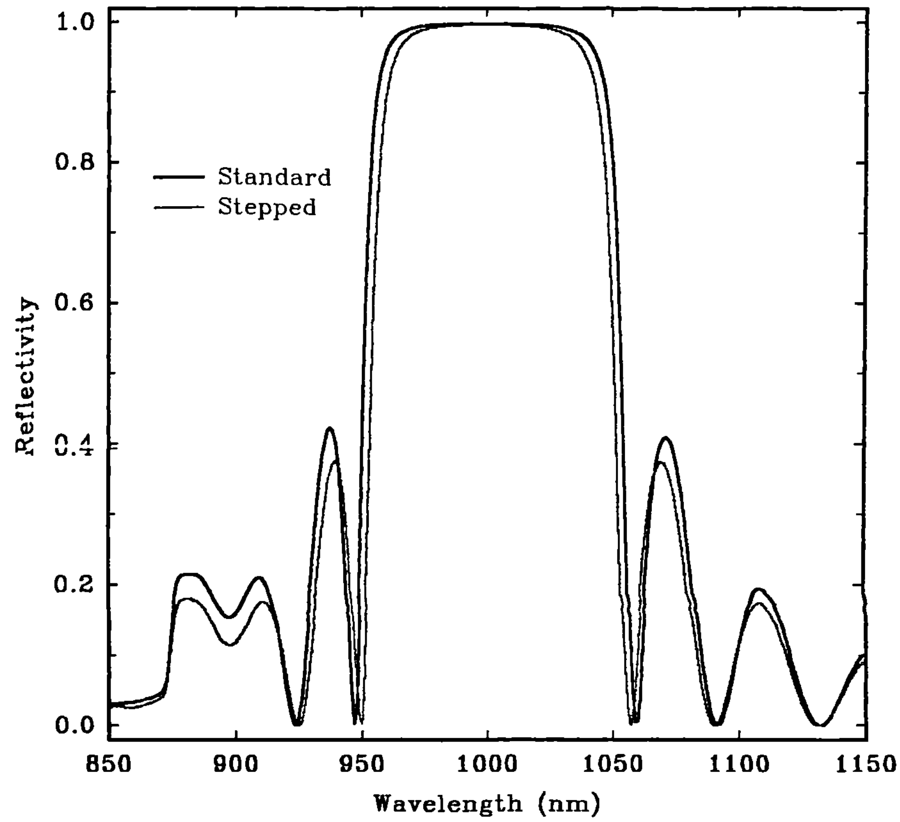

Fig.5.27. Reflectivity spectra of 24½ pair AlAs /GaAs Bragg reflectors centred at 1.0μm with abrupt interfaces and with $Al_{0.5}Ga_{0.5}As$ intermediate layers

Intermediate Layer	24½ pairs		15½ pairs	
	R	1-R	R	1-R
None	0.9980	1.962×10^{-3}	0.9792	2.078×10^{-2}
50% Al	0.9965	3.512×10^{-3}	0.9684	3.163×10^{-2}
30% Al	0.9967	3.340×10^{-3}	0.9695	3.052×10^{-2}
Superlattice	0.9977	2.284×10^{-3}	0.9768	2.323×10^{-2}

Table 5.6. Peak reflectivities and losses of Bragg reflectors of differing designs.

It is seen from this table that the peak reflectivities are indeed little changed, ≤ 0.15% for 24½ pair reflector and ≤1.08% for the 15½ pair reflector. The losses are increased by a factor of 1.78 in the worst case. This is not a catastrophic reduction in performance and can be regained by the addition of a few extra reflector pairs.

References:

[1] S.Adachi, *GaAs, AlAs & $Al_xGa_{1-x}As$: Material parameters for use in research & device applications*, J. Appl. Phys., **58**, 3, pR1-R29, 1985.

[2] S.M.Sze, *Semiconductor devices, physics and technology*, Wiley, New York, 1985.

[3] M.Jaros, *Physics and applications of semiconductor microstructures*, Oxford University Press, Oxford, 1989.

[4] R.F.Kopf, E.F.Schubert, S.W.Downey & A.B.Emerson, *N- and P-type dopant profiles in distributed Bragg reflectors and their effect on resistance*, Appl. Phys. Lett., **61**, 14, pp1820-1822, 1992.

[5] K.Tai, L.Yang, Y.H.Wang, J.D.Wynn & A.Y.Cho, *Drastic reduction of series resistance in doped semiconductor distributed Bragg reflectors for surface-emitting lasers*, Appl. Phys. Lett., **56**, 25, pp2496-2498, 1990.

[6] S.A.Chalmers, K.L.Lear & K.P.Killeen, *Low resistance wavelength-reproducible p-type (Al,Ga)As distributed Bragg reflectors grown by molecular beam epitaxy*, Appl. Phys. Lett., **62**, 14, pp1585-1587, 1993.

[7] M.R.Leys, *Metal organic vapour phase epitaxy for the growth of semiconductor structures and strained layer lasers*, chapter in *Low dimensional structures in semiconductors*, A.R.Peaker & H.G.Grimmeiss Eds., NATO ASI Series B: Physics, **281**, Plenum, 1991.

[8] K.Bacher, B.Pezeshki, S.M.Lord & J.S.Harris Jr., *Molecular beam epitaxial growth of vertical cavity optical devices with in situ corrections*, Appl. Phys. Lett., **61**, 12, pp2387-1389, 1992.

[9] Y.H.Lee, B.Tell, K.Brown-Goebeler, J.L.Jewell & J.V.Hove, *Top-surface-emitting GaAs four-quantum well lasers emitting at 0.85μm*, Electron. Lett., **26**, 11, pp710-711, 1990.

[10] R.S.Geels, S.W.Corzine, J.W.Scott, D.B.Young & L.A.Coldren, *Low threshold planarized vertical-cavity surface-emitting lasers*, IEEE Photon. Technol. Lett., **2**, 4, pp234-236, 1990.

[11] K.Kurihara, T.Numai, I.Ogura, A.Yasuda, M.Sugimoto & K.Kasahara, *Reduction in the series resistance of the distributed Bragg reflector in vertical cavities using quasi-graded superlattices at the heterointerfaces*, J. Appl. Phys., **73**, 1, pp21-27, 1993.

---

[12] T.E.Sale, J.Woodhead, R.Grey & P.N.Robson, *Wide operating wavelength range and low threshold current* $In_{0.24}Ga_{0.76}As$ */ GaAs vertical-cavity surface-emitting lasers*, IEEE Photon. Technol. Lett., **4**, 11, pp1192-1194, 1992.

[13] J.S.Blakemore, *Semiconducting and other major properties of gallium arsenide*, J. Appl. Phys., **53**, 10, ppR123-R181, 1982.

[14] M.Sugimoto, H.Kosaka, K.Kurihara, I.Ogura, T.Numai & K.Kasahara, *Very low threshold current density in vertical-cavity surface-emitting laser diodes with periodically doped distributed Bragg reflectors*, Electron. Lett., **28**, 4, pp385-387, 1992.

[15] H.Künzel, J.Bötcher, S.Gramlich, P.Harde & A.Paraskevopoulos, *Effect of growth temperature on beryllium doping in isotope GaAs / AlAs heterojunctions*, 7'th Euro. workshop on MBE, Palazzo delle Feste, Italy, 1993.

[16] J.S.Roberts, T.E.Sale, C.C.Button, J.P.R.David & A.Jennings, *High performance microcavity resonator devices grown by atmospheric pressure MOVPE*, J. Crystal Growth, **124**, pp792-800, 1992.

[17] Using the mathematical models developed in chapter 2 a CAD package was developed to model reflection spectra and similar parameters for complex multilayer structures in the AlGaAs system. This has been used extensively to design the structures reported in this thesis and to determine growth errors by fitting to measured spectra.

6. Results of Experiments on MBE Grown Devices.

This chapter is concerned with the experimental measurements made on the MBE grown VCSEL structure RMB627. It presents I-V, L-I and other measurements made under pulsed and c.w. conditions on devices defined by reactive ion etching of mesas and by proton implant.

6.1. Structure.

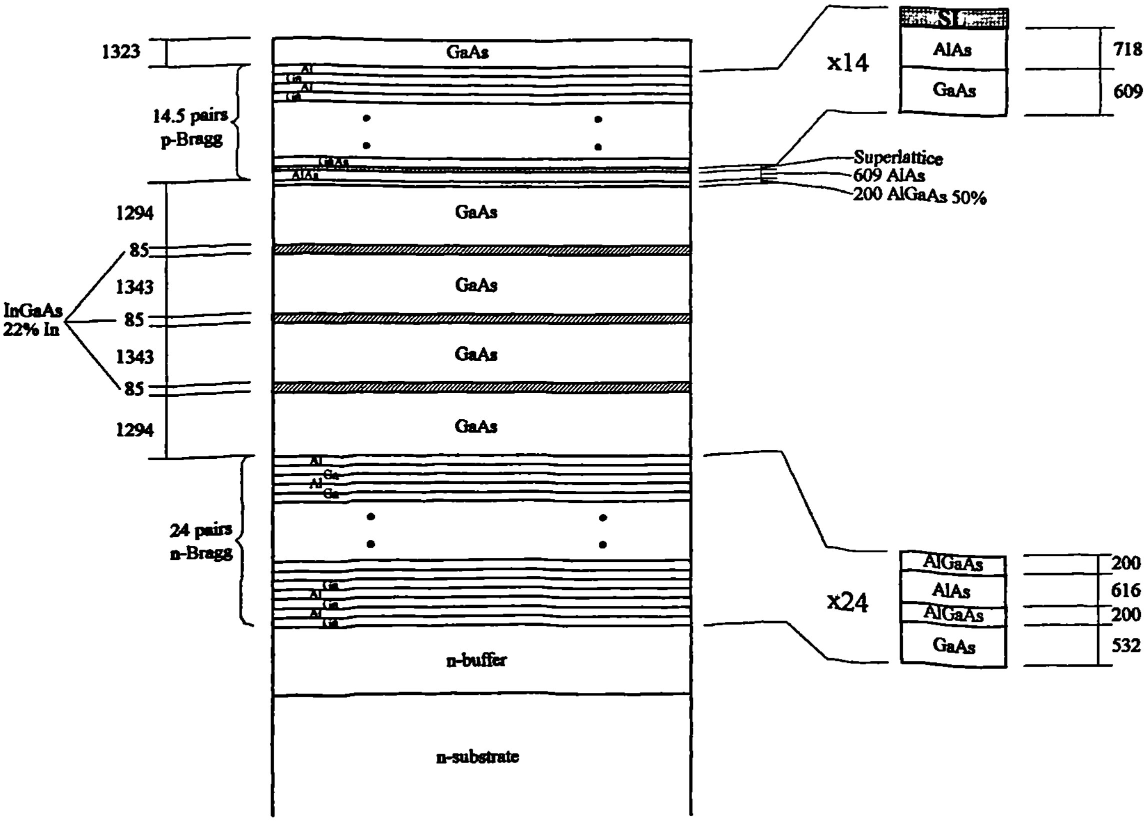

Fig. 6.1. Full layer structure of RMB627 MBE grown VCSEL.

Fig. 6.1 shows the full layer structure of RMB627 [1]. The structure incorporates many of the points made in the previous chapters and the following sentences describe the nominal intended design prior to growth. The structure is intended to operate at a wavelength λ=1000nm. The undoped cavity region comprises three strained 85Å $In_{0.22}Ga_{0.78}As$ quantum wells spaced by $\lambda/2$ in a 2λ long GaAs cavity to coincide with the antinodes of the optical field in the cavity; the wells are predicted to have an e_1hh_1 transition at 1011nm at room temperature. The cavity region is bound by the upper and lower dielectric cavity reflectors grown to the following designs.

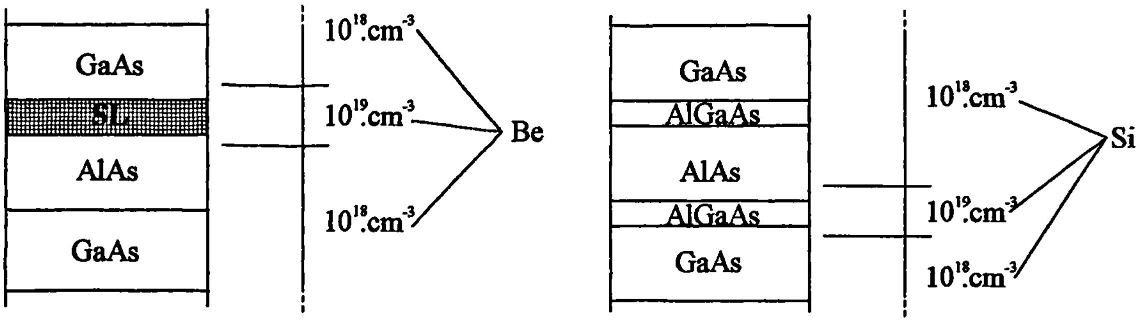

(a) *(b)*

Fig. 6.2 Doping detail of reflector stacks showing increased dopant concentration in the region of the reverse biased mirror interfaces for the reduction of resistance.

The reflector stacks are similar to those used in the test structures RMB607 and RMB638 described in section 5.3. The lower reflector consists of a 23½ pair AlAs / GaAs stack with 200Å intermediate Al$_{0.5}$Ga$_{0.5}$As layers for the reduction of interface resistances. It is doped n-type with Si to a nominal concentration of 1×10^{18}.cm^{-3}. The stack dimensions are designed for maximum reflectivity as described in section 5.4.

The upper reflector consists of a 15 pair AlAs / GaAs stack with variable period AlAs / Al$_{0.5}$Ga$_{0.5}$As / AlAs superlattice grading at the upper, reverse biased, heterointerfaces. The stack is doped p-type with Be to a nominal concentration of 5×10^{17}.cm^{-3} with increased doping of 5×10^{18}.cm^{-3} in the vicinity of the graded interfaces. Inclusion of superlattice grading and modulation doping is necessary to achieve an acceptable resistance whilst maintaining efficient optical reflectivity (refer to chapter 5). As in the case of the lower reflector, the dimensions are designed for maximum reflectivity.

The structure was grown on a double polished Si doped GaAs substrate which was rotated during growth. The reflector stacks were grown at a temperature of 600°C, this was reduced to 540°C for the cavity region which was found to provide optimal growth conditions for the strained quantum wells.

6.2. Material Assessment

Before devices were fabricated from the grown wafer, photoluminescence and photoreflectance measurements were made to asses whether the growth had been to the design and also to identify areas of the wafer suitable for making devices.

6.2.1. Photoreflectance

The photoreflectance spectrum was measured at several points across the wafer using a monochromated white light system. Fig. 6.3 shows a typical reflectance spectrum measured from this layer. The high reflectance band of the Bragg reflectors is clearly visible as is the dip in reflectance caused by the cavity mode. Fig. 6.4. shows the spectrum for the ideal structure as calculated by the RCAD program[2]. The measured spectrum is similar to that calculated for the ideal structure and shows the cavity mode centred in the high reflectivity band of the Bragg reflectors.

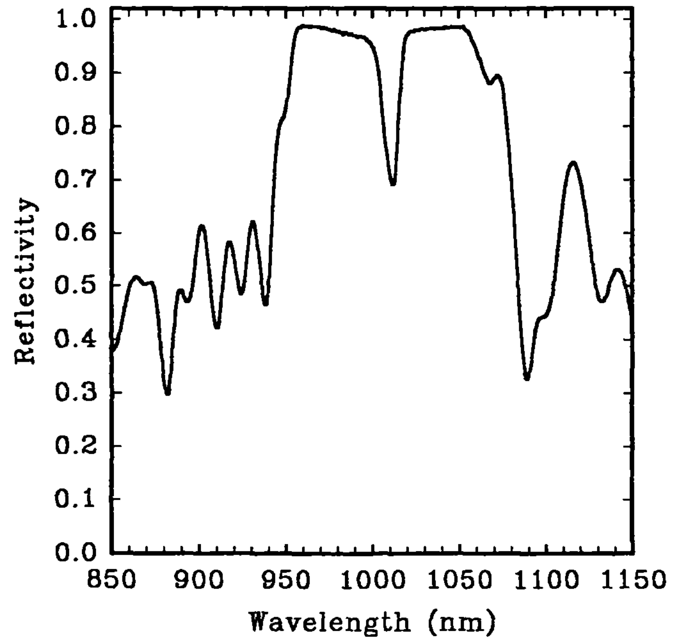

Fig. 6.3. Photoreflectivity spectrum measured at a point on the wafer RMB627.

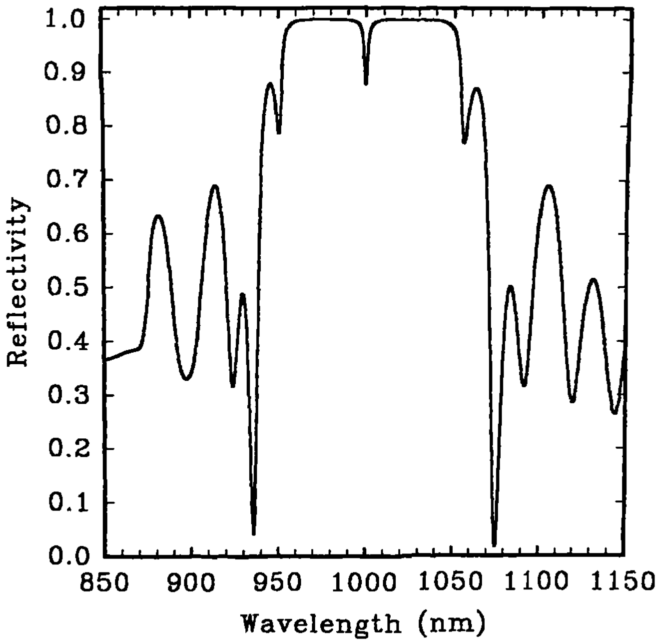

Fig. 6.4. Calculated photoreflectivity spectrum for the VCSEL structure shown in fig. 6.1.

There is a variation in material growth thickness across the wafer as a result of the geometry of the effusion cells used in the VGV80 MBE reactor. The substrate is rotated during growth so the variation is circularly symmetric and has a paraboloid profile. All layer thickness vary in the same proportion across the wafer so that the reflectivity spectrum is found to maintain its shape but shift bodily at different points on the wafer. Fig. 6.5. shows a contour plot of the position of the cavity resonance across the wafer derived from reflectance measurements. The resonant wavelength varies from 940 to 1060nm, with slower variation in the centre of the wafer where the growth is thicker. This constitutes a ±6% thickness variation about the nominal value of 1000nm.

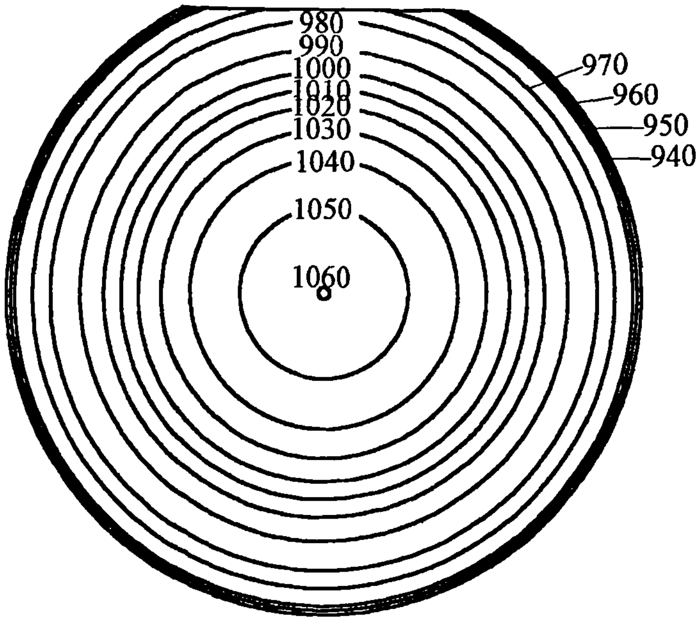

Fig. 6.5. Variation of cavity resonant wavelength in nm across the grown VCSEL wafer RMB627 determined by reflectance measurements.

6.2.2. Photoluminescence

Photoluminescence (PL) measurements can give useful information about the InGaAs quantum wells. Emission from an optically excited well is detected at an energy a few meV below the e_1hh_1 transition energy. Bright narrow linewidth emission indicates good quality wells. For a VCSEL structure, room temperature PL measurements are not feasible due to the presence of the Bragg reflectors. At low temperatures however the absorption of the stacks to the excitation light (514nm Ar$^+$ ion laser) and their reflectivity at the luminescence wavelength are much reduced and good PL measurements may be made.

Fig. 6.6. shows typical PL spectra taken from the layer at a temperature of approximately 15K. Emission is seen at an energy of 1.294-1.299eV with a FWHM linewidth of 7 to 10meV. There is little change across the wafer except right at the edge of the grown area where a dimmer emission at higher energy is detected.

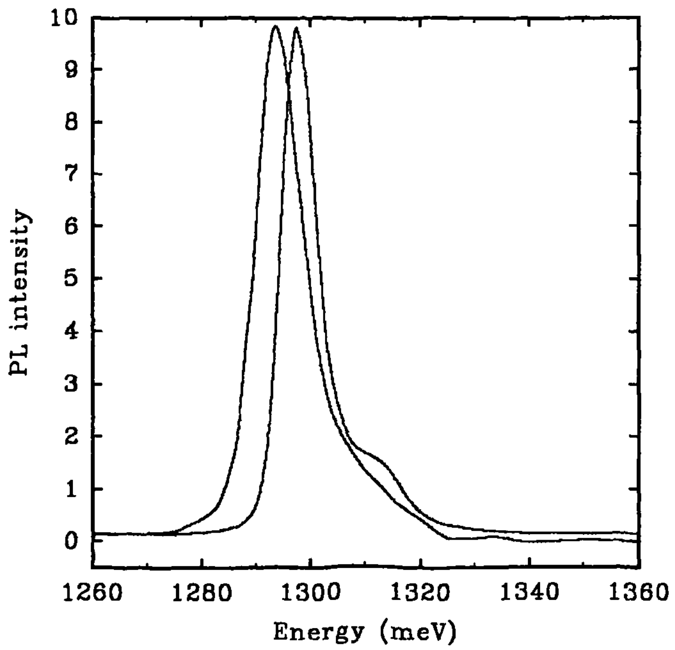

Fig. 6.6 Low temperature (15K) photoluminescence emission from RMB627 VCSEL structure illuminated with argon ion laser. The lower energy peak is from the centre of the wafer where the slightly thicker quantum well causes a reduction in the confined energies as compared to the other peak from a point further towards the wafer edge.

The uniform emission energy and narrow linewidth across the wafer indicates high quality strained quantum wells with few dislocations. All three wells must be essentially the same as only one peak is detected. The high energy emission detected at the wafer edge is a result of a much thinner growth thickness right at the edge. The quantum wells are subject to the same variation in growth thickness as the other layers in the stack. An emission energy of 1.296eV corresponds to a well with an indium fraction of 23.5% assuming an 85Å well (see section 3.2.2). This is slightly greater than the intended fraction of 22.0%. If the ±6% thickness variation is applied to the well, we would expect a variation in emission energy of ±4nm across the wafer. Since no change larger than this is detected we can assume that there is no significant variation in the indium fraction across the wafer. At room temperature the e_1hh_1 transition in these wells should occur at 1024nm [3].

6.2.3. Processing

The assessment measurements above have shown that the growth has been close to the design. The predicted room temperature transition energy of 1024nm lies well within the variation in cavity resonance. Assuming an optical gain bandwidth of 30nm, we might predict that devices fabricated from the annular segment of wafer with resonant wavelengths in the range 994-1024nm would work efficiently. Devices outside of this area may operate but with higher threshold currents.

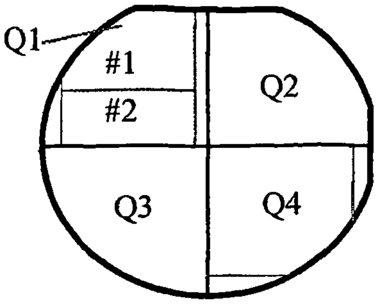

Fig. 6.7. Figure showing material selected for fabrication of devices. Devices on Q1 were defined by etching and polyimide passivation was applied to those on piece #1. Devices on Q4 were defined by proton implant.

Fig. 6.7 shows areas of the wafer selected for processing. Quarters Q1 and Q4 were processed, each quarter exhibiting the full range of variation over the wafer. Devices on Q1 were reactive ion etched in $SiCl_4$ to produce mesas with a nominal height of 3.5μm and those in piece #1 were further processed by passivation with polyimide and large contact pads were applied. Devices on Q4 were defined by a 200keV H^+ implant at a dose of $2\times10^{13}.cm^{-3}$ and isolated on large mesas by reactive ion etching. Full details of the fabrication were given in chapter 4.

6.3. Experimental Method

Current-voltage (I-V) and current-light (L-I) measurements were made on individual devices. In addition output emission spectra were recorded. Contact was made to devices as shown in fig. 6.8. The fabricated sample is fixed down to a part metallized glass slide using conductive paint. The majority of the devices on the chip lie above transparent glass which allows the emission of light. Needle pointed probe tips are brought into contact with the metal on the slide to make the cathode contact and with the top contact of individual device mesas to make the anode contact. The probes allow contact to devices of 20μm diameter and larger to be made directly.

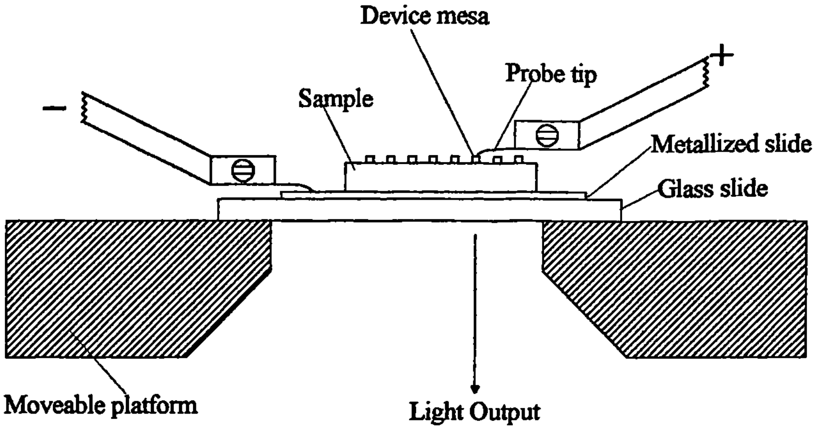

Fig. 6.8. Method by which contact is made to fabricated VCSEL devices.

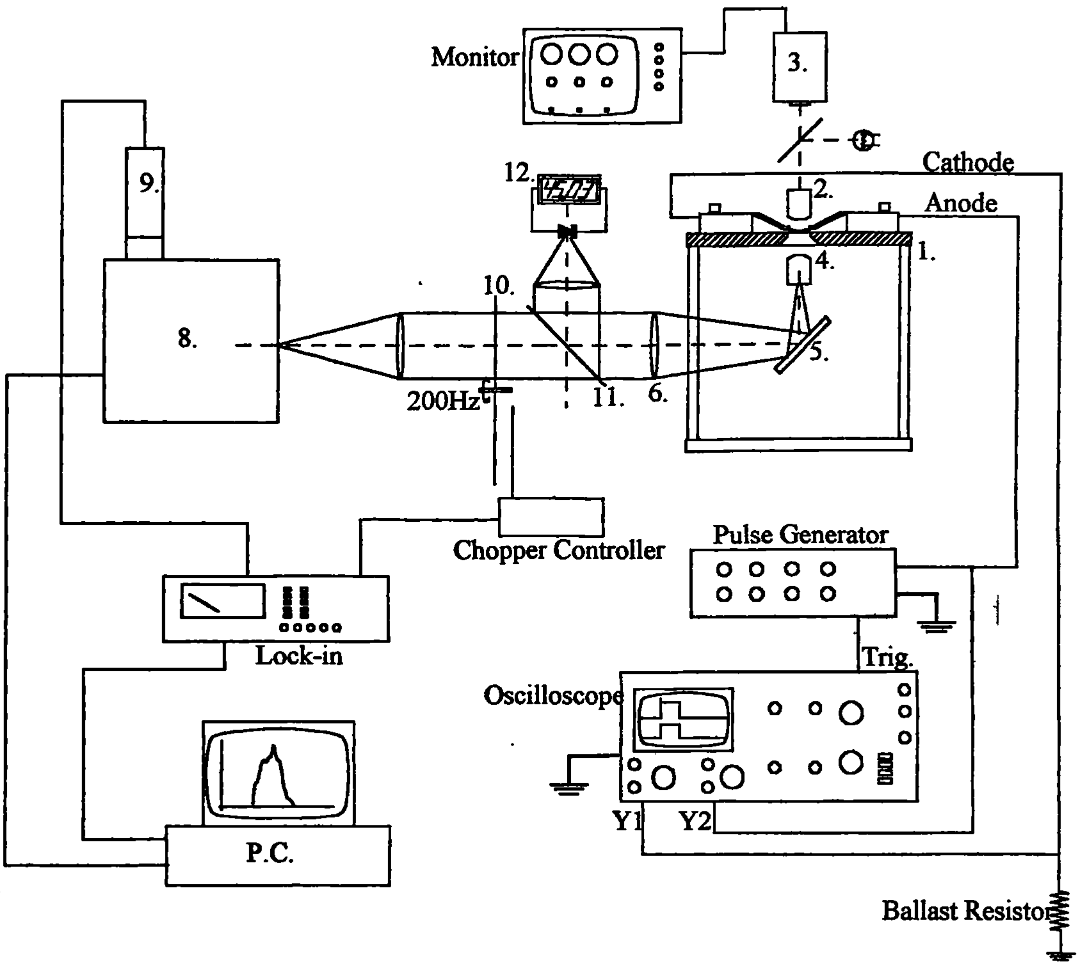

Fig. 6.9. Full experimental system for characterising VCSEL devices. Details are given in the text.

Fig. 6.9. shows the full experimental system which is assembled on an optical table for mechanical stability. The devices and probes sit on a moving platform *1* which has fine *x-y* position control. This allows individual devices to be positioned within an accuracy of a few microns. The devices are imaged by an objective lens *2*

onto a vidicon camera *3* which shows the device being probed on a monitor screen. Light output from the device passes through an opening in the platform and is collected by a second objective lens *4*. The output is reflected by a mirror *5*, collimated by a simple lens at *6* and refocused *7* onto the slits of a 0.5m grating monochromator *8* which has a maximum resolution of 0.1Å. This is controlled by a personal computer (PC) which also records the signal detected at the output by a cooled (77K) Ge detector *9*. Standard lock-in techniques are used to improve the sensitivity; the mechanical chopper *10* operates at around 220Hz. A 50/50 plate beamsplitter *11* re-directs half of the optical signal; this is focused onto a power meter *12* sensitive to powers down to 10nW.

The measurements of power were scaled using the wavelength calibration data supplied with the power meter. System losses were quantified by measuring the losses of a laboratory laser directed through the system along the same path as light from a VCSEL device.

DC measurements were made using a microprocessor controlled current / voltage source and measurement unit. The resistance of the leads and probes was measured and taken into account. To remove the detrimental effects of ohmic heating on devices with a large operating voltage, many of the measurements were made under pulsed conditions. Pulses of up to 50V in amplitude and as short as 200ns were supplied by a pulse generator. Current and voltage were monitored on an oscilloscope. The current is determined from the voltage dropped across a suitable ballast resistor, typically 100Ω. The power meter has a slow time constant of the order of 1s so may be used to measure average output power when pulses with repetition rates of several kHz are applied.

6.4. Measurements on etched mesa devices

6.4.1. I-V measurements

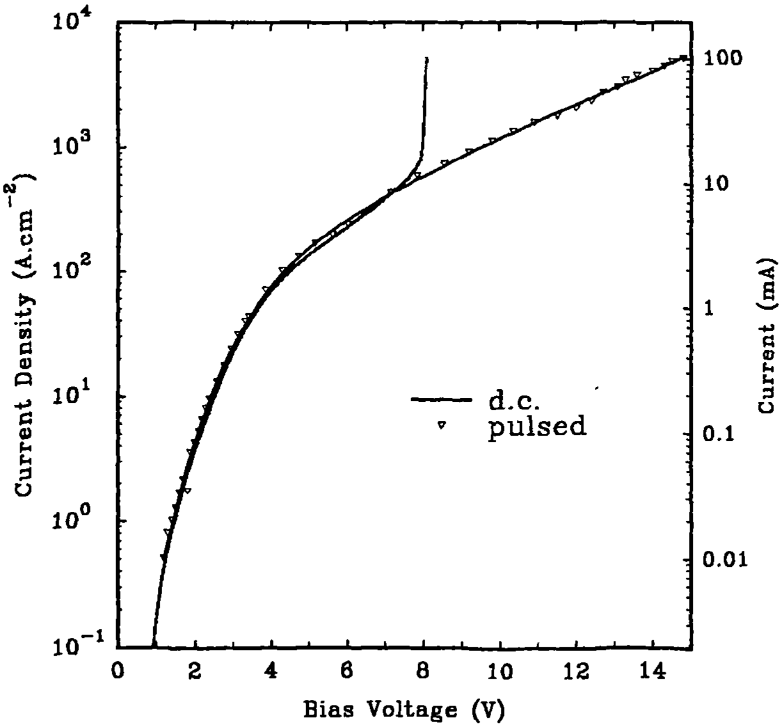

Fig. 6.10. I-V measurements on 50μm diameter VCSEL devices RMB627Q1#2. The two curves show the results of pulsed and d.c. measurements.

Fig. 6.10 shows the results of pulsed and d.c. I-V measurements on 50μm diameter etched mesa devices from Q1#2. At low bias voltages the current is dominated by the diode but at voltages much larger than 1.0V the resistance of the Bragg reflectors begins to limit the current flow. At the typical current density for threshold in a VCSEL (1→2kA.cm^{-2}) the bias voltage under pulsed conditions is 9.5 →11.5V. This characteristic could be predicted from measurements on the test reflector structures RMB607 and RMB637 (section 5.3). Ohmic heating causes a reduction in the device resistance under D.C. operation (at ~8V bias), the condition of thermal runaway is approached at the current densities described above. D.C. measurements are discussed further in section 6.4.3.

Pulsed measurements

6.4.2. L-I measurements

Devices were probed using the experimental set-up described above and current pulses were applied. The output power was measured on the μW power meter and scaled according to the calibration factors which had been previously determined. Typical current light characteristics of two 50μm devices are shown in fig. 6.11. All pulsed measurements described here were conducted with 430ns long pulses with an 18μs repetition period.

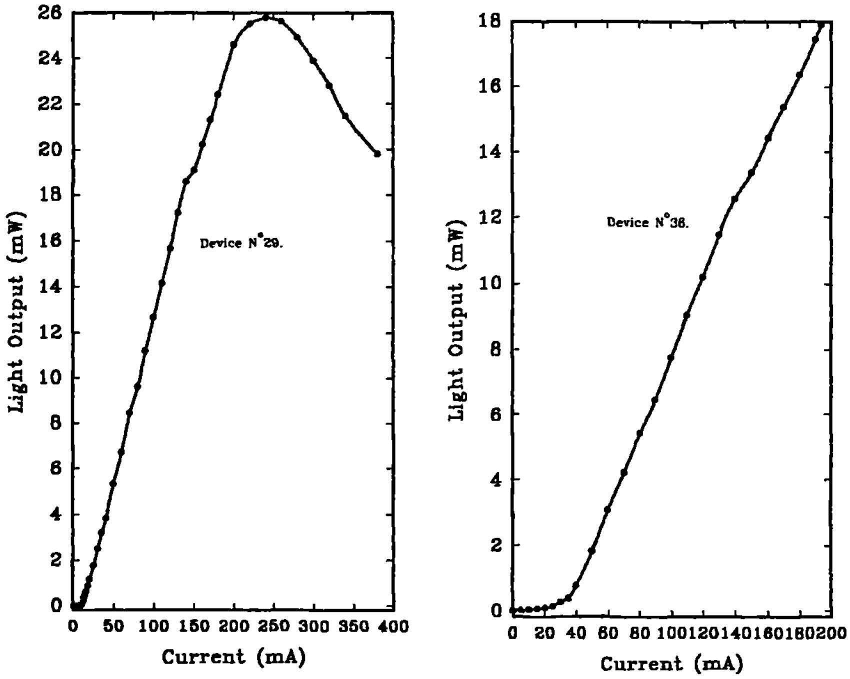

Fig. 6.11. Pulsed current light measurements on two typical 50μm diameter devices (a) device operating at 1009.42nm. (b) device operating at 1041.55nm.

The devices all gave little output at currents below a threshold value, followed by a superlinear increase in output power at higher currents as is typical of laser operation. Observation of the output spectrum close to the lasing threshold reveals a narrow mode (FWHM <5Å). With increasing current the device begins to heat during the length of the current pulse and chirping of the output occurs. Fig. 6.12 shows the output spectrum and how it develops with increasing current. The spectrometer resolution for these measurements was 2Å. The modal structure is thought to arise from interaction with Fabry-Perot modes in the substrate which are spaced by 3.56Å.

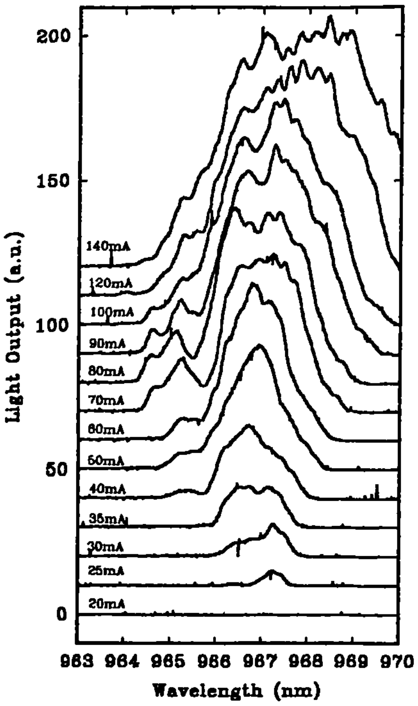

Fig. 6.12. Output lasing spectra of device at different pulse currents.

The far field pattern as viewed on a phosphor card is seen to narrow considerably when threshold is reached indicating the transition from amplified spontaneous to coherent stimulated emission (fig. 6.13).

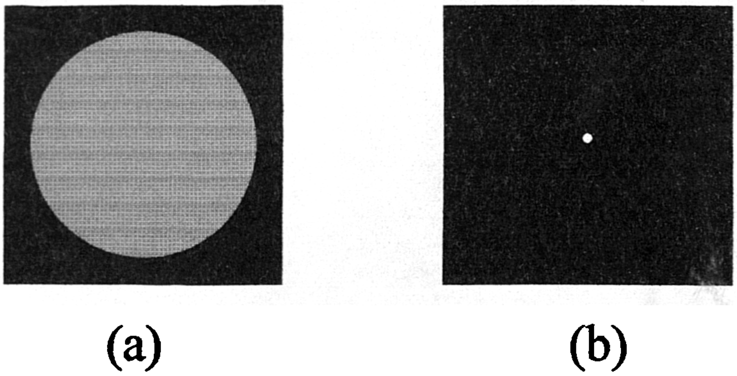
(a) (b)

Fig. 6.13. Far field pattern as viewed on phosphor card. (a) below threshold the output is very dim and diffuse. (b) Once threshold is reached the output narrows considerably and a small bright spot is seen.

A large number of devices were examined and all those tested were found to lase. There was a large variation in threshold currents from device to device as is seen from table 6.1.

Device N^o.	I_{th} (mA)	J_{th}(A.cm^{-2})	η_{diff}(%)	λ(nm)
3	25	1273	11.7	965.3
4	18	917	9.7	978.3
5	18	917	11.5	979.5
6	19	968	13.0	982.9
7	39	1968	10.4	1041.3
9	10	509	10.4	1024.0
10	22	1120	8.9	1038.9
11	32	1630	7.0	1034.1
12	17	866	9.1	1033.8
13	12.5	637	9.2	1026.5
14	7.5	382	10.9	1020.6
15	10	509	10.5	1013.2
16	11	560	6.1	1006.6
17	12	611	13.5	999.4
18	16	815	10.8	982.7
19	22	1120	9.9	973.8
20	22	1120	7.12	964.8
21	18	917	12.5	988.2
22	26	1324	11.8	963.2
23	28	1426	10.2	961.8
24	27	1375	11.1	958.1
25	42	2139	10.7	950.3
26	9.0	4508	—	1020.6
27	7.2	367	—	1017.8
29	11.0	560	18.0	1009.4
30	11.0	560	13.0	1005.8
31	9.7	494	9.9	1020.3
32	9.3	474	13.4	1023.8
33	11.3	576	13.4	1027.9
34	8.2	418	14.9	1014.8
35	8.6	438	15.1	1008.1
36	35	1783	14.8	1041.5

Table 6.1. Operating parameters of 50μm diameter VCSEL devices from RMB627Q1#2

The wavelengths in the above table are peak emission wavelengths measured for 60mA current pulses. The lasing wavelength corresponds directly with the cavity resonance wavelength as seen in the photoreflectance spectrum and thus shows the same systematic variation across the wafer. The differential quantum efficiencies η_{eff} has an average value of 11.28% with a standard deviation between devices of 2.54%. There appears to be little correlation between the efficiency and either cavity wavelength or threshold current. It is therefore likely to be a function of local defects in devices and quality of fabrication which is rather variable between devices.

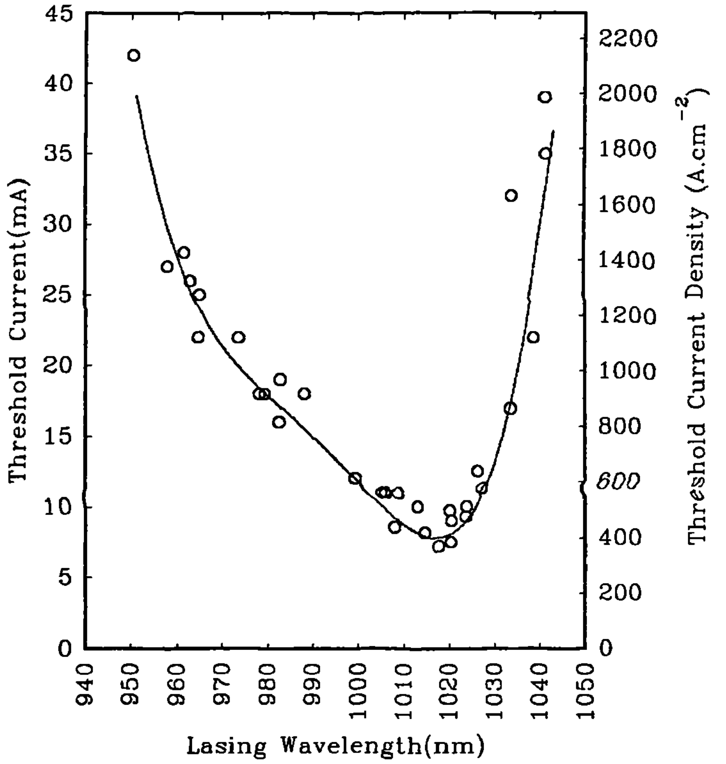

Fig. 6.14. Variation of threshold current with lasing wavelength for 50μm diameter VCSEL devices.

A distinct relation is evident between the threshold current and operating wavelength. This is illustrated in fig. 6.14. Minimum values of threshold current (below 10mA) are obtained at wavelengths around 1020nm which is close to the lowest transition energy as determined by PL (1024nm). At shorter wavelengths devices operate with increased thresholds, e.g. 20mA at 973nm. There is similarly an increase at longer wavelengths but this is much more rapid; the threshold has risen to 20mA at a wavelength of 1036nm. The shape of the $I_{th}(\lambda)$ curve relates directly to the gain spectra of the InGaAs quantum wells (chapter 3.). This is discussed in detail in chapter 8. A relation of this form is reported for external cavity edge emitting lasers in the InGaAsP / InP material system by O'Gorman & Levi[4,5].

Some scatter around the fitted line is evident on the data in fig. 6.14. This results from the following:

(i) Devices with contacts damaged during fabrication or probing.

(ii) Isolated regions of the wafer with large amounts of crystal defects which may cause scattering in the reflector stacks or non-radiative recombination in the active quantum wells.

(iii) Fabry-Perot effects in the un-coated substrate which are wavelength dependant (the substrate mode spacing is 3.56Å at a wavelength of 1.0μm).

Thus the line is drawn towards the lowest data as these indicate achievable results for undamaged devices made on good areas of the wafer.

The lowest threshold current measured for a 50μm diameter device was 7.2mA for a device operating at 1018nm at a bias of 6.8V. This corresponds to a current density of $366A.cm^{-2}$ or $122A.cm^{-2}$ per quantum well[1]. The previous lowest reported threshold current densities for a VCSEL devices, at any wavelength, were $450A.cm^{-2}$ for a device incorporating a single well[6] and $600A.cm^{-2}$ for a three well structure[7]. The best single well stripe geometry lasers operate at current densities as low as $56A.cm^{-2}$ for an InGaAs / GaAs single quantum well structure[8]; this is at the theoretical limit for two dimensional structures as defined by Yariv[9]. Most of the reported high quality VCSEL structures operate at currents in the range 1→$2kA.cm^{-2}$ [10,11,12].

6.4.3. D.C. operation

Due to the very large ohmic resistance of the Bragg reflector stacks the c.w. operating range is severely limited. At a current of 20mA d.c. the bias voltage across a 50μm device is 9.7V only 1.2V of which exists across the diode, the remainder is the ohmic loss and results in heating of the device. The d.c. I-V measurements are shown in fig. 6.10. and show the thermal runaway which occurs at currents above 20mA where the elevated temperature causes a drop in device resistance. The optical gain deteriorates at elevated temperatures and many devices will not lase under d.c. bias. Fig. 6.15. shows the L-I characteristic of a 50μm and a 20μm device operating c.w.

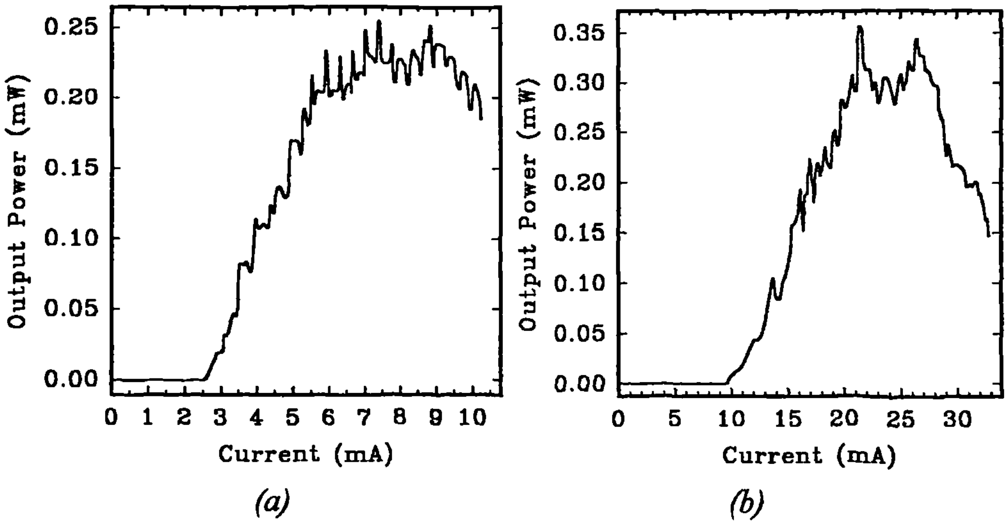

Fig. 6.15. Continuous wave L-I response of etched VCSEL devices (a)20μm diameter and (b) 50μm diameter.

The threshold current of the 50μm device is 10.0mA under pulsed operation. The increased temperature of the active region from ohmic heating causes this to rise slightly to 10.6mA when operated c.w. Note that only devices with resonant wavelengths close to the minimum value of $J_{th}(\lambda)$, 1018nm, may operate c.w. due to the effects of heating. The uneven nature of the L-I response is due to variation of the cavity wavelength as the device heats up. Fabry-Perot modes in the substrate cause feedback into the lasing mode (3.56Å spacing).

With increasing temperature the gain and quantum efficiency are severely reduced as the Fermi function broadens so that carriers move to higher states within the quantum wells and escape[13,14]. For devices with a 10mA threshold current the maximum output is achieved at a current of 20mA. At higher currents the output reduces rapidly towards zero. By 30mA there is very little output and many devices fail catastrophically.

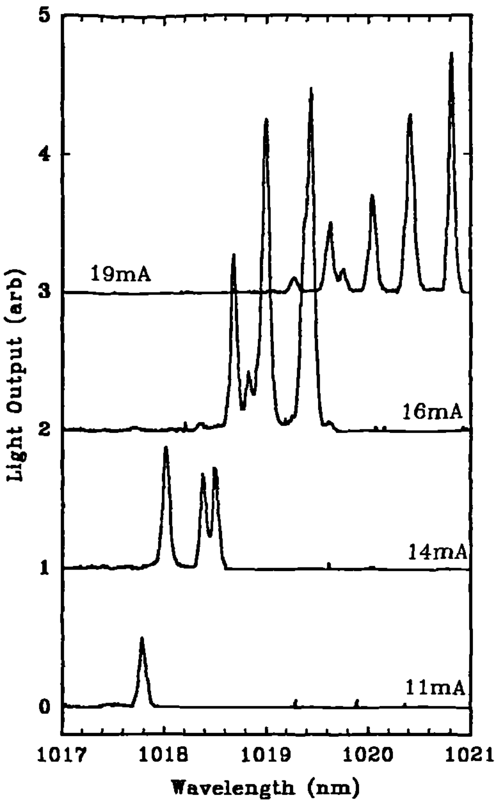

Fig. 6.16. c.w. output spectra of 50μm diameter mesa etched device.

The c.w. output spectra at a number of currents (fig. 6.16) illustrate the effect of heating on the output wavelength. A non-uniform temperature profile develops across the device cross section as it heats and gives rise to an average shift in the cavity resonance of 0.282nm.mA^{-1}. A number of modes are seen to develop indicating filamentous operation[15] in areas where the cavity wavelength corresponds to a substrate mode. Fig. 6.17. illustrates this: at low currents the temperature profile is almost uniform and a single mode may resonate; at higher currents the temperature profile varies markedly across the device diameter and lasing may occur in a number of localized areas where the cavity resonance corresponds to substrate resonances.

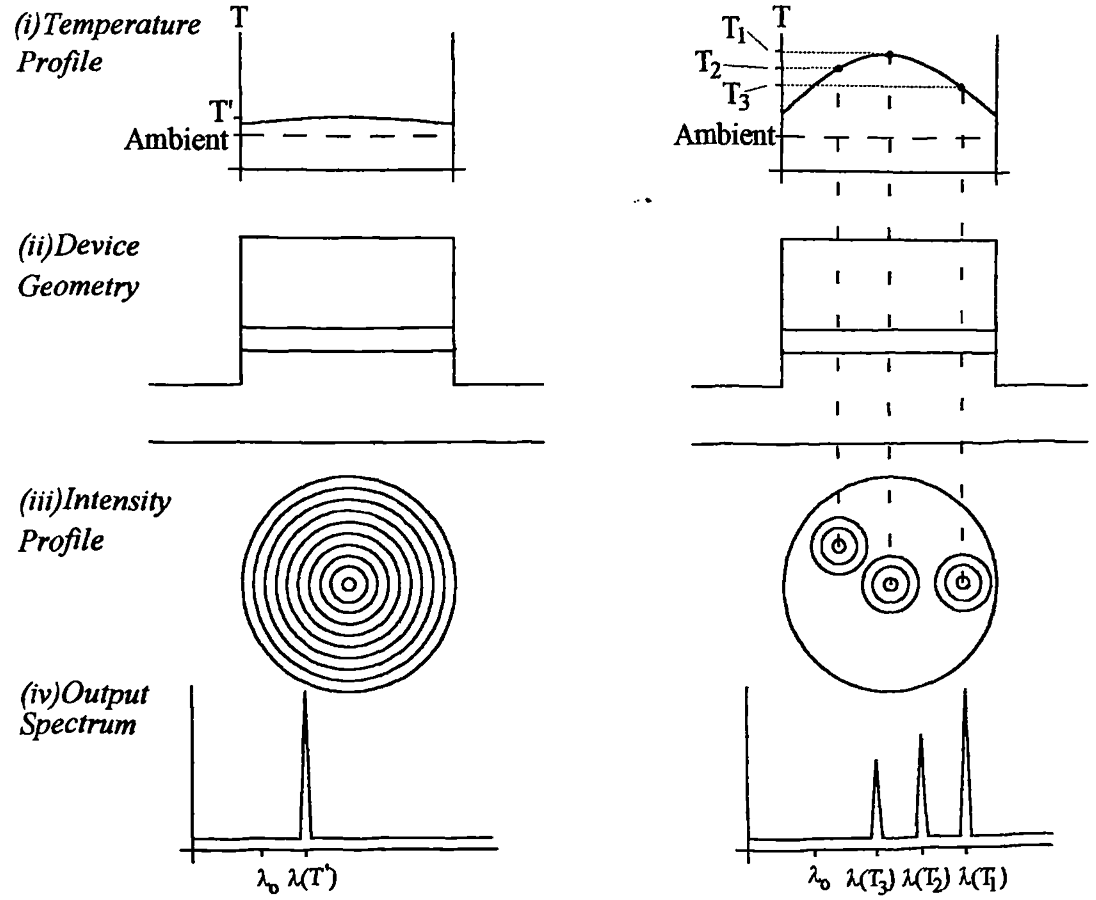

(a) Low Current **(b) High Current**

Fig. 6.17. Temperature profiles and filamentation.

Spectra of 20μm diameter devices were also measured. Fig. 6.18 shows these. As for the larger 50μm device, a shift in the emission wavelength occurs as the current is increased and the device heats but, due to the smaller size, the temperature profile is more uniform so only one peak is ever seen in the output spectrum. The shift in this case is 0.823nm.mA^{-1} and is larger because the current density for 1mA is larger in the smaller device and outweighs the reduced thermal resistivity (see section 8.2.3). The spectrum for 4.5mA is interesting as it indicates a local minimum in the light output as the cavity resonance shifts from one substrate mode to the next.

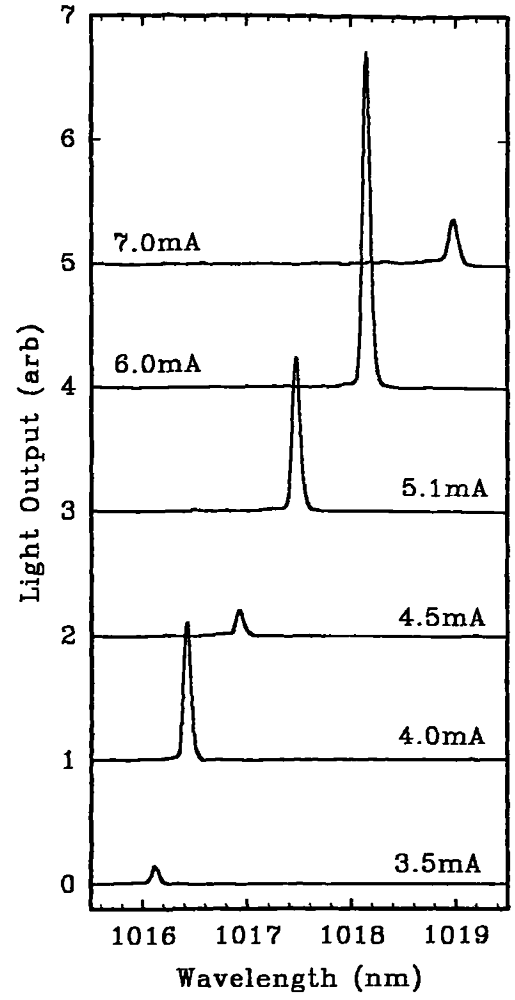

Fig. 6.18. c.w. output spectra of 20µm diameter mesa etched device.

6.5. Polyimide passivated devices

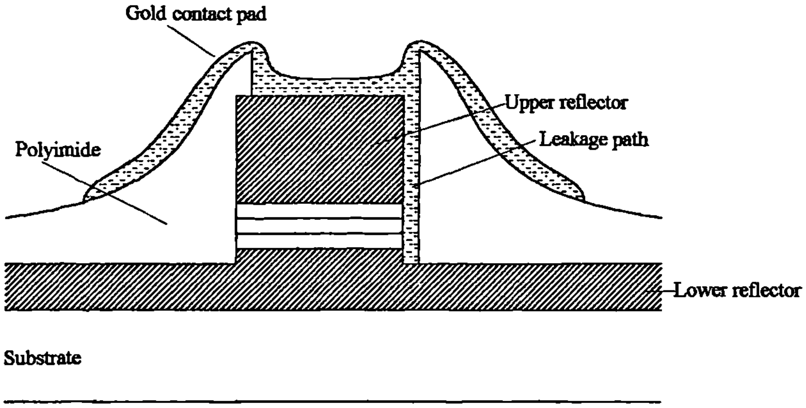

Fig. 6.19. Diagram of polyimide passivated etched mesa device showing leakage path down side of mesa caused by misalignment and damage to the via etch mask.

Devices in the piece of wafer RMB627Q1#1 were passivated with polyimide and had 80μm square contact pads applied as described in chapter 4. This allows contact to be made to the smaller mesa etched devices.

There is a small amount of misalignment and during lift off some tearing of the aluminium mask used to etch vias takes place. This means that there are leakage paths down the side of the mesas which are much more significant in the case of small mesas (fig. 6.19).

6.5.1. Resistance measurements

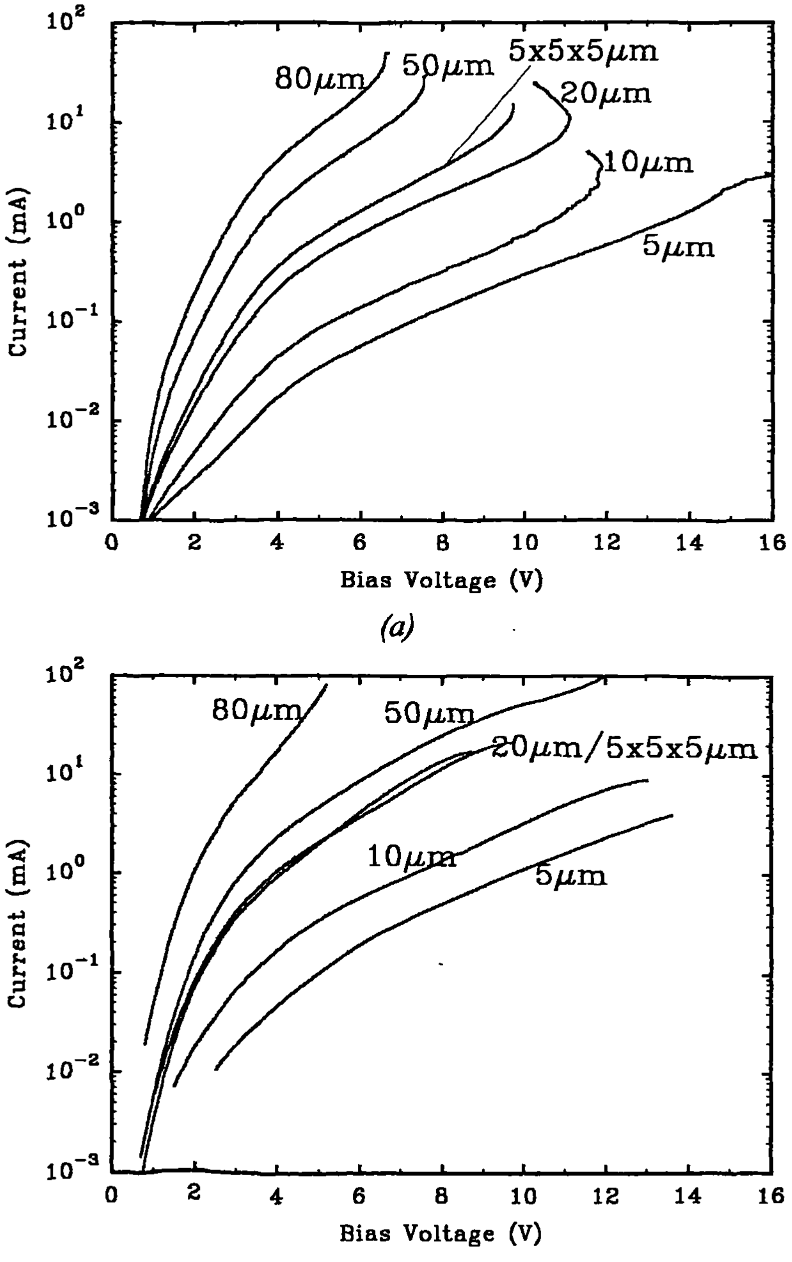

(a)

(b)

Fig. 6.20. (a) d.c. and (b) pulsed I-V measurements on various size VCSEL devices passivated with polyimide.

Fig. 6.20 shows the results of d.c. and pulsed I-V measurements on varying sizes of device. Results for the 50μm diameter devices are very similar to those for un-passivated devices showing that the devices are essentially the same and that the polyimide offers little thermal benefit. Smaller devices do not suffer from heating effects until higher current densities (see section 8.2) are reached as can be seen from the bias voltages at which thermal runaway occurs. These are the points where the resistance reduces substantially due to excessive ohmic heating. Individual devices show significant variation from these curves as the amount of leakage from device to device varies.

6.5.2. Pulsed L-I measurements

L-I responses of a number of devices were measured under pulsed conditions. Devices with diameters of 80, 50, 20, 10 and 5μm were tested as well as 5×5 arrays of 5μm diameter devices. Fig. 6.21 shows L-I responses for a selection of devices of various sizes and table 6.2. lists the results for the devices examined.

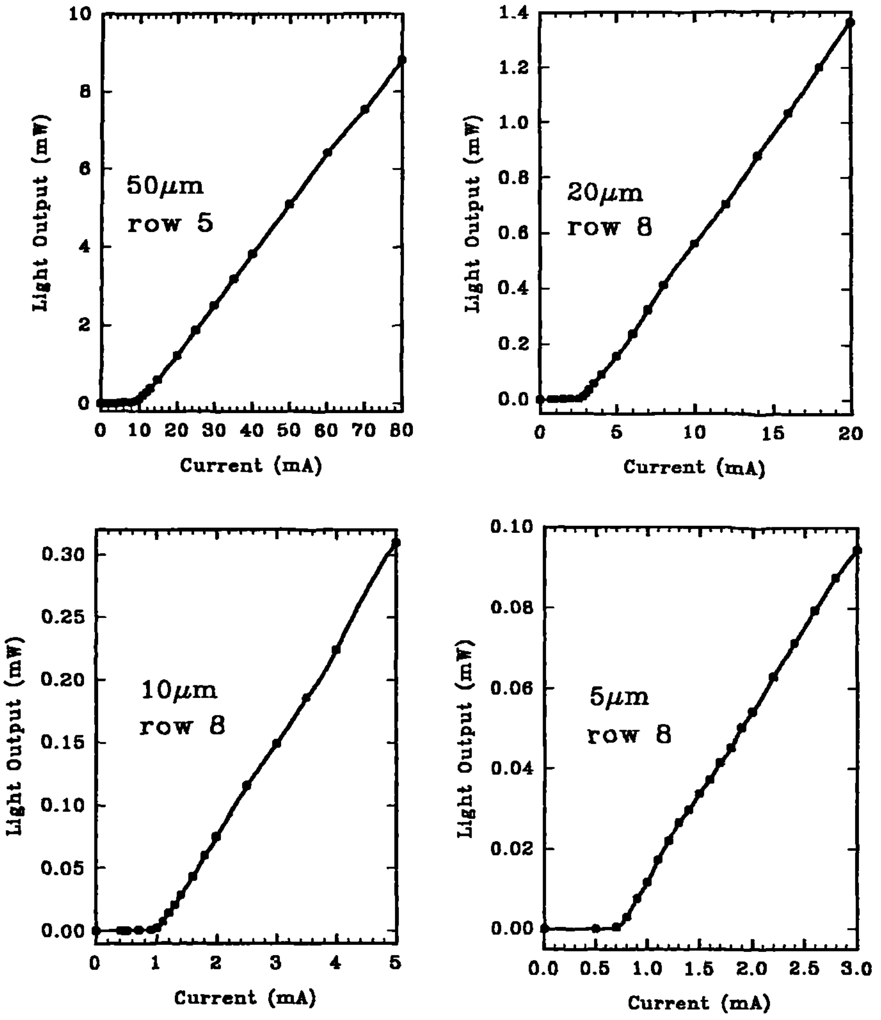

Fig. 6.21. Selection of pulsed L-Is for polyimide passivated mesa etched devices of different sizes. Results for 50, 20, 10 and 5μm diameters are shown.

Device Position					
Square	**Row**	**Diameter (μm)**	**I_{th}(mA)**	**J_{th}(A.cm^{-2})**	**λ (nm)**
(8,3)	5	50	30	1527.9	966.2
(8,3)	5	20	5.8	1846.2	966.2
(8,3)	4	10	3.3	4201.7	966.2
(8,3)	5	5	1.44	7333.9	966.2
(8,3)	6	50	20.5	1044.1	966.2
(8,3)	6	20	5.4	1718.9	966.2
(8,3)	6	10	4.1	5220.2	966.2
(8,3)	6	5	1.93	9829.4	966.2
(8,3)	6	5×5×5	18	3666.9	966.2
(10,5)	1	50	68	3463.2	942.3
(10,5)	1	20	15.0	4774.6	942.3
(10,5)	1	10	4.0	5093.0	942.3
(10,5)	1	5	3.77	19200.4	942.3
(5,3)	1	50	18	916.7	985.5
(5,3)	2	20	6.7	2132.7	985.5
(5,3)	2	10	2.7	3437.4	985.5
(5,3)	1	5×5×5	16.5	3361.3	985.5
(4,3)	8	50	12.6	641.7	990.0
(4,3)	8	20	3.7	1177.7	990.0
(4,3)	6	10	3.2	4074.4	990.0
(4,3)	8	5×5×5	19	3870.6	990.0
(4,3)	8	5	1.02	5194.8	990.0
(6,4)	3	50	21	641.7	970.8
(6,4)	3	20	4.8	1527.9	970.8
(6,4)	3	10	1.9	2419.2	970.8
(6,4)	5	5	1.4	7130.1	970.8
(6,4)	2	5×5×5	21.5	4379.9	970.8
(6,4)	5	50	25	1273.2	970.8
(6,4)	4	20	5.2	1655.2	970.8
(6,4)	5	10	3.7	4711.0	970.8
(7,1)	8	50	20	1018.6	981.6
(7,1)	7	20	5.5	1750.7	981.6
(7,1)	6	10	3.5	4456.3	981.6
(7,1)	7	5×5×5	17	3463.2	981.6
(9,6)	1	50	58	2953.9	941.7
(9,6)	1	20	12.2	3883.4	941.7
(9,6)	1	10	4.7	5984.2	941.7
(9,6)	1	5×5×5	75	15278.9	941.7
(2,5)	8	5	0.79	4023.4	981.5
(2,1)	8	5×5×5	14	2852.0	1011.5

Table 6.2. Results for polyimide passivated devices from RMB627Q1#1.

The first two columns of table 6.2 indicate the position of the device on the chip RMB627Q1#1. Wavelengths of the 50μm devices were measured at a current of 60mA except where the threshold current is higher, as in section 6.4.2: wavelengths of smaller devices are estimated from their position on the chip in relation to measured 50μm devices. The threshold current densities for the different size devices are plotted as a function of wavelength in fig. 6.22. Note that there is a lot of scatter on the data as a result of the large leakage currents in some devices.

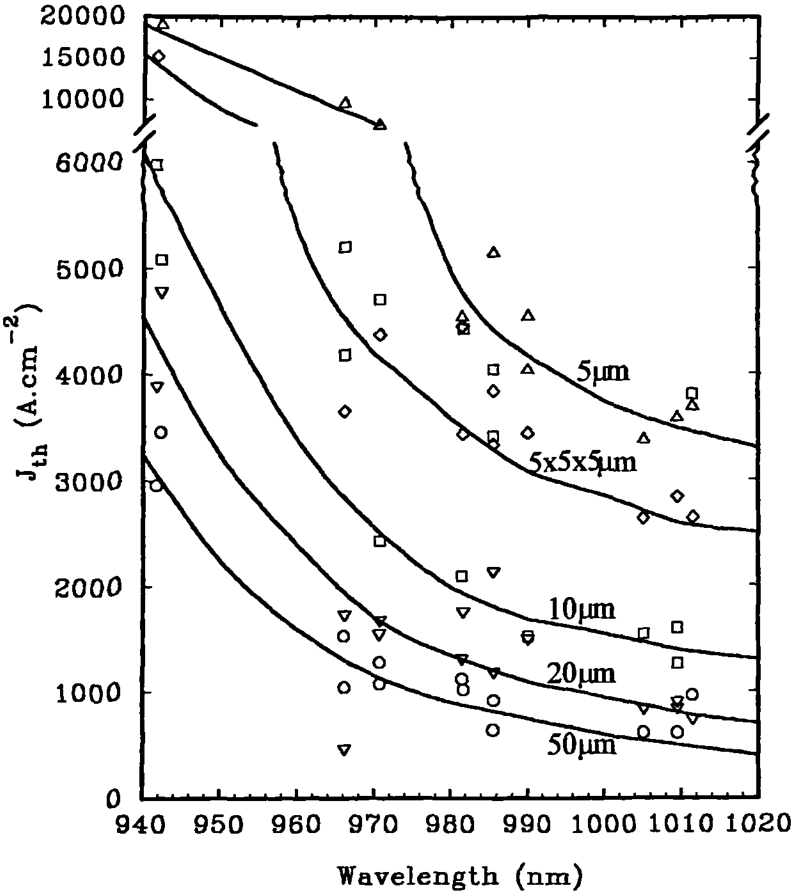

Fig. 6.22. Variation of threshold current density with wavelength for polyimide passivated VCSEL devices of varying diameters: 50μm (O), 20μm (∇), 10μm (□), 5μm (◊) and 5x5x5μm arrays (Δ).

The curve for 50μm devices is a portion of that shown in fig. 6.14 for un-passivated devices. There are no devices on piece #2 operating at wavelengths longer than 1012nm. The general relation evident from the curves is that smaller devices have larger threshold current densities[11]: this is a result of losses such as surface recombination, optical scattering from the sidewalls and leakage which scale proportionally with device diameter so are more significant in smaller devices.

Diffraction losses mean that the gain required in a small device will be larger. It is observed that the curves in fig. 6.22 diverge at shorter wavelengths so that a 5μm device operating at 950nm has a threshold current density 8.5 times that of a 50μm device whereas at 1020nm the difference is only a factor of 6.8. This indicates that there is greater gain compression away from the exciton at shorter wavelengths. This is discussed in more detail in chapter 8.

6.5.3. D.C. Measurements

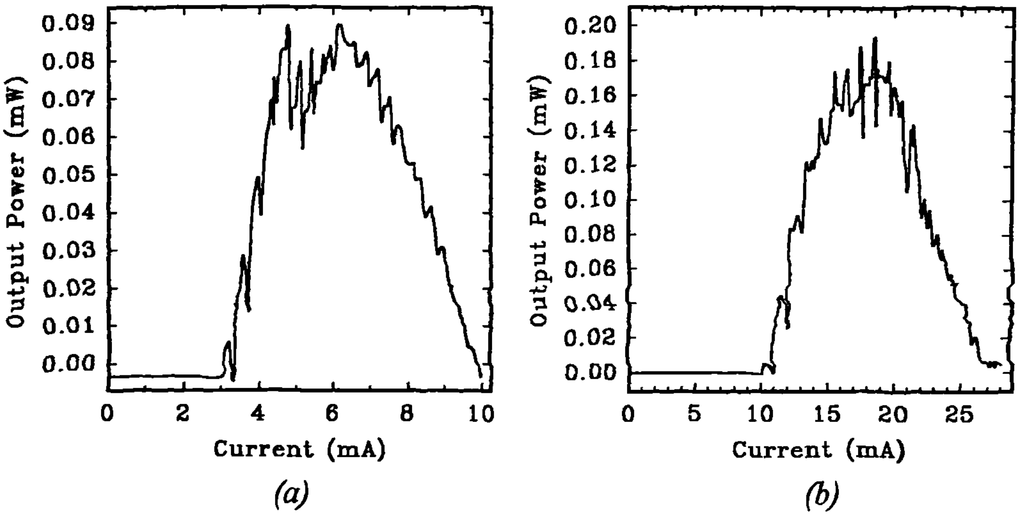

Fig. 6.23. c.w. L-I response of polyimide passivated VCSEL devices (a)20μm and (b) 50μm diameter.

Fig. 6.23 shows c.w. L-I responses from typical 50 and 20μm devices. Smaller devices did not operate reliably c.w. The current for maximum output is tabulated in table 6.3. The response of these larger devices is similar to the un-passivated devices, however it is thought that passivated devices, especially smaller ones will last longer as moisture will be prevented from reaching the deliquescent AlAs layers. Un-passivated devices are of limited practical use since arrays may not be easily contacted.

Size (μm)	I_{max}(mA)	J_{max}(A.cm^{-2})
50	20	1018
20	7	2228

Table 6.3. Currents for max light out for passivated etched VCSEL devices.

6.6. Ion Implanted devices

RMB627Q4 was patterned with 1μm thick Ti / Au dots as an implant mask. A dose of $2\times10^{13}.\mathrm{cm}^{-2}$ 200keV H^+ ions[16] were implanted into the sample to define devices, as described in chapter 4. The dose was selected from results presented by Orenstein *et al.*[17]; too low a dose will result in a leaky implanted region, too high and lattice damage will result in carriers being captured by traps (see also section 7.7.2).

80μm square contact pads were applied. Neighbouring devices were isolated by reactive ion etching to a depth of 3.5μm using the contact pads as an etch mask.

6.6.1. I-V measurements

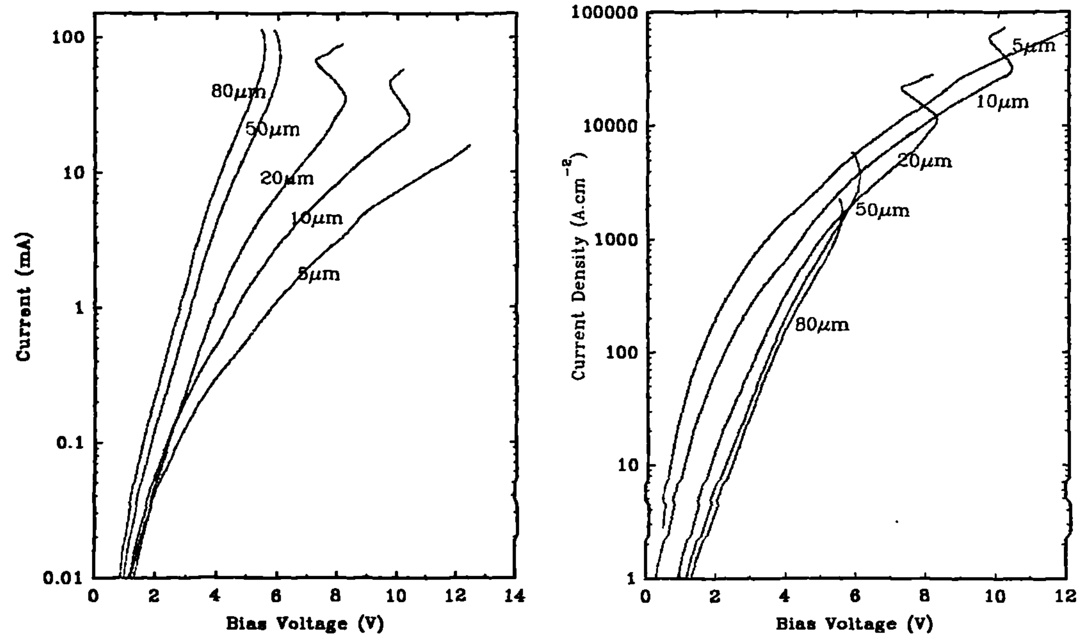

(a) *(b)*

Fig. 6.24. Results of d.c. I-V measurements on implant defined devices: (a) on current scale; (b) shown as apparent current densities the effects of leakage and heating are seen more clearly.

Fig. 6.24 shows the results of d.c. I-V measurements on the implanted devices. At high current densities the device heats sufficiently to achieve thermal runaway and a region of negative differential resistance is reached. From the figure it is seen that smaller devices may operate at much higher current densities before this condition is reached. This illustrates that the smaller devices receive more effective heatsinking; this is discussed in more detail in chapter 7. Also it is noted that smaller devices appear to have a smaller areal resistance; this is due to the effects of leakage through the implanted region which are more significant in the case of small active areas.

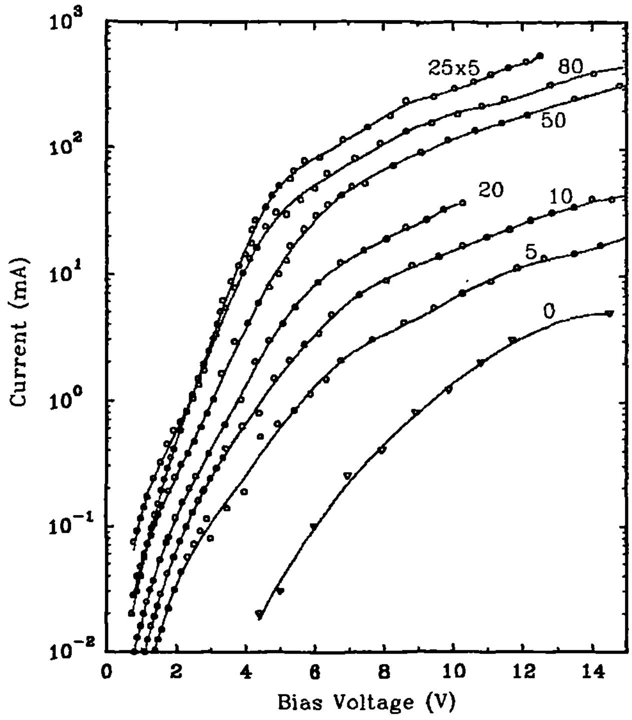

Fig. 6.25. Pulsed I-V on implanted devices.

Fig. 6.25 shows the results of I-V measurements made under pulsed conditions so to remove the heating effects. The line labelled 0μm is for a device which had no implant mask. The current flowing through this indicates the size of the leakage current through the implanted areas. The current density through a 5μm device appears to be approximately 20 times larger than that through a 50 μm device under the same bias (true for voltages in excess of 6V). The difference is thought to be mainly due to this leakage.

6.6.2. Pulsed L-I characteristics

Devices were tested under pulsed conditions as for the etched devices. The difference from etched devices is immediately obvious on examining the L-I response. Fig. 6.26 shows the response of a typical 50μm device from the implanted sample for 430ns pulses at 18μs repetition. The maximum light output is obtained for 560mA pulses. After being driven with 1.4A pulses there is no noticeable degradation in the performance.

The response of two mesa etched devices are also shown in the figure for comparison. Device #29 is the best mesa etched device found, #31 is a more typical device. Maximum light output is detected at around 200mA and devices are permanently damaged or destroyed when 300mA pulses are applied.

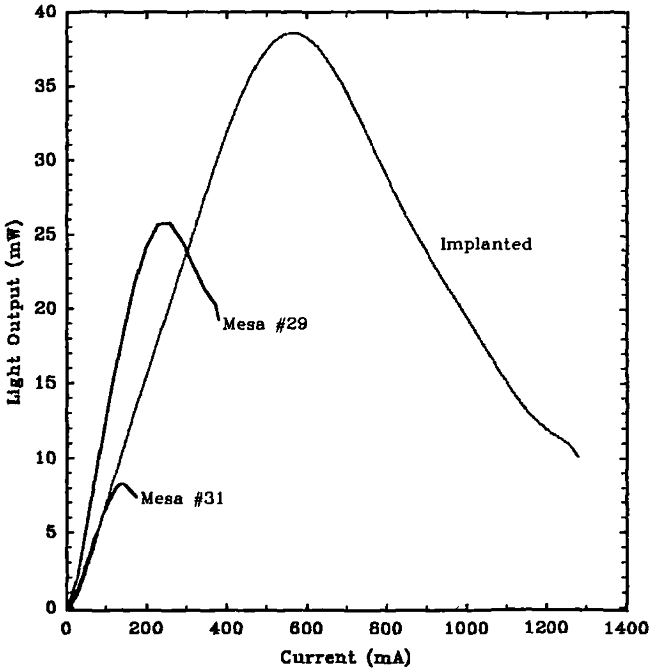

Fig. 6.26. Pulsed L-I response of 50μm diameter implant defined device (—), also shown are the responses of two etched mesa type devices (—).

Square	Row	I_{th}(mA)	J_{th}(mA)	λ(nm)
(1,1)	8	185	9422	1058.7
(1,2)	8	145	7385	1054.1
(1,3)	8	105	5348	1050.6
(1,4)	8	85	4329	1045.8
(1,5)	8	40	2037	1040.9
(1,6)	8	24	1222	1035.1
(1,7)	8	24	1222	1029.1
(1,8)	7	13	622	1024.1
(1,9)	2	14	713	1019.0
(1,9)	8	12	611	1016.8
(1,10)	8	11	560	1008.9
(1,10)	2	10.5	535	1013.8
(1,11)	8	12	611	1001.8
(1,12)	8	15.5	789	994.1
(1,13)	6	17	866	985.4
(1,14)	8	22	1120	977.1
(1,15)	6	25	1273	969.8
(1,16)	7	33	1681	960.4

Table 6.4. Summary of results for measurements on 50μm diameter implant defined devices.

The results of probing a number of devices across the sample are tabulated in table 6.4. The variation of threshold current with lasing wavelength is shown in fig. 6.27.

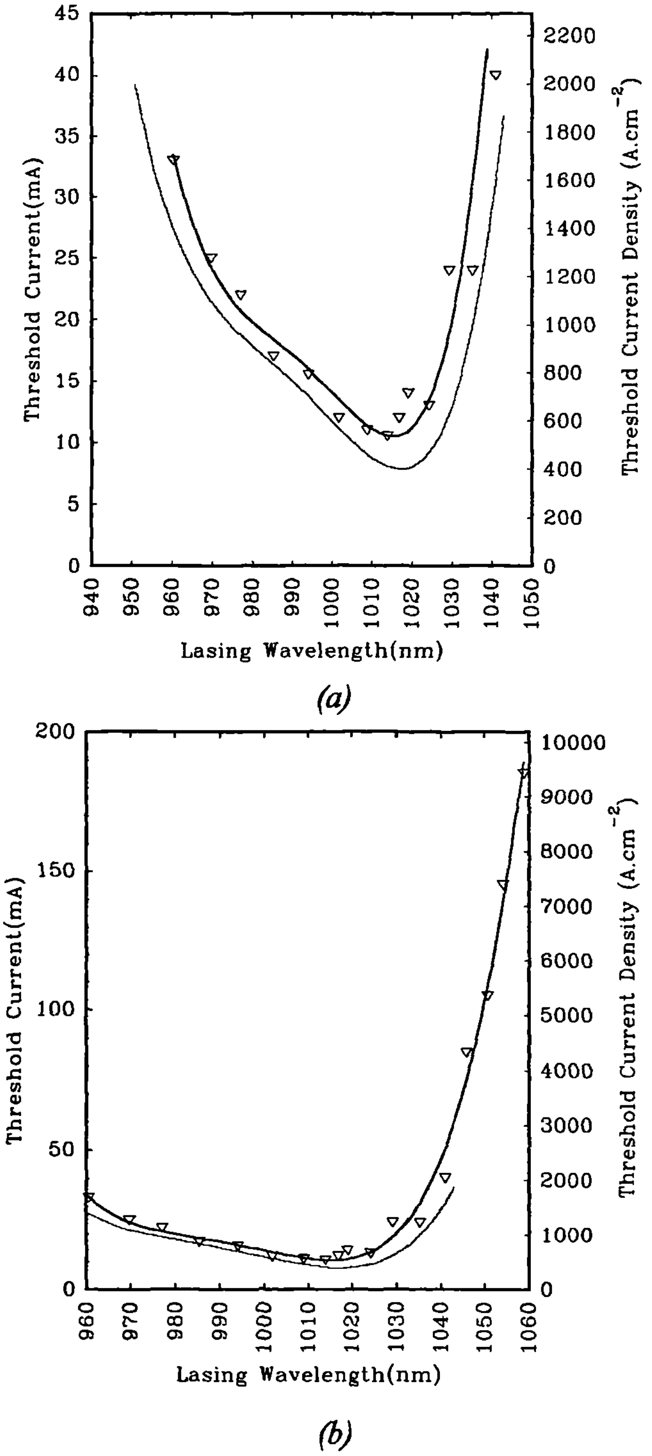

Fig. 6.27. (a) Plot showing variation of threshold current with lasing wavelength for implant defined VCSEL devices (—). Also shown is the relation for mesa etched devices (—) for comparison. (b) Plot showing extended range of data.

As the figure shows, threshold current varies with wavelength in a similar way to mesa etched devices. The minimum threshold current is now 50% higher as a result of current leakage through the current blocking layer. The difference is less obvious away from the minimum where the leakage is less significant. The minimum threshold current measured was 10.5mA at a wavelength of 1013.8nm, which corresponds to a current density of 535A.cm^{-2} or 178A.cm^{-2} per quantum well. The bias voltage at this current is 5.0V. As fig. 6.26 above shows the increased threshold is far outweighed by the improved power handling capacity of the device.

6.6.3. Smaller Devices

Smaller ion implanted devices were tested also. The results of pulsed I-V measurements is given in table 6.5. Operating wavelength is estimated from 50μm diameter devices in the vicinity.

Square	Row	Diameter (μm)	I_{th}(mA)	J_{th}(A.cm^{-2})	λ(nm) ♦
(1,8)	6	10	14	17825	1025.1
(1,8)	8	5	12	61115	1023.9
(1,9)	7	20	16	5093	1017.2
(1,9)	7	10	11.5	14642	1017.2
(1,7)	8	20	16	5093	1029.1
(1,7)	8	10	16	20372	1029.1
(1,7)	7	5	6	30558	1029.7
(1,8)	6	20	18	5370	1025.1
(1,6)	7	20	40	12732	1035.7
(1,6)	7	10	16	20372	1035.7
(1,6)	7	5	13	66208	1035.7
(1,9)	7	5	5	25465	1017.2
(1,10)	8	20	7	2228	1008.9
(1,10)	8	10	13	16552	1008.9
(1,10)	8	5	9	45837	1008.9
(1,4)	8	10	20.5	26101	1045.8
(1,4)	8	5	11	56023	1045.8
(5,1)	8	20	41	14961	—
(5,1)	8	10	20	25465	—
(5,1)	8	5	14	71301	—
(1,4)	7	20	57	18144	1046.3
(1,3)	8	10	30	38197	1050.6
(1,11)	8	20	5.8	1846	1001.8
(1,11)	8	10	7	8913	1001.8
(1,11)	8	5	5	25465	1001.8

Table 6.5 continued overleaf...

......Table 6.5 continued.

(1,12)	8	20	6.8	2165	994.1
(1,12)	8	10	6.4	12732	994.1
(1,12)	8	5	5.3	26993	994.1
(1,13)	7	20	6.3	2005	976.4
(1,13)	7	20	8.7	2769	976.4
(1,13)	7	5	4.5	22918	976.4
(1,14)	8	20	9.5	3024	977.1
(1,14)	7	10	5.3	6748	977.8
(1,14)	6	5	7.0	35651	978.5
(1,15)	5	20	7.5	2387	970.7
(1,15)	6	10	8.0	10186	969.8
(1,15)	2	5	6.5	33104	973.5
(1,16)	7	20	9.5	3024	960.4
(1,16)	7	10	12.5	15915	960.4
(1,16)	7	5	10.5	53476	960.4

Table 6.5. Summary of results of pulsed measurements on 20, 10 and 5μm diameter implant defined devices on RMB627Q4. ✝ Wavelengths are estimated from neighbouring 50μm devices.

Fig. 6.28 shows pulsed L-I response of different diameter devices situated within 1mm of each other on the chip and operating close to 977nm. Note that the threshold current decreases with device size but does not scale with area as there is a leakage of 3→5mA through the implanted region which limits the minimum threshold current. This indicates that the ion dose should be increased for better isolation and that the mesa area should be made smaller for smaller active diameters.

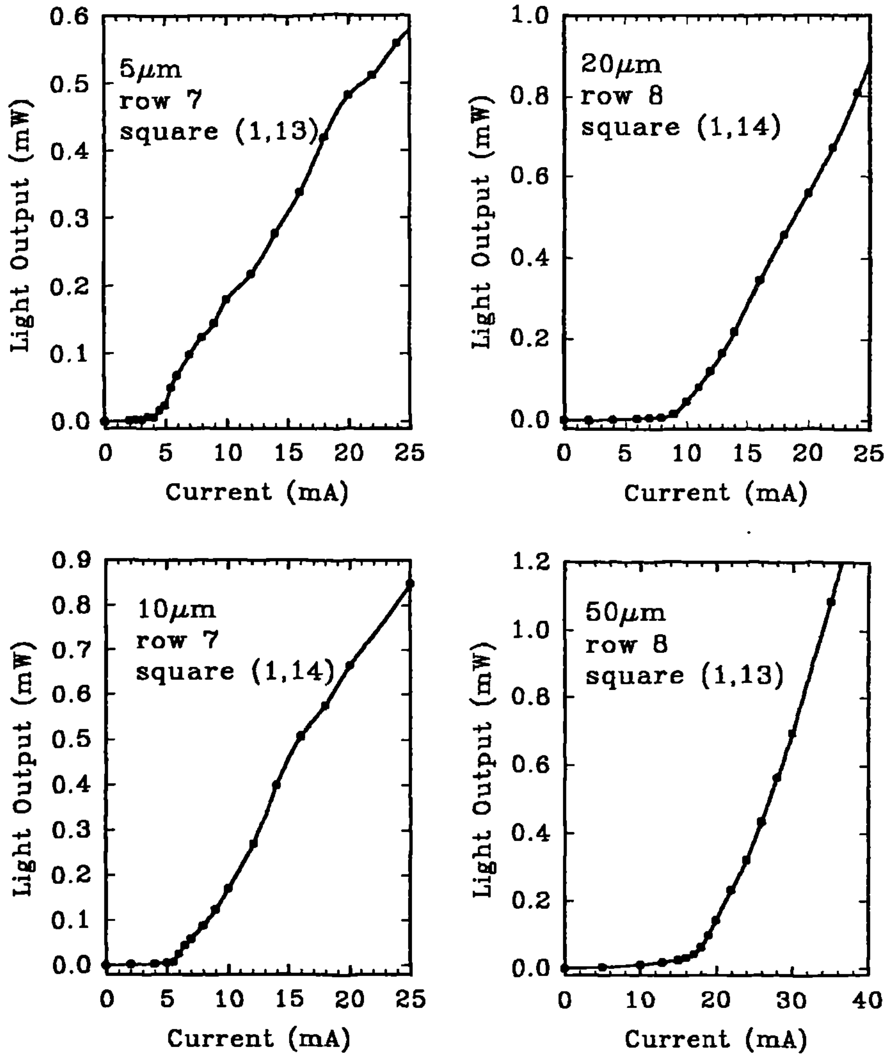

Fig. 6.28. Pulsed L-I response of 5, 10, 20 and 50µm diameter implant defined devices operating at wavelengths near 977nm. The effects of leakage through the implanted region are demonstrated by the minimum threshold of ~5mA.

The threshold data of table 6.5 are plotted as a function of wavelength in fig. 6.29 together with the data for 50µm diameter devices from table 6.4. There is a large amount of scatter on the data so it is difficult to draw lines through them. However it is apparent that the minimum threshold current is limited to ~5mA due to leakage and that the shape of the curve is changed for smaller diameters. The minimum appears to be flattened and occurs at around 985nm rather than 1018nm for 50µm devices. This could indicate that the threshold gain is higher for the smaller diameters due to increased optical losses. This is discussed in chapter 7.

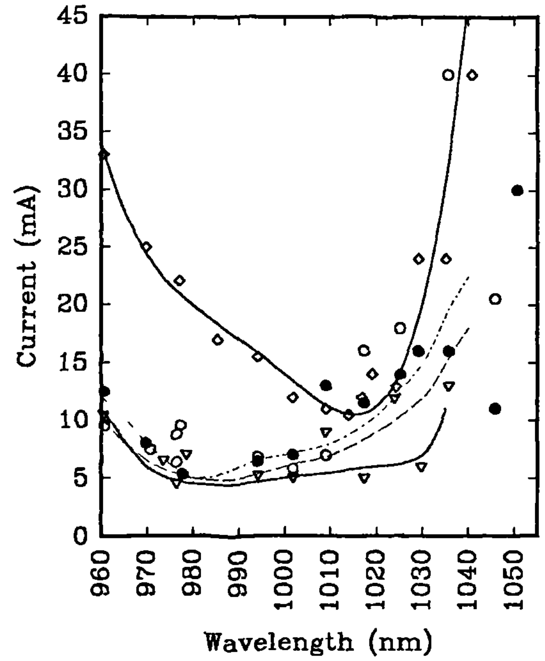

Fig. 6.29. Plot showing dependence of threshold current on lasing wavelength of ion-implanted devices of various dimensions. Data taken from tables 6.4 and 6.5. Device diameters are: (◊——) 50μm, (○– –) 20μm, (●– · –) 10μm and (∇——) 5μm. Lines are drawn towards lowest data.

6.6.4. D.C. L-I characteristics

From I-V data presented in fig. 6.4 it is noted that the bias voltage required to pass a d.c. current of 10mA through a 50μm device is reduced from 7.5V in the case of an etched mesa device to 4.6V in the case of an implant defined device. This results from the funnelling of current into the same active area from a much larger mesa. Combined with the reduced thermal resistance resulting from the extra semiconductor material in the mesa, this should allow c.w. operation to be achieved at much higher currents.

Fig.6.30 shows the L-I plot of a 50μm device. On the same diagram the output of a mesa etched device is also shown, not to the same vertical scale.

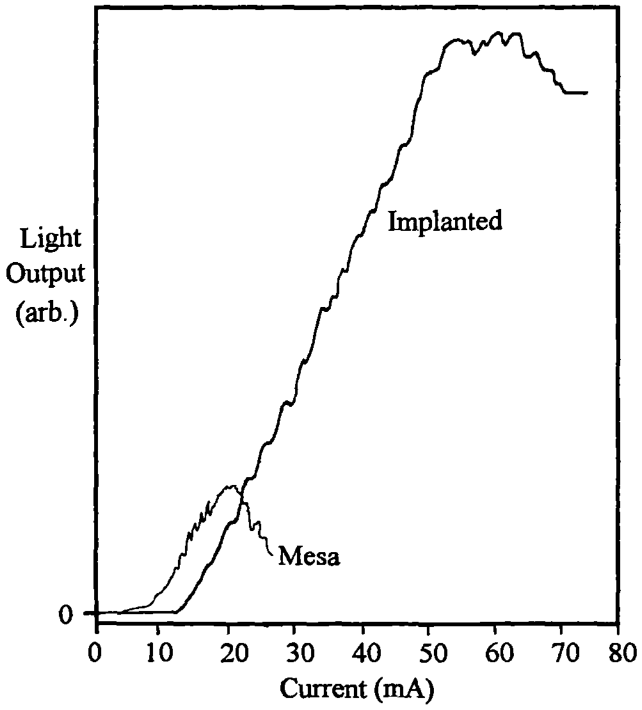

Fig. 6.30. c.w. L-I response of implant 50μm defined and mesa etched devices (to different vertical scales) illustrating increased power handling of the implanted device. The two devices operate at different wavelengths.

Maximum optical power is detected at a current of 60mA, three times the value in mesa etched devices. There is still significant output at 75mA where the power supply used reaches its current limit. In contrast with the catastrophic failure of the mesa device at 30mA, the implanted device undergoes no detectable permanent damage at the maximum current and the same L-I curve may be traversed an arbitrary number of times.

Devices smaller than 50μm diameter also work reliably c.w. as is shown by the L-I curves in fig. 6.31 which also shows 20, 10 and 5μm devices as well as 5×5 arrays of 5μm devices operating. All of these devices operate close to the wavelength for minimum pulsed threshold current (i.e. ~1018nm), the variation with resonant wavelength is discussed in section 6.6.5. The currents for maximum light output are tabulated in table 6.6. Notice that the smaller devices can handle higher current densities but the leakage through the implanted region is much more significant so the threshold current densities appear to be large. A leakage current of 5mA is assumed for calculation of the effective current density through the active region at maximum light output.

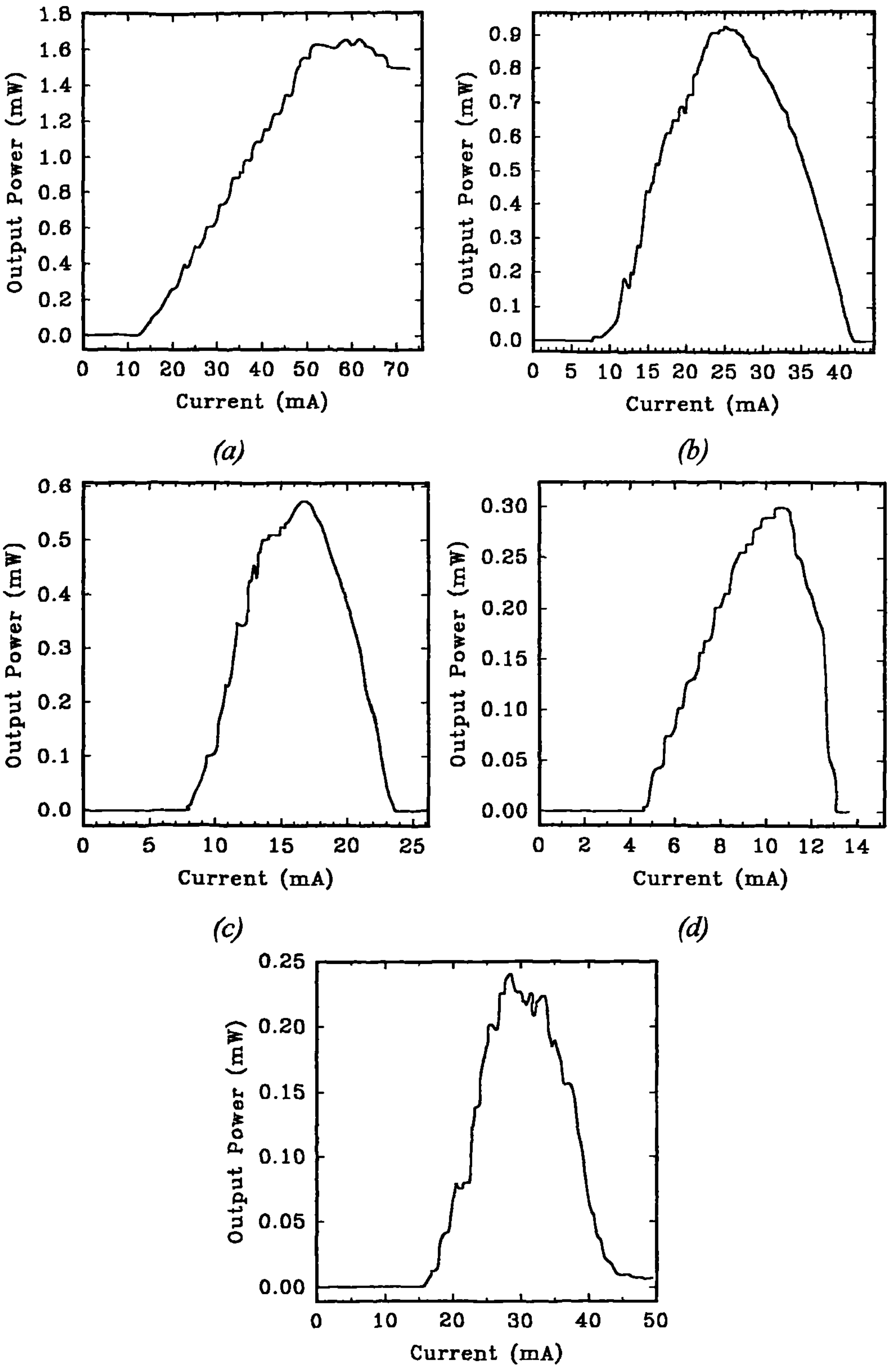

(a) *(b)*

(c) *(d)*

(e)

Fig. 6.31. c.w. L-I curves for implant defined devices of different diameters: (a) 50μm. (b) 20μm, (c) 10μm, (d) 5μm and (e) 5x5 arrays of 5μm diameter devices.

Diameter (μm)	I for L_{max}	J for L_{max}	J (deduced)
50	60mA	3056A.cm^{-2}	2801A.cm^{-2}
20	26mA	8276A.cm^{-2}	6684A.cm^{-2}
10	17mA	21645A.cm^{-2}	15279A.cm^{-2}
5	11mA	56022A.cm^{-2}	30558A.cm^{-2}
5×5×5	31mA	6315A.cm^{-2}	5296A.cm^{-2}

Table 6.6. Currents for maximum light output from various sized implant defined devices. The third column shows the apparent current density at this condition which is large due to leakage currents. The final column is the calculated current density through the active region assuming a leakage current of 5mA.

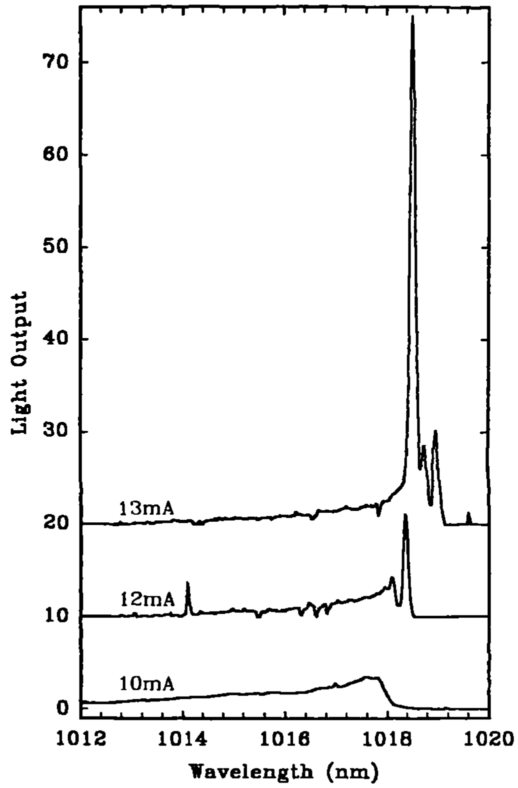

Fig. 6.32. c.w. lasing spectra from 50μm diameter implant defined device showing development of the narrow lasing mode from the spontaneous emission.

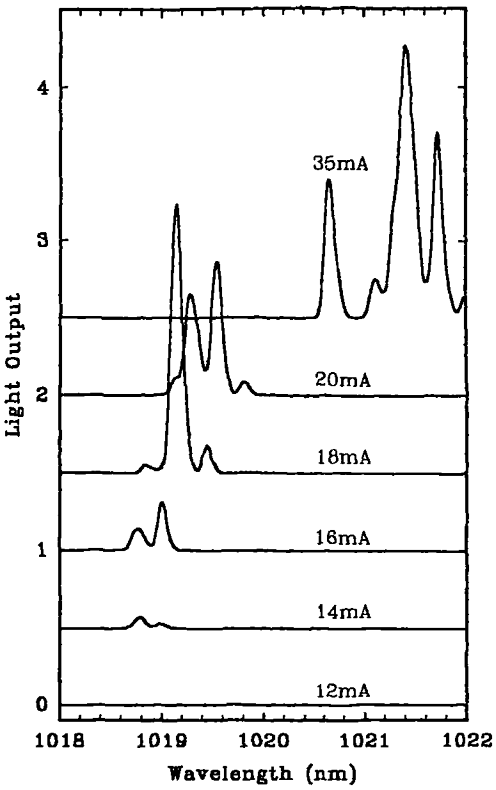

Fig. 6.33. c.w. lasing spectra from 50μm diameter implant defined device at higher currents showing effects of heating in the wavelength red shift and development of multiple modes.

The much improved reliability afforded by implantation allows a more detailed study of lasing spectra to be made. Fig. 6.32 shows how the development of the narrow lasing mode from the broad band spontaneous emission for a typical 50μm device. The development of the spectrum at higher currents is shown in fig. 6.33: with increasing current the device heats and we see a red shift in the emission wavelength and the development of multiple modes as a non-uniform temperature profile emerges. The shift in the output is much less than for etched devices (0.282nm.mA^{-1}) and is 0.152nm.mA^{-1} in the device centre and 0.090nm.mA^{-1} at the device periphery.

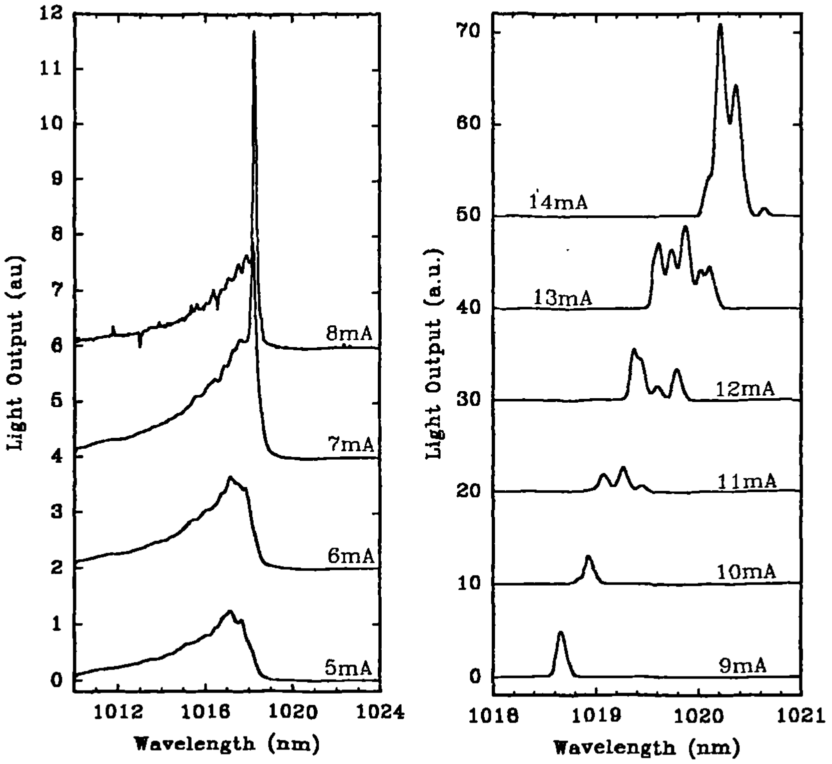

(a) *(b)*

Fig. 6.34. Spectra for 20μm diameter implant defined device; (a) showing development of narrow mode at threshold, (b) development above threshold showing red-shift due to heating.

Fig. 6.34. shows spectra for a 20μm device showing reduced shift compared to the etched mesa device (0.823nm.mA^{-1}) of 0.380nm.mA^{-1} in the device centre and 0.280nm.mA^{-1} at the device periphery.

6.6.5. Variations of c.w. operating characteristics in devices with different resonant wavelengths.

Due to the improved thermal performance of the ion-implant defined devices, they may be operated to much higher direct currents. This means that devices other than those with minimum threshold currents are able lase c.w. Fig. 6.35 shows c.w. L-I response of eight implanted 50μm diameter devices with various cavity resonances in the range 990.4 to1059.9nm. These wavelengths are determined under 60mA pulsed conditions and correspond closely to 0mA d.c. values before the device has heated above the ambient temperature.

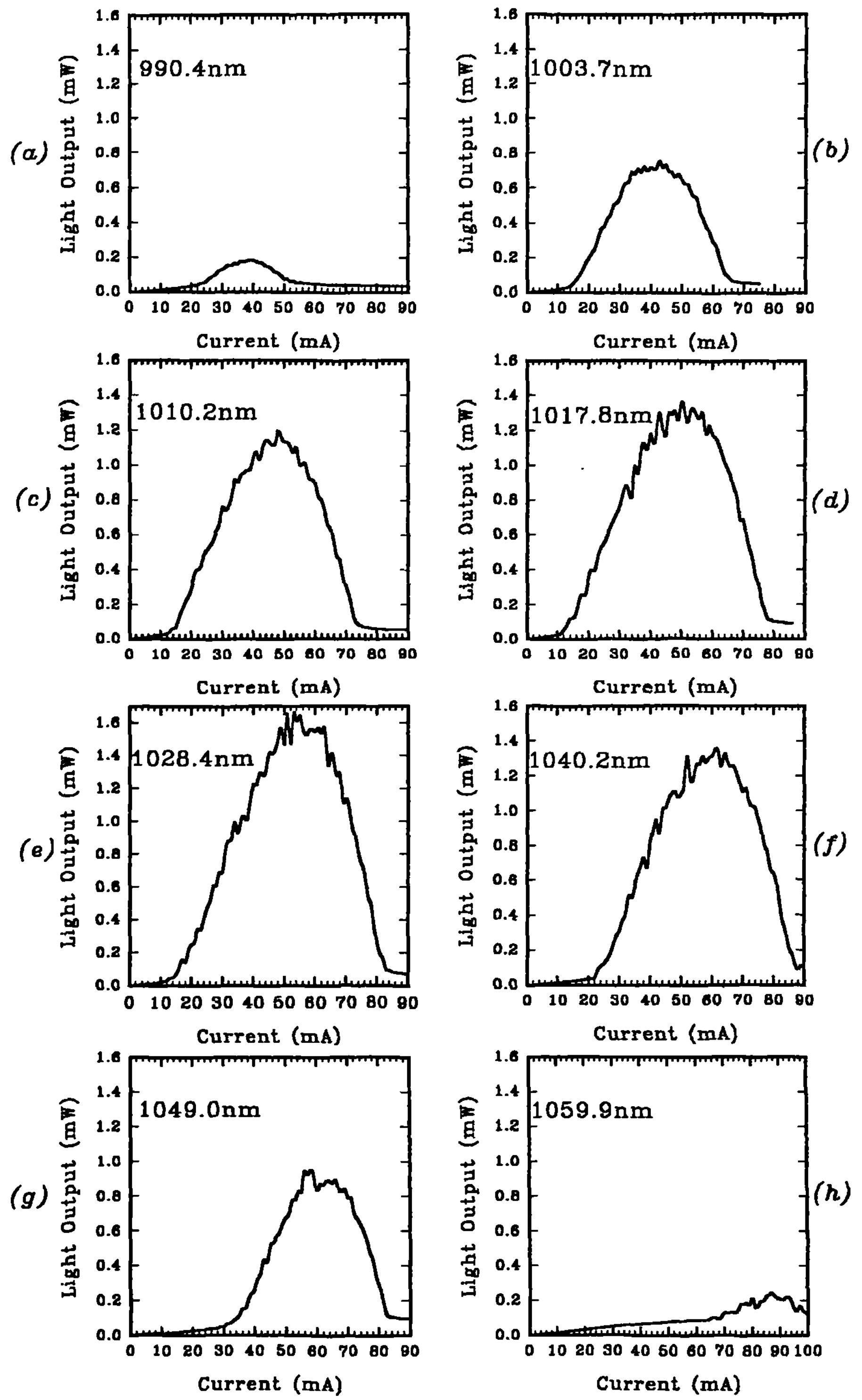

Fig. 6.35. c.w. L-I response of 50μm diameter ion implanted devices with cavity resonances (at 0mA) in the range 990.4 to 1059.9nm. (a)→(f) show progression of the response with increasing resonant wavelength.

It is seen from this figure that the threshold current I_{th} varies in a similar manner to that for pulsed operation with a minimum of ~12mA at around 1020nm. With ohmic heating of the device, the gain is eventually limited and a maximum output power P_0 is reached. The current at which this occurs I_{max} tends to increase with wavelength due to the relative alignment of the cavity mode (which is temperature and hence also current dependant) and the gain spectrum. In the same way, the current at which the coherent output power falls to zero I_0 also increases with wavelength. Due to the relative position of I_{th} and I_{max}, there is a maximum value of P_{max}. These effects will be discussed in more detail in chapter 7. Table 6.7 lists the parameters described in this paragraph for the a number of devices including those described in fig. 6.35.

λ(nm)	P_{max}(mW)	I_{max}(mA)	I_0(mA)	I_{th}(mA)
986.9	0	—	—	>100
990.4	0.19	39	55	22
995.1	0.40	41	60	18
1003.7	0.73	42	66	14
1010.2	1.17	48	74	14
1017.8	1.30	50	80	12
1024.8	1.08	50	75	13
1025.4	1.38	53	82	15
1028.4	1.65	57	86	13
1031.7	1.43	56	86	15
1036.1	1.12	56	83	18
1040.2	1.32	60	89	22
1044.9	1.02	60	85	27
1049.0	0.93	62	84	34
1054.4	0.65	64	82	36
1056.0	0.63	68	89	42
1059.9	0.23	86	100	66

Table 6.7. Summary of information for c.w. operation of 50μm diameter ion implanted devices. Cavity wavelengths are measured under a pulsed current of 60mA and correspond to 0mA d.c. values. I_{th} is the threshold current, P_{max} the maximum power output and I_{max} the current at which this is measured. I_0 is the current at which the coherent emission falls to zero.

The data in table 6.7. is presented graphically in figs. 6.36 and 6.37. In the first of these graphs the currents I_{th}, I_{max} and I_0 are plotted as a function of cavity wavelength. The envelope of c.w. operation is determined by the area between the lines I_{th} and I_0. The minimum threshold is shifted slightly to 1025nm from the minimum observed under pulsed operation. And to long wavelengths the threshold current is reduced, this occurs since heating effects cause shifts in the resonance wavelength and gain spectrum which bring them into better alignment[18,19].

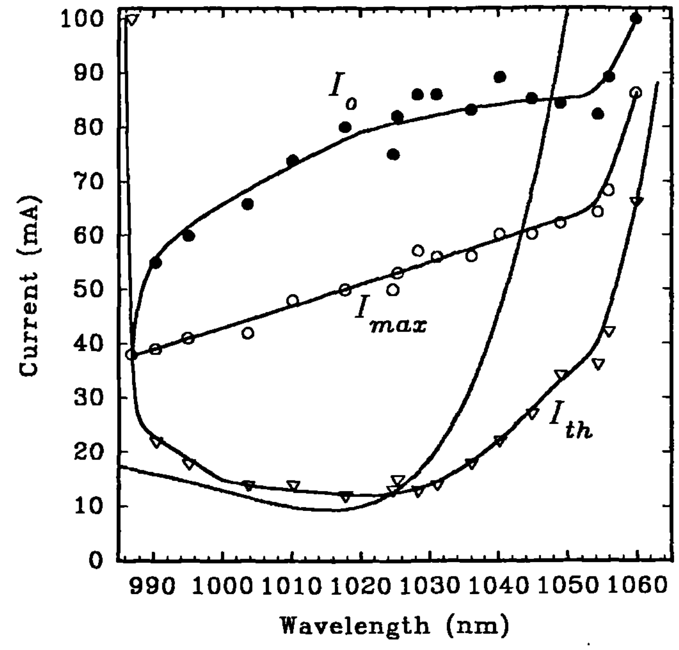

Fig. 6.36. Variation of current parameters for c.w. L-I response of 50μm diameter implant defined devices. I_{th} is the threshold current, P_{max} the maximum power output and I_{max} the current at which this is measured. I_0 is the current at which the coherent emission falls to zero. The grey line show the function $I_{th}(\lambda)$ for pulsed operation.

A line is fitted through the data in fig. 6.37 which shows the variation of the maximum output power as a function of cavity wavelength. There is some scatter on the data due to differences between devices; the fitted line indicates a maximum at 1028nm of 1.4mW. The maximum output falls to zero at 987 and 1066nm where excessive heating prevents lasing. The operating range would be increased and the maximum output power be increased, particularly to shorter wavelengths, if the device resistance could be further reduced so that there was less heating. Similarly in smaller devices where effects of heating are reduced we would expect a wider operating range.

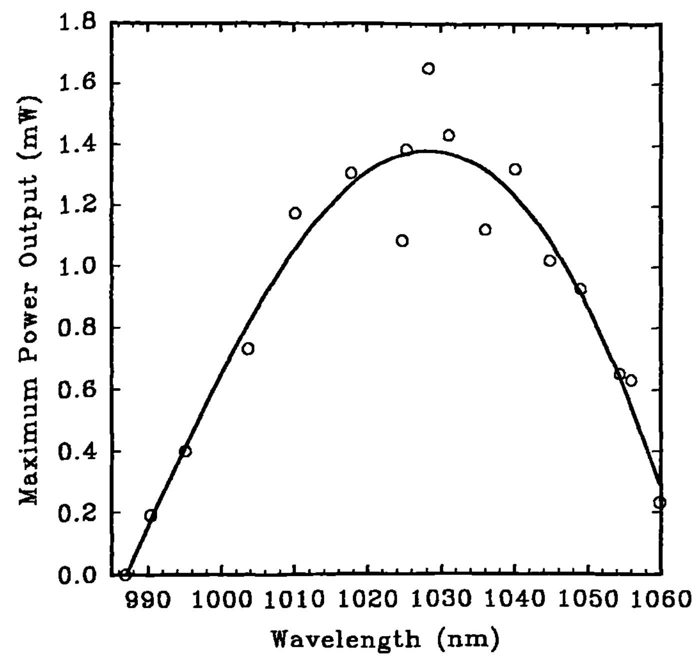

Fig. 6.37. Variation of the maximum output power P_0 with cavity resonance position for implant defined devices operating c.w.

References:

[1] T.E.Sale, J.Woodhead, R.Grey & P.N.Robson, *Wide operating range and low threshold current $In_{0.24}Ga_{0.76}As$ / GaAs vertical-cavity surface-emitting lasers*, IEEE Photon. Technol. Lett., 4, 11, pp1192-2294, 1992.

[2] Using the mathematical models developed in chapter 2, a CAD package was developed to model reflection spectra and similar parameters for complex multilayer structures in the AlGaAs system. This has been used here to determine growth errors by fitting to the measured spectrum.

[3] J.Woodhead, *Photoluminescence measurements on various InGaAs / GaAs quantum well samples at 10K and 300K provides a calibration relation for the shift of the transition energy between the two temperatures*, Private communication.

[4] J.O'Gorman & A.F.J.Levi, *Effect of fixed emission wavelength on threshold current of InGaAsP semiconductor laser diodes*, Electron. Lett., **28**, 22, pp2091-2093, 1992.

[5] J.O'Gorman & A.F.J.Levi, *Wavelength dependence of T_0 in InGaAsP semiconductor laser diodes*, Appl. Phys. Lett., **62**, 17, pp2009-2011, 1993.

[6] M.Sugimoto, H.Kosaka, K.Kurihara, I.Ogura, T.Numai & K.Kasahara, *Very low threshold current density in vertical-cavity surface-emitting laser diodes with*

periodically doped distributed Bragg reflectors, Electron. Lett., **28**, 4, pp385-387, 1992.

[7] R.S.Geels, S.W.Corzine, J.W.Scott, D.B.Young & L.A.Coldren, *Low threshold planarized vertical-cavity surface-emitting lasers*, IEEE Photon. Technol. Lett., **2**, 4, pp234-236, 1990.

[8] R.L.Williams, M.Dion, F.Chatenoud & K.Dzurko, *Extremely low threshold current strained InGaAs / AlGaAs lasers by molecular beam epitaxy*, Appl. Phys. Lett., **58**, 17, pp1816-1818, 1991.

[9] A.Yariv, *Scaling laws and minimum threshold currents for quantum-confined semiconductor lasers*, Appl. Phys. Lett., **57**, 4, pp1033-1035, 1988.

[10] Y.H.Lee, J.L.Jewell, A.Scherer, S.L.McCall, J.P.Harbison & L.T.Florez, *Room temperature continuous-wave vertical-cavity single-quantum-well microlaser diodes*, Electron. Lett., **25**, 20, pp1377-1378, 1989.

[11] P.Zhou, J.Cheng, C.F.Schaus, S.Z.Sun, K.Zheng, E.Armour, C.Hains, W.Hsin, D.R.Myers & G.A.Vawter, *Low series resistance high-efficiency GaAs / AlGaAs vertical-cavity surface-emitting lasers with continuously graded mirrors grown my MOCVD*, IEEE Photon. Technol. Lett., **3**, 7, pp591-593, 1991.

[12] A.Von Lehmen, C.Chang-Hasnain, J.Wullert, L.Carrion, N.Stoffel, L.Florez & J.Harbison, *Independently addressable InGaAs / GaAs vertical cavity surface-emitting laser arrays*, Electron. Lett., **27**, 7, pp583-585, 1991.

[13] J.W.Scott, S.W.Corzine, D.B.Young & L.A.Coldren, *Modelling the current to light characteristics of index-guided vertical-cavity surface-emitting lasers*, Appl. Phys. Lett., **62**, 10, pp1050-1052, 1993.

[14] J.W.Scott, R.S.Geels, S.W.Corzine & L.A.Coldren, *Modelling temperature effects & spatial hole burning to optimize vertical-cavity surface-emitting laser performance*, IEEE J. Quantum Electron., **29**, 5, pp1295-1308, 1993.

[15] R.A.Morgan, K.Kojima, M.Mullally, G.D.Guth, M.W.Focht, R.E.Leibenguth & M.Asom, *High-power coherently coupled 8×8 vertical cavity surface emitting laser array*, Appl. Phys. Lett., **61**, 10, pp1160-1162, 1992.

[16] P.Ressell, H.Strunsy, S.Gramlich, U.Zeimer, J.Sebastian & K.Vogel, *Optimised proton implantation step for vertical-cavity surface-emitting lasers*, Electron. Lett., **29**, 10, pp918-919, 1993.

---

[17] M.Orenstein, N.G.Stoffel, A.C.Von Lehmen, J.P.Harbison & L.T.Florez, *Efficient continuous wave operation of vertical-cavity semiconductor lasers using buried-compensation layers to optimise current flow*, Appl. Phys. Lett., **59**, 1, p31-33, 1991.

[18] D.B.Young, J.W.Scott, F.H.Peters, B.J.Thibeault, M.G.Peters, S-L.Lee & L.A.Coldren, *High-power temperature-insensitive gain-offset InGaAs / GaAs vertical-cavity surface emitting lasers*, Electron. Lett., **29**, 5, pp466-467, 1993.

[19] K.D.Choquette, N.Tabatabaie & R.E.Leibenguth, *Detector-enclosed, vertical-cavity surface emitting lasers*, Electron. Lett., **29**, 5, pp466-467, 1993.

7. Results of Experiments on MOCVD Grown Devices.

This chapter presents the experimental measurements made on the MOCVD grown VCSEL structures QT233 and QT421. Much of what is said in the previous chapter concerning experimental methods and material assessment applies equally to this chapter. QT233 was an early design so is mentioned only briefly in section 7.1. for comparative purposes. QT421, being of a much more mature design, constitutes the major part of this chapter, QT233 being included to show illustrate improvements made in the layer structure and growth process.

7.1. QT233

7.1.1. Structure

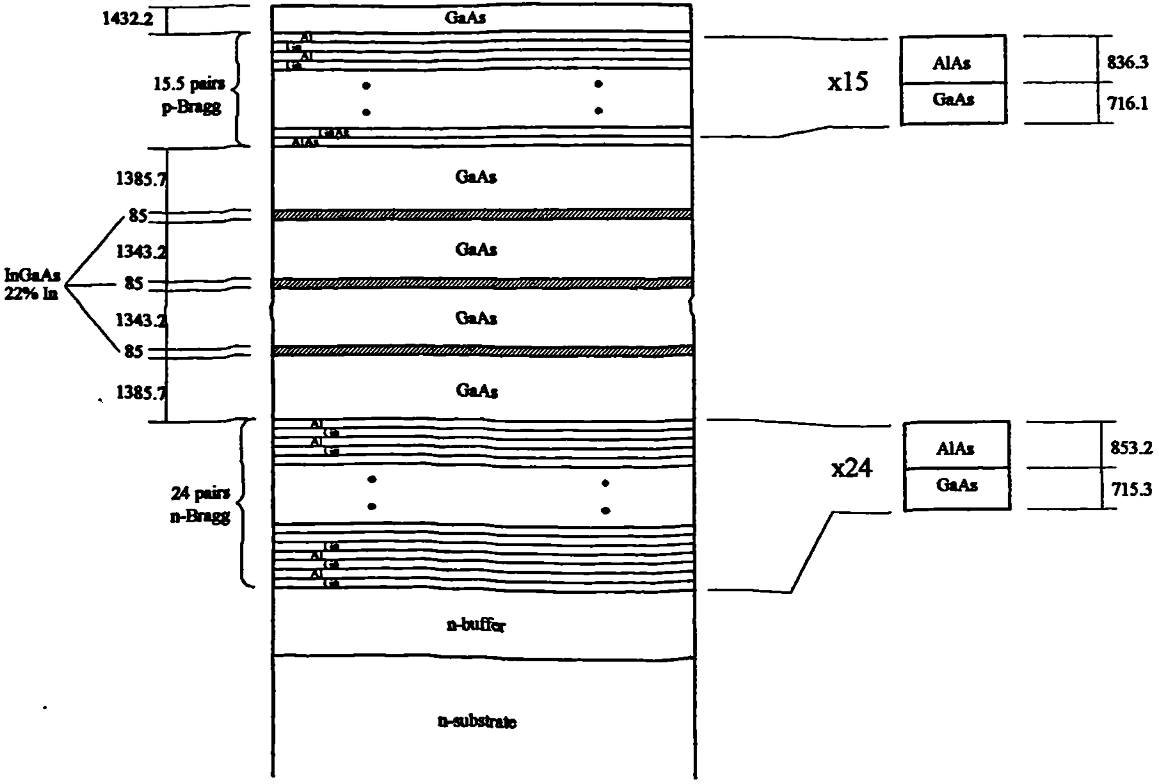

Fig. 7.1. Full layer structure of QT233, MOCVD grown VCSEL. Dimensions are given in units of Å.

Fig. 7.1 shows the full layer structure of QT233. It is intended to operate at a wavelength of λ=1000nm. It is of a much simpler design than the structures RMB627 and QT421. It incorporates 3×85Å $In_{0.22}Ga_{0.78}As$ quantum wells spaced by λ/2 as in RMB627. The upper and lower cavity reflectors are of the simple design described as type A in section 5.3.1.

The lower reflector consists of a 23½ pair AlAs / GaAs stack. No intermediate layers are included at the heterointerfaces, so the layer thicknesses are quarter wavelengths. It was doped n-type with silicon to give a carrier concentration of $3\times 10^{18}.\text{cm}^{-3}$ in the GaAs layers, reducing to $1\times 10^{18}.\text{cm}^{-3}$ AlAs layers, the difference being due to the p-type counter-doping by C as a result of decomposition of TMA during the growth of AlAs (see section 5.3.1).

The upper reflector consists of a 15 pair AlAs / GaAs stack also of the simple quarter wave design. This was doped p-type with zinc to a concentration of $1\times 10^{18}.\text{cm}^{-3}$. Impurity concentrations were determined by electrochemical profiling.

The structure was grown simultaneously on two Si doped GaAs substrate wafers which had sawn back surfaces. The reflector stacks were grown at a temperature of 700°C whilst the cavity region and quantum wells were grown at the lower temperature of 650°C.

7.1.2. Assessment

The reflectivity spectrum was measured at the centre of the upstream wafer. It is similar to that calculated for the ideal structure except it shows a cavity resonance slightly offset from the centre of the mirror high reflectance band. The growth reactor interior had not been suitably optimised for uniform deposition thickness giving rise to a large variation across the two wafers, fig.7.2 shows the map of the position of the cavity resonance across the upstream wafer. There is no clear single resonance detectable on the downstream wafer indicating variable or turbulent gas flows during growth.

The uniformity of the resonance wavelength is ±1% around an average value of 995nm over approximately 50% of the wafer. There is more variation to the upper left side shown in fig. 7.2. where the resonance is not measured.

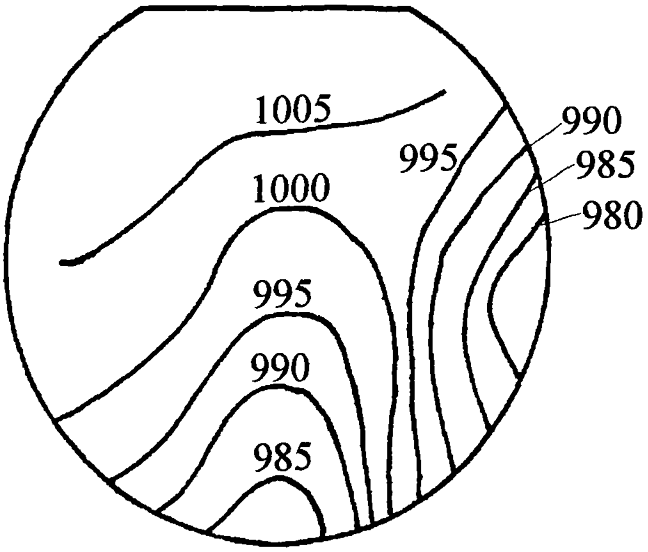

Fig. 7.2. Map of the cavity resonance wavelength variation in nm across the upstream wafer QT233.

Fig. 7.3. shows a typical photoluminescence spectrum measured at 15K from the upstream wafer of QT233. It exhibits a broad peak of 30meV FWHM at an energy of 1280meV. This corresponds to an indium fraction of 25.0% (determined from model in section 3.2.2) and a 300K transition at 1038nm[1].

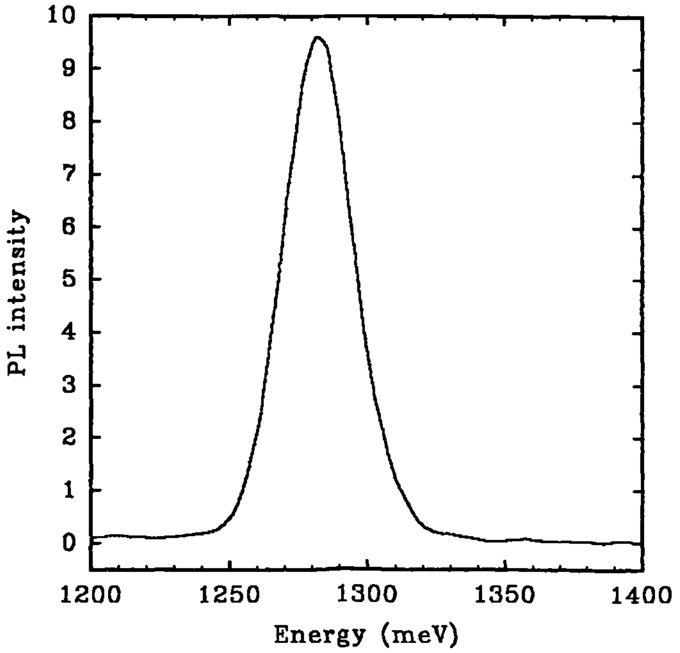

Fig. 7.3. Typical photoluminescence spectrum from QT233 upstream wafer.

Mesa etched devices were fabricated from a suitable piece of the upstream wafer with a resonance close to 1000nm (see chapter 4 for fabrication details). The relative alignment of the cavity resonance and quantum well transition is not optimum but should allow reasonable lasers to be made (see fig. 6.14).

7.1.3. I-V Measurements

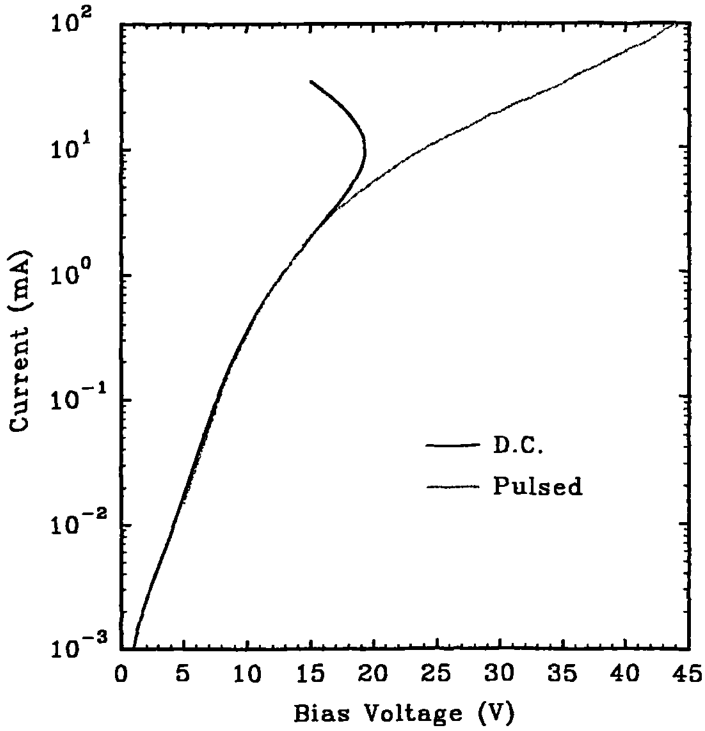

Fig. 7.3. Pulsed and c.w. I-V measurements on 50μm diameter devices from QT233.

Fig. 7.3. shows the results of pulsed and d.c. I-V measurements made on 50μm diameter devices. As the graph shows the bias required to pass a current density of 1kA.cm^{-2} is 30V under pulsed conditions and 18V d.c. Device heating causes thermal runaway and negative differential resistance at 19V where the current flowing is 10mA or 510kA.cm^{-2}.

7.1.4. L-I measurements

50μm diameter devices were driven with 800ns pulses. Output spectra were measured for current pulses of varying amplitudes and are shown in fig. 7.4. At low currents little output is detected. Above 20mA a broad emission of several nanometers linewidth becomes evident. This is thought to be amplified stimulated emission (ASE) filtered by the cavity resonance mode. At 50mA a narrow mode develops, with a FWHM linewidth of approximately 0.5nm (equivalent to the spectrometer resolution). This grows rapidly with increasing current illustrating laser operation. Heating during the 800ns pulse causes a broadening of the spectrum at higher currents.

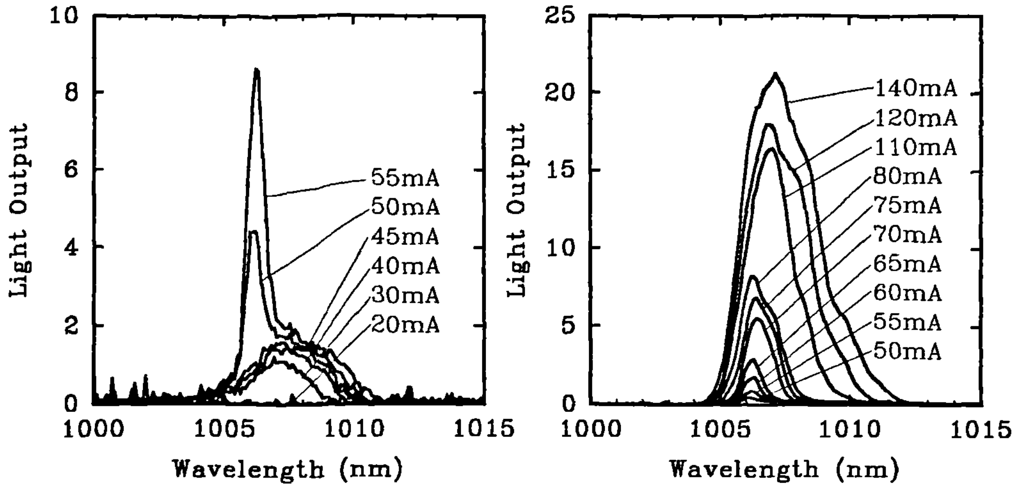

Fig. 7.4. Output spectra from 50μm diameter device from QT233 driven with 800ns current pulses of various amplitudes. A narrow mode becomes evident at 50mA, this broadens at higher current as heating causes chirp during the pulse width.

Fig. 7.5. shows the L-I response derived from the spectra of fig. 7.4. From this a threshold current of 65mA is deduced. This corresponds to a current density of 3310A.cm^{-2}. From fig. 7.3 it can be understood that these devices cannot operate c.w. as ohmic heating would take the device well into the region of negative differential resistance and thermal runaway. These measurements represent the best devices available on the wafer; the quantum well quality over much of the area is very poor and most devices did not work at all.

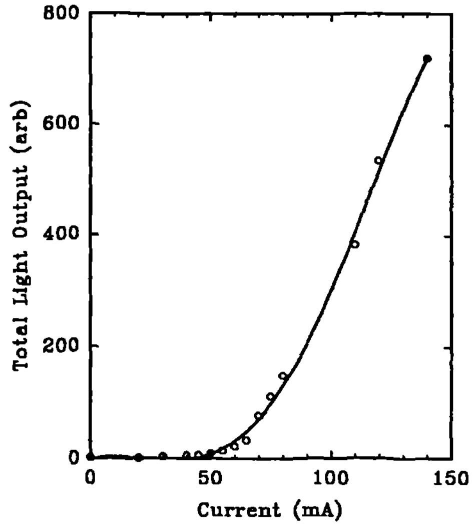

Fig. 7.5. L-I response of 50μm diameter device from QT233 driven with 800ns pulses. Data is deduced from fig. 7.4.

QT421

7.2. Structure

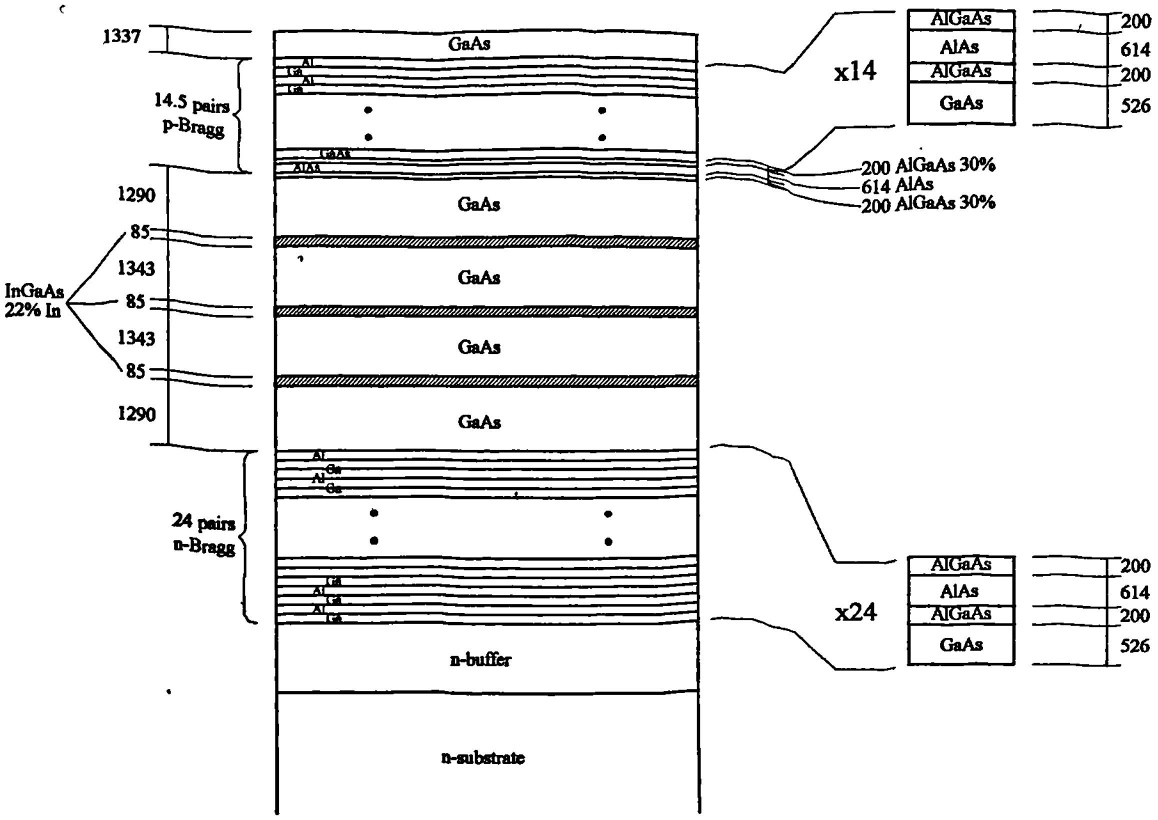

Fig. 7.6. Full layer structure for QT421 MOCVD grown VCSEL. Dimensions are given in units of Å.

The full growth structure of QT421 is shown in fig. 7.6. As for RMB627 and QT233 it is designed to operate at a wavelength λ=1000nm and so has a similar undoped active cavity region. This comprises three 85Å $In_{0.22}Ga_{0.78}As$ quantum wells spaced by $\lambda/2$ in a 2λ thick region of GaAs.

The structure was grown in two separate growth runs. First the lower reflector stack was grown. Two double polished Si doped GaAs wafers were used as substrates. The reflector was grown at a temperature of 700°C. Preliminary assessment was carried out on the wafers before the downstream wafer was returned to the reactor for the growth of the remainder of the VCSEL structure; i.e. quantum wells and cavity region and the upper reflector stack. The top reflector was again grown at a temperature of 700°C and the quantum wells and cavity region were grown at the reduced temperature of 510°C to prevent desorption of the indium phase (see chapter 4). A separate monitor piece of substrate was included in each growth run to enable mesas for I-V measurements to be fabricated and electrochemical profiling to be performed, both destructive tests, on the top and bottom reflectors individually. As described in chapter 4 the AlAs layers were grown with TMA which had been fractionally distilled within the growth system and left to settle for several weeks[2]. Commercial supplies of TMA are contaminated with oxygen and, if used directly for growth, gives rise to a concentration of oxygen in the grown AlAs of 2→3× 10^{18}.cm^{-3}. Oxygen acts as a trap in AlGaAs compounds reducing the effect of doping; this is particularly important in the vicinity of the reflector heterointerfaces. Use of the distilled TMA allows the oxygen concentration incorporated in AlAs to be significantly reduced to 5×10^{17}.cm^{-3}. The interior geometry of the growth reactor had been altered from that used in QT233 to provide more uniform gas flows and hence a more uniform deposition rate over the wafer. In particular the susceptor angle was reduced to from 1.0° to 0.5°.

The reflector stacks are those described in section 5.3.7. The lower reflector is a 23½ pair AlAs / GaAs stack with 200Å intermediate $Al_{0.3}Ga_{0.7}As$ layers for the reduction of interface resistances[2,3]. It is doped n-type with Si to a mean concentration of 1.6×10^{18}.cm^{-3}.

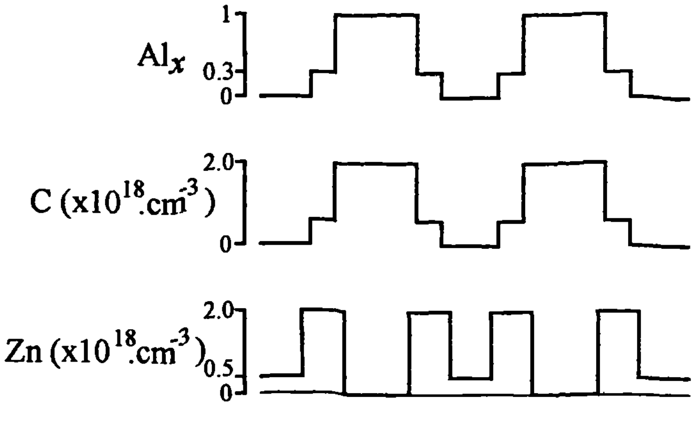

Fig. 7.7. Doping detail of upper (p-type) reflector. Carbon is incorporated from decomposition products of TMA and zinc is intentionally added from TMZ.

The upper reflector is a 15 pair AlAs / GaAs stack of similar design. It incorporates 200Å intermediate $Al_{0.3}Ga_{0.7}As$ layers and is doped p-type. Modulation doping as shown in fig. 7.7 is used to achieve minimal optical loss for a structure with low resistance. The AlAs layers need no intentional doping as the residual C doping of ~2×10^{18}.cm^{-3} from TMA decomposition products is sufficient. The GaAs layers are doped with Zn to a level of 5×10^{17}.cm^{-3}. The intermediate layers and the material immediately surrounding them is zinc doped to 2×10^{18}.cm^{-3}. The electrochemical profile of this stack indicates a constant doping level of 1×10^{18}.cm^{-3} but this measurement cannot reveal any detail finer than a few 100Å.

7.3. Material Assessment

As for the structures mentioned previously, photoluminescence and photoreflectance measurements were made to identify areas of the wafer suitable for the fabrication of devices.

7.3.1. Photoreflectance

The photoreflectance spectrum was measured at a number of points across the wafer. Fig. 7.8 shows a spectrum measured at a point close to the centre of the wafer. The shape of the spectrum is similar at different points across the wafer indicating that thicknesses of individual layers vary in sympathy. There is little wavelength variation across much of the wafer.

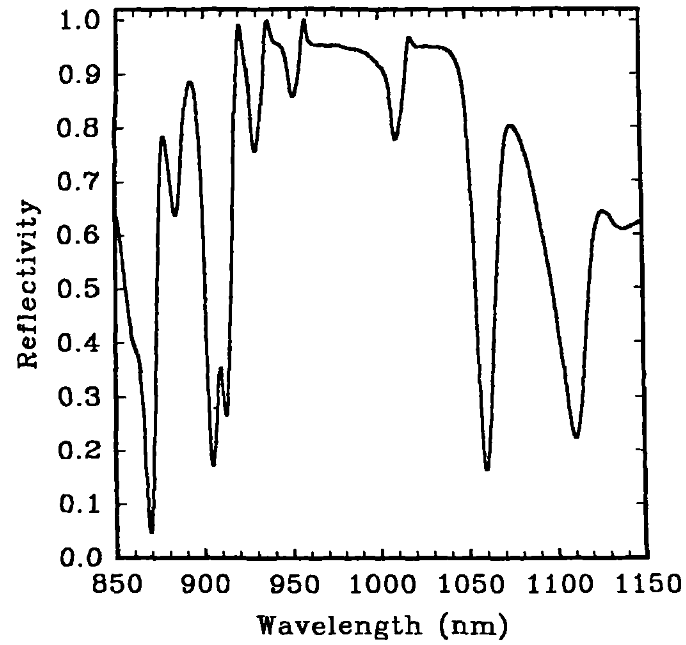

Fig. 7.8. Photoreflectance spectrum measured close to the centre of the MOCVD grown VCSEL structure QT421.

As can be seen from the spectrum, the main cavity resonance, identified in fig. 7.8, is not in the centre of the high reflectance band. This might cause problems by reducing the cavity finesse at the resonant wavelength. The high reflectance band appears broader than for previous structures indicating an offset in the periods of the two reflector stacks. Simulation of the structure using the RCAD^{4} program identifies the layer thicknesses to an accuracy better than 0.5%, these are given in table 7.1. The calculated spectrum for a structure with these dimensions is shown in fig. 7.9.

	Ideal Value	As Grown	Error
Period of upper reflector stack	1548Å	1500Å	-3.2%
Period of lower reflector stack	1548Å	1548Å	0%
Cavity length	5750Å	4257Å	+7.4%
Resonant wavelength	1000nm	1010	+1%

Table 7.1. Layer thicknesses of QT421 at a point close to the wafer centre compared to ideal values.

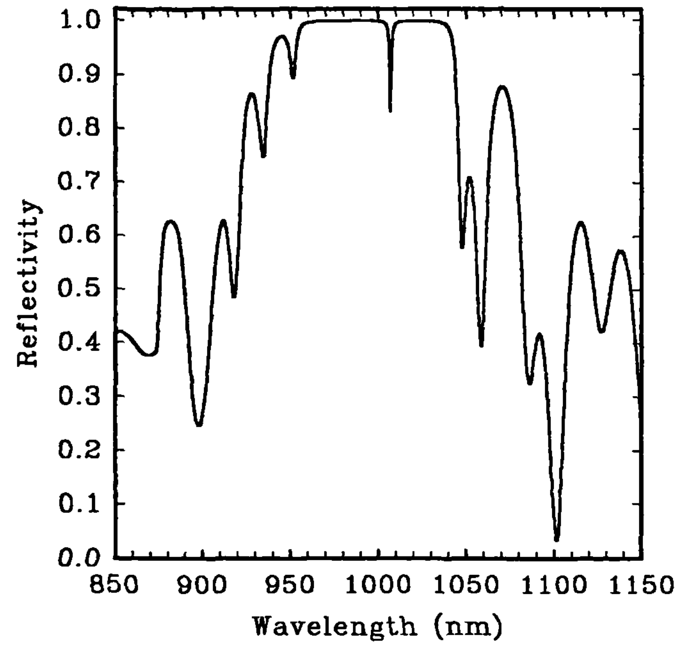

Fig. 7.9. Calculated photoreflectance spectrum to fit spectrum measured in centre of wafer QT421

As the table shows the bottom reflector was grown very close to the design. A photoreflectance measurement was made in the clean room on the lower reflector before the growth of the cavity and top reflector. This reveals a high reflectance band centred at 998.7nm at the wafer centre and is agreement with the figures in the table. The top reflector was grown slightly too thin. The cavity region was grown 7.4% too thick as it proved difficult to calibrate the growth rate for the reduced temperature. The error in the cavity resonance is only +1.0% since the phase compensation (see section 2.2.5) of the reflectors reduces the error. The lower reflector retains a high reflectivity over a relatively broad band (20nm) as a result of absorption in its layers, which tends to flatten the reflectivity spectrum. The upper reflector, although it is centred some way from the cavity resonance, still has a high reflectivity at the resonant wavelength as it is augmented with a gold layer in fabricated devices. This layer broadens the high reflectivity band considerably. The complete structure is only slightly worse than the ideal having a estimated gain for threshold of 441.cm^{-1} compared with 346.cm^{-1} for the ideal structure (see chapter 8).

As suggested above, the uniformity of the cavity wavelength across the wafer is excellent. Fig. 7.10 shows a contour map derived from photoreflectance spectra taken at points across the wafer. The resonance lies between 1000 and 1020nm over approximately 80% of the wafer. This is a ±1% variation about 1010nm and is achieved by optimisation of the growth reactor interior for uniform gas flows.

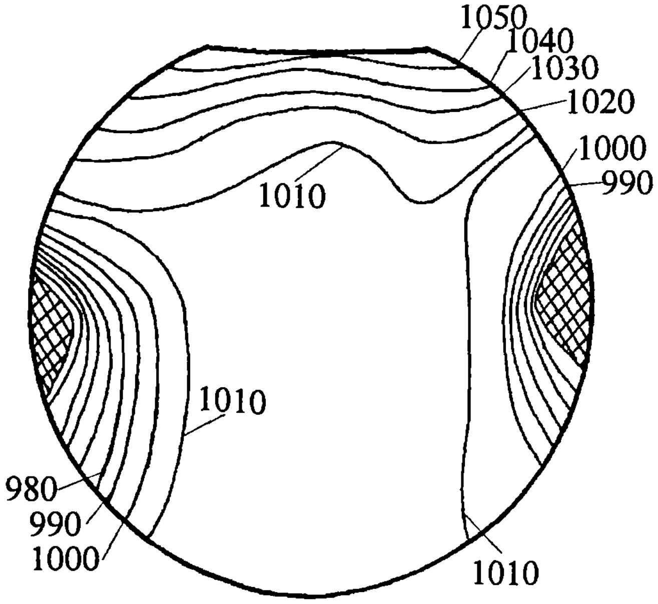

Fig. 7.10. Contour map showing variation of cavity resonance wavelength in nm across the wafer QT421.

7.3.2. Photoluminescence

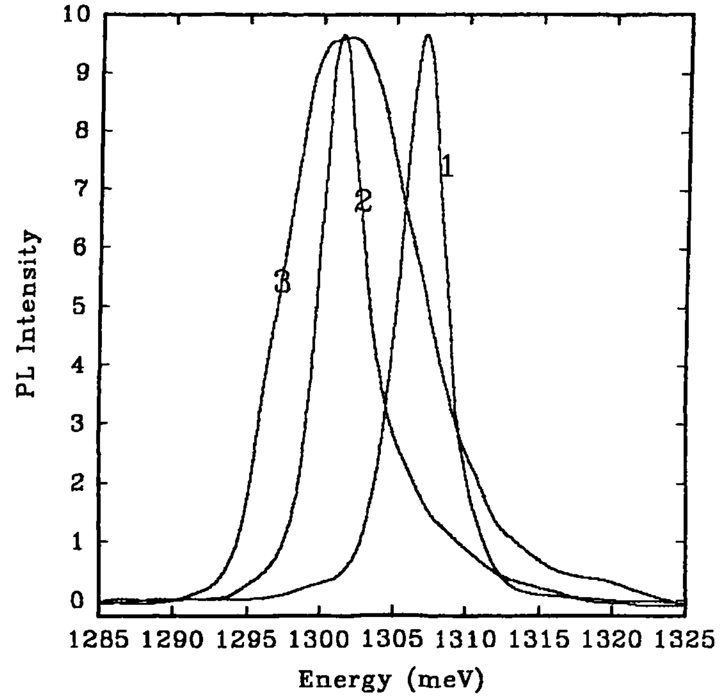

Fig. 7.11. 15K PL spectra taken from wafer QT421. Lines 1 and 2 indicate variation of narrow linewidth emission detected from central region of the wafer. Line 3 gives an example of the broader emission detected close to the wafer's edge.

Low temperature (15K) photoluminescence measurements were made at a number of points across the wafer to determine the quality and indium fraction of the quantum wells. Fig. 7.11 shows typical PL spectra taken at three of these points. Except right at the edge of the wafer, the PL emission is in a single peak at an energy ranging from 1.300 to 1.320eV depending on the position and is bright with a FWHM linewidth of 10meV or less. Over much of the wafer (80%) the variation is 1.302 to 1.310eV with a FWHM of ~3meV. Table 7.2. summarises this data and gives the corresponding e_1hh_1 transitions calculated for room temperature, also listed are the well indium fractions assuming 85Å wells (determined as in section 3.2.2).

The well compositions estimated from the PL results are very close to the desired value of 22% indicating lowest energy transitions occurring at wavelengths in the range 1005 to 1022nm. These wavelengths are close to the cavity resonant wavelengths. From the data collected on MBE grown devices in the previous chapter and from the estimates of gain spectra made in chapter 3 one would predict that a large fraction of the wafer would produce devices with low threshold currents. Devices made from regions of the wafer where the cavity resonance and e_1hh_1 transition are coincident should operate with the lowest threshold currents. Over much of the wafer the cavity resonance is to the short wavelength side of the e_1hh_1 transition; this is the preferred side for minimal increase in threshold current.

	Across Wafer	Central Region
15K PL energy	1.300→1.320eV	1.302→1.310eV
Linewidth FWHM	≤10meV	~3meV
λ (300K)	1005.5→1021.8nm	1013.1→1020.0nm
In (%)	21.3→23.2%	22.2→23.0%

Table 7.2. PL results from QT421. The estimated indium fractions assume 85Å well widths. The wavelengths are the estimated lowest e_1hh_1 transitions at room temperature.

7.4. Processing

Much of the wafer QT421 is suitable for producing devices. The better devices would be expected to come from the uniform area of the wafer where the cavity resonance lies in the range 1000 to 1020nm. The wafer was cleaved into quarters as shown in fig. 7.12. Both parts of Q4 were fabricated into etched mesa devices by reactive ion etching using $SiCl_4$ to a depth of 3.5μm. A 200keV proton implant[5] was used to define devices in Q1 which had been divided into several pieces so that different implant doses[6] in the range $3\times10^{12}.cm^{-2}$ to $1\times10^{15}.cm^{-2}$ could be used for each. Further details of the fabrication are given in chapter 4.

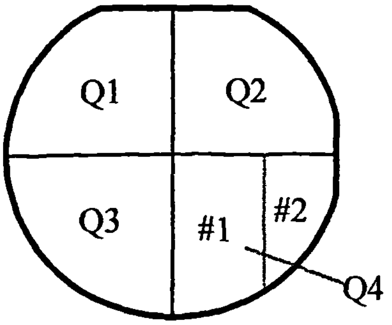

Fig. 7.12. Quarters of wafer QT421 selected for processing.

7.5. Measurements on etched mesa devices

The experimental apparatus and method is the same as previously used for MBE grown devices and is described in section 6.3.

7.5.1. I-V measurements

Pulsed and d.c. I-V measurements were made on 50μm diameter etched mesa devices. Fig. 7.13. Shows the results of these measurements on both logarithmic and linear scales.

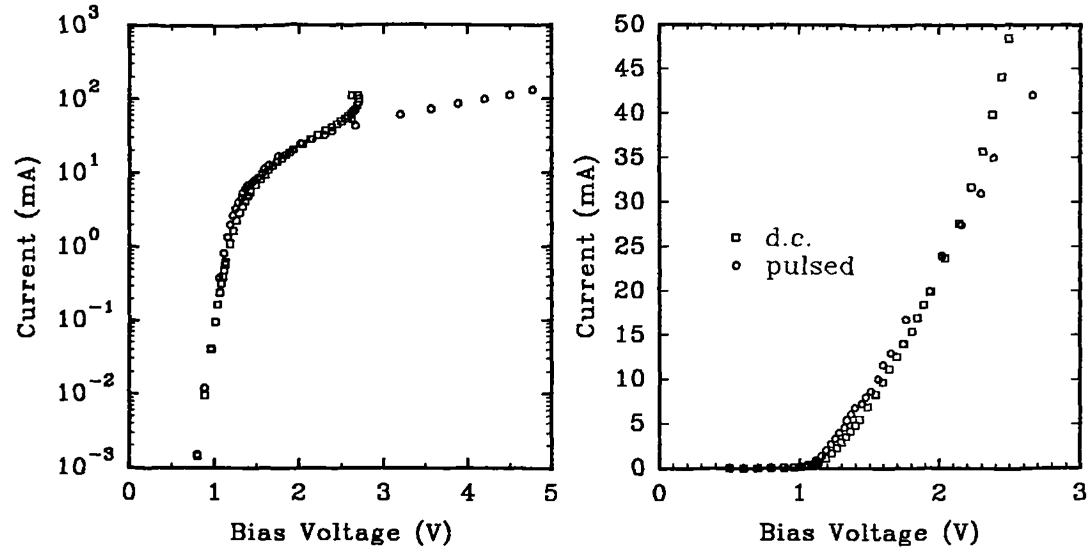

Fig. 7.13. Pulsed and d.c. I-V measurements made on 50μm diameter mesa etched devices from QT421Q4 shown on (a) logarithmic and (b) linear scales.

As the graphs show the bias for a current density of 1kA.cm^{-2} (19.6mA) is less than 2V (1.95V) for both d.c. and pulsed operation. There is little difference between the two curves at this current density indicating little detrimental heating effect. Even at 100mA or 5.1kA^{-2}, the limiting current of the supply equipment, d.c. operation is still possible without permanent damage to the device.

7.5.2. Pulsed L-I measurements

Devices were tested under pulsed conditions. 430ns pulses were applied with an 18μs repetition period. Output was monitored on the μW power meter as in 6.4.2. Fig. 7.14 shows current light responses for two typical 50μm diameter devices. The device driven to higher currents delivers a maximum peak output power of 46mW at a current of 340mA.

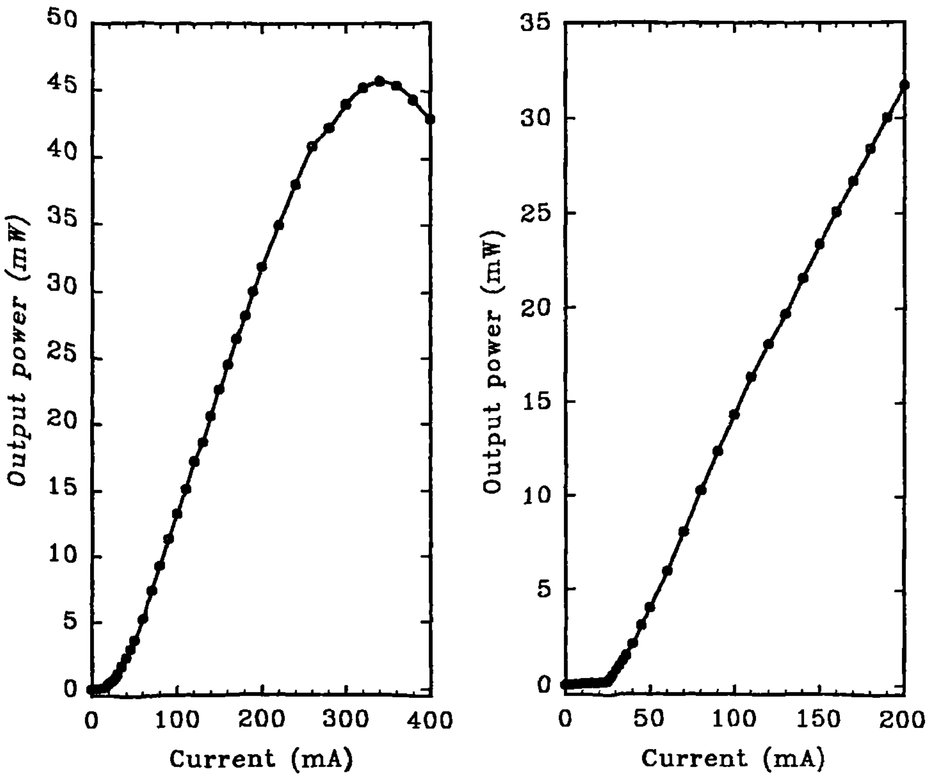

Fig. 7.14. Pulsed current light measurements on two typical 50μm diameter devices from QT421 (a) device operating at 1012.1nm, (b) device operating at 1010.9nm.

All devices more than ~8mm away from the wafer edge operate as lasers with the characteristic superlinear increase in light output with increasing current above a threshold value. The threshold current of most devices is close to 20mA with a minimum value of 15mA. Table 7.3 summarises the results for 50μm devices from different locations across the sample. Wavelengths are determined from the maximum spectral output at a pulsed current of 60mA.

Due to the good wafer uniformity, the range of wavelengths is rather narrow; 997 to 1022nm. There are some devices closer to the edge of the wafer with shorter cavity wavelengths but these do not operate. There are two reasons for this: (i) Indium desorption close to the wafer edges gives very shallow wells which provide little carrier confinement; (ii) Rapid changes of growth thickness with lateral distance close to the wafer edge reduces the finesse of the optical cavity. Device number 19 (table 7.3) is close to the wafer edge and there is considerable growth thickness variation across its 50μm diameter so it operates in several wavelength modes simultaneously. All other devices tested operate at a single wavelength in the absence of d.c. heating effects, the spectrum of a more typical device is shown in fig. 7.15. The linewidth for 60 mA pulses is ~0.5nm as is a result of chirp caused by device heating during the pulse.

Number	Square	I_{th}(mA)	J_{th}(A.cm^{-2})	λ(nm)	η_{eff}(%)
1	(11,6)	19	968	1017.8	—
2	(1,5)	15	764	1020.2	—
3	(13,5)	18	917	1012.1	16.0
4	(2,5)	22	1120	1020.2	12.8
5	(3,5)	28	1426	1020.4	11.1
6	(4,5)	28	1426	1020.6	13.2
7	(5,5)	26.8	1365	1020.9	16.0
8	(6,5)	27.5	1401	1021.4	14.0
9	(7,5)	27.5	1401	1021.3	13.2
10	(8,5)	27.0	1375	1021.3	12.8
11	(9,5)	50	2546	1021.1	2.1
12	(10,5)	24.8	1263	1020.3	16.5
13	(11,5)	18.6	947	1018.5	13.2
14	(12,5)	23	1171	1017.2	19.3
15	(13,5)	25.7	1309	1010.9	21.4
16	(14,5)	18.8	957	1005.3	18.1
17	(15,5)	24	1222	997.0	9.1
19	(15,5)	23	1171	985→995	—
20	(15,5)	29.3	1492	999.6	15.2
21	(14,5)	25	1273	1002.1	17.3
22	(14,5)	20.5	1044	1003.2	20.6
23	(14,5)	22.4	1141	1003.9	18.1
24	(14,5)	26	1324	1005.0	19.7
25	(14,5)	21.2	1080	1007.4	16.9
26	(13,5)	17.2	876	1008.7	14.4
27	(13,5)	23	1171	1009.8	17.3
28	(13,5)	22.8	1161	1012.1	20.6
29	(12,5)	22	1120	1013.7	18.9
30	(12,5)	20	1019	1014.9	14.8
31	(11,5)	22.6	1151	1017.5	15.2
32	(11,5)	23.6	1202	1019.1	16.9
33	(15,5)	29.5	1502	999.1	14.4

Table 7.3. Summary of results of pulsed L-I measurements on QT421Q4#1 50μm diameter etched mesa VCSEL devices.

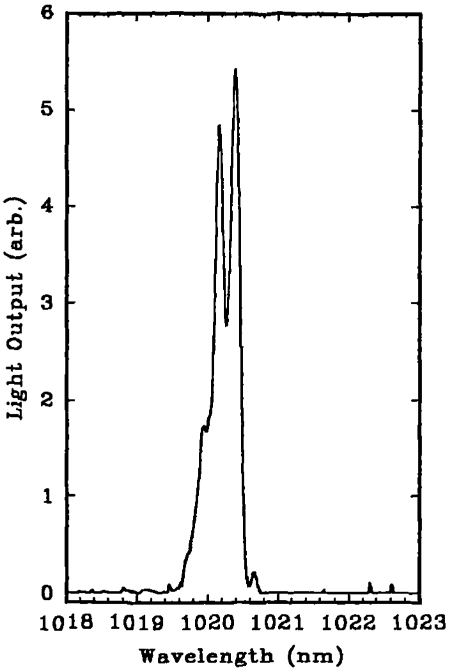

Fig. 7.15. Output spectrum of typical 50μm diameter device (number 5) operating under pulsed conditions. Emission is in a single narrow line which is broadened slightly due to chirp during the 430ns pulse.

The variation of threshold current with wavelength is shown in fig. 7.16. Compared with the MBE grown devices (see section 6.4.2), there is little variation in the cavity wavelength (997→1022nm) between the working devices and there is a comparable variation in the e_1hh_1 transition (1005→1022nm). So for most devices the transition and cavity resonance likely to be within 10nm of each other. By comparison with the MBE grown devices one would expect that these devices would also operate with low threshold currents. Referring to the curve in fig. 6.14, the variation in threshold currents is expected to be small and is what we observe in fig. 7.16. There appears to be little wavelength dependence of threshold current but a large scatter of the data around a value of 20mA. This scatter is a result of variation in the relative wavelengths of the cavity and lowest transition, which gives rise to thresholds in the region 15 to 30mA. The minimum value of 15mA, or 764A.cm^{-2}, indicates that devices fabricated from the part of the wafer close to this device possess the optimum alignment of quantum well transition and cavity resonance wavelengths. The threshold voltage of this device is 1.7V. Devices fabricated on parts of the wafer where the quantum well quality is poor, either due to defects or indium desorption near the wafer edges, have increased thresholds or do not lase. The differential quantum efficiency η_{eff} has an average value of 15.48% and the variation between devices has a standard deviation of 3.86%. This efficiency is 1.37 times that measured for devices fabricated from the layer RMB627. The improvement is likely to be due to the higher quality quantum wells in the structure QT421. The narrow linewidth of the PL emission suggests that the non-radiative lifetime of carriers in this layer is much higher which will result in higher quantum efficiency. The standard deviation between devices is a similar proportion of the mean value for both layers

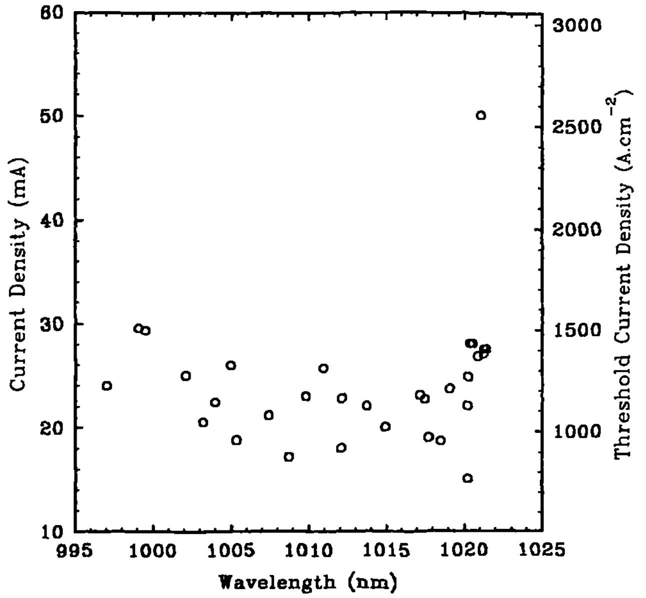

Fig. 7.16. Variation of threshold current with wavelength for 50μm diameter MOCVD grown VCSEL devices.

7.6. c.w. operation

7.6.1. c.w. L-I measurements

At a current of 20mA, which is above threshold for many of the devices, the bias voltage across a 50μm diameter device is 1.96V. This is considerably less than for other structures reported in this thesis. The ohmic heating is therefore much reduced, allowing an extended c.w. operating range.

Devices were driven c.w. using a microprocessor controlled current source measurement unit. No external heatsinking was used. Fig. 7.17 shows L-I responses of two typical 50μm devices. As for the MBE grown devices described in chapter 6, oscillations are observed in the light output as the current is varied[7]. This is due to a thermally induced shift with current of the cavity resonance past the almost static Fabry-Perot modes in the substrate. The period of the oscillations is longer than for devices from RMB627 as the low resistance of the mirrors means that the heating is considerably reduced. Anti-reflection coating of the lower surface of the surface of the substrate should remove these oscillations[7].

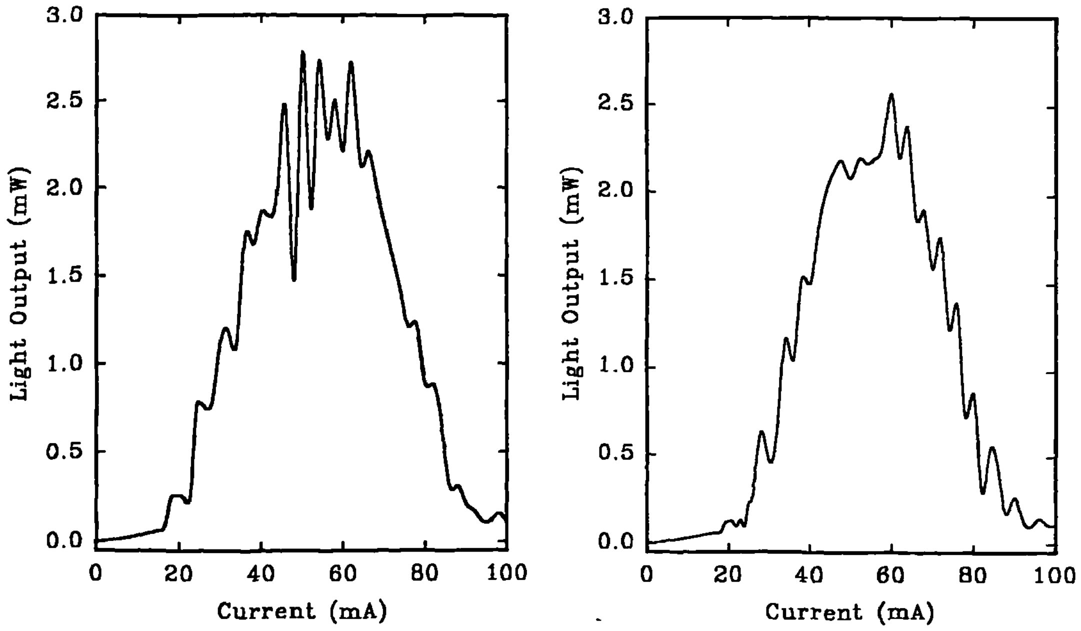

Fig. 7.17. c.w. L-I response of two typical 50μm diameter devices.

Note that for both devices a maximum light output is obtained at a current of ~55mA, giving maximum output powers of 2.8mW and 3.6mW. The threshold currents measured are 17mA & 19mA and are the same as the values measured under pulsed conditions. The bias voltages at threshold for these devices are 1.86V and 1.93V. The current source is limited to 100mA output; at this current there is still some light output and no permanent deterioration of the device performance occurs; i.e. the curves in the figure may be traversed an arbitrary number of times without significant change. These threshold voltages are comparable with the lowest reported for VCSELs with current injection through the reflector stacks[8,9,10], except for one structure operating at 1.5V for a structure employing continuously graded reflectors[11].

20μm diameter devices were also measured. A typical L-I response of one of these is shown in fig. 7.18.

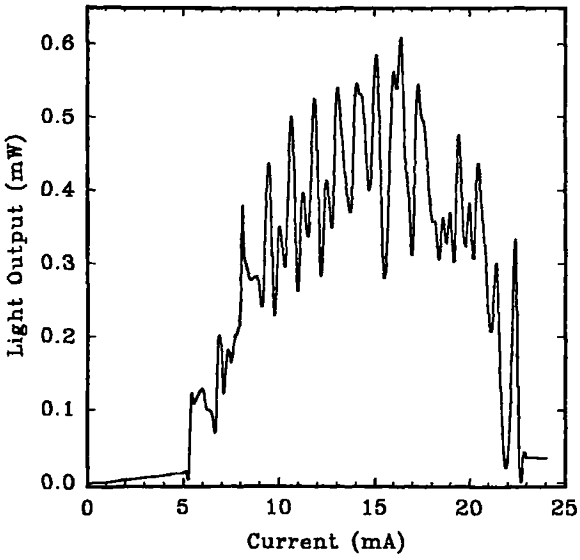

Fig. 7.18. c.w. L-I response of a typical 20μm diameter device.

For this device we measure a threshold current of 5.2mA (1655A.cm^{-2}). The L-I response is similar in form to those for the larger devices but the oscillations are more pronounced. This is possibly due to the reduced number of transverse modes in the smaller diameter mesa. A maximum output of 0.61mW is detected at a current of 16mA. Excessive heating has reduced the stimulated emission to zero at a current of 23mA.

The limiting currents for maximum light output from these devices are summarised in table 7.4. As expected the smaller device is limited at a higher current density because it has a larger periphery in proportion to its area (see chapter 8).

Diameter (μm)	**I for L_{max}**	**J for L_{max}**
50	55mA	2801A.cm^{-2}
20	16mA	5093A.cm^{-2}

Table 7.4. Current for maximum light output for 50 and 20μm diameter etched mesa devices from QT421.

7.6.2. Lasing spectra and thermal parameters

For a number of different currents the c.w. lasing spectra of a 50μm diameter device were measured. Fig. 7.19 shows how the output spectrum develops with increasing current. From the spectra in fig. 7.19a the output appears to be confined to modes spaced in wavelength by ~0.36nm. This corresponds to the Fabry-Perot (FP) mode spacing in a 400μm GaAs cavity, 3.56Å to be exact, which corresponds to the substrate thickness. At currents below 30mA (~1500A.cm^{-2}) only one peak is observed in the spectrum, this indicates a small temperature variation, less than 0.70°C, across the device (see section 8.2). At higher currents a non-uniform temperature profile develops and multiple peaks may be observed. At currents where FP mode switching occurs, the light output passes through a local minimum as the cavity resonance passes through a substrate anti-resonance.

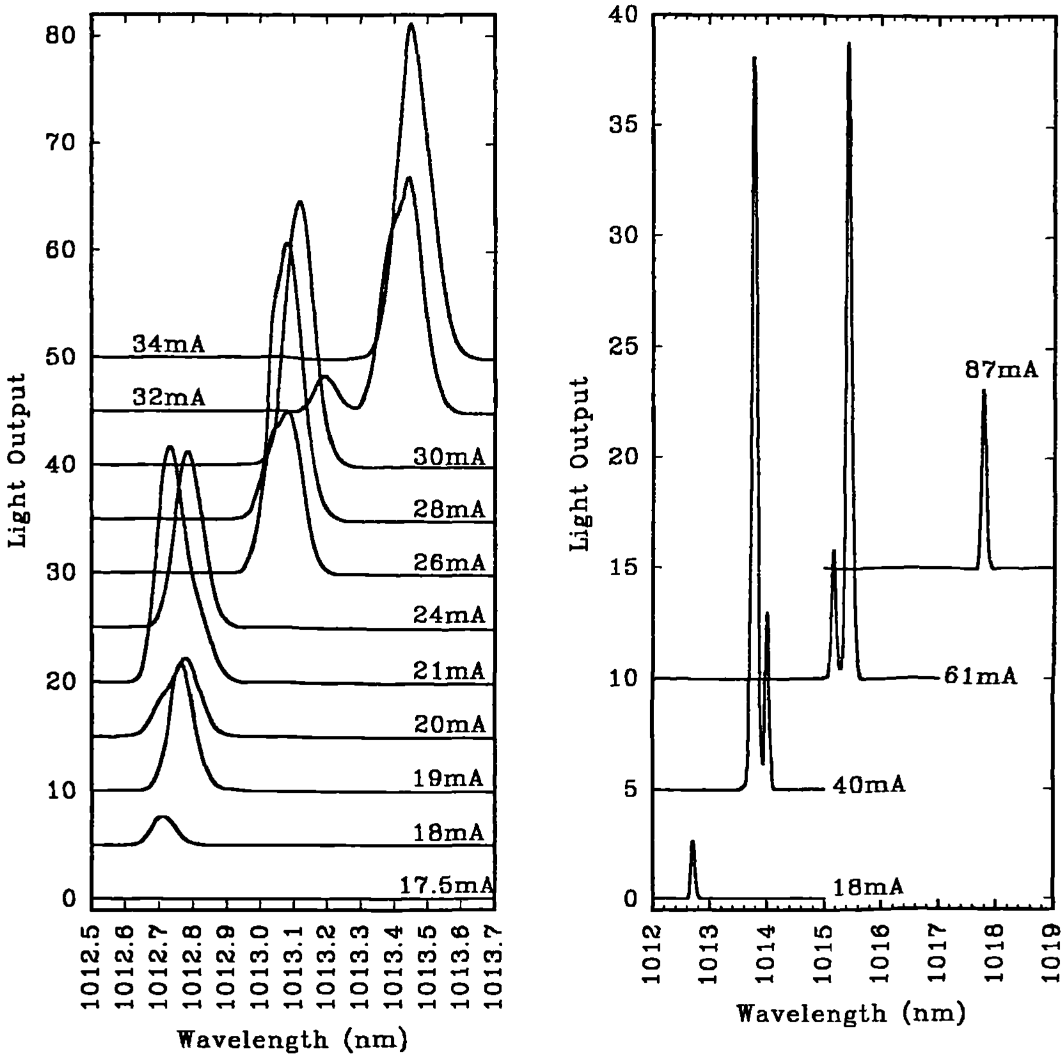

(a) (b)

Fig. 7.19. c.w. lasing spectra from 50μm diameter device. (a) low current regime showing selection of substrate Fabry-Perot modes and (b) higher currents.

In the region 18→61mA the following thermal parameters are measured from the above graph:

$$\frac{\partial \lambda}{\partial I} = 0.056 nm.mA^{-1} \tag{7.1}$$

Bias voltages of 1.9V and 2.6V were measured at currents of 18mA and 61 mA respectively. The shift with power is therefore:

$$\frac{\partial\lambda}{\partial P} = 0.0243 nm.mW^{-1} \tag{7.2}$$

20μm diameter devices were also investigated. Fig. 7.20 shows c.w. lasing spectra of a typical 20μm device. The threshold current of this device is ~4.0mA.

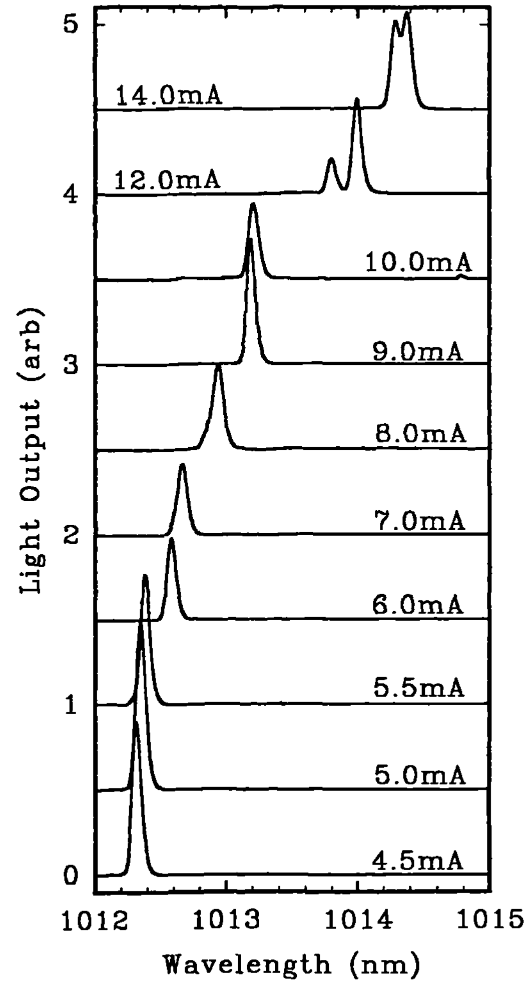

Fig. 7.20. c.w. lasing spectra from 20μm diameter device.

As for the 50μm device the 20μm device output jumps between Fabry-Perot modes in the substrate as the drive current is increased. Due to the smaller size, the temperature profile is more uniform across the device and the output is single moded below 12mA (~3800A.cm^{-2}).

In the region 4.5→12.0mA the following thermal parameters are deduced:

$$\frac{\partial\lambda}{\partial I} = 0.210 nm.mA^{-1} \tag{7.3}$$

Bias voltages of 2.45V and 3.56V were measured at currents of 4.5mA and 12.0 mA respectively which are 35% higher than for the larger device. The difference arises due to current spreading effects in the lower reflector[12]. The shift with power is therefore:

$$\frac{\partial \lambda}{\partial P} = 0.0497 nm.mW^{-1} \tag{7.4}$$

These parameters are studied in more detail in chapter 8.

7.6.3. Far field patterns

The low operating voltage of these devices means that they do not suffer permanent degradation when driven with direct currents of up to 100mA (within the time scale of the measurements). Thus we can examine the far field modal structure which appears quite stable when driven with a stable current source. An air-clad semiconductor pill-box optical resonator, such as the mesa etched devices studied in this thesis, is transversely multimoded if the diameter is more than about half the free space wavelength. Thus a 50μm diameter device operating at 1.0μm will be heavily overmoded and a certain amount of transverse mode hopping would be expected to take place[13].

Fig. 7.21 shows the far field output patterns of the device for which the output spectra are shown in fig. 7.19. These are detected by a sensitive vidicon camera and photographs taken from the monitor screen. The pictures are slightly squashed in the vertical direction by an artefact of the camera and monitor system.

Below threshold the light emission is spontaneous, so is very diffuse and cannot be detected by the camera. Once threshold is reached a narrow beam develops (fig. 7.21a) and it is found that at higher currents all appreciable light output is contained in a cone with a half angle of approximately 4.5°. Close to threshold the amplitude variation is uniform in θ and appears to approximate to a radial $\sin^2\theta/\theta^2$ variation[14]. The half angle at 50% maximum intensity for the central lobe is ~1.8° and the first null is at 2.8°. This corresponds to a TE_{01} type transverse mode in the cavity, the lowest supported mode. The effective emitting aperture calculated for this beam profile is 20.5μm where we assume a uniformly illuminated diameter d which produces beam with a central lobe half angle of $\theta=\sin^{-1}(\lambda/d)$ [14]. This indicates the existence of a filament with a diameter approximately 40% that of the mesa, possibly as a result of thermal lensing effects.

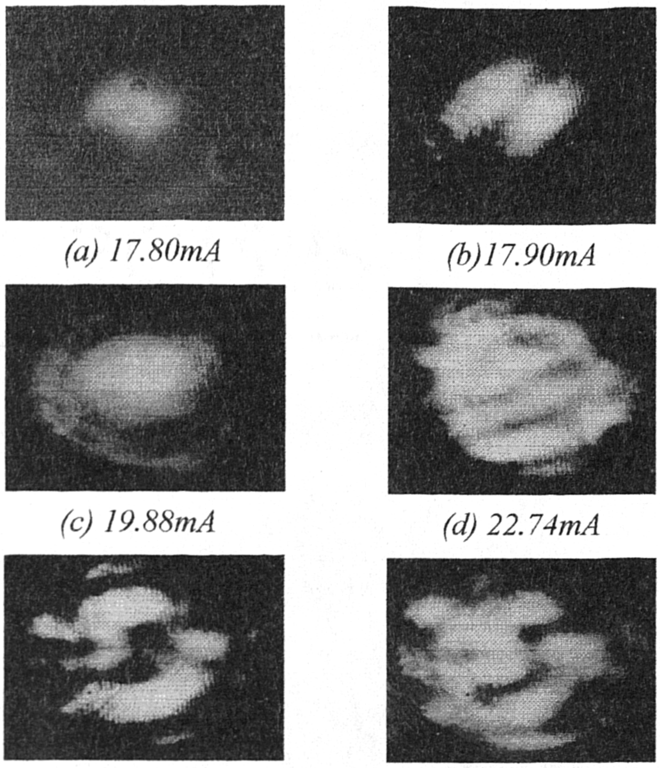

(a) 17.80mA

(b)17.90mA

(c) 19.88mA

(d) 22.74mA

(e) 30.48mA

(f) 33.40mA

Fig. 7.21. Far field patterns of 50μm device operating c.w. as detected by a vidicon camera. Profiles at currents of (a) 17.80mA, (b) 17.90mA, (c) 19.88mA, (d) 22.74mA, (e) 30.48mA and (f) 33.40mA. The angular extent of the pictures is approximately 10^c.

With increasing current mode hopping occurs rapidly. For a current increase of just 0.1mA, a higher order mode is seen (fig. 7.21b). At higher currents a large variety of other modes appear (fig. 7.21c,d,e,f), these are often mixed so the structure is difficult to determine. Once the output has switched to a different substrate FP mode the TE_{01} mode is seen to reappear close to the local minimum in light output (fig. 7.21e). With further increase in current, switching through higher modes occurs again.

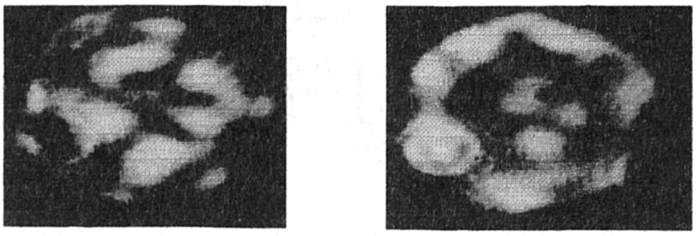

(a) 50.38mA *(b) 56.88mA*

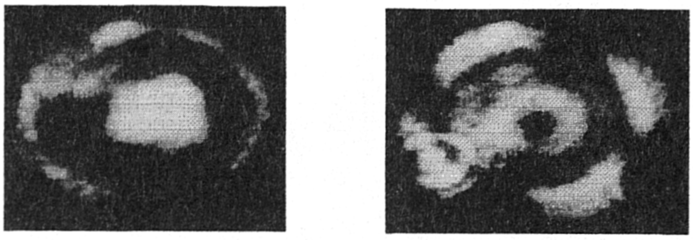

(c) 71.34mA *(d) 72.00mA*

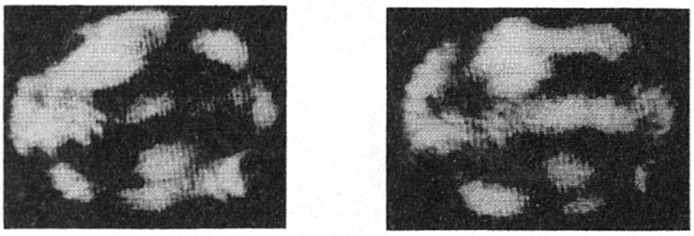

(e) 74.17mA *(f) 75.13mA*

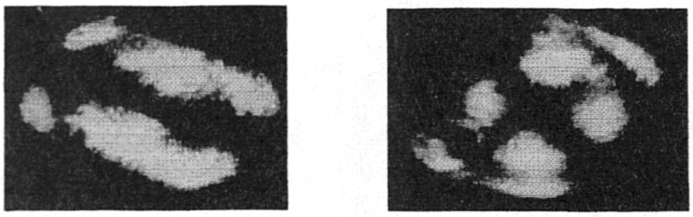

(g) 79.75mA *(h) 80.73mA*

(i) 80.81mA *(j) 82.19mA*

Fig. 7.22. Far field output modes of 50μm device at high direct currents. (a) 50.38mA, (b) 56.88mA, (c) 71.34mA, (d) 72.00mA, (e) 74.17mA, (f) 75.13mA, (g) 79.75mA, (h) 80.73mA, (i) 80.81mA and (j) 82.19mA.

At much higher currents, in excess of 50mA, the far field patterns become considerably more distinct; a selection of which are shown in fig. 7.22. This may be due to thermal lensing effects[10,15] which tend to select single modes in preference to mixed modes. From photographs taken of the output patterns it was noticed that many of the patterns are symmetrical about axes at 45° to the horizontal. These lines correspond to the ⟨100⟩ directions in the semiconductor crystal lattice. This indicates some inhomogeneity in the crystal lattice giving rise to increased optical gain or reflectivity for polarizations along the polar lattice directions.

It appears that transverse mode hopping occurs to keep the output wavelength close to a substrate FP mode. As the cavity heats and the modes within it shift in wavelength, the ones closest in wavelength to a substrate mode will tend to lase. The spectra in fig. 7.21 show some evidence of a fine structure which could be evidence of multiple transverse modes.

7.7. Ion implanted devices

7.7.1. Fabrication of devices

Ion implanted devices were fabricated from quarter 1 of QT421. The full quarter wafer was processed and 1.0μm thick Cr / Au pads were applied as the implant mask. It was then cleaved into 11 pieces labelled *a* to *k* as shown in fig. 7.23. Pieces *a, b, e, g, h, i, j, & k* were implanted with 200keV H^+ ions with doses ranging from $3\times10^{12}.cm^{-2}$ to $1\times10^{15}.cm^{-2}$. Table 7.5 identifies the proton dose implanted into each of the samples. These samples should allow the implant dose for optimum VCSEL performance to be identified.

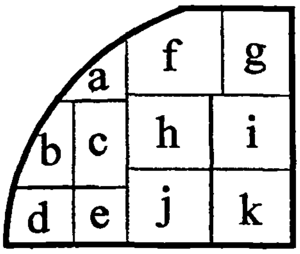

Fig. 7.23. QT421Q1 showing chips cleaved from the quarter wafer for proton implant.

80μm square Au / Zn / Au contact pads were applied over implanted devices. Neighbouring devices were isolated by a 3.5μm deep $SiCl_4$ reactive ion etch using the pads as a mask. The contacts were then annealed to 400°C to diffuse in the Zn.

Sample	Dose (ions .cm^{-2})
a	3×10^{12}
b	1×10^{13}
e	1×10^{15}
g	3×10^{13}
h	1×10^{14}
i	3×10^{14}
j	1×10^{14}
k	3×10^{13}

Table 7.5. Proton implant doses delivered to samples cleaved from QT421Q1.

7.7.2. I-V measurements

D.C. I-V measurements were made on the implant defined devices on the pieces of QT421Q1. Devices ranging from 5µm to 80µm diameter as well as 5×5 arrays of 5µm devices were available on the chips. Fig. 7.24. shows the result of these measurements.

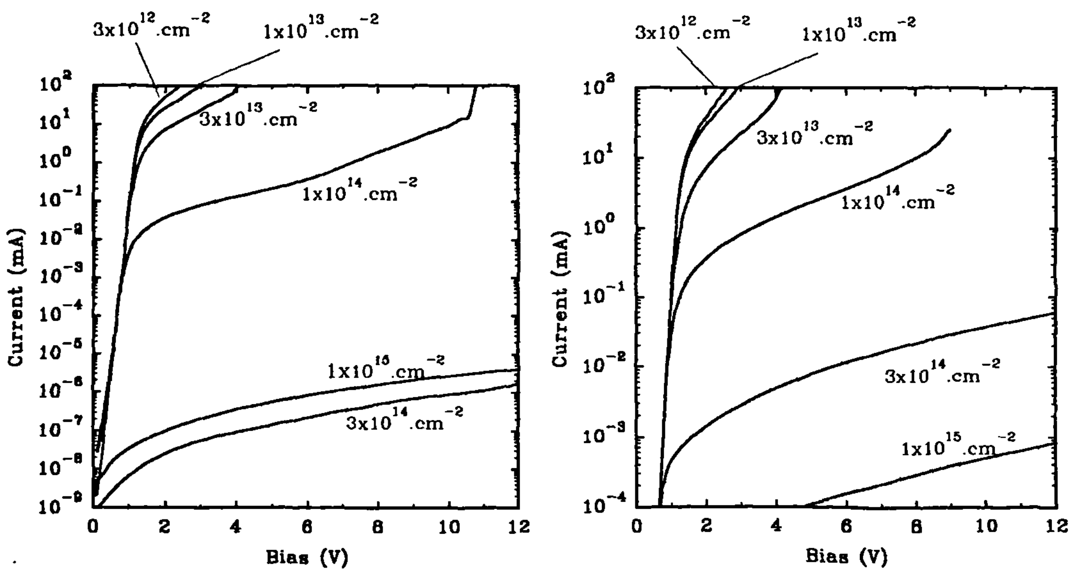

(a) 0µm

(b) 5µm

Fig. 7.24. D-C I-V measurements on ion implanted devices from QT421, continued over page.

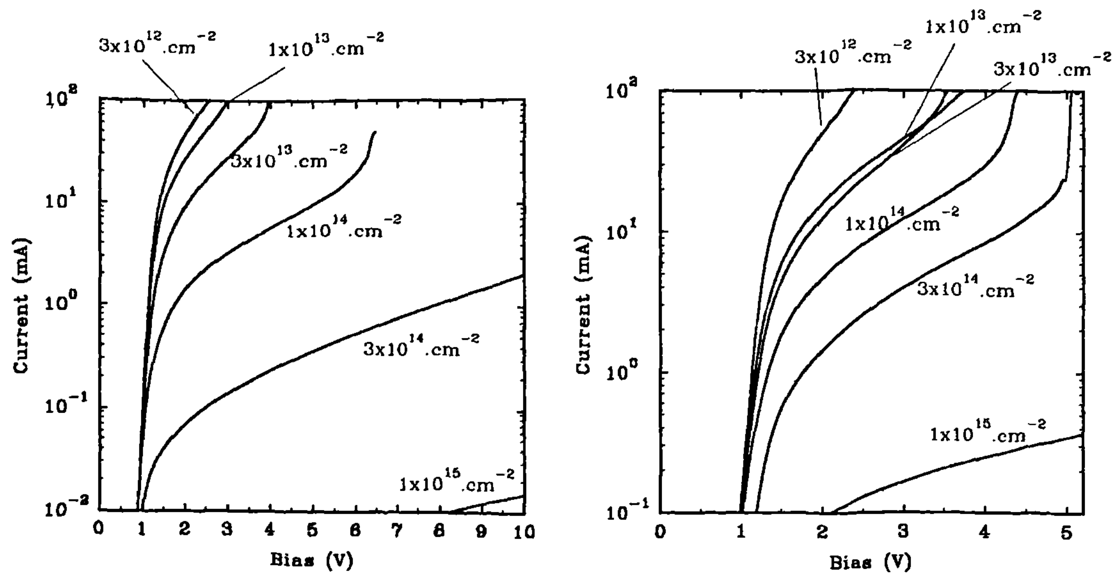

(c) 10μm *(d) 20μm*

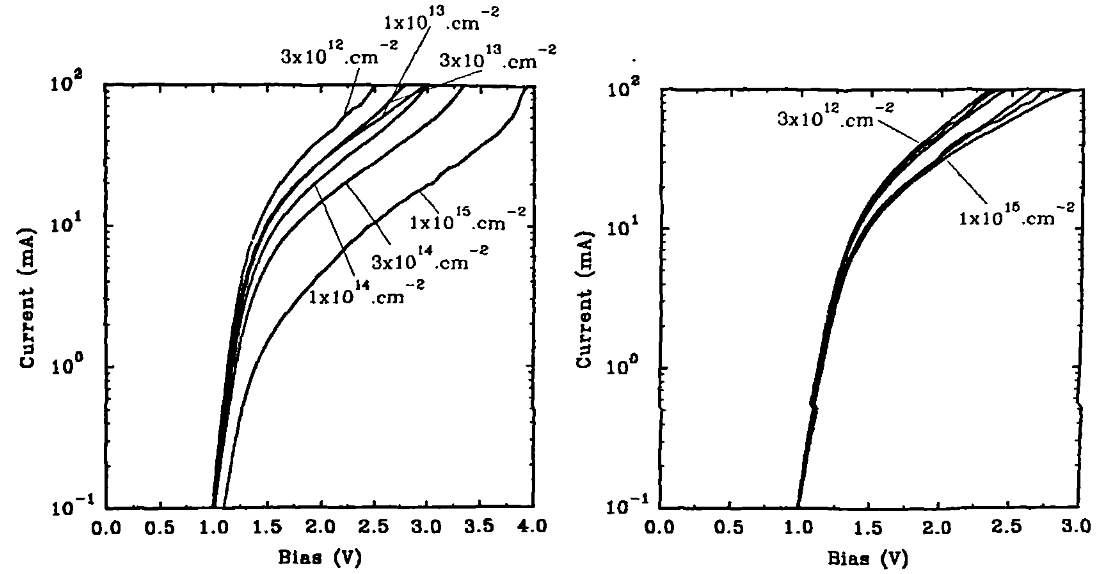

(e) 50μm *(f) 80μm*

Fig. 7.24. D.C. I-V measurements on ion implanted devices from QT421 implanted with doses from $3x10^{12}.cm^{-2}$ to $1x10^{15}.cm^{-2}$ on various diameter devices (a) 0μm, (b) 5μm, (c) 10μm, (d) 20μm, (e) 50μm and (f) 80μm.

Comparing the I-V results for an implant dose of $3\times10^{12}.cm^{-2}$ we see little difference between the currents flowing in the different sizes of device. This means that there is effectively no current blocking in the implanted region for this dosage. Increasing the implant dose, differences begin to emerge as ion damage takes place.

Looking at the curves for a 0μm device, i.e. no implant mask was used, we see that a dose of $\sim1\times10^{14}.cm^{-2}$ is required to produce a significant blocking resistance[6]; the leakage under a 2V bias is reduced to 0.4mA which is 2% of the threshold current of a 50μm diameter device. For implants of $3\times10^{14}.cm^{-2}$ and above, the leakage at 12V is less than 5nA and is probably more dependant on surface currents outside of the mesa, which are fabrication dependant, rather than the implant dose.

For a 50μm device we notice that increasing the implant dose above $1\times 10^{14}.cm^{-2}$ requires an increase in the bias required to maintain the same current. This is because the current blocking layer is effectively widened as the implant dose is increased. This causes a pinch off effect of the conduction channel in the upper reflector which reduces the effect of current funnelling (this is discussed in more detail in section 8.4). For this size of device, an implant dose of $1\times10^{14}.cm^{-2}$ gives an acceptable compromise between low leakage and low resistance.

For smaller, non-implanted areas more serious effects may arise. There is some sideways straggle on the position of implanted protons which tends to produce some implant under the peripheral region of the implant mask and into the active area. Thus at excessively high implant doses the diameter of the current funnel may be reduced unduly. For example; in a 5μm device implanted with $1\times10^{15}.cm^{-2}$ protons, the reduction in funnel diameter reduces the current flowing at 12V to 0.8μA which is an apparent current density of just $4.1A.cm^{-2}$.

For small diameters the effect of funnel narrowing must be considered; rather than use a high implant dose it would be better to reduce leakage current by reducing the area of the mesa.

7.7.3. L-I measurements.

A number of devices from each of the ion-implanted samples of QT421 were probed. Current pulses were applied and the light output monitored. No evidence of lasing was found for any of the devices. From PL and photoreflectance data, these samples should have produced viable lasers. However it was noticed that the spontaneous emission intensity for the same drive current tended to decrease for devices implanted with higher doses. This indicates that the quantum well active region has been damaged by the implant. This could occur if the implant mask were slightly thinner than that used for the MBE grown devices examined in chapter 6. A reduction of 0.2μm, which is the standard deviation of the implant range[16], could make a significant difference to the number of ions getting through the mask. There was no material available to repeat the fabrication of these devices.

References:

---

[1] J.Woodhead, *Photoluminescence measurements on various InGaAs / GaAs quantum well samples at 10K and 300K provides a calibration relation for the shift of the transition energy between the two temperatures*, Private communication.

---

[2] J.S.Roberts, T.E.Sale, C.C.Button, J.P.R.David & A.Jennings, *High performance microcavity resonator devices grown by atmospheric MOVPE*, J. Crystal growth, **124**, pp792-800, 1992.

[3] K.Tai, L.Yang, Y.H.Wang, J.D.Wynn & A.Y.Cho, *Drastic reduction of series resistance in doped semiconductor distributed Bragg reflectors for surface-emitting lasers*, Appl. Phys. Lett., **58**, 25, pp2496-2498, 1990.

[4] Using the mathematical models developed in chapter 2 a CAD package was developed to model reflection spectra and similar parameters for complex multilayer structures in the AlGaAs system. This has been used to determine growth errors by fitting to measured spectra.

[5] P.Ressell, H.Strunsy, S.Gramlich U.Zeimer, J.Sebastian & K.Vogel, *Optimised implantation step for vertical-cavity surface-emitting lasers*, Electron. Lett., **29**, 10, pp918-1919, 1993.

[6] M.Orenstein, N.G.Stoffel, A.C.Von Lehmen, J.P.Harbison & L.T.Florez, *Efficient continuous wave operation of vertical-cavity semiconductor lasers using buried compensation layers*, Appl. Phys. Lett., **59**, 1, pp31-33, 1991.

[7] R.S.Geels, S.W.Corzine, J.W.Scott, D.B.Young & L.A.Coldren, *Low threshold planarized vertical-cavity surface-emitting lasers*, IEEE Photon. Technol. Lett., **2**, 4, pp234-236, 1990.

[8] T.Kawakami, Y.Kadota, Y.Kohama & T.Tadokoro, *Low-threshold current low-voltage vertical-cavity surface-emitting lasers with low-Al-content P-type mirrors grown by MOCVD*, IEEE Photon. Technol. Lett., **4**, 12, pp1325-1327, 1992.

[9] T.J.Rogers, C.Lei, D.G.Deppe & B.G.Streetman, *Low threshold voltage continuous wave vertical-cavity surface-emitting lasers*, Appl. Phys. Lett., **62**, 17, pp2027-2029, 1993.

[10] D.Vakshoori, J.D.Wynn, G.D.Zydzik, R.E.Leibenguth, M.T.Asom, K.Kojima & R.A.Morgan, *Top-surface emitting lasers with 1.9V threshold voltage and the effect of spatial hole burning on their transverse mode operation and efficiencies*, Appl. Phys. Lett., **62**, 13, pp1448-1450, 1993.

[11] K.L.Lear, S.A.Chalmers & K.P.Killeen, *Low threshold voltage vertical cavity surface-emitting laser*, Electron. Lett., **29**, 7, pp584-586, 1993.

[12] Y.H.Lee, J.L.Jewell, B.Tell, K.F.Brown-Goebeler, A.Scherer, J.P.Harbison & L.T.Florez, *Effects of etch depth and ion implantation surface emitting microlasers*, Electron. Lett., **26**, 4, pp225-227, 1990.

---

[13] C.J.Chang-Hasnain, M.Orenstein, A.Von Lehmen, L.T.Florez, J.P.Harbison & N.G.Stoffel, *Transverse mode characteristics of vertical cavity surface-emitting lasers*, Appl. Phys. Lett., **57**, 3, pp218-220, 1990.

[14] K.F.Sander & G.A.L.Reed, *Transmission and propagation of electromagnetic waves*, 2nd Edition, Cambridge University Press, Cambridge, 1986.

[15] N.K.Dutta, L.W.Tu, G.Hasnain, G.Zydzik, Y.H.Wang & A.Y.Cho, *Anomalous temporal response of gain guided surface emitting lasers*, Electron. Lett., **27**, 3, pp208-210, 1991.

[16] C.Jeynes, *From results of scattering calculations performed at the University of Surrey, the range of 200keV* H^+ *ions in GaAs is found to be 1.4μm with a standard deviation of 0.2μm*, Private communication.

8. Discussions

This chapter discusses the experimental results presented in the previous two chapters. Comparison is made between devices grown by MBE and MOCVD and between mesa etched and ion-implant defined devices. Comparison with theoretical models and reference to the literature is also made.

8.1. Threshold Conditions

8.1.1. Effect of growth variations

This thesis has presented data on low threshold VCSEL devices. Material grown by both MBE and MOCVD produces devices capable of operating at threshold currents below 800A.cm^{-2}, for structures incorporating three InGaAs / GaAs quantum wells. But as was shown in fig. 6.14 there is a wide variation in threshold currents between devices situated at different positions across the wafer, which depends on the operating wavelength and hence the epitaxial deposition thickness.

For most semiconductor device applications variations in epitaxial layer thickness up to ±10% give little variation in the device performance. Typical epitaxial growth processes, such as MBE or MOCVD, will have ±5% variation in deposition thickness across a substrate. However for resonant optical devices with a vertical cavity the variation will give rise to a corresponding ±5% variation in the wavelength of resonant modes (the effects of material dispersion are second order). That is a variation of ±50nm for a 1000nm nominal resonance. This is large compared to the extent of the gain spectrum of a quantum well at low carrier concentrations ($2\times 10^{18}.\text{cm}^{-3}$), see chapter 3. Variation of the quantum well width is less significant, the same ±5% change in the thickness of an 85Å $\text{In}_{0.22}\text{Ga}_{0.78}$ / GaAs well produces a ± 2.7nm variation in the e_1hh_1 transition about the nominal 1011.4nm provided the composition is not affected. This is insignificant compared to the resonance shift.

To provide lasers for commercial applications it would be necessary to specify the operating wavelength within 10nm or better. Thus to achieve good yield it is necessary to specify the growth thickness accurately and have high uniformity growth (±1% for ±10nm specification). Uniform operating wavelength implies a small variation in the threshold current, which is desirable. The MBE grown wafer RMB627 has a variation of ±6% in the growth thickness across the wafer; this is not fundamental to MBE growth and is a result of the geometry of the effusion cells in the reactor used to grow this layer. *Bandgap Technology Corp.*[1] claim to achieve ±0.2% uniformity across a 2" wafer by MBE growth. The MOCVD grown layer QT421 shows ±1% variation over 80% of the grown wafer (the edges are very non-uniform and not of any use), this is achieved by optimisation of the interior of the growth reactor for uniform and laminar gas flows. QT233, in contrast, was grown before the reactor had been refined and is considerably less uniform. The down-time for servicing is generally less for an MOCVD reactor than for an MBE machine used for the same purpose.

8.1.2. Effect of non-uniformities on threshold condition

The variation across the wafer RMB627 is, for research purposes, actually an advantage as it allows us to probe throughout the quantum well optical gain spectrum. The single high finesse cavity mode fixes the lasing wavelength which is in contrast to edge emitting Fabry-Perot lasers where the device lases at the wavelength at which the gain is maximum and equal to the threshold gain. The systematic variation in thickness gives cavity resonances over the range 940→1060nm whilst the confined e_1hh_1 transition, as deduced from the low temperature PL measurements, is almost unchanged at 1022±2.0nm corresponding to an indium fraction of 23.5%. The threshold gain (g_{th}) is estimated to be ~287.cm^{-1} using the models in chapter 2. The variation of the threshold current with wavelength (fig. 6.14) indicates the variation with wavelength of the current density required to maintain a constant (approximately as losses in the cavity are weakly wavelength dependant) optical gain g_{th}. In an attempt to model this variation, the gain spectra for an 85Å $In_{0.235}Ga_{0.765}As$ / GaAs well were calculated at 300K for a number of carrier concentrations using the model of chapter 3. These are shown in fig. 8.1.

The spectra of fig. 8.1 indicate that transparency is reached at a carrier concentration of approximately 1.4×10^{18}.cm^{-3} at a wavelength of 1055nm for the e_1hh_1 transition. There is a particularly large shift in the this wavelength from the PL emission indicating that the quantum well bandgap has been under-estimated in the model, the spectra thus need to be shifted to ~1020nm. Transparency for the e_2hh_2 transition is reached at 5.0×10^{18}.cm^{-3} at a wavelength of 965nm but this transition is of little concern for the devices described here. With increasing carrier concentration the bandwidth for positive gain increases as carriers fill higher energy states within the well. At around 2.4×10^{18}.cm^{-3} the population of states around the hh_2 band edge becomes significant. It is here that the density of states in the hh_1 band begins to increase significantly. This results in an enhanced gain for transitions to these states thus we see the emergence of a peak in the spectrum 15nm to the short wavelength side of the lowest energy transition. At higher carrier concentrations this peak becomes the dominant feature. This shall now be referred to as the ***state expansion peak***. Similar spectra are calculated by Li *et al.*[2]

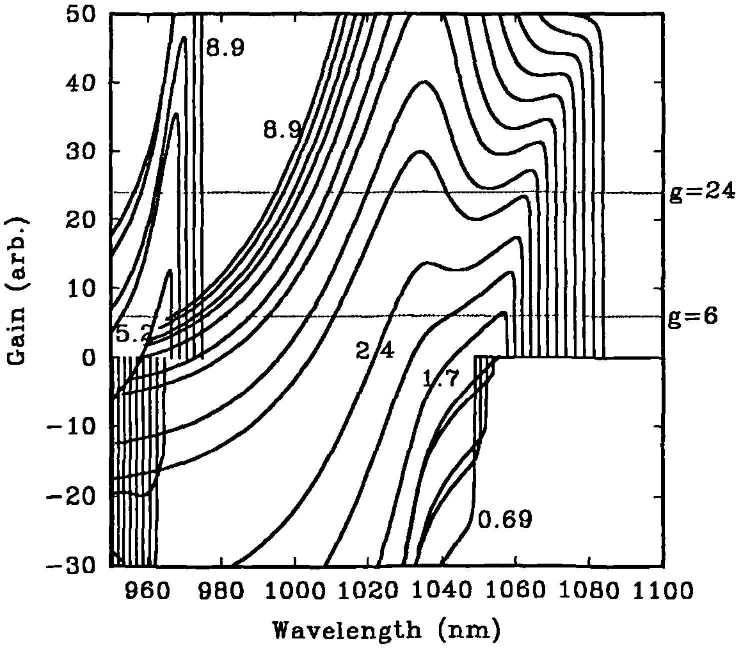

Fig. 8.1. Gain spectra calculated for 85Å $In_{0.235}Ga_{0.765}As$ */ GaAs quantum well at 300K. Gain is in arbitrary units. Curves are shown for carrier concentrations of 0.69, 0.83, 0.99, 1.19, 1.42, 1.69, 2.01, 2.38, 2.80, 3.29, 3.85, 4.49, 5.20, 5.99, 6.87, 7.84 and* $8.90\times10^{18}.cm^{-3}$*. Curves show relations for both* e_1hh_1 *and* e_2hh_2 *transitions which are clearly identified from their wavelength.*

How does the $J_{th}(\lambda)$ relation of fig. 6.14 arise from the gain spectra? We may construct a surprisingly similar curve from the modelled spectra if we assume the threshold gain to be 6 units on the arbitrary scale of fig. 8.1. From the spectra in the figure we see that the threshold condition (g=6) is first reached at a carrier concentration (n_{th}) of $1.7\times10^{18}.cm^{-3}$.

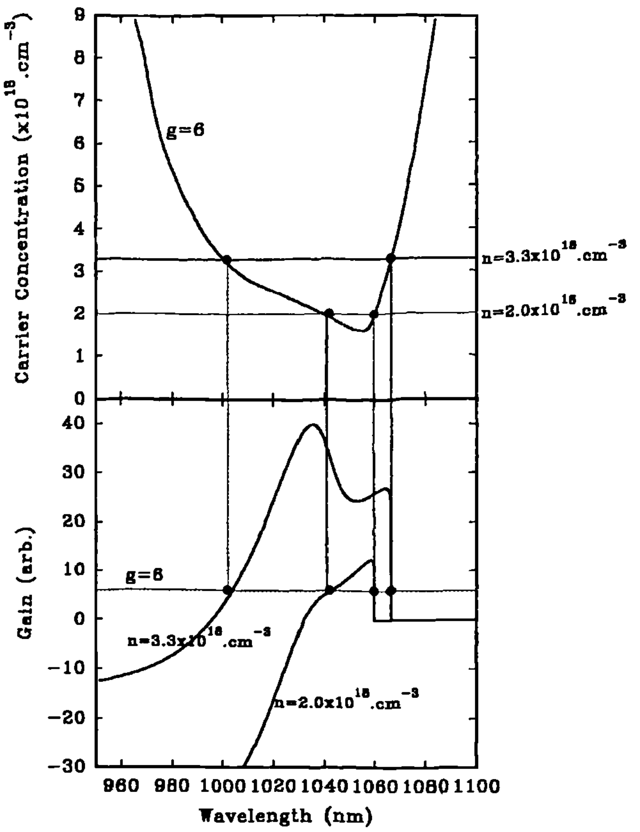

Fig. 8.2. The lower curve shows gain spectra for the VCSEL quantum wells at carrier concentrations of 2.0 and 3.3x10^{18}.cm^{-3}. The points at which the curve intercept the g=6 line indicate resonance wavelengths of lasers which will be at threshold at these concentrations. These points are projected up to give the relation of $g_{th}(\lambda)$ shown in the upper curve.

Looking at the curve for n=2.0×10^{18}.cm^{-3} in fig. 8.1 we note that it intersects the line g=6 twice, once at 1060nm and again at 1042nm. This means that lasers resonant at either of these wavelengths will be at the threshold condition for this carrier concentration. Fig. 8.2 shows how these two points are projected onto a plot of $n_{th}(\lambda)$. Since we do not yet know τ we do not know the corresponding current density. Using the full family of spectra in fig. 8.1 the curve $n_{th}(\lambda)$ relation of fig. 8.2 is completed. Fig. 8.3 shows the relation for threshold gains of g=6 and g=24 for both the e_1hh_1 and e_2hh_2 transitions. Note that the $\Delta n \neq 0$ transitions are '*not allowed*' since there is no wave function overlap.

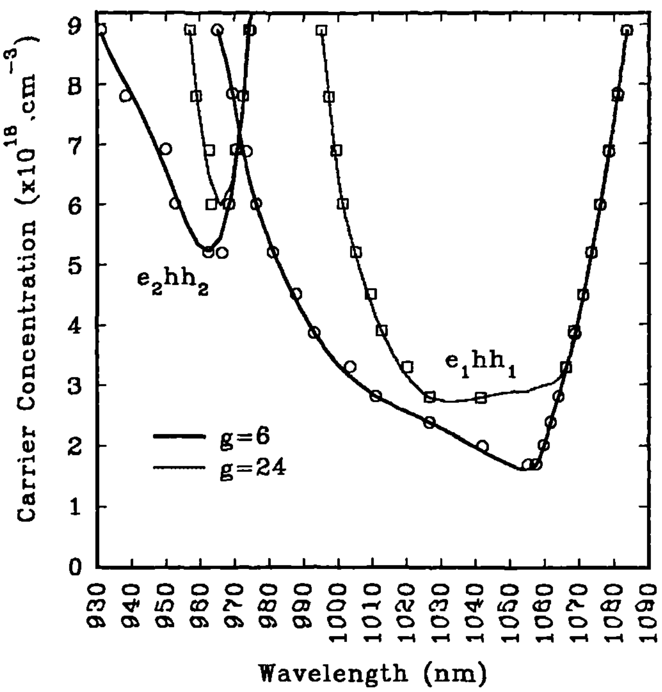

Fig. 8.3. Dependence of threshold carrier concentration with cavity resonance wavelength for VCSEL devices assuming threshold gains of (a) 6 and (b) 24. Relations for e_1hh_1 and e_2hh_2 transitions are shown.

The $n_{th}(\lambda)$ relation for the e_1hh_1 transition assuming g=6 bears a number of similarities to the $J_{th}(\lambda)$ relation measured for devices from the layer RMB627; there is a wavelength for minimum threshold with a rapid increase towards longer wavelengths. Operation to longer wavelengths is allowed due to bandgap renormalization with increased carrier concentration. At shorter wavelengths than the minimum the threshold increases more slowly and an inflexion occurs ~20nm from the minimum value. The operating wavelength range increases with carrier concentration as higher energy states are filled. The inflexion is a result of the increased density of states at higher energies in the hh_1 band. The n=2 transition is not within the cavity resonance range of the devices studied here. As described above the main discrepancy is a wavelength shift probably due to an error in the quantum well bandgap renormalization.

In the absence of an optical field (such is the case below threshold) the carrier concentration n is related to the current density J by the rate equation of (8.1).

$$\frac{\partial n}{\partial t}=-\frac{J}{eNd_w}+\frac{n}{\tau}+R_{spon}(n)+Cn^3 \tag{8.1}$$

Under steady state the equation is equal to zero. N is the number of quantum wells and d_w is their width. R_{spon} is the spontaneous recombination rate and tends to vary as Bn^2. It can be calculated in a similar way to $g(n)$ (see chapter 3). B is typically

10^{-10}cm^3.s^{-1} [3] corresponding to a lifetime of 10ns for n=1×10^{18}.cm^{-3}, however other losses are generally much more significant. In the case of the VCSEL it is likely that the effect of spontaneous recombination will be reduced by photon recycling within the high finesse cavity. The non-radiative recombination lifetime τ is a result of impurity and surface states in the vicinity of the well and is independent of carrier concentration. For a typical quantum well the non-radiative lifetime is in the range of a few 100ps to a few nanoseconds and is likely to be the dominant recombination mechanism at low to medium carrier concentrations. The final term C is the Auger coefficient concerning a variety of three body recombination processes[3]. It is a thermally activated process dependant on the bandgap and is a significant loss mechanism in long wavelength (1.6μm) lasers. For a laser operating at a wavelength of 1.0μm, C is of the order 10^{-30}cm^6.s^{-1} [3], corresponding to a lifetime of 1μs for n=1 ×10^{18}.cm^{-3} or 10ns for n=1×10^{19}.cm^{-3}. It is clear that τ is an important carrier loss mechanism and, especially at low carrier concentrations, is likely to be dominant. We shall therefore use the simplified equation (8.2).

$$J = \frac{neNt_w}{\tau} \tag{8.2}$$

This equation concerns recombination of carriers within the well. They may also be lost by thermal activation out of the well into the barrier. This loss mechanism is small if the band offsets are many kT but if the barriers are low or the temperature is elevated the lifetime may be reduced further[4,5,6]. This is not considered here but is mentioned elsewhere in relation to the c.w. operating characteristics.

A fit is attempted between the experimental and modelled data by providing a shift in wavelength and assuming a carrier lifetime as in (8.2). Fig. 8.4 shows this fit obtained for a -25nm shift and assuming a lifetime of 900ps. The inclusion of Auger and radiative terms in the relation for the carrier lifetime does not improve the fit. This indicates that the lifetimes associated with these process are significantly larger than τ for carrier concentrations less than 5×10^{18}.cm^{-3} so may be ignored. The fit to the long wavelength side of the minimum is very good, this illustrates the effects of bandgap renormalization of the form (8.3).

$$\Delta\lambda = \frac{hc}{Rn^{\frac{1}{3}}} \tag{8.3}$$

Where the renormalization coefficient R=3.2×10^{-8}eV.cm [7].

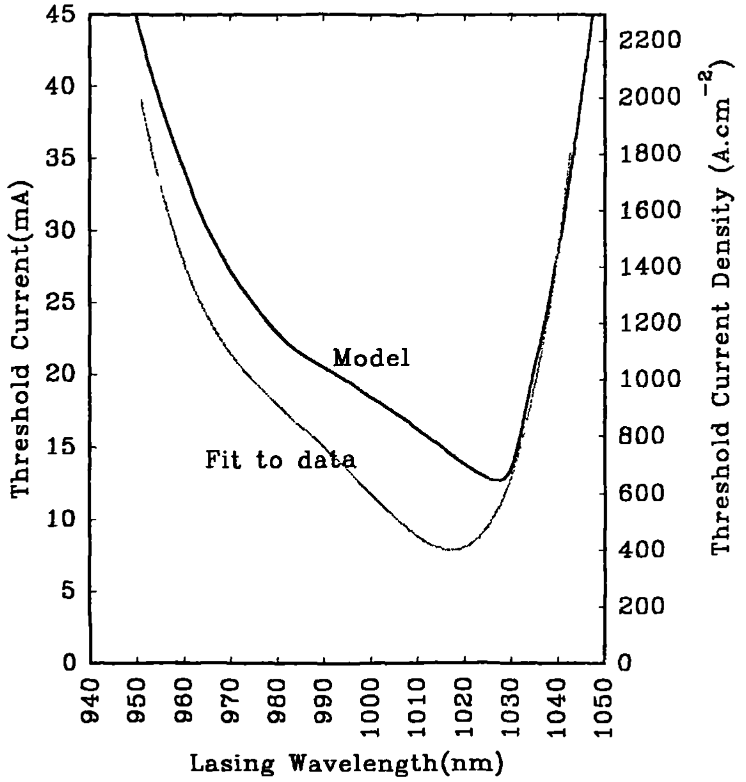

Fig. 8.4. Fit of model to experimental relation $J_{th}(\lambda)$ obtained by wavelength shift of -25nm and assuming a non-radiative lifetime τ of 900ps. The fit is not improved by considering the higher order effects of Auger and radiative recombinations.

The shape of the experimental curve indicates that a threshold condition $g=6$ is of the right order; i.e. minimum threshold may be reached before the development of the state expansion peak in the gain spectrum which relates to an increased density of states. The operating range of the devices and the position of the inflexion in the curves are in good agreement between model and experiment. Similar $J_{th}(\lambda)$ relations are measured for InGaAsP based external cavity lasers by O'Gorman & Levi[8,9].

The discrepancy between the two curves could result from the use of an infinite well model. This tends to overestimate the interaction between the valence bands at large wavenumber leading to an overestimate of the density of states in the hh_1 band at energies close to the hh_2 band edge. At room temperature there is significant population of these states at transparency, hence the carrier concentration in this regime of the model (around 2×10^{18}.cm^{-3}) is overestimated. In the real case transparency is probably around 1.0×10^{18}.cm^{-3}, which would reduce the minimum point of the modelled $J_{th}(\lambda)$ curve to around 400A.cm^{-2}. This would agree with a 900ps lifetime.

8.1.3. Devices requiring higher gain for threshold

Figure 8.3 also shows the $n_{th}(\lambda)$ relation for a threshold gain of 24 units on the arbitrary scale if fig. 8.1. As the figure shows, the operating range for devices for $n<6 \times 10^{18}.\text{cm}^{-3}$, equivalent to $J_{th}<2400\text{A.cm}^{-2}$, is reduced from 975→1078nm for g=6 to 1002→1078nm (or 974→1050nm applying the -25nm corrective shift). This is a 27nm reduction in the tuning range to short wavelengths. The minimum threshold is increased to $2.8\times10^{18}.\text{cm}^{-3}$ (1120A.cm^{-2}) but more importantly the minimum has become flatter and is shifted to shorter wavelengths by ~30nm. This is a result of the emergence of the state expansion peak in the gain spectrum.

Compare the curves of fig. 8.3 to those in fig. 6.29 which shows the $J_{th}(\lambda)$ relation for implanted devices of varying sizes. The curve for 50μm devices is shifted upwards from that for etched devices owing to leakage of 3→5mA through the implanted region which is not completely isolated. Data for smaller diameter devices, for example 5μm, lie on much flatter $J_{th}(\lambda)$ curves (partly due to the increased effect of leakage) with minima close to 985nm as opposed to 1018nm for 50μm diameters. Comparing to fig. 8.3 we see the similarity to the curve for g=24. Thus it appears that a 5μm diameter implant defined device requires of order 2 to 5 times the gain to reach threshold than does a 50μm device[10]. The increased loss of smaller devices results from increased diffraction from a smaller aperture and the increased absorption from sideways straggle implant damage. It is also likely that the implant damage produces recombination centres which would act to reduce the lifetime of carriers in the active region. The effect of this will be more pronounced in small devices.

8.1.4. Figures of gain

From modelling in chapter 2, figures of Q_{max} (see equation 2.25) are calculated for the structures RMB627 and QT421 using the structural dimensions determined from photoreflectance measurements and absorption values dependant on the doping profiles. Table 8.1 shows these results along with the values of gain required from the three quantum wells for threshold. Use of resonant periodic gain (see section 2.2.2) is assumed which enhances the effective gain by a factor of two.

	Q_{max}	g_{th}
RMB627	342	287.cm^{-1}
QT421	222	441.cm^{-1}
QT421 intended	283	346.cm^{-1}

Table 8.1. Values of Q_{max} and threshold gain for VCSEL structures studied here. Growth errors in QT421 caused a reduction in Q_{max} from 283 to 222.

The higher g_{th} for QT421 results from the higher average doping concentration throughout the mirror stacks and from the relative errors in the mirror and cavity growth thicknesses. The threshold values in table 8.1 are for broad area devices where there are minimal edge losses. If we assume this is the case for 50μm devices then we would predict that g=6 is approximately a gain of 287.cm^{-1} and that 5μm implanted devices have a threshold gain in the region of 500→1500.cm^{-1}. On the gain spectra of fig. 8.1, 50μm devices from QT421 would operate at g=9.3. This should give slightly higher thresholds than RMB627 and a more flattened minima in the $J_{th}(\lambda)$ curve. The experimental data for QT421 covers a rather limited range of wavelengths (998→1022nm) and there appears to be little overall trend (fig. 6.15), the picture is further complicated by a variation in indium fraction and well quality across the wafer. For a very simple comparison if we assume a constant $\partial g/\partial n$ for the minimum threshold and the same 900ps lifetime we would predict from RMB627 a minimum threshold current density of 562A.cm^{-2} for this structure. The minimum measured is 764A.cm^{-2}; it is unlikely that a device close to the optimum wavelength has been found and the absorption losses could well be larger than assumed. The prediction is reasonable considering the crudity of the model.

8.1.5. Design of quantum well

Above we have only considered the use of 85Å $In_{0.235}Ga_{0.765}As$ / GaAs wells as used in the structure RMB627. It is worth considering other well widths and indium compositions to see if the quantum well design could be improved. In the following figures we consider a cavity with the same finesse and the same carrier lifetime as RMB627 and calculate the $J_{th}(\lambda)$ relation as before. In fig. 8.5 we see the curves for g_{th}=6 and 24 for 85Å wells with In fractions of 20 and 25%. Table 8.2 summarises the main differences.

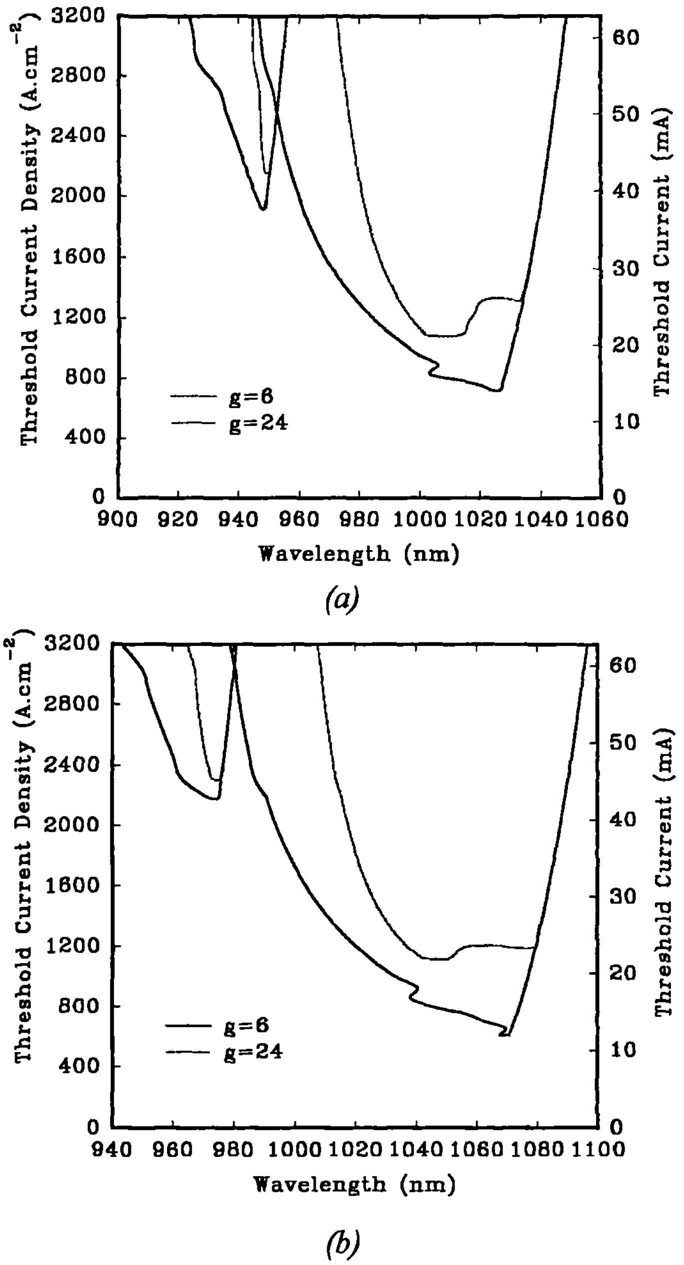

Fig.8.5. $J_{th}(\lambda)$ relations calculated for VCSEL structures incorporating 85Å quantum wells with (a) 20% and (b) 25% Indium. The right hand axis shows the threshold currents for 50μm diameter devices. A carrier lifetime of 900ps is assumed.

	20% In		25%In	
	g_{th}=6	g_{th}=24	g_{th}=6	g_{th}=24
n_{th}(min)	1.81×10^{18}	2.72×10^{18}	1.53×10^{18}	2.81×10^{18}
J_{th}(min)	722A.cm^{-2}	1088A.cm^{-2}	612A.cm^{-2}	1122A.cm^{-2}
Tuning range for J=2000A.cm^{-2}	81.8nm	60.1nm	95.6nm	71.3nm

Table 8.2 Comparison of $J_{th}(\lambda)$ relations for 85Å quantum wells incorporating 20 and 25% indium.

The first observation is that for higher indium fractions the curves are shifted to longer wavelengths since the quantum wells are deeper. The curve for the n=1 transition is broadened and lowered slightly for low loss lasers. This will give benefits only for high finesse resonators. The n=1 and n=2 transitions are separated further and the n=2 is suppressed with increasing In. The curves are flatter bottomed for In rich wells giving a higher yield of low threshold devices from a typical wafer. In reality the carrier lifetime will increase in a deeper well as thermionic emission from the well is reduced. This will make the high indium fraction well even more attractive. The same effect is produced by putting aluminium in the barrier material[5]. Note the kinks in the curves of fig. 7.5; these result when the differential gain is low such as beside a rapidly growing peak, the effect of bandgap renormalization is more significant at these points and produces an effective negative differential gain.

In fig. 8.6 we show similar curves for quantum wells of 70 and 100Å width for $In_{0.235}Ga_{0.765}As$ / GaAs wells. Again we assume a carrier lifetime of 900ps and a cavity finesse equivalent to g_{th}=6 in the above case. Adjustments are made for the change in active length. Table 8.3 summarises the major differences.

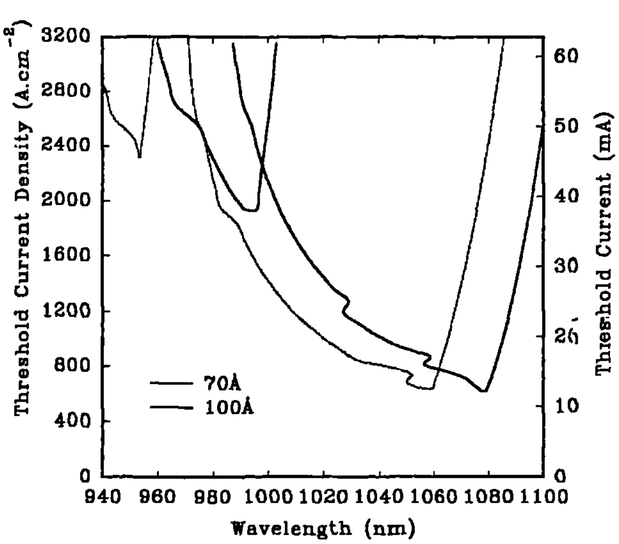

Fig. 8.6. $J_{th}(\lambda)$ relations calculated for VCSEL structures incorporating 75 and 100Å quantum wells with 23.5% Indium. The right hand axis shows the threshold currents for 50μm diameter devices. Carrier lifetime of 900ps is assumed.

	Transition	**70Å**	**100Å**
n_{th}(min)	n=1	1.94×10^{18}	1.32×10^{18}
	n=2	7.08×10^{18}	4.14×10^{18}
J_{th}(min)	n=1	640A.cm^{-2}	619A.cm^{-2}
	n=2	2331A.cm^{-2}	1946A.cm^{-2}
Tuning range for J=2000A.cm^{-2}	n=1	95.7nm	94.3nm

Table 8.3. Comparison of $J_{th}(\lambda)$ relations for 70 and 100Å quantum wells incorporating 23.5% indium.

The shape of the $J_{th}(\lambda)$ relation changes little with well width. For the narrower well the curves are shifted to shorter wavelengths as the confinement increases. Also the splitting of the bound states increases moving the n=2 transition to even shorter wavelength which has the effect of suppressing it. The tuning range for the two widths of well is virtually the same. There is little difference in the minimum points since the effect of a change in active length on the gain requirement is offset by the effect of the change in active volume on the current density. The minimum is approximately 3.5% lower in the case of the wider well. Therefore it is marginally more advantageous to use a wider well but one must be aware to keep clear of the critical layer thickness[11]. 85Å is about the widest well that is suitably far from the critical condition for 23.5% In.

8.2. Thermal Modelling

The surface emitting lasers described in this thesis are limited in output power by the ohmic heating effects of current injection. The major source of heating, particularly in the case of MBE grown devices, is a result of the reverse biased heterointerfaces in the Bragg reflectors. The second heat source is due to the p-i-n diode formed about the optical cavity. This drops approximately 1.0V in forward bias. The external differential efficiency above threshold is ~20% so at least 0.8V of this bias is comprised of a thermal source in the active region. This is most significant in the case of the MOCVD grown devices from QT421 where the threshold voltage is below 2V. The design of the reflector stack has a critical effect on the ohmic resistance and was discussed in detail in chapter 5. The effect of bulk resistivity in-between heterointerfaces and in the substrate is likely to be small in comparison.

8.2.1. A simple thermal model

Here we attempt to produce a thermal model of the of the device. We shall approximate a mesa etched device as a circular disc shaped heat source of diameter d on a semi-infinite GaAs substrate as shown in fig. 8.7.

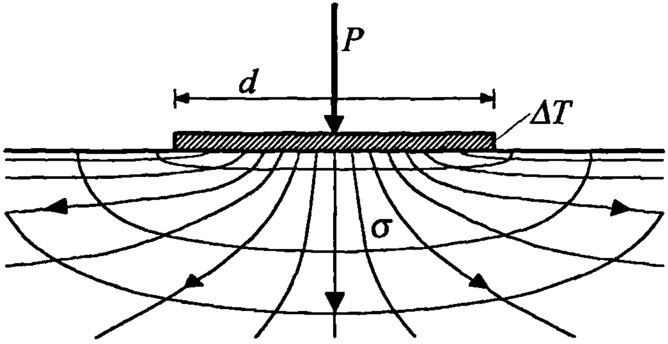

Fig. 8.7. Approximation used for thermal model of mesa etched VCSEL device; circular disc heat source of diameter d at uniform temperature ΔT above temperature at boundary of semi-infinite substrate medium of thermal conductivity σ.

The substrate thickness is 8 times the diameter of the large 50μm devices so the semi-infinite model should be acceptable. In reality, the thermal conductivity of the mesa is not infinite so a temperature profile will develop across the diameter d.

If the disc is a source of thermal power P and rises to a temperature ΔT, which we shall approximate as uniform, above that far from the device, then the solution to the problem is analytic and given by equation (8.3)[12].

$$\Delta T = \frac{P}{2d\sigma} \tag{8.3}$$

Where σ is the thermal conductivity of the substrate. For GaAs at 300K σ =0.45W.cm^{-1}.°C^{-1} [13].

A temperature rise produces a change in the refractive index Δn and in the dimensions of the semiconductor material Δl due to the thermal expansion coefficient α, at 300K (8.4) [14].

$$\Delta n = n_o\left(1 + 4.5\times10^{-5}\Delta T\right) \tag{8.4a}$$

$$\alpha = \frac{1}{l}\frac{\partial l}{\partial T} = 5.5\times10^{-6}.K^{-1} \tag{8.4b}$$

Where the temperature T is in degrees Kelvin and n_o is the original value of refractive index. For a GaAs based Fabry-Perot resonator of length l the wavelength of the Nth mode is given by equation (8.5).

$$\lambda_N = \frac{nl}{2N} \tag{8.5}$$

This is caused to shift with temperature as (8.6).

$$\frac{\partial\lambda_N}{\partial T} = \lambda_{No}\left(\frac{\partial(n/n_o)}{\partial T} + \frac{\partial(l/l_o)}{\partial T}\right) = \lambda_{No}5.05\times10^{-5}.K^{-1} \tag{8.6}$$

Where o refers to the original conditions. It is reasonable to assume similar temperature variations for Al$_x$Ga$_{1-x}$As compounds; thus for a VCSEL resonator all layers in the structure will be affected likewise and a shift as in (8.6) is expected.

For a structure resonant at λ_o=1000nm we expect a shift of (8.7).

$$\frac{\partial\lambda}{\partial T} = 0.0505nm.^{o}C^{-1} \tag{8.7}$$

A temperature rise of a few degrees in the temperature of a device will be readily detectable as a shift in the wavelength of the emission spectrum.

For a VCSEL device the thermal power dissipated is almost equal to the electrical input since the power conversion efficiency is low (and is almost zero below threshold). Thus at a current density J we expect a temperature rise above the ambient of ΔT (8.8)

$$\Delta T = \frac{P}{2d\sigma} = V.J\frac{\pi d}{8\sigma} \tag{8.8}$$

Where V is the bias voltage. Thus ΔT at threshold should increase in proportion to the device dimensions.

8.2.2. Results for etched mesa devices

Fig. 6.16 shows the c.w. output spectrum from a 50μm diameter etched mesa device from RMB627 at a number of different currents. The spectra show a red shift in the output with increasing drive current as well as an increase in the number of lasing modes. This was described in 6.4.3 as the development of filaments across a temperature profile. Increasing the current from 11 to 19mA corresponds to ΔP=62.4mW and gives a wavelength shift of 1.5nm towards the periphery of the device and 3.0nm towards the device centre. Using (8.7) we calculate the temperature rise as 29.70→59.41°C and the thermal impedance $\partial T/\partial P$=0.476→0.952°C.mW^{-1}. Table 8.4 shows the results for 50 and 20μm diameter devices from both RMB627 and QT421 layers. From these values an effective thermal conductivity σ_{eff} is calculated using equation (8.8), this is also shown in the table.

	50μm	**20μm**
$\Delta\lambda$	1.5→3.0*nm*	*2.88nm*
ΔI	8mA	3.5mA
ΔP	62.4mW	36.5mW
$\Delta\lambda/\Delta I$	0.188→0.375nm.mA^{-1}	0.823nm.mA^{-1}
$\Delta T/\Delta I$	3.723→7.426°C.mA^{-1}	16.29°C.mA^{-1}
$\Delta T/\Delta P$	0.476→0.952°C.mW^{-1}	1.564°C.mW^{-1}
σ_{eff}	0.105→0.210W.cm^{-1}.°C^{-1}	0.160W.cm^{-1}.°C^{-1}

(a)

	50μm	**20μm**
$\Delta\lambda$	2.1→2.7nm	1.48→1.67nm
ΔI	43mA	7.5mA
ΔP	98.4mW	31.7mW
$\Delta\lambda/\Delta I$	0.048→0.063nm.mA^{-1}	0.197→0.223nm.mA^{-1}
$\Delta T/\Delta I$	0.095→1.248°C.mA^{-1}	3.908→4.409°C.mA^{-1}
$\Delta T/\Delta P$	0.422→0.543°C.mW^{-1}	0.925→1.043°C.mW^{-1}
σ_{eff}	0.237→0.184W.cm^{-1}.°C^{-1}	0.240→0.270W.cm^{-1}.°C^{-1}

(b)

Table 8.4. Thermal parameters for etched mesa VCSEL devices under c.w. operation. Devices from; (a) RMB627 and (b) QT421.

Note that the active region has finite thermal conductivity and the assumption that the temperature rise is uniform is not valid. For 50μm diameter devices we deduce an effective thermal conductivity σ_{eff} of 0.105→0.210W.cm^{-1}.°C.$^{-1}$. This is somewhat less than the thermal conductivity of GaAs (0.45W.cm^{-1}.°C^{-1}) for two reasons: i) The thermal source is more distributed than is estimated in fig. 8.7 so there are extra thermal impedance terms which have not been considered, in particular the thermal resistance for heat flow down through the mesa; ii) The heterointerfaces in the Bragg reflectors have a high resistance due to potential spikes impeding the passage of electrons. Electrons play a part in the distribution of thermal energy so preventing their flow reduces the thermal conductivity. It is not necessary to use a more complete model since we may use the effective conductivity measured above in further calculations.

For the smaller 20μm diameter devices we calculate an effective thermal conductivity σ_{eff}=0.160W.cm^{-1}.°C.$^{-1}$. This is very close to the average value (0.158W.cm^{-1}.°C.$^{-1}$) for 50μm devices. This validates the model described above. As predicted the specific temperature rise $\partial T/\partial J$ varies in proportion to the diameter d which implies that smaller mesas can handle higher power densities[15].

Now considering the QT421 devices. For 50μm devices the *shift per unit* current is reduced by a factor 6.0 compared with RMB627 devices. This is largely due to the large reduction in series resistance afforded by the highly doped reflectors reducing the threshold voltage from 7.8 to 1.9V for the two devices studied here. Comparing the thermal impedances ($\Delta T/\Delta P$) of the two devices reveals a reduction by a factor of 1.75 in the centre of the devices. The thermal mass of the QT421 device indicates an average effective thermal conductivity of 0.211W.cm^{-1}.°C.$^{-1}$. This increased conductivity may be due to increased charge carrier conductance through the Bragg reflectors or a reduced mesa height. This may explain the more uniform temperature profile evident in the output spectra as the ratio of minimum to maximum shifts of the output modes: for 50μm devices the ratio of maximum to minimum shifts is only 1.3 compared to 2.0 for RMB627 devices.

For 20μm devices from QT421 we calculate a slightly larger average value of σ_{eff}(0.255W.cm^{-1}.°C.$^{-1}$) than for the larger device. This indicates a more distributed thermal source than for the RMB627 devices. This would be the case if the resistance of the lower reflector, which is not fully etched, becomes more significant as a heat source. In this case significant power is dissipated in areas away from the mesa, the effect of which is to reduce the amount of heating particularly for small devices.

8.2.3. Implanted devices

The geometry of the implant defined devices is somewhat different. The current flow is funnelled through the top reflector so heating is more distributed and there is more semiconductor around the device to aid conduction. Fig. 8.8 shows a device with active diameter d in a square mesa of side a. For the devices studied here a=80μm.

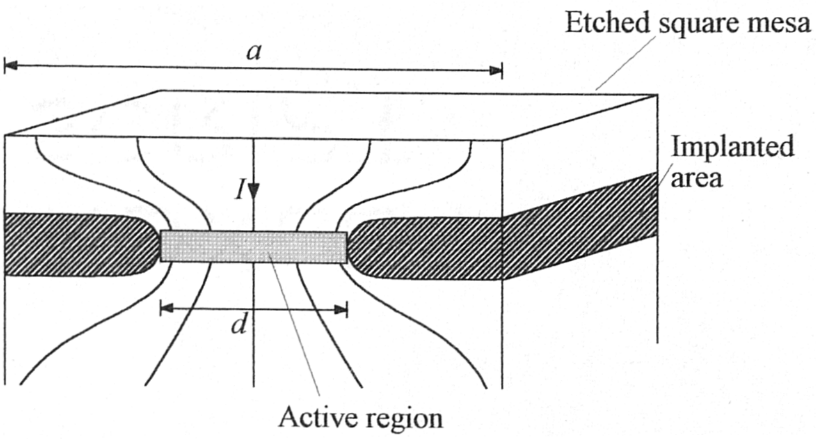

Fig. 8.8. Geometry of implant defined devices. Active diameter d lies within a square mesa of side a. Funnelling of the current I is indicated by the curved lines

Dimensional analysis may be used to analyse the problem. If we consider the important parameters as *a*, *d*, *σ* and *∂T/∂P* we can form two independent dimensionless groups (8.9).

$$\frac{\sigma d}{\partial T/\partial P} \quad , \quad \frac{d}{a} \tag{8.9}$$

By comparison with (8.3) we see that the solution is of the form (8.10)

$$\frac{\partial T}{\partial P}=\frac{1}{2d\sigma}\cdot f(d/a) \tag{8.10}$$

For some function *f*. Limits for *f* are defined by comparison with (8.3) and by considering an infinite mesa (8.11). A similar treatment of the problem is made by Nakwaski & Osinski[16].

$$f(1)\approx 1 \tag{8.11a}$$

$$f(x\rightarrow 0)=C \tag{8.11b}$$

For some constant $C<1$. A 50μm device occupies only 30% of the 80μm mesa so for this and smaller devices we take the infinite mesa approximation (8.12).

$$\frac{\partial T}{\partial P}\approx\frac{C}{2d\sigma} \tag{8.12}$$

C will depend on the device geometry so we shall refer to it as the ***shape factor***.

8.2.4. Results for ion implanted devices

The table 8.5 presents thermal data for ion-implanted devices from RMB627. We note that, for 50μm devices, the ratio of maximum to minimum shifts is reduced from 2.0, in the case of etched mesa devices, to 1.7. This indicates that the temperature profile in the ion-implanted devices is more uniform as a result of the large surrounding mesa. However for 20μm etched devices only one mode is evident in the output spectrum, indicating the possibility of thermal lensing effects[17,18].

The ratio of thermal masses for 20 and 50μm devices is 2.36 for measurements at the device centres. The ratio of diameters is 2.50. This suggests that equation (8.12) is valid. By comparing with data for etched mesa devices we determine that the shape factor C is 0.49 (as determined from 50μm devices, a similar value of 0.44 is determined from 20μm devices). Also shown in table 8.5 is the reduced effective thermal conductivity σ_{eff}/C.

	50μm	**20μm**
$\Delta\lambda$	1.9→3.2nm	1.4→1.9nm
ΔI	21mA	5mA
ΔP	133.7mW	31.5mW
$\Delta\lambda/\Delta I$	0.090→0.152nm.mA^{-1}	0.280→0.380nm.mA^{-1}
$\Delta T/\Delta I$	1.78→3.01°C.mA^{-1}	5.54→7.52°C.mA^{-1}
$\Delta T/\Delta P$	0.281→0.474°C.mW^{-1}	0.880→1.119°C.mW^{-1}
σ_{eff}/C	0.211→0.356W.°C^{-1}.cm^{-1}	0.223→0.284W.°C^{-1}.cm^{-1}

Table 8.5. Thermal parameters for RMB627 ion-implanted devices.

By comparing the temperature rise with current for the etched and implanted devices we see another advantage of the implanted geometry in addition to the shape factor. This ratio is 2.47 which is 1.23/C or 1.23 times the difference due to C alone. Considering the change of electrical power with current, which is equivalent to a voltage V_P (8.13) we can explain this difference.

$$\frac{\partial P}{\partial I} = V + I\frac{\partial V}{\partial I} = V_P \tag{8.13}$$

For the etched mesa device the differential slope resistance is effectively zero above threshold hence V_P is the bias voltage of 7.8V (fig. 6.10). For the implanted device around 22.5mA (mean current) the bias voltage is 5.3V and the differential slope resistance is 42Ω giving V_P=6.24V (fig. 6.20). The ratio of these two is 1.25 accounting for the difference noted above.

Thus as well as a reduced thermal mass (by a factor 1/C=2.01) the implanted device operates at lower voltages since the effect of current funnelling[19] in the implanted mesa (fig. 8.7) reduces the device resistance. This would give an improvement of 1.47 but the etched device is approaching the thermal runaway.

condition where the differential resistance is zero hence the change of power with voltage is reduced and the ratio is reduced to 1.25 (1.23 is the measured value).

8.3. Operating power range

8.3.1. Ohmic heating effects

When operating under c.w. conditions the effects of ohmic heating are most severe. As the temperature of the device rises the Fermi distributions of electrons and holes is broadened. This has two effects; i) the population of low energy states is reduced as carriers are thermally excited into higher states. These lower states are important for lasing transitions, thus the optical gain is reduced. ii) Carriers with increased thermal energy can be thermionically ejected out of the quantum wells and lost to other recombination mechanisms. This results in a reduced carrier concentration for the same drive current. This is a thermally activated process and around room temperature increases rapidly with temperature[6]. Similarly other thermally activated recombination processes such as Auger[3] are increased and in the same way can reduce the carrier concentration. Both of these effects, i) and ii), result in a reduced optical gain. These effects vary exponentially with temperature and thus with current.

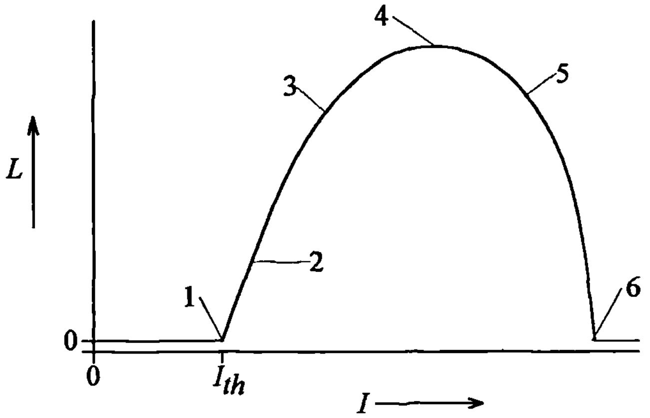

Fig. 8.9. L-I response expected from VCSEL device operated c.w. The regimes of operation (1-6) are described in the text.

Under c.w. operation we would expect an L-I response as shown in fig. 8.9 as a result of ohmic heating. The regimes of operation (*1-6*) are described in the following:

Close to threshold *1* the familiar linear L-I relationship *2* is expected. As the current is increased the power dissipated in the ohmic heating sources will increase and the device performance will begin to be affected. With increasing temperature in the active region the optical gain of the quantum wells will drop. The carrier concentration will rise to maintain the threshold gain and consequently the current available to produce light output is reduced as the current due to non-radiative recombinations increases[4,20], as illustrated in fig. 8.10. This is manifested in a reduction in the differential quantum efficiency seen as a reduction in slope of the L-I curve *3*. At higher currents the increase in the loss mechanisms begins to outweigh the increase in current and the light output reaches its maximum value *4*. With further increase in current the output falls as the losses increase ever more rapidly *5*. Eventually the non-radiative losses become so large that the threshold condition cannot be maintained *6*. At currents higher than this there is no net stimulated emission.

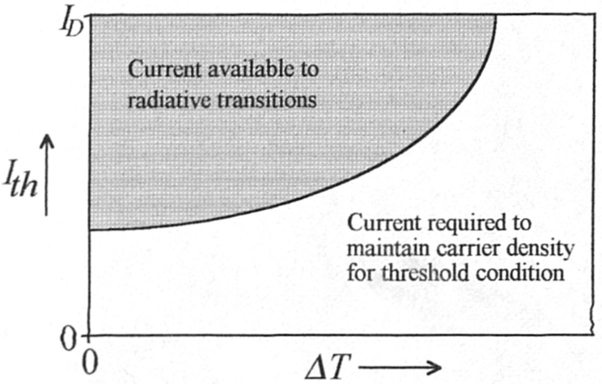

Fig. 8.10. Illustration of variation of radiative and non-radiative currents with device temperature. With increasing temperature increasing carrier loss mechanisms require a larger fraction of the drive current I_D to maintain threshold and the current available for light emission is reduced.

8.3.2. Thermal model for size effects

Assuming a linear increase in device temperature ΔT with current (this is reasonable since under c.w. conditions the forward voltage is almost constant above threshold) we would expect the temperature of the active region at which we measure maximum light output to be constant for devices fabricated from similar material. Let this temperature be ΔT_{max} above ambient conditions, i.e. room temperature ~22°C, and let it occur at a current density J_{max} in a particular device. From section 8.2. we would expect a relation of the form (8.14).

$$J_{max} = \frac{8\sigma\Delta T_{max}}{C\pi d V_{th}} \propto \frac{1}{d} \qquad (8.14)$$

Where C=1 for etched mesa devices and C=0.49 for implant defined devices. Thus J_{max} should scale with $1/d$.

8.3.3. Results for devices of varying size

Fig. 8.11 shows the relation $J_{max}(1/d)$ for ion-implanted and mesa etched devices from RMB627. Data is from tables 6.3 and 6.6. Note that it is necessary to adjust the ion-implanted data to account for a 5mA leakage current through the implanted area. This current is assumed not to contribute to heating since it is distributed over a large area. The adjusted data and data for mesa devices lie very close to straight lines the slope of which are given in (8.15).

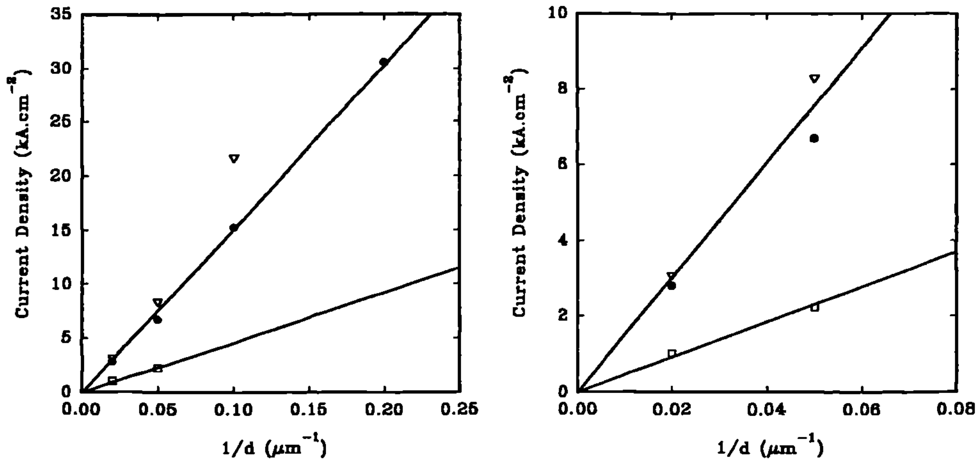

(a) *(b)*

Fig. 8.11. (a) Variation of current density for maximum light output for VCSEL devices from RMB627; ∇ ion-implanted devices raw data and ● adjusted to account for leakage, □ mesa etched devices. (b) Data for large devices on expanded scale.

$$J_{max} = 152 kA.cm^{-2}.\mu m/d \text{ - ion implanted} \qquad (8.15a)$$

$$J_{max} = 46.2 kA.cm^{-2}.\mu m/d \text{ - mesa etched} \qquad (8.15b)$$

This confirms equation (8.14). The ratio of the two slopes is 3.29 this means that the output of implant defined devices is limited at a value 3.29 times that in etched mesa devices of the same active diameter. From 8.2.2 and 8.2.4 we have $(\Delta T/\Delta P)_{etched}/(\Delta T/\Delta P)_{implanted}=2.01$ for the device centre. This is the factor $1/C$ in equation (8.12). There is also a change in bias voltage $V_{etched}/V_{implanted}=1.59$. The product of these two ratios is 3.20 equal to $J_{max(etched)}/J_{max(implanted)}$ within experimental error.

For mesa etched devices from QT421 we plot corresponding data for maximum light output on fig. 8.12. A line is fitted through the data; the fit is not as good as for RMB627 devices, possibly due to distributed heating effects[21] mentioned in section 8.2.2 or to material variations between devices. The slope of this line is given in (8.16).

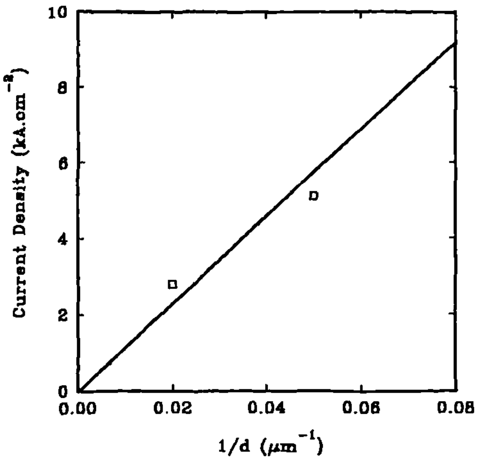

Fig. 8.12. Variation of current density for maximum light output for mesa etched VCSEL devices from QT421.

$$J_{max} = 115kA.cm^{-2}.\mu m/d \text{ - mesa etched} \tag{8.16}$$

This is 2.5 times the current density as in RMB627 devices. There is a factor of 6.0 difference between the values of $\Delta T/\Delta I$ for these structures. This indicates a limiting temperature rise for maximum output 2.5/6.0=42% of that in the MBE grown structure.

Thermal runaway is not a problem for the smaller devices hence the differential resistances of the two devices scale with the bias voltages. We may therefore use the bias voltage V in place of the term V_P of equation (8.12).

We can calculate ΔT_{max} (8.17):

$$\Delta T_{max} = \frac{\partial T}{\partial I} \cdot I_{max} \tag{8.17}$$

For RMB627, using results for 50µm devices, we calculate ΔT_{max}=148°C (etched), 165°C (implanted). Thus the active region temperature for maximum light output is approximately 178°C in the device centre.

Similarly for QT421 etched devices we calculate ΔT_{max}=85°C corresponding to an active region temperature of 107°C. It is unclear why this temperature is so much lower than for RMB627 devices. One explanation might be that the maximum temperature rise in the device is not the limiting one i.e. in a device in which the centre is heated by ΔT_{max} the edges are at a lower temperature and filaments may still lase there. However we calculate similar temperatures for etched and implanted devices of RMB627, which have different temperature profiles, suggesting that this is not the case. From 8.1 we remember that QT421 has a higher threshold gain. As the temperature rises it is conceivable that gain compression increases also. This would mean that the threshold current for a laser with higher threshold gain will rise faster with temperature and give a reduced ΔT_{max}. Scott *et al.*[6] calculate a value of ΔT_{max}

=75°C for similar structures but note that it will be much increased if the active region is clad by larger potential barriers.

8.3.4. Pulsed operation

For a current step dissipating power P applied at time t=0 from (8.12) we would expect the device temperature to rise with time as shown in equation (8.18).

$$\frac{\Delta T}{P} = \left(1-e^{-t/\tau}\right)\cdot\frac{C}{2d\sigma} \qquad (8.18)$$

For some time constant τ. If now the pulse length is t then (8.18) describes the maximum temperature rise of the device during the pulse. If the pulse is short compared with the time constant we may approximate (8.19).

$$\Delta T \approx \frac{Pt}{\tau}\cdot\frac{C}{2d\sigma} = \left(\frac{\partial T}{\partial P}\right)_{c.w.}\cdot\frac{Pt}{\tau} \qquad (8.19)$$

Where Pt is the pulse energy and the c.w. thermal impedance is as previously determined. From Fig. 6.11 we see that for 50μm diameter RMB627 devices driven by 0.43μs pulses a maximum light output is obtained. Table 8.6 presents this information and equation (8.19) is used to calculate the time constant τ assuming ΔT_{max}≈150°C as found above.

	Etched	**Implanted**
$(\Delta T/\Delta P)_{cw}$	0.952°C.mW^{-1}	0.474°C.mW^{-1}
$I_{max\ light}$	200mA	560mA
$V_{max\ light}$	15V	10V
P	3.0W	5.6W
Lt	6.5nJ	16.3nJ
Pt	1.29μJ	2.41μJ
τ	8.2μs	7.6μs

Table 8.6. Figures used to calculate thermal time constant τ for 50μm diameter RMB627 VCSEL devices.

A value of τ≈8μs is calculated for both etched and implant defined devices. Thus the assumption that the pulse length of 0.43μs is short was correct. The values of Pt in the table give the pulse energy for maximum light output for any short pulse. The value Lt is the maximum output pulse energy. Thus an implant defined device is able to supply optical pulses 2.5 times the energy of those from an etched mesa device.

Similarly for etched 50μm devices from QT421, data from fig. 6.14a we estimate $\tau \approx 6.8\mu s$. A faster thermal response would be consistent with increased thermal conductivity. Notice that the maximum optical pulse is 3.0 times that for etched devices from RMB627 despite the reduced value of ΔT_{max}. This is a result of the lower bias resistance. This is summarised in table 8.7.

	Etched
$(\Delta T/\Delta P)_{cw}$	0.543°C.mW^{-1}
I_{max} ***light***	340mA
V_{max} ***light***	7.3V
P	2.5W
Lt	19.8nJ
Pt	1.07μJ
τ	6.8μs

Table 8.7. Figures used to calculate thermal time constant τ for 50μm diameter QT421 mesa etched VCSEL devices.

Electrical gain switching has been successfully observed in VCSELs by Hasnain *et al*[22]. The spectral linewidth of 22ps pulses is almost transform limited because the cavity resonance is not readily chirped by changes in the index of the thin quantum wells. The maximum pulse energy, as determined above, will limit the output of gain switched devices. Picosecond pulses are useful for pumping solid state lasers with high thresholds and for making use of optical non-linearities. They may be used to excite solitons in optical fibres for which low chirp is also required.

8.3.5. Wavelength dependence of operating range

In operation, VCSEL devices heat up due to the flow of current through the reflector layers; a number of effects result. The cavity resonance mode shifts to longer wavelengths due to changes in the refractive index and the device dimensions. The bandgap of the semiconductor material shrinks causing the optical gain spectrum also to shift to longer wavelengths. The relative positions of the cavity resonance and the gain spectrum will determine the laser output for a given carrier injection.

Other important effects include the carrier loss mechanisms. (i) Thermionic emission of carriers from the quantum wells at elevated temperatures increases the current required to maintain the carrier concentration required for threshold. The effect of this is more severe in shallower quantum wells[4,23]. (ii) Auger recombinations tend to follow an Arrhenius thermal activation law; the recombination rate can increase very rapidly with temperature[3]. (ii) For a given carrier concentration n, the gain $g(n)$ will tend to fall as the temperature rises. The Fermi distribution of carriers in the conduction and valence band states broadens with increasing temperature; this tends to decrease the proportion of carriers in lower energy states which are important for lasing, so the gain falls. The effect of a reduction in $g(n)$ is to cause n to rise to maintain the threshold condition and the result is in an increased spontaneous recombination current (varies as n^2). The effect of (i)-(iii) is to reduce the current available for conversion to light output.

For etched devices from RMB627 the effects of resistive heating are so severe that only those with the smallest pulsed threshold currents (cavity resonance close to 1018nm) are able to lase c.w (see section 6.4.3). Thermal reduction of the gain limits the maximum output to 0.35mW at ~20mA. This is a power conversion efficiency of 0.22%.

For ion implanted devices the reduced heating effects, afforded by the lower ohmic and thermal resistances[19], allow higher operating currents and thus higher output powers. For example, a power of 1.65mW is produced at a current of 60mW (section 6.6.4). This corresponds to a power conversion efficiency of 0.46%, an improvement by a factor of 2.1 over etched mesa devices. The larger operating range means that devices with less well positioned cavity resonances may operate c.w. In section 6.6.5, measurements on a number of devices identified the c.w. operating range as devices with cavity resonances from 987 to 1066nm. A minimum c.w. threshold of 12mA was identified for devices resonant at ~1020nm (resonant wavelength measured under pulsed conditions). This is compared with a minimum of 10.5mA at 1014nm under pulsed conditions. The maximum c.w. light output is 1.4mW (as determined from the curve fitted through data) for a cavity resonant at 1028nm. The wavelength difference observed between the minimum threshold and maximum light output conditions is due to the red shift with temperature of the gain spectrum with respect to the cavity resonance[23]. This improves the alignment between the gain spectrum and cavity resonance for devices resonant at wavelengths longer than ~1014nm.

This change in alignment also causes a reduction in the threshold current for devices resonant at long wavelengths; for example the device resonant at 1059.9nm has a c.w. threshold current of 66mA, the corresponding pulsed value is ~200mA. The reduction is less for devices closer to the minimum threshold. The reverse happens at short wavelengths, i.e. the c.w. threshold current is higher than under pulsed conditions (see fig. 6.36).

In order to clarify these data we can adjust for the effects of shifts in the cavity resonance and gain spectrum. This leaves only the thermal effects due to the loss mechanisms (i)-(iii) above. From equation (7.7) we have the wavelength shift of the cavity mode (7.20).

$$\frac{\partial \lambda_{FP}}{\partial T} = 0.0505 nm.^{o}C^{-1} \qquad (8.20)$$

The bandgap of GaAs varies with the temperature in Kelvin T as (8.21) [14], from which we find the shift per unit temperature (8.22).

$$E_g = 1.519 - \frac{5.405 \times 10^{-4} T^2}{T + 204} (eV) \qquad (8.21)$$

$$\frac{\partial E_g}{\partial T} = -5.405 \times 10^{-4} \frac{(408 + T)T}{(T + 204)^2} \left(eV.K^{-1}\right) \qquad (8.22)$$

At room temperature (300K) the shift is –0.4519meV.°C^{-1}. Assuming a similar shift for the dependence of bound transitions in InGaAs / GaAs quantum wells we calculate the shift in the gain spectrum. The transition wavelength λ_{tr} corresponding to an energy E_{tr} is given by equation (8.23).

$$\lambda_{tr} = \frac{hc}{E_{tr}} \qquad (8.23)$$

This will shift with temperature as (8.24)

$$\frac{\partial \lambda_{tr}}{\partial T} = -\frac{\lambda_{tr}}{E_{tr}} \cdot \frac{\partial E_{tr}}{\partial T} \qquad (8.24)$$

Using the figure for GaAs we find that for a transition at 1000nm (1.24eV) the shift is 0.3644nm.°C^{-1}. The relative shift is therefore (8.25):

$$\frac{\partial \lambda}{\partial T} = \frac{\partial \lambda_{tr}}{\partial T} - \frac{\partial \lambda_{FP}}{\partial T} = 0.3139 nm.^{o}C^{-1} \qquad (3.25)$$

From table 7.5 we find the device temperature rise with current is on average 2.4°C.mA^{-1}. Combining this with (3.25) the relative shift with current is (3.26).

$$\frac{\partial \lambda}{\partial T} = 0.7534 nm.mA^{-1} \qquad (3.26)$$

Using this figure the measured data is adjusted to give effective values of wavelength taking into account the relative shifts of cavity mode and gain spectrum. This is shown in fig. 8.13.

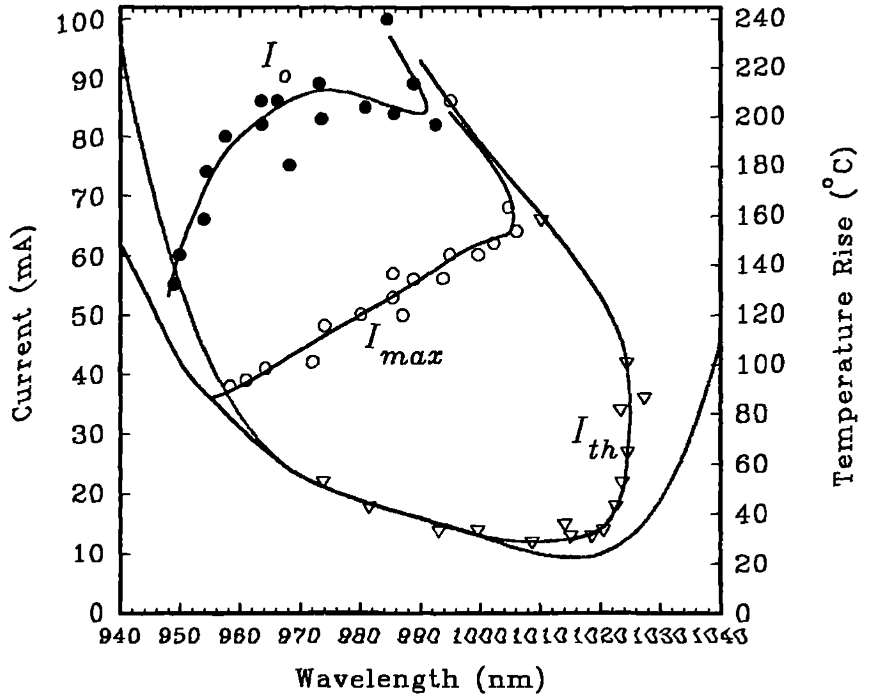

Fig. 8.13. Variation of current parameters for c.w. L-I response of 50μm diameter implant defined devices. The wavelength scale is adjusted to account for relative shifts of the cavity resonance and gain spectrum with temperature. I_{th} *is the threshold current,* P_{max} *the maximum output power and* I_{max} *the current at which this is measured.* I_o *is the current at which the coherent emission falls to zero. The grey line shows the function* $I_{th}(\lambda)$ *for pulsed operation.*

The threshold data now lie much closer to the line for pulsed data, with a minimum at ~1010nm. At wavelengths longer than 1020nm the threshold is seen to increase much more rapidly than under pulsed conditions. This indicates the true effect of temperature on the threshold current[20,24] (see right hand axis in fig. 8.13). The current at which the output falls to zero I_o tends to increase with wavelength because the resonance is moving closer to the gain peak situated at ~1020nm. This reaches a limit at 990nm where it joins the I_{th} curve. The region between these two curves gives the c.w. operating range for the devices. This envelope relates only to devices of this size made from the same material. For devices with a lower resistance or more effective heatsinking the envelope will be widened ant the value of I_{th} will correspond more closely to the pulsed value.

Fig. 8.14 shows the relation between the peak output and the current I_{max} at which it occurs. The low current end of this graph indicates devices resonant at short wavelengths. Heating causes the gain spectrum to shift away from the resonance so the output is limited at a low value. As the wavelength moves closer to the gain peak the maximum output increases until, for cavities resonant at wavelengths longer than

1028nm (where the temperature rise at the peak is 130°C), temperature begins to limit the maximum available gain and we note a drop in the maximum output. If the temperature did not limit the gain the curve would continue to rise.

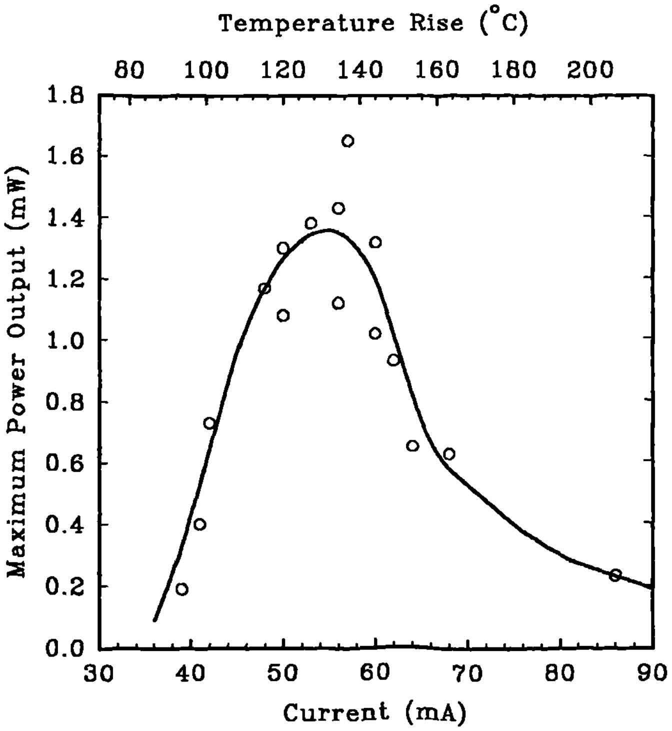

Fig. 8. 14. Variation of maximum output P_{max} from implanted 50μm diameter lasers from RMB627 with current I_{max}, indicating the reduction due to excessive heating.

Fig. 8.15 provides a summary of the operation of these devices. Fig. 8.15a shows a device operating at a short wavelength: at *1* the gain is below threshold so there is little light output. As the current is increased the gain increases until threshold is reached, somewhere below *2*. With increasing current the gain spectrum is continually moving to longer wavelengths, so the peak gain must increase to maintain the threshold gain g_{th} at the cavity resonance. This requires an increasing proportion of the current and eventually *4* the threshold can no longer be maintained. There is also a reduction in the gain at elevated temperatures *5*.

Fig. 8.15b shows a device operating at a long wavelength: at low currents *1* the cavity resonance lies outside the gain spectrum. With increasing current the spectrum shifts into better alignment with the resonance due to the increase in temperature and to bandgap renormalization; the threshold condition is then reached *2*. The improvement in the wavelength alignment continues to improve *3* and the threshold carrier density is reduced. Eventually *4*, *5* and *6*, thermal effects begin to increase the threshold carrier density and limit the light output, even in devices in which the wavelength alignment continues to improve.

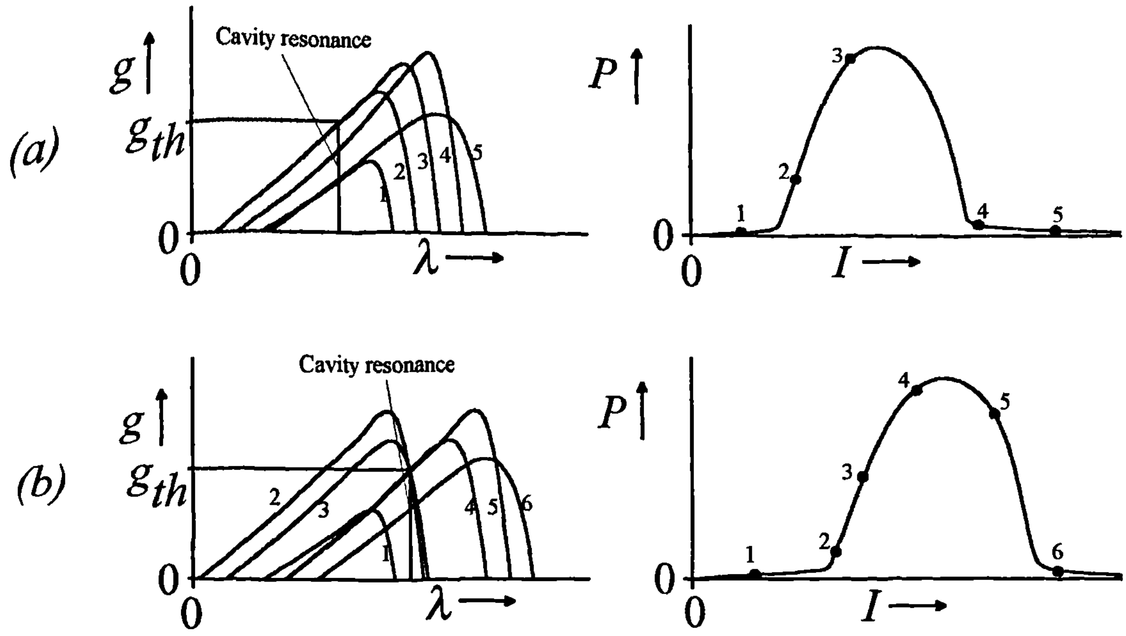

Fig. 8.15. Diagrams illustrating the effect of shifts in the gain spectrum (left) on the current light response (right), the shift in the cavity resonance is small in comparison and ignored for clarity. (a) device operating to the short wavelength side of minimum threshold current; (b) device operating to long wavelength side of this point.

There have been a number of studies on the subject of the wavelength alignment between the optical gain spectrum and the FP resonance in VCSELs[5,23,25,26,27]. Choquette *et al.*[25] observe a monotonic increase with current of the spontaneous emission emitted laterally from a VCSEL, even above I_0. They argue that this must imply a continued increase in the maximum gain available: i.e. P_{max} is limited by wavelength alignment effects rather that a reduction in the maximum gain. This is not entirely true since the spontaneous emission will vary as n^2, whilst the transparency density varies as $(kT)^{3/2}$ (3.23). Thus we would expect the spontaneous emission to increase as T^3 if the gain remains unchanged. Measurements presented here (fig. 8.14) confirm that the gain is limited at device high temperatures and we cannot continue to get increased light output by going to longer and longer wavelengths.

Young *et al.*[23] examine the use of a gain offset to increase P_{max} and study the temperature variation due to tuning of the threshold current in these structures; however they do not specify the offset needed or examine the limits of operation.

From the data presented here we find a maximum output power of 1.4mW for a devices resonant at 1028nm. The minimum pulsed threshold current occurs for devices resonant at 1014nm; a difference in wavelength of only 1.4%. The maximum output power here is reduced to 1.2mW, a reduction of 14%. Therefore the design of a structure for maximum peak power requires a structure little different from that for minimum threshold current, and the maximum output power in this case is only 14% less. The difference in these specifications is less than likely growth errors (see chapter 4). In most practical situations, the linear part of the L-I response is more important than the peak value; better performance in this part of the spectrum requires devices with minimum threshold.

Scott *et al.* consider the effects of carrier loss mechanisms, in particular thermionic emission from the wells and leakage currents, and, using a thermal model for mesa etched devices, predict accurately the c.w. L-I response of devices operating at different ambient temperatures. They also predict the improvements of using higher confinement barriers in the quantum wells. This identifies a major factor in limiting the gain and hence maximum output power as carrier escape from the wells.

8.4. Reflector resistance

8.5.1. General comments

The problem of resistance has already been discussed in detail in chapter 4. The conclusions here were that the band edge discontinuities at heterointerfaces in an AlAs / GaAs reflector stack cause an excessive resistance even when very highly doped. To reduce this it is necessary to disrupt the interface by including layers of intermediate composition or using a superlattice grade. The effects of this on the reflectivity are small, especially if doping to high concentrations is only included in the vicinity of the interfaces. The problems of solubility of Be in AlGaAs were highlighted. By using Zn and C p-type dopant in MOCVD and also by reducing the concentration of O traps, devices were produced with threshold voltages as low as 1.8V (15mA pulsed threshold), this is comparable to the lowest reported for devices with current injection through the mirror stacks, except for continuously graded structures. The reduction of resistance reduces the bias voltage required for operation; this increases the power conversion efficiency and increases the operating range of the devices since the temperature rise due to the current flow is reduced.

8.5.2. Ion implanted devices

Ion implanted devices were successfully made from the MBE grown structure RMB627 (section 6.6). The current blocking layer so produced (section 4.3.5) allows current to be funnelled from a large contact pad into a smaller active diameter. The increased size of mesa gives a reduction in resistance. At threshold the bias voltage for a 50μm active diameter was reduced[19] from 7.5V in the case of etched mesa device to 4.6V in a proton implanted device. Further to this reduction in bias, there is also a reduction in the thermal resistance[16] (8.2.3). Both of these improvements allow operation to higher currents.

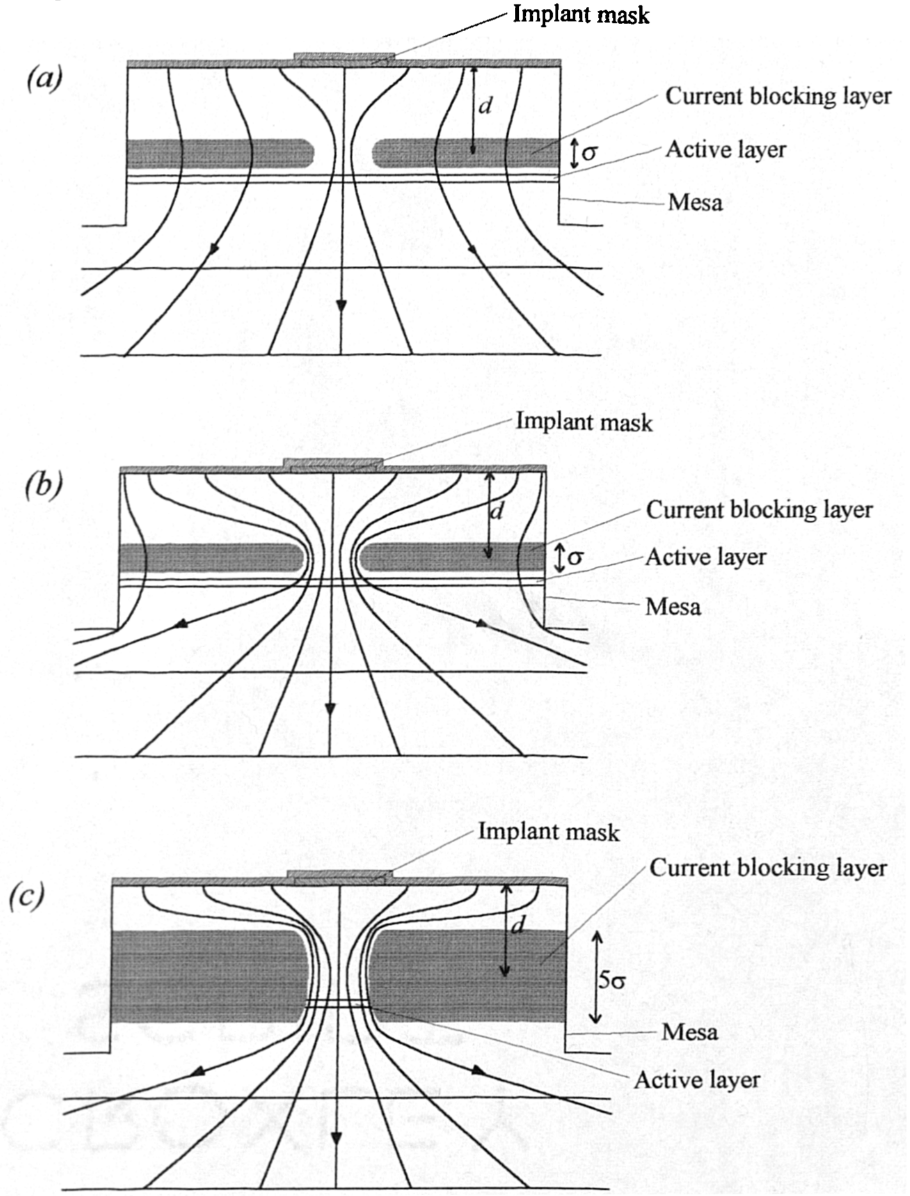

Fig. 8.16. Current flow in ion implanted devices. (a) A device implanted with 3×10^{12}*.cm*$^{-2}$ *200keV protons, there is little isolation in the implanted region and much current leaks through it. (b) Device implanted with dose of* $\sim1\times10^{14}$*.cm*$^{-2}$*, there is little leakage through the implanted region and current is funnelled effectively into the intended active area. (c) Device with excessive implant dose,* $>1\times10^{15}$*.cm*$^{-2}$ *ions, current blocking layer is thicker and lateral conduction channel in upper reflector is narrowed. There is also a similar pinch off of the active diameter.*

Only one ion dose was used for the RMB627 devices (2×10^{13}.cm^{-2}); this was an estimated optimum value[28]. In section 7.7 a number of samples from QT421 were prepared and implanted with doses in the range $3\times10^{12}.cm^{-2} \rightarrow 1\times10^{15}.cm^{-2}$. None of these operated as lasers but useful I-V measurements were made. The conclusions of these measurements include: The lowest dose used ($3\times10^{12}.cm^{-2}$) provides very little isolation, as shown in fig. 8.16a. A dose of $\sim1\times10^{13}.cm^{-2}$ is required to reduce the current flowing by a factor of two. A dose of $1\times10^{14}.cm^{-2}$ reduces the leakage through the implanted region to 2% of the threshold of a 50μm device which is 0.4mA (fig. 8.16b). Higher doses improve the isolation and reduce the leakage through the 80μm square mesa below 5nA. But the device resistance continues to increase for what is a rather insignificant reduction in operating current. This is illustrated in fig. 8.16c. The implanted protons create insulating material at a depth d=0.76μm with a vertical and lateral straggle of σ=0.2μm [29]. At an implant dose of $1\times10^{15}.cm^{-2}$ the ion damage is equivalent to the current blocking created by an ion dose of $1\times10^{13}.cm^{-2}$ at a distance of 2.3σ from the mean implant depth (using the normal distribution). The thickness of the current blocking layer is therefore increased to almost 1.0μm in this case. This produces an increase in the resistance of the current funnel by pinching off the conducting region in the top reflector. A similar lateral narrowing of the active diameter occurs from the lateral straggle.

From this we conclude that the optimum implant dose for 200keV protons[30] is in the range $3\times10^{13}.cm^{-2}$ to $1\times10^{14}.cm^{-2}$. To reduce leakage in smaller active diameters it is better to reduce the mesa size than to increase the implant dose. Increased implant doses are likely to increase carrier losses from the active region and create absorption centres, particularly for small active areas.

References:

[1] J.L.Jewell & G.R.Olbright, *Surface-emitting lasers emerge from the laboratory*, Laser Focus World, pp213-223, May 1993.

[2] Z-M.Li, M.Dion, S.P.McAlister, R.L.Williams & G.C.Aers, *Incorporation of strain effects into a two-dimensional model of quantum-well lasers*, IEEE J. Quantum Electron., **29**, 2, pp346-354, 1993.

[3] G.P.Agrawal & N.K.Dutta, *Long-wavelength semiconductor lasers*, Van Nostrand Reinhold, New York, 1986.

[4] P.R.Claisse & G.W.Taylor, *Internal quantum efficiency of laser diodes*, Electron. Lett., **28**, 21, pp1991-1992, 1992.

---

[5] J.W.Scott, S.W.corzine, D.B.Young & L.A.Coldren, *Modelling the current to light characteristics of index-guided vertical-cavity surface-emitting lasers*, Appl. Phys. Lett., **62**, 10, pp1050-1052, 1993.

[6] J.W.Scott, R.S.Geels, S.W.Corzine & L.A.Coldren, *Modelling temperature effects and spatial hole burning to optimize vertical-cavity surface-emitting laser performance*, IEEE J. Quantum Electron., **29**, 6, pp1295-1308, 1993.

[7] F.Stern, *Calculated spectral dependence of gain in excited GaAs*, J. Appl. Phys., **47**, 12, pp5382-5386, 1976.

[8] J.O'Gorman & A.F.J.Levi, *Wavelength dependence of T_0 in InGaAsP semiconductor laser diodes*, Appl. Phys. Lett., **62**, 17, pp2009-2011, 1993.

[9] J.O'Gorman & A.F.J.Levi, *Effect of fixed emission wavelength on threshold current of InGaAsP semiconductor laser diodes*, Electron. Lett., **28**, 22, pp2091-2093, 1992.

[10] P.Zhou, J.Cheng, C.F.Schaus, S.Z.Sun, K.Zheng, E.Armour, C.Hains, W.Hsin, D.R.Myers & G.A.Vawter, *Low series resistance high-efficiency GaAs / AlGaAs vertical-cavity surface-emitting lasers with continuously graded mirrors grown by MOCVD*, IEEE Photon. Technol. Lett., **3**, 7, pp591-593, 1991.

[11] J.W.Matthews & A.E.Blakeslee, *Defects in epitaxial multilayers*, J. Crystal Growth, **27**, pp118-125, 1974.

[12] J.P.Holman, *Heat transfer*, 6th Edition, McGraw Hill, Singapore, 1986.

[13] S.Adachi, *GaAs, AlAs & $Al_xGa_{1-x}As$: material parameters for use in research and device applications*, J. Appl. Phys., **58**, 3, ppR1-R29, 1985.

[14] J.S.Blakemore, *Semiconducting and other major properties of gallium arsenide*, J. Appl. Phys., **53**, 10, ppR123-R181, 1992.

[15] M.G.Peters, F.H.Peters, D.B.Young, J.W.Scott, B.J.Thiebeault & L.A.Coldren, *High wallplug efficiency vertical-cavity surface-emitting lasers using lower barrier DBR mirrors*, Electron. Lett., **29**, 2, pp170-172, 1993.

[16] W.Nakwaski & M.Osinski, *Thermal resistance of top-surface-emitting vertical-cavity semiconductor lasers and monolithic two-dimensional arrays*, Electron Lett., **28**, 6, pp572-574, 1992.

[17] D.Vakshoori, J.D.Wynn, G.J.Zydzik, R.E.Leibenguth, M.T.Asom, K.Kojima & R.A.Morgan, *Top-surface emitting lasers with 1.9V threshold voltage and the effect of spatial hole burning on their transverse mode operation and efficiencies*, Appl. Phys. Lett., **62**, 13, pp1448-1450, 1993.

---

[18] N.K.Dutta, L.W.Tu, G.Hasnain, G.Zydzik, Y.H.Wang & A.Y.Cho, *Anomalous temporal response of gain guided surface emitting lasers*, Electron. Lett., **27**, 3, pp208-210, 1991.

[19] W.Nakwaski, M.Osinski & J.Cheng, *Spreading resistance in proton-implanted vertical-cavity surface-emitting diode lasers*, Appl. Phys. Lett., **61**, 26, pp3101-3103, 1992.

[20] N.K.Dutta, J.Lopata, D.L.Svico & A.Y.Cho, *Temperature dependence of threshold of strained quantum well lasers*, Appl. Phys. Lett., **58**, 11, pp1125-1127, 1991.

[21] M.Osinski & W.Nakwaski, *Effective thermal conductivity of 1.55μm InGaAsP / InP vertical-cavity surface-emitting microlasers*, Electron. Lett., **29**, 11, pp1015-1016, 1993.

[22] G.Hasnain, J.M.Weisenfeld, T.C.Damen, J.Shah, J.D.Wynn & A.Y.Cho, *Electrically gain-switched vertical-cavity surface-emitting lasers*, IEEE Photon. Technol. Lett., **4**, 1, pp6-9, 1993.

[23] D.B.Young, J.W.Scott, F.H.Peters, B.J.Thibeault, S.W.Corzine, M.G.Peters, S-L.Lee, & L.A.Coldren, *High-power temperature insensitive gain-offset InGaAs / GaAs vertical-cavity surface-emitting lasers*, IEEE Photon. Technol. Lett., **3**, 4, pp129-132, 1993.

[24] R.J.Fu, C.S.Hong, E.Y.Chan, D.H.Booher & L.Figueroa, *High-temperature operation of InGaAs strained quantum-well lasers*, IEEE Photon. Technol. Lett., **3**, 4, pp308-310, 1991.

[25] K.D.Choquette, N.Tabatabaie & R.E.Leibenguth, *Detector-enclosed vertical-cavity surface emitting lasers*, Electron. Lett., **29**, 5, pp466-467, 1993.

[26] B.Tell, K.F.Brown-Goebeler, R.E.Leibenguth, F.M.Baez & Y.H.Lee, *Temperature dependence of GaAs / AlGaAs vertical cavity surface emitting lasers*, Appl. Phys. Lett., **60**, 6, pp683-685, 1992.

[27] P.L.Gourley, S.K.Lyo, T.M.Brennan, B.E.Hammons, C.F.Schaus & S.Sun, *Lasing threshold in quantum well surface-emitting lasers: Many-body effects and temperature dependence*, Appl. Phys. Lett., **55**, 26, pp2698-2700, 1989.

[28] M.Orenstein, N.G.Stoffel, A.C.Von Lehmen, J.P.Harbison & L.T.Florez, *Efficient continuous wave operation of vertical cavity semiconductor lasers using buried-compensation layers to optimize current flow*, Appl. Phys. Lett., **59**, 1, pp31-33, 1989.

[29] C.Jeynes, *Results of ion scattering calculations performed at the University of Surrey*, Private communication.

---

[30] P.Ressel, H.Strunsy, S.Gramlich, U.Zeimer, J.Sebastian & K.Vogel, *Optimised proton implantation step for vertical-cavity surface-emitting lasers*, Electron. Lett., **29**, 10, pp918-919, 1993.

9. Conclusions and Further Work

9.1. Conclusions of this thesis

9.1.1. Introduction

The theory of operation of vertical cavity surface emitting lasers (VCSELs) has been studied in detail in this thesis. The results of these studies were used to design VCSEL structures which were subsequently grown by MOCVD and MBE. The operating characteristics of fabricated devices were investigated and the become the subject of further theoretical study.

The basic design of the structures incorporates three strained InGaAs active quantum wells placed resonantly in a GaAs optical cavity two wavelengths long. The cavity is formed between AlAs / GaAs multilayer Bragg reflectors with reflectivities of ~0.998. The use of strained InGaAs quantum wells gives emission at wavelengths longer than the GaAs band edge so output may be taken through the transparent GaAs substrate; strain effects alter the band structure to reduce the transparency carrier density.

9.1.2. Reflectivity issues

In chapter 2 the reflectivity spectra of the multilayer reflectors is calculated and their effects on the optical gain required for threshold is considered. It is found that an absorption coefficient of $10.\mathrm{cm}^{-1}$ in all layers of the laser is sufficient to require double the threshold gain of that for a device made from lossless material. This absorption corresponds to dopant concentrations of the order $10^{18}.\mathrm{cm}^{-3}$. If, by modulation of the doping, the absorption is confined only to thin regions around the heterointerfaces in the reflector stacks which are subject to a reverse bias, then the absorption may be increased to $160.\mathrm{cm}^{-1}$ for the same increase in gain at threshold.

The effects of growth errors in the thickness of reflector layers is considered. Random layer to layer variations with standard deviation up to 5% may be tolerated. However, offsets between the upper and lower reflector centre wavelengths and the cavity dimension can significantly reduce the laser performance. This is more noticeable in higher quality structures (see fig. 2.1.5). Offsets of this type may, in part, give rise to the increased threshold current of the MOCVD grown device QT421 as compared to the MBE grown structure.

9.1.3. Resistance considerations

Chapter 5 considers the ohmic resistance of the reflectors. AlAs / GaAs interfaces present large potential barriers to the flow of carriers into the higher bandgap material (AlAs) due to the large conduction and valence band offsets.

Thermionic emission over these will be small so the resistance will be large unless the dopant concentration is large enough so that band bending in the vicinity of the interface narrows the depletion width sufficiently to allow a significant tunnel current to flow through the potential spike created.

In practice it was not possible to dope the interfaces sufficiently to reduce the bias across a working device to an acceptable level. A complete VCSEL structure with abrupt reflector interfaces will drop more than 10V at threshold. Any voltage in excess of 1V acts purely as a thermal source. By splitting the interface discontinuity into smaller junctions it is possible to reduce the resistance considerably. For example; an n-type reflector grown by MOCVD incorporating abrupt interfaces drops a voltage of 0.29V/pair for a current of 20mA through a 50μm diameter mesa. By the inclusion of a 200Å intermediate layer of $Al_{0.3}Ga_{0.7}As$, the bias is reduced to 0.10V/pair. This is reduced even further to 0.029V/pair in low oxygen containing material.

MBE grown reflectors make use of 50% Al intermediate layers in the n-type reflectors; p-type mirrors incorporate a superlattice grade. The superlattice attempts to provide a continual grade of the miniband edge throughout the junction. A design making use of AlAs / $Al_{0.5}Ga_{0.5}As$ / GaAs layers was used. This structure presents less strain on the fragile MBE effusion cell shutters and provides more strongly coupled quantum wells than the binary compound superlattices used by other groups.

Be is used as an acceptor in MBE growth. It has a solubility limit of around $5\times 10^{17}.cm^{-3}$ in AlAs so it is difficult to achieve low resistance p-type reflectors. The bias at threshold for 50μm diameter mesa etched devices is 7.5V. This is reduced to 4.6V in implant defined devices by the use of a current funnel.

In MOCVD C and Zn act as acceptors. P-type concentrations in excess of $2\times 10^{18}.cm^{-3}$ are readily achievable in all AlGaAs compounds. With the use of low oxygen containing precursors and by modulation doping, it was possible to produce mesa etched devices with current injection through the full reflector stacks, which have threshold voltages as low as 1.7V (Note that 1V of this is the p-i-n diode forward bias voltage). It should be possible to reduce this voltage further by including more intermediate layers to achieve a more gradual grade in the reflector interfaces.

9.1.4. Effects of gain spectra

In the MBE system used for this work (VGV80), there is a paraboloidal variation in deposition thickness across the wafer. This is due to the geometry of the effusion cells. Devices with cavity resonances in the range 950 to 1059nm result from this variation. The e_1hh_1 transition in the $In_{0.235}Ga_{0.765}As$ quantum wells is essentially unchanged at ~1020nm ±2nm because of the weak relation of this energy to the well width. The variety of devices allowed a detail study to be made of the relation between the relative alignment of the cavity resonance (which determines the lasing wavelength) and the optical gain spectrum. The function relating the variation of the threshold current density with lasing wavelength $J_{th}(\lambda)$ was determined experimentally. This has a minimum of 366A.cm^{-2}, the lowest threshold current density reported for a VCSEL device, and is measured for devices operating at 1018nm, which is close to the e_1hh_1 transition. A gradual increase in threshold current is observed to shorter wavelengths as the gain spectrum broadens with increased carrier concentration. To longer wavelengths operation is also permitted because of bandgap renormalization effects.

A simple model incorporating strain effects is used to predict the gain spectra of the quantum wells. These are used to derive a $J_{th}(\lambda)$ relation; best fit to the experimental data is achieved assuming a 900ps non-radiative carrier lifetime and ignoring density dependant recombination mechanisms. The model predicts a flattening of the minimum in the $J_{th}(\lambda)$ relation for devices requiring a high threshold gain. This is observed to be the case for small diameter etched mesa devices.

Ion implanted devices show a similar wavelength relation. The minimum value of threshold is increased to 535A.cm^{-2}, in this case, by incomplete isolation of the implanted region. A higher implant dosage ($\sim 1\times10^{14}$.cm^{-3} 200keV H^+ ions) is necessary to reduce the leakage current. The thermal and ohmic resistances of these devices are greatly reduced; and the current for maximum light output is increased by a factor of three when that for compared to etched devices.

The effects of relative alignment of cavity mode and gain spectrum are particularly important for c.w. operation. Thermal heating causes bandgap shrinkage at high currents and the output power of devices resonant at short wavelengths is limited by the shift of the gain spectrum away from the cavity mode. For devices resonant to the long wavelength side of the e_1hh_1 transition, heating causes the alignment to improve and we observe that the threshold current under c.w. operation is lower than the value measured under pulsed conditions. However, at elevated temperatures the available gain is limited by the reorganisation of the carrier population and by an effective reduction of the non-radiative carrier lifetime. This means that the maximum output power of devices is ultimately limited by an increasing threshold current with increasing device temperature. Maximum output is obtained for devices resonant at 1028nm (measured for device at room temperature). This is only a 1% difference from the wavelength required for minimum threshold current.

9.1.5. Thermal model

A simple thermal model was developed for the dissipation of heat from mesa and implant defined VCSEL devices. There is good agreement between the model and experimental data. The model accurately predicts that the effects of heat are reduced in smaller devices; i.e. smaller devices may handle a larger current density. Since loss mechanisms related to edge effects give an increased threshold current density in smaller devices, the optimum device size is probably a 10 to 20μm diameter device.

9.1.6. MOCVD grown devices

The MOCVD grown devices described have threshold current densities as low as $764A.cm^{-2}$. This is higher than for the MBE grown devices because of errors in the growth thicknesses and non-optimal alignment of the gain spectrum and cavity resonance mode. The wafer these devices were fabricated from shows a uniformity of ±1% in the cavity resonance wavelength over 80% of its 2 inch diameter. Consequently it is suitable for the fabrication of very large arrays of uniform devices.

The low threshold voltage of these devices (as low as 1.7V) allows for low power consumption and reduced thermal heating effects.

9.2. Further work

In the introduction (chapter 1) a number of applications for VCSELs and laser arrays were mentioned. Much development is required to integrate devices into such systems. Here I shall only point out more immediate issues for the improvement of isolated devices.

The VCSEL devices produced during this work have been very successful. This is due to the growers ability to faithfully reproduce design specifications considered important for high performance. These specifications were determined from the theoretical analysis in this work. A margin of error was allowed in the design. The high quality of the interfaces in the epitaxially grown reflectors is evident in the low threshold current densities obtainable. This suggests that single quantum well devices may operate at even lower current densities, perhaps below $200A.cm^{-2}$, with no major changes in the design strategy.

As investigated in chapter 8, an increased In fraction in the quantum wells should produce lower threshold current devices. In deeper wells the $hh2$ and $lh1$ bands are removed further from the $hh1$ ground hole state. This gives a reduced density of valence states over a larger energy range and reduces the carrier density required for transparency. Indium fractions up to 35% should be possible. Carriers are better confined to deeper wells so improving the high temperature and high power operating range. Similarly growth on non-polar crystallographic axes (e.g. (111) or (211)) may be used to provide increased splitting by altering the heavy and light hole masses.

From results on test reflectors it should be possible to reduce the threshold voltage of MBE grown mesa etched devices below 4V and below 2.5V for ion-implanted devices.

MOCVD grown devices already operate at very low voltages. Better control of layer thickness, perhaps with the provision of in-situ optical monitoring, should allow threshold current densities more comparable with values obtainable with MBE grown material. Finer grading of the interfaces will allow reduced threshold voltages. Existing devices should operate at ~1.4V in the ion-implanted geometry.

Further modelling could be performed to include a more accurate solution of the InGaAs quantum well band structure. Other simplifications made in the gain calculations of chapter 3 could be reviewed to provide a better fit to the experimentally determined $J_{th}(\lambda)$ relation and allow a more educated design methodology. Most of the theoretical models presented in this thesis should be transferable to similar devices in other material systems.

Modelling could be performed on the effects of the relative offset between the gain spectrum and cavity resonance to predict the c.w. performance. This should take into account self heating effects which will depend on the reflector resistance. A more complex thermal model could consider the effects of current spreading in ion-implanted devices and examine the development of thermal lenses.

Devices in other materials systems are another interesting diversion. In particular InGaAsP based devices lattice matched to GaAs allow visible emission at red to orange wavelengths. Bragg reflectors may be constructed from AlGaAs compounds. Much learned in this thesis should be applicable to these new devices and high efficiency two-dimensional visible laser arrays should be possible in the near future. As mentioned in the introduction these have obvious display applications.

The End.